DAMAGE DETECTION IN LAMINATED COMPOSITE STRUCTURES USING DYNAMIC ANALYSIS

By

Ahmed Noori Uwayed

UNIVERSITY OF
LEICESTER

Department of Engineering

Leicester

United Kingdom

A thesis submitted to

The University of Leicester

For the degree of

Doctor of Philosophy (Ph.D.)

August 2018

Acknowledgments

Abstract

Thesis: Damage detection in laminated composite structures using dynamic analysis

Author: Ahmed Uwayed

Laminated composite materials are used in different applications, for example mechanical, civil and aerospace structures, due to their light weight and excellent mechanical properties. However, fibre breakage and delamination are among the more serious damage that often initiate and propagate due to a number of mechanical and, specifically, dynamic loads during the operational life. Also, these damages destroy design functionality of these structures. To address this issue, damage detection is required in time to provide a good understanding of structure state in advance of any potential failure. There are a number of damage detection approaches reported in the literature and reviewed herein. Some of these are base-line free, whilst others use the intact data as a reference for the detection of damaged sections. However, currently there are a very limited number of experimental studies in the literature that use vibration-based damage detection to detect the delaminated areas, and are almost non-existent for fibre breakage; the majority of simulated studies consider delamination only.

Defects in laminated structures are quite complicated and in most cases are hidden. Frequency-based damage detection is considered to be a global approach and is not useful when dealing with complex structures. There has been extensive research to develop the curvature mode shape as a reference for damage detection because it is highly sensitive at show the effects of damage. This sensitivity is tested in this research, as it is extremely difficult to detect damaged sections within composite materials, even with an active approach.

Hence, the main objective of this research is to develop the curvature damage index by calculating the irregularity curvature index, and the proposal of a novel index, called the Haar index, to support the damage detection process. Both these indexes are used to detect delamination and fibre breakage on high modulus CFRP plate structures under condition of free vibration. Using these indexes gives an efficient method by which to quantify and localize damaged areas in both theoretical and experimental considerations of different lay-ups. In the modelling section, two finite element software programs, COMSOL Multiphysics 5.1 (Licence No. 7074366) and ABAQUS 6.14-1 (Licence No. 200000000008515), are used. This thesis includes development procedure of the curvature index, calculates the Haar index, gives details of the theoretical and experimental analysis, and reports the consequent results and discussion.

List of symbols

Symbol	Meaning	Unit
$\overrightarrow{\phi}$	Displacement vector	m
A_k, B_k	Chebyshev coefficients	
$\left(\phi_{ij}\right)_D$	Damaged mode shape	
$\left(\phi_{ij}\right)_H$	Healthy mode shape	
$\overline{C_{J,k}}$	Coefficients of wavelet transform function with two orthogonal signals	
$\bar{Q}_{ij}$	Reduce stiffness matrix in random directions	Pa
$\vec{X}^{(i)}$	i^{th} modal vector	m
$\widetilde{e_1}$	Local base vector	
$\widetilde{u_1}$	Displacement component	m
$\widetilde{\beta_1}$	Rotational displacement component	rad
$\overline{\psi_{J,k}}$	Wavelet function with two scaling functions	
ϕ_r	Normalized mass mode	
A_i , A	Constant, cross sectional area	, m^2
A_{ij}	Extensional matrix of laminate	N/m
B_{ij}	Bending- extension matrix of laminate	N
C_0, C_1, C_2, C_3, C_4	Constants	
C_{ij}	Stiffness matrix of composite materials	Pa
$\ddot{D}$	Acceleration	m/s^2
DI_j	Damage index	
D_f	Stiffness reduction factor	
D_{ij}	Bending matrix of laminate	$N.m$
E_1, E_{11}	Young's modulus in $0°$	GPa
E_2, E_{22}	Young's modulus in $90°$	GPa
E_θ	Modulus of elasticity at any direction	GPa
G_{12}	Shear modulus	GPa

$[K]$	Stiffness matrix	N/m
K_ψ	Constant depends on the wavelet type	
M_x, M_y, M_{xy}	Bending and twisting moment components	$N.m$
N_x, N_y, N_{xy}	Axial and shear force components	N
$\vec{P}$	Load vector	
Q_i	$i\,th$ generalized force	
Q_{ij}	Reduce stiffness matrix	Pa
R^2	Irregularity index	
S_i	Vector generated by the original wave	
S_{ij}	Compliance matrix	$1/Pa$
T_k	k^{th} Chebyshev polynomials	
V_a, V_b	Velocity at point a and b	m/s
W_i	Deflection of W at $t = t_i$	m
e_{ij}	Error in the natural frequency	
f_D	Difference in frequency	Hz
f_n	Natural frequency	Hz
f_r, f_p	Frequency of receiver , frequency of particle	Hz
k_x, k_y, k_{xy}	Curvature along x and y axis and xy-plane	$1/m$
p_0, p_2, p_3	Constants	
q_n	Generalized coordinates	
$u_\circ, v_\circ, w_\circ,$	Components of the displacement vector at the laminate's mid-surface	m
u_c	Displacement of point C in laminate	m
v_{12}, v_{ij}	Major Poisson's ratio	
$v_{21,} v_{ji}$	Minor Poisson's ratio	
v_i	Displacement of mode shape	m
v_i''	Curvature index	
$\ddot{x}$	Acceleration component	$\dfrac{m}{s^2}$
$\dot{x}$	Velocity component	m/s

$x_0, \dot{x_0}$	Displacement and velocity at $t = 0$	$m, m/s$
z_{k+1}, z_{k-1}	The location of lamina to the middle surface	m
$\beta_{i,j}$	Damage index	
δ_i	Damage index	
ε_j	Strain components	
$\varepsilon_x, \varepsilon_y, \gamma_{xy}$	Strains along x and y axes and shear strain in xy-plane	
$\varepsilon_x^\circ, \varepsilon_y^\circ, \gamma_{xy}^\circ$	Strain of middle surface in laminate and shear strain	
λ_b	Laser beam wave length	m
μ_i	Mean	
$\sigma_1, \sigma_2, \tau_{12}$	Stresses along the fiber orientation and shear stress	MPa
$\sigma_x, \sigma_y, \tau_{xy}$	Stresses along x and y axes and shear stress in xy-plane	MPa
σ_i	Stress components , Standard deviation	$MPa, -$
ω_c	Damaged natural frequency	rad/s
ω_i	$i\,th$ Natural frequency	rad/s
ω_n, ω	Angular natural frequency	rad/s
ϕ_h''	Healthy curvature	
ϕ_d''	Damaged curvature	
ϕ_i	Eigenvector, mode shape	
$\emptyset$	Angle, phase angle	rad
$\emptyset(x), \psi(x)$	Reciprocally orthogonal components of the vibrational velocity distribution	m/s
Δ	determinant	
ΔF	Increment in F	N
ΔW	Energy dissipated in cycle	J
Δf	Measured frequency change	Hz
Δt	Increment in time t	s
Δx	Increment in x	m
C	Constant, Point through laminate thickness	

h	Element length	m
$h(x)$	weighted function	
u, v, w	Displacement along u, v and w axes	m
V_f	Fibre volume fraction	
w	waviness of the mode shape, weight	-, N
x, y, z	Cartesian coordinates	
$C(a, b)$	Coefficients of wavelet transform function	
D	Displacement matrix	m
F	Force	N
I	Area moment of inertia	m^4
J	Polar moment of inertia	m^4
L	Lagrange equation, Likelihood ratio, curve length	J, , m
M	Mass matrix	kg
N	Layer number, degrees of freedom, number of modes	
$P(\Delta\omega)$	Probability densities	
T	Kinetic energy, torque	J, N. m
U	Potential energy	J
V	Potential energy in Lagrange equation, shear force in vibration analysis	J, N
$V(t)$	Scanning LDV velocity output	m/s
W	Transverse deflection , weight	m, N
a, b	Scaling parameter in wavelet function, position parameter	
b, r, p	Subscripts of laser beam, receiver and particle	
c	Wave velocity	m/s
d	Max estimated diameter between the first point and the ith point in mode shape	m
dwt	Haar function in MATLAB	
e	Unit vector, error	
f	Force per unit length	N/m

$f(x)$	Function of x	
k	Spring constant, sequence of layers in laminate	N/m,
m	Mass of system	kg
m, n	Number of observations	
r	Radius of rotating shaft	m
t	Plate thickness, lamina thickness, time	m, m, s
$v(x, t)$	distribution of velocity	m/s
$x(t)$	Displacement mode	m
z	Distance from neutral axis to given lamina	m
Ω	Angular velocity	rad/s
β	Slop of middle surface of laminate, hysteresis damping constant, crack location ratio	
γ	Constant	
δ	Logarithmic decrement	
δD	Damage vector	
δW	Virtual work	$N.m$
δf	Analytical frequency change	Hz
θ	Angular orientation of a lamina , constant, angular displacement	
$\mu(x)$	Probability density	
ρ	Density	$\dfrac{kg}{m^3}$
τ	Period of oscillation	s
$\psi(t)$	Gabor wavelets	
$\psi(x)$	Mother wavelet function	

List of Abbreviations

A: Style of symmetric laminated layup

ADM: Absolute difference method

AE: Acoustic emissions

ASDEC: Advanced structural dynamic evolution center

AWCD: Approximated waveform capacity dimension

B: Another style of symmetric laminated layup

CDF: Curvature damage factor

CDT: Curvature damage factor

CFRP: Carbon fiber reinforced polymer

CNSH: Cumulative of normalize summation harmonic

CWT: Continues wavelet transform

Del: Delamination

DI: Damage index

DIM: Damage index method

EMA: Experimental modal analysis

ESPI: Electronic Speckle Pattern Interferometry

FB: Fiber breakage

FCM: Frequency curvature method

FD: Fractal dimension index

FDIDL: FD-based index for damage localization

FE: Finite element

FEA: Finite element analysis

FEM: Finite element method

FLS: Fuzzy Logic System

FRF: Frequency response function

GFD: Generalized fractal dimension index

GSM: Gapped smoothing method

GUI : Graphical user interface

KCD: Kurtosis crack detector

LDV: Laser Doppler vibrometer

MaTIC: Materials technology integration center

MC: Modal curvature

MDLAC: Multiple Damage Location Assurance Criterion

MDLAC: Multiple damage location assurance criterion

MoM lab: Mechanics of materials lab

NDE: Non-destructive evaluation

NDT: Non-destructive testing

ODS: Operating deflection shape

PT: Pulse thermography

SHM: Structural Health Monitoring

SQUID: Super Conducting Quantum Interference Device

SSI: Structural irregularity index

TSP: Thermographic signal processing

ULS: Uniform load surface

VDS: Vibration damage shapes

WTM: Wavelet Transform Method

$SGS(x)$: Simplified gapped-smoothing

List of Contents

List of Figures

List of Tables

Part 1

Introduction, Background Theories and Literature Review

Chapter 1: Introduction

Over the past few decades, composite materials have begun to see extensive use in different civil and mechanical structures. According to material terminology, composite materials are a combination of two or more materials on a macroscopic scale to produce a new high-performance form which can be used in different applications. A number of mechanical properties such as stiffness, strength, corrosion resistance, weight, fatigue life, thermal insulation, and conductivity, etc., can be improved by manufacturing this type of materials [1].

In the history of development, composite materials were found naturally in the wood of trees. This was utilized by the Egyptians (1500 B.C.) in the construction of reinforced walls in their living areas. Around 1800-A.D., metal strips were considered a remarkable source of new material, seeing use in military applications to manufacture weapons. In recent decades, composite materials have played an important role in daily life through their use in all types of civil and military applications and industries [2].

1.1   Classification of composite materials

Composite materials can be classified into four main categories according to the methods utilized in producing them. These types can be in form of fibres, particles, laminated composite structures, and mixture of these three types. The current research focuses on the investigation of the laminated type due to its extensive use in different mechanical structures.

Unidirectional laminated structure can be produced when fibres are laid up in matrix to produce fibre-reinforced composite structures. These structures offer high strength and stiffness to weight ratio, and this feature is considered important for applications that take the weight of individual components to account. In such cases, fibres might be configured in various form such as long, short, continuous and discontinuous, as well being aligned in single or multiple orientations depending on the design requirements, as shown in Fig 1-1.
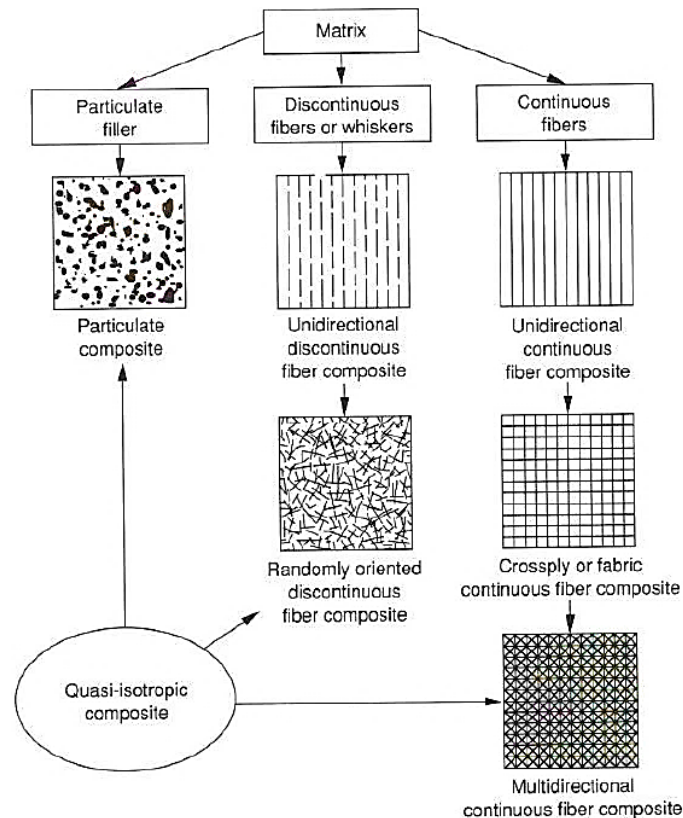
Fig 1-1: Fibre-reinforced composite material systems [3].

Long fibres in composite structures have dominated the field of laminated structures in particular, due to a number of their associated features. Long, continuous fibres are considered easy to orient in any direction and process, provide high impact resistance, show low shrinkage and have good surface finishing properties [2]. These features are important in engineering designs. Within composite structures, fibres are configured in a thin form called a lamina, or ply. In composite structures, lamina (also called a ply or a layer) is a single flat ply of a unidirectional nature or with woven fibres organized in a matrix. To explain this, the composite structure shown in Fig 1-2 shows that the basis of these structures consists of fibre and a matrix which are mixed in specific proportions to produce lamina, which are then combined in different orientations to produce the laminate; the final composite structure is produced by the combination of a number of laminates.
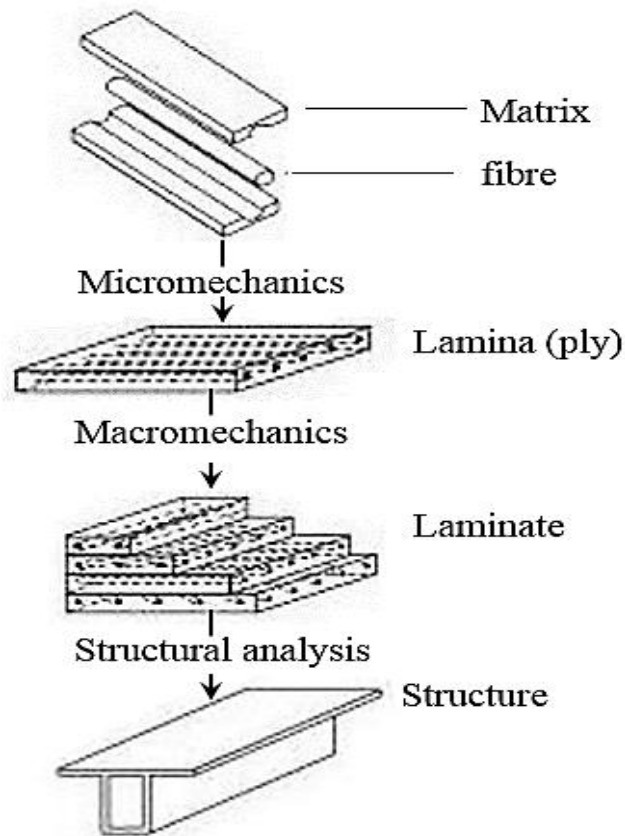
Fig 1-2: The level analysis of laminated structures starts from the individual elements that are combined to ultimately create the entire structure [4].

The second important concept is that composite materials can be classified into two main groups according to their physical properties. These two groups are isotropic and orthotropic materials. The mechanical definition of an isotropic material that this material's properties are the same in all directions, otherwise these properties are independent on location within a given component. Mathematically, if E represents the Young's modulus of an isotropic material, this means $E = E_\theta$, where E_θ is the modulus of elasticity in any direction within the plane of the ply (see Fig 1-3). In this type of structure, the material has an infinite number of symmetry planes. However, most of composite materials are neither isotropic nor homogeneous. For example, particulate composites consist of particles with different sizes and random distributions, so these composites might be considered as quasi-isotropic and quasi-homogeneous. The same concept can be applied with short or discontinuous fibres, where both of these composites can be anisotropic or quasi-isotropic as per Fig 1-1 [3].

By contrast, orthotropic materials have three mutually perpendicular planes of symmetry. The principal axes of this material are the intersections of these planes. In terms of unidirectional composites, orthotropy means that properties along the fibre direction are quite different to those in the perpendicular directions. Fig 1-3 illustrates this concept, so if the Cartesian coordinate system (which corresponds to the fibre orientation) is represented by axes 1, 2 and 3 (axis 3 is perpendicular to the plane of ply), then the modulus of elasticity in the direction of fibre can be defined as E_{11}, while in the perpendicular direction is E_{22} and in the normal axis is E_{33}.[5].
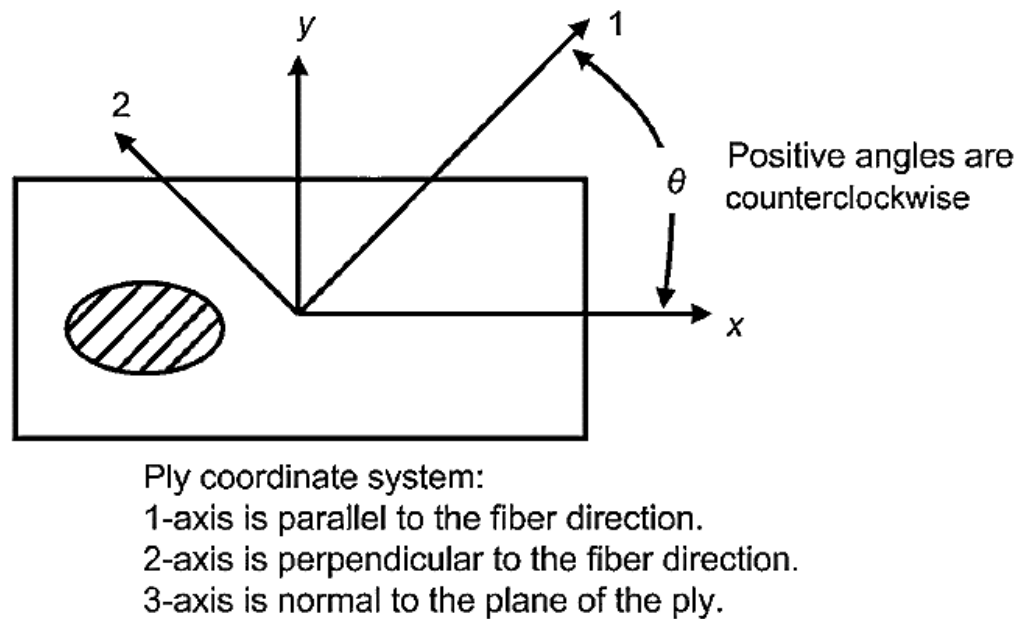
Fig 1-3: Ply angle definition [5].

According to the principles of materials and fibre-reinforced composite structures in particular, the properties of any structure depend on the properties of its individual components. In high performance structures, the fibres' role is significant due to their high stiffness and strength. To explain this point, Fig 1-4 provides stress-strain relationship for both matrix and fibres individually, and also as a composite. This means in a fibrous composite, the fibres have a strength that is greater than the matrix itself, and by mixing them one can introduce a composite structure with a strength that is dependent on the strength of the fibres and the matrix. Also, it is clear from Fig 1-5 that the fibres are principally responsible for composite materials' properties because, although they have small diameters, they can provide high strength and good ability to

carry different loads. Photomicrographs of transverse cross sections shown in Fig 1-6 are for two composites. It can be seen that the composite with the larger fibre diameter, 15 μm, (Fig 1-6a) has a fibre volume ratio that is less than for the composite with a low fibre diameter of 8 μm (Fig 1-6b). This confirms that composites with low fibre diameters have a greater strength than composites with large fibre diameters [3]. In addition, fibres show high crack resistance on their surfaces due to their excellent strength [5, 6].
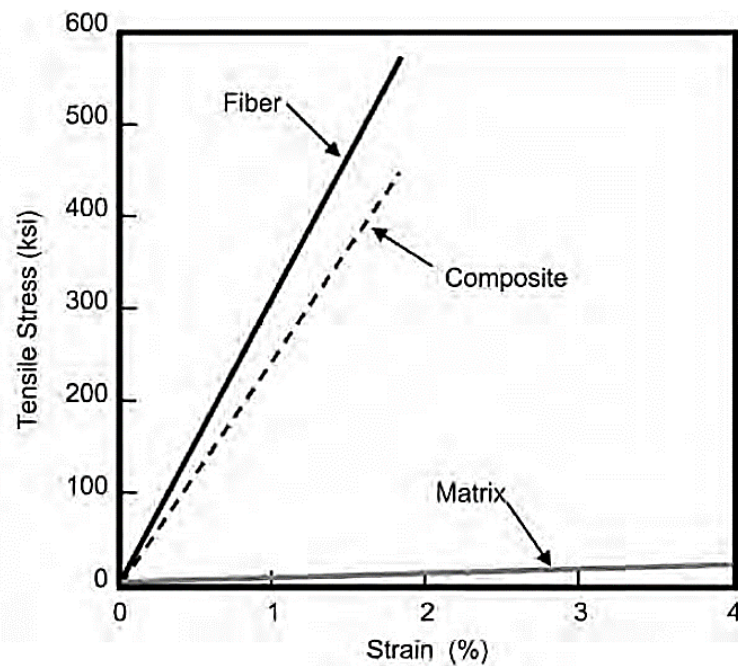
Fig 1-4: Illustration of fibre, matrix and composite of stress-strain behaviours [5].
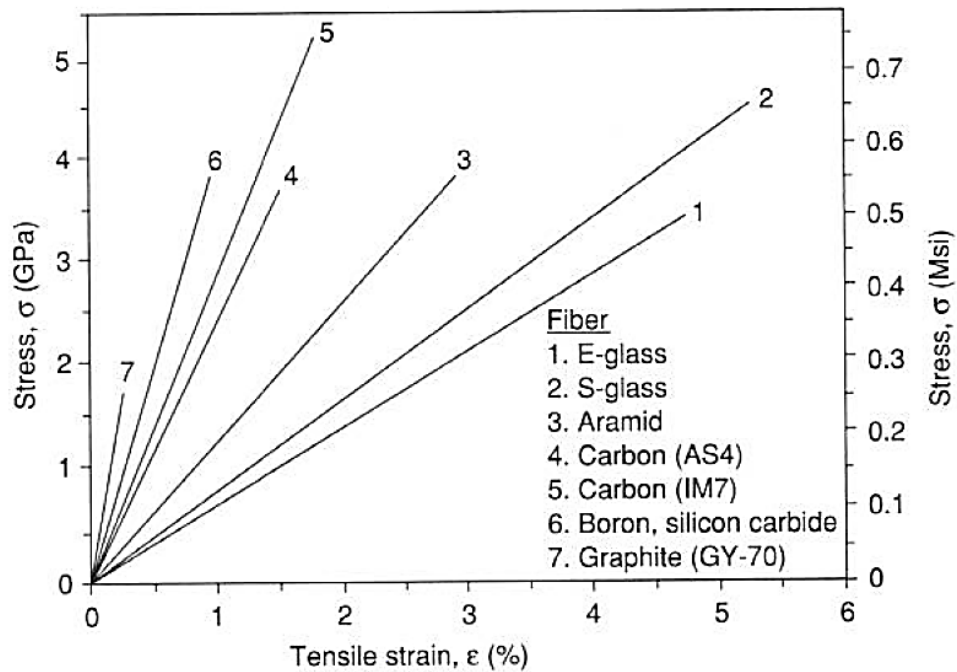
Fig 1-5: Stress-strain relationships for different types of reinforcing fibres [3].
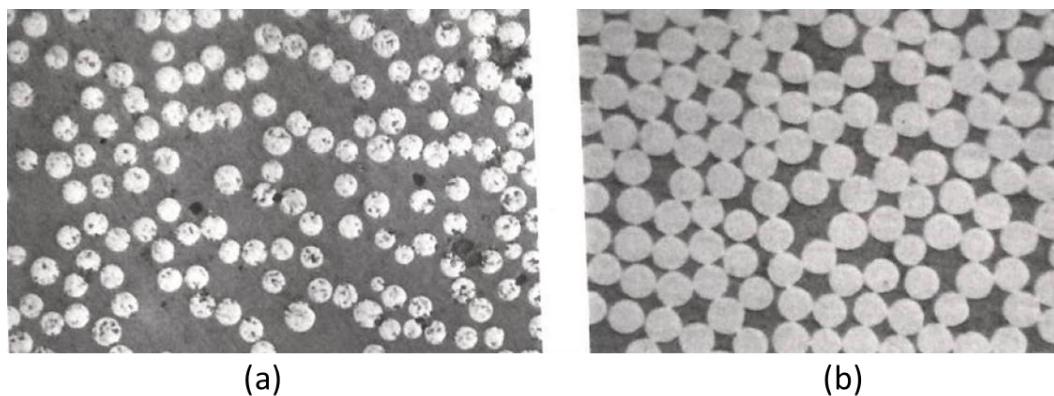
Fig 1-6: Typical transverse cross section areas of unidirectional composites: (a) silicon carbide/ glass ceramic average fibre diameter15 μm, fibre volume fraction V_f = 0.40 and (b) carbon/epoxy fibre diameter 8 μm, fibre volume fraction V_f = 0.70 [3].

Due to the use of composite materials in different mechanical industries, an extensive literature have produced on this subject. Jones [1] explained that since the 1960, the use of composite materials has been developed in four stages. First was mere hypothesising about utilizing this type of material, per the philosophy "let's see if we can build it ", while the second step was the testing of small pieces of composite materials by replacement of their traditional counterparts in aircraft. The third step was

the use of composites as essential parts of the airframe. Finally, there was the aspiration to build all-composite aircraft.

One of the most important characteristics in composite materials is their ability to provide a superior level of mechanical features such as the ratio of stiffness or strength to their weight. In some applications this can be greater than 16:1 (N / m. kg), (MPa / kg), and with graphite fibre composite structures may be greater than 40:1. In fact, there are many examples of the use of composite materials in the military aircraft industry. One example was the use of composite materials in manufacturing the General Dynamic F-111 wing-pivot fittings to avoid fatigue crack problems. Another example was replacement a metal 56 kg speed brake, which is used to reduce the speed of the Vought A-7 aircraft during landing, by a piece of composite of only 36 kg in weight. Moreover, the Boeing F-18 is another example of the use composite materials in various structures such as the wings, tail, vertical fins and regions that experience high static and dynamic stresses. In addition, composite materials are utilized in civil aircraft industries, for instance, the rear vertical fins in aircraft are comprised of composite materials to save on weight and costs [1]. The Boeing B787 ("Dreamliner") uses a composite material in different components in its original design, as seen in Fig 1-7. The list of the use composite materials in civil transport, space applications, and obviously in automotive implementations, is too extensive to consider in depth.
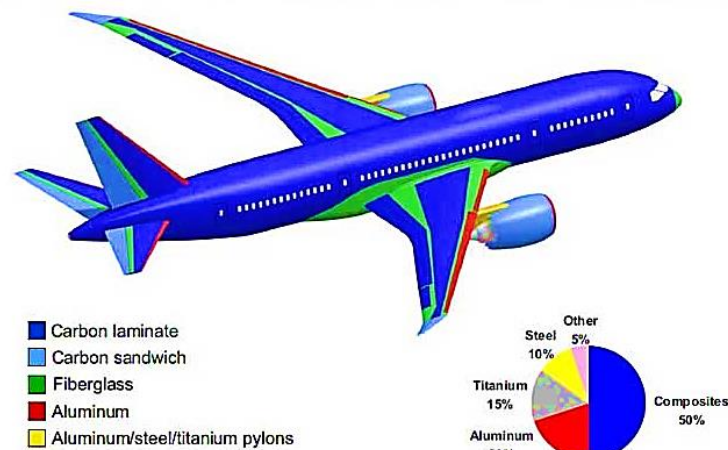
Fig 1-7: Use of composite materials in different parts of the Boeing 787 [7].

1.2   Influence of damages on composite structures

The demand for utilizing advanced materials such as composite materials with good mechanical properties and low weight has become increasingly common in civil and mechanical applications. These types of materials may require special manufacturing conditions during their production. In general composite materials in different applications show high damage resistance. However, the possibility of different types of damage modes are still expected under different applied loads during working life [8].

For the best understanding of the most important damage modes and the most serious influences of these types on composite structure behaviour, there are some significant definitions that should first be clarified. As Heslehurst [9] reported, the terms defect, flaw, and discontinuity in composite structures mean any accidental or unplanned local change of a physical state or mechanical characteristics of material that may cause an effect on the performance of the structure. Moreover, failure in composite materials can be found when either the entire structure or some of its components lose their functionality. Within laminated structures, when damage occurs to one lamina, the function of the entire structure is affected, due to the reduction of local stiffness. Another important concept is that damage in laminated structures can be classified into two main types, as reported by Tita [10]. The first type is called the intra-ply failure mode, as shown in Fig 1-9a, and Fig 1-9b. In this mode, damage occurs to the fibres, polymeric matrix and might happen to interface between fires and matrix. This means damage occurs to the ply itself. The second mode is inter-ply failure mode, when failure mode is essentially delamination between the adjacent plies, as per Fig 1-8.

There are a number of fibres damage mechanisms in the intra-ply damage mode as shown in Fig 1-9b, where mechanism 4 represents the fibre rupture. However, in composites, fibre failure depends on the type of applied load, where tensile loads can produce fibre rupture, while the compressing loads encourage the micro-buckling. The intra-ply damage in matrix depends on the temperature that matrix serve-in and its ductility. Whereas matrix can show brittle or plastic deformation (mechanism 5). Other failure mechanisms occur because the interface between matrix and fibre is weak, which is called "Pull-Out" (mechanism 1). Then fibre is pulled out after the occurrence of

debonding (mechanism 3). Moreover, fibre failure may occur due to the crushing of fibres by high concentrated loads or high velocity impact loads.

The inter-ply (delamination) occurs when the matrix cracks propagate into the inter-laminar surface and begin to debond the damaged region into two parts, as shown in Fig 1-8. In general, all forms of damage have a negative effect on the functionality of laminated composite structures by reducing their stiffness, even when this only happens locally. In fact, it reduces the entire strength of the damaged structure. In this sense, a damaged sample offers a completely different load-carrying ability. For a better understanding of failure mechanisms in laminated composite structures, Fig 1-9 shows all of these damage modes in more detail [10].
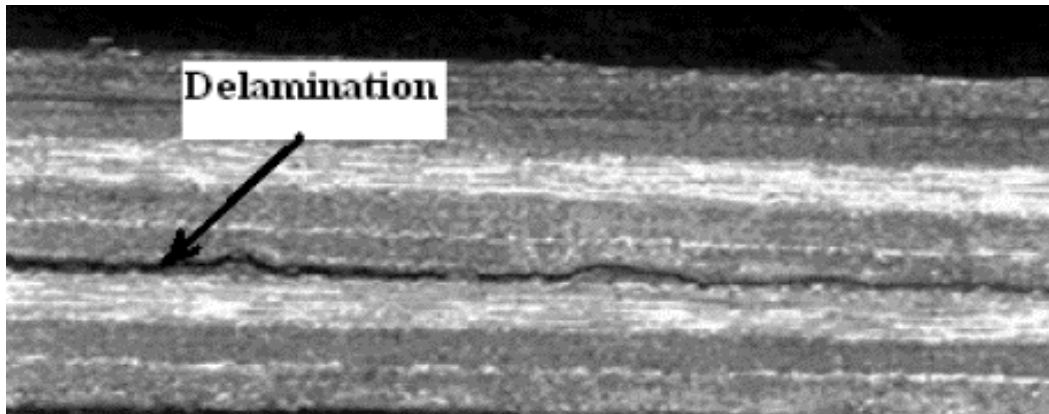
Fig 1-8: Microscopic-photo of delamination in FRP composites [11]
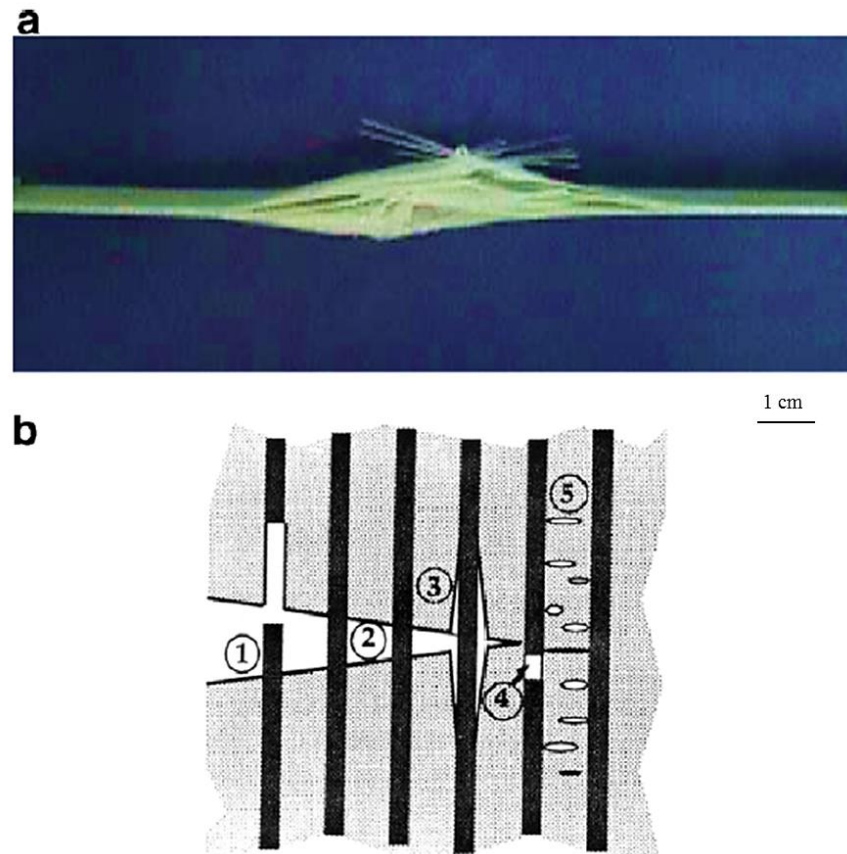
Fig 1-9: (a) Failure mechanisms of composite materials :intra-ply and inter-ply failures and (b) Intra-ply damages [10].

1.3   Damage detection methods in laminated composite structures

Damage analysis in laminated composite structures has been investigated by a number of researchers due to the extensive use of these structures in different practical applications. Although composite materials offer a high level of reliability in terms of mechanical properties, they are susceptible to the initiation and propagation of different forms of damage, though commonly in form of matrix cracks, fibre breakage and delamination [12]. The damage detection process in complex materials such as laminated composites is not a straightforward topic for all researchers and experimenters investigating structural health monitoring. The overall aim of damage detection is to ensure that these materials remain in the safe domain during their working lives. In general, the damage detection methods can be categorised into non-destructive testing (NDT) and vibration-based damage detection techniques.

Doebling and Farrar [13] reported that NDT (the inspection of an sample to test its integrity without affecting the use of this sample in the future) damage identification methods that depend on visualization, observation, and localization of damaged regions can be classified as experimental methods. For example, some of them depend on ultrasonic waves, analysis of the magnetic field of examined structures, radiographic monitoring of constructions, utilizing acoustic emission or by the thermal field method. However, in a more practical sense these methods have a number of limitations due to the data they provide and their actual utility for complex structures.

To overcome these limitations, researchers have tried to develop modern techniques to work with significant damage problems. Zhang et al. [14] reported that there have been remarkable efforts made to develop more modern techniques that are more practical in use than the more methods mentioned above. It was mentioned that vibration-based detection is one of the most important alternative methods. The key feature of this method that dynamic characteristics such as natural frequency, mode shape, and damping ratios are affected directly by any change in mechanical properties caused by the existence of damage in a given mechanical structure. In addition, vibration techniques can be used to identify and localize damage in a number of complicated, large and even in inaccessible structures. Furthermore, finite element technique provides useful role in modelling the mechanical problems, as recently this technique has been implemented in finite element software programs.

1.4   The objectives of the current Ph.D. research

The main purpose of the present research is to focus on damage detection in laminated carbon fibre-reinforced polymer (CFRP) structures, and to propose and develop vibration-based damage detection methods to quantify and localize delamination and fibre breakage in laminated structures under condition of free vibration. The specific purposes of this thesis can be listed as follows:

Objective 1:

> The finite element modelling (FEM) of a simple cantilever beam with and without damage using finite element FE software COMSOL Multiphysics 5.1 to evaluate a number of dynamic indexes and determine the most sensitive index under free vibration condition.

Objective 2:

> Manufacturing carbon fibre reinforced polymer (CFRP) plates with and without delamination and fibre breakage.

Objective 3:

> Damage detection (fibre breakage and delamination) in CFRP plates using vibration-based damage techniques. The numerical modelling is achieved using ABAQUS 6.14-1 software.

Objective 4:

> Experimental verification to methods described in objective 3.

Objective 5:

> Using the improved dynamic indexes (the irregularity and the Haar) to compare delamination and fibre breakage during the analysis of dynamic responses.

1.5   Thesis structure

The thesis is divided into eight chapters, which includes details of the research criteria. All the references cited in this thesis are listed in the "References" section. The following paragraphs briefly describe the content of each chapter in this thesis.

- Chapter 1 provides an introduction about the composite materials, effects of damage on composite structures, a brief definition of damage detection methods and the major objectives of this thesis.

- Chapter 2 includes two main parts. Part 1 provides an overview of the mechanics of composite materials. Stress-strain relationships of laminated structures are demonstrated. Part 2 explains the fundamentals of dynamic analysis, vibration of continuous systems and the most important issue, which is the fundamentals of calculating mode shape.

- Chapter 3 contains a literature review of common methods used to detect and localize damaged areas in different structures. The advantages and limitations of each method are also briefly discussed.

- Chapter 4 includes a comparative study on beam element models. The aim of this study is to evaluate a number of dynamic indexes and find the most sensitive for the purpose of damage detection.

- Chapter 5 summarises the practical steps used to prepare the experimental samples. The principles of laser Doppler vibrometer and data collection are presented.

- Chapter 6 presents modelling the laminated carbon fibre reinforced polymer with and without damage using ABAQUS to detect the damaged areas. FEA analysis results and discussion are discussed. Two plates with different lay-ups are used in this chapter. Comparison between detection of fibre breakage and delamination is illustrated.

- Chapter 7 presents the experimental results and discussion for the same laminated plates explained in chapter 6. In both chapter 6 and 7 vibration-based damage detection techniques are used to detect the damaged areas.

- Chapter 8 provides the conclusions and future work for this line of study.

Chapter 2: A review of constitutive law and dynamic analysis of laminated composite structures

2.1 Introduction

This chapter presents the mechanics of composite materials and fundamentals of dynamic analysis. To this end, it is divided into two sections, section 2.2, which is devoted to review the mechanics of laminated structures. Further, the aim is also to understand the effect of damage on reducing the local stiffness, which is the main premise behind the modelling of damaged sections. On the other hand, section 2.3 includes the demonstration of the fundamentals of the dynamic analysis of the vibrated objects. The relationship between mechanical properties and modal characteristics such as natural frequency, damping ratio and mode shape is explained to provide a good understanding for the effect of damaged sections on these characteristics.

2.2 A review of constitutive law of laminated composite structures

Composite structures, especially in laminate form with continuous fibres, show non-homogenous mechanical characteristics during their working life. This issue is not only due to their construction of bi- or sometimes multi-phases, but also according to lamination features; for instance, fibre orientations and lay-up sequence. In this sense, laminated structures clearly have different stress-strain relationships during their loading. This means the stiffness of laminated structures depends on the orientations of the fibres in each ply. In other words, each lamina might have different fibre orientations and consequently different stiffness. Also, the extension-shear or twisting-bending coupling has an important effect on the stress-strain relationship. This occurs due the un symmetry in layout of the layers and due to the complexity [composite structure consists of more than one material] of these structures [15]. Thus, it is important to demonstrate the mathematical principles of composite materials.

2.2.1 Elastic stress-strain relations for solid materials

The main purpose of this section is to provide a clear understanding of the relationships between different stress categories (principal and shear stresses) that are later used to formulate these relationships for laminated structures. To this end, the generalized form of Hooke's law given by Eq. (2.1) can be used [1]. In this formula, σ_i represent the stress components applied in direction i, C_{ij} is stiffness matrix and ε_j represents strain components.

$$\sigma_i = C_{ij}\, \varepsilon_j \qquad i,j = 1,\dots,6 \tag{2.1}$$

The stress-strain correlation as proposed by Kollár and Springer [4] can be formulated as per Eq. (2.2). Using Hooke's law, it is possible to calculate the components of stress-strain relations in the principal material coordinates 1, 2 and 3. Mathematically, according to the concept of equilibrium applied to any element in the elastic material, stress-strain relations can be written as shown in Eq. (2.2).

$$\begin{bmatrix} \sigma_1 \\ \sigma_2 \\ \sigma_3 \\ \tau_{23} \\ \tau_{13} \\ \tau_{12} \end{bmatrix} = \begin{bmatrix} C_{11} & C_{12} & C_{13} & C_{14} & C_{15} & C_{16} \\ C_{21} & C_{22} & C_{23} & C_{24} & C_{25} & C_{26} \\ C_{31} & C_{32} & C_{33} & C_{34} & C_{35} & C_{36} \\ C_{41} & C_{42} & C_{43} & C_{44} & C_{45} & C_{46} \\ C_{51} & C_{52} & C_{53} & C_{54} & C_{55} & C_{56} \\ C_{61} & C_{62} & C_{63} & C_{64} & C_{65} & C_{66} \end{bmatrix} \begin{bmatrix} \varepsilon_1 \\ \varepsilon_2 \\ \varepsilon_3 \\ \gamma_{23} \\ \gamma_{13} \\ \gamma_{12} \end{bmatrix} \tag{2.2}$$

Here, the matrix $[C_{ij}]$ represents the stiffness matrix of any material, and by calculating the inverse of Eq.(2.2), the strain-stress relationships can be formulated as per Eq.(2.3).

$$\begin{bmatrix} \varepsilon_1 \\ \varepsilon_2 \\ \varepsilon_3 \\ \gamma_{23} \\ \gamma_{13} \\ \gamma_{12} \end{bmatrix} = \begin{bmatrix} S_{11} & S_{12} & S_{13} & S_{14} & S_{15} & S_{16} \\ S_{21} & S_{22} & S_{23} & S_{24} & S_{25} & S_{26} \\ S_{31} & S_{32} & S_{33} & S_{34} & S_{35} & S_{36} \\ S_{41} & S_{42} & S_{43} & S_{44} & S_{45} & S_{46} \\ S_{51} & S_{52} & S_{53} & S_{54} & S_{55} & S_{56} \\ S_{61} & S_{62} & S_{63} & S_{64} & S_{65} & S_{66} \end{bmatrix} \begin{bmatrix} \sigma_1 \\ \sigma_2 \\ \sigma_3 \\ \tau_{23} \\ \tau_{13} \\ \tau_{12} \end{bmatrix} \tag{2.3}$$

where $[S_{ij}]$ is the compliance matrix in the 1, 2, and 3 coordinates system. Also, it should be noted that the above two Eqs.(2.2) and (2.3) clarify the general mathematical form that can be used to represent stiffness for any element in the composite material. In isotropic materials, where the material has an infinite number of symmetry planes, the

stiffness and compliance matrix require just two independent constants as demonstrated in Eqs. (2.4) and (2.5).

$$\begin{bmatrix} \sigma_1 \\ \sigma_2 \\ \sigma_3 \\ \tau_{23} \\ \tau_{13} \\ \tau_{12} \end{bmatrix} = \begin{bmatrix} C_{11} & C_{12} & C_{12} & 0 & 0 & 0 \\ C_{12} & C_{11} & C_{12} & 0 & 0 & 0 \\ C_{12} & C_{12} & C_{11} & 0 & 0 & 0 \\ 0 & 0 & 0 & (C_{11}-C_{12})^2 & 0 & 0 \\ 0 & 0 & 0 & 0 & (C_{11}-C_{12})^2 & 0 \\ 0 & 0 & 0 & 0 & 0 & (C_{11}-C_{12})^2 \end{bmatrix} \begin{bmatrix} \varepsilon_1 \\ \varepsilon_2 \\ \varepsilon_3 \\ \gamma_{23} \\ \gamma_{13} \\ \gamma_{12} \end{bmatrix} \quad (2.4)$$

$$\begin{bmatrix} \varepsilon_1 \\ \varepsilon_2 \\ \varepsilon_3 \\ \gamma_{23} \\ \gamma_{13} \\ \gamma_{12} \end{bmatrix} = \begin{bmatrix} S_{11} & S_{12} & S_{12} & 0 & 0 & 0 \\ S_{12} & S_{11} & S_{12} & 0 & 0 & 0 \\ S_{12} & S_{12} & S_{11} & 0 & 0 & 0 \\ 0 & 0 & 0 & 2(S_{11}-S_{12}) & 0 & 0 \\ 0 & 0 & 0 & 0 & 2(S_{11}-S_{12}) & 0 \\ 0 & 0 & 0 & 0 & 0 & 2(S_{11}-S_{12}) \end{bmatrix} \begin{bmatrix} \sigma_1 \\ \sigma_2 \\ \sigma_3 \\ \tau_{23} \\ \tau_{13} \\ \tau_{12} \end{bmatrix} \quad (2.5)$$

However, in an orthotropic material with two perpendicular symmetry planes, the stiffness matrix is represented by nine independent constants. Otherwise, there is no coupling between the linear, shear stress and strain components, as shown in Eqs.(2.6) and (2.7). Here, an orthotropic material has two perpendicular symmetry planes, (a special case of three symmetry planes in an orthotropic material), according to the assumption that the material is subjected to plane stress. Subsequently, any layer in the laminate is extremely thin.

$$\begin{bmatrix} \sigma_1 \\ \sigma_2 \\ \sigma_3 \\ \tau_{23} \\ \tau_{13} \\ \tau_{12} \end{bmatrix} = \begin{bmatrix} C_{11} & C_{12} & C_{13} & 0 & 0 & 0 \\ C_{12} & C_{22} & C_{23} & 0 & 0 & 0 \\ C_{13} & C_{23} & C_{33} & 0 & 0 & 0 \\ 0 & 0 & 0 & C_{44} & 0 & 0 \\ 0 & 0 & 0 & 0 & C_{55} & 0 \\ 0 & 0 & 0 & 0 & 0 & C_{66} \end{bmatrix} \begin{bmatrix} \varepsilon_1 \\ \varepsilon_2 \\ \varepsilon_3 \\ \gamma_{23} \\ \gamma_{13} \\ \gamma_{12} \end{bmatrix} \quad (2.6)$$

$$\begin{bmatrix} \varepsilon_1 \\ \varepsilon_2 \\ \varepsilon_3 \\ \gamma_{23} \\ \gamma_{13} \\ \gamma_{12} \end{bmatrix} = \begin{bmatrix} S_{11} & S_{12} & S_{13} & 0 & 0 & 0 \\ S_{12} & S_{22} & S_{23} & 0 & 0 & 0 \\ S_{13} & S_{23} & S_{33} & 0 & 0 & 0 \\ 0 & 0 & 0 & S_{44} & 0 & 0 \\ 0 & 0 & 0 & 0 & S_{55} & 0 \\ 0 & 0 & 0 & 0 & 0 & S_{66} \end{bmatrix} \begin{bmatrix} \sigma_1 \\ \sigma_2 \\ \sigma_3 \\ \tau_{23} \\ \tau_{13} \\ \tau_{12} \end{bmatrix} \quad (2.7)$$

2.2.2 Stress-strain relations for a thin lamina

2.2.2.1 Stress-strain relations for a thin lamina in an orthotropic material

In this section, the stress-strain relationships of a thin unidirectional lamina, as per Fig 2-1, is discussed when subject to plane stress. Within this analysis, plane stress has been chosen because the stress vector across normal direction (3-axis) is zero and this often applicable in thin flat plate structures. For the unidirectional composite structures shown in this figure, the stresses due to plane stress are $\sigma_3 = 0$, $\tau_{23} = 0$, $\tau_{13} = 0$ [16].
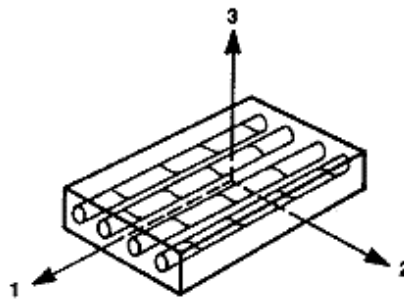
Fig 2-1: Unidirectional lamina in composite structures [1].

Applying a plane stress to the unidirectional laminated structures, and using the relationship between Young's modulus and Poisson's ratio for orthotropic material given by Eq.(2.8), the strain-stress relationship can be formulated as per Eq.(2.9). This formula is valid for all layers throughout the thickness of the laminate.

$$\frac{v_{ij}}{E_i} = \frac{v_{ji}}{E_j} \tag{2.8}$$

$$\begin{bmatrix} \varepsilon_1 \\ \varepsilon_2 \\ \gamma_{12} \end{bmatrix} = \begin{bmatrix} S_{11} & S_{12} & 0 \\ S_{12} & S_{22} & 0 \\ 0 & 0 & S_{66} \end{bmatrix} \begin{bmatrix} \sigma_1 \\ \sigma_2 \\ \tau_{12} \end{bmatrix} \tag{2.9}$$

And the compliance matrix can be found from Eq.(2.10):

$$S_{11} = \frac{1}{E_1}, S_{12} = -\frac{v_{12}}{E_1} = -\frac{v_{21}}{E_2}, S_{22} = \frac{1}{E_2}, S_{66=} \frac{1}{G_{12}} \tag{2.10}$$

The inverse of Eq.(2.9) provides the stress-strain, Eq.(2.11), of an orthotropic material, where Q_{ji} in this formula represents the reduced stiffness matrix.

$$\begin{bmatrix} \sigma_1 \\ \sigma_2 \\ \tau_{12} \end{bmatrix} = \begin{bmatrix} Q_{11} & Q_{12} & 0 \\ Q_{12} & Q_{22} & 0 \\ 0 & 0 & Q_{66} \end{bmatrix} \begin{bmatrix} \varepsilon_1 \\ \varepsilon_2 \\ \gamma_{12} \end{bmatrix} \qquad (2.11)$$

Then Q_{ji} matrix can be calculated using the engineering constants for any orthotropic material, as written in Eq.(2.12).

$$Q_{11} = \frac{E_1}{1 - v_{12}v_{21}}, Q_{22} = \frac{E_2}{1 - v_{12}v_{21}}, Q_{12} = \frac{v_{21}E_1}{1 - v_{12}v_{21}}$$
$$= \frac{v_{12}E_2}{1 - v_{12}v_{21}}, Q_{66} = G_{12} \qquad (2.12)$$

Isotropic material can be considered a special case of orthotropic state, where in a plane stress state the compliance and reduced stiffness matrix are given by Eq.(2.13):

$$\begin{bmatrix} S_{11} & S_{12} & 0 \\ S_{12} & S_{11} & 0 \\ 0 & 0 & 2(S_{11} - S_{12}) \end{bmatrix}, \begin{bmatrix} Q_{11} & Q_{12} & 0 \\ Q_{12} & Q_{11} & 0 \\ 0 & 0 & Q_{66} \end{bmatrix} \qquad (2.13)$$

Eq.(2.14) shows the above matrix in terms of engineering constants. It is obvious for this material that only Young's modulus, Poisson's ratio, and shear modulus are required to find these quantities:

$$S_{11} = \frac{1}{E}, S_{12} = -\frac{v}{E}, Q_{11} = \frac{E}{1 - v^2}, Q_{12} = \frac{vE}{1 - v^2}, Q_{66} = \frac{E}{2(1 + v)} = G \qquad (2.14)$$

2.2.2.2   Stress-Strain relations for a thin lamina in arbitrary directions

In section (2.2.1), stress-strain relations were defined in the principal coordinates for an orthotropic material. However, the principal directions in orthotropic materials do not always correspond with the local coordinate directions that are required in some structures to be the solution of the problem. As an example for this, laminated plate structures consist of a number of layers in different orientations. Thus, a formula is required to determine the stresses and strains in both the principal directions and those in the body itself. In this regard, the example of the laminate structure shown in Fig 2-2, is analysed to provide the transformations for the stresses and that allow the stress-strain relationships for this structure to be determined [1].
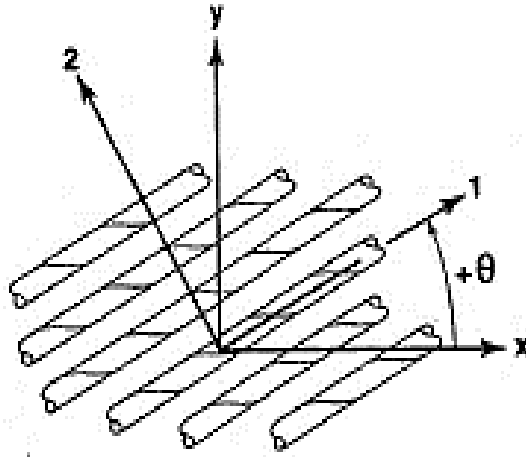
Fig 2-2: Global and local coordinates definition [1].

If it is assumed that x and y are the coordinates system of material and 1 and 2 the coordinate system that coincides locally with the fibre orientations. Then, the transformation matrix of stress components between the principal and local directions can be formulated as shown in Eq.(2.15):

$$\begin{bmatrix} \sigma_x \\ \sigma_y \\ \tau_{xy} \end{bmatrix} = \begin{bmatrix} cos^2\theta & sin^2\theta & -2\sin\theta\cos\theta \\ sin^2\theta & cos^2\theta & 2\sin\theta\cos\theta \\ \sin\theta\cos\theta & -\sin\theta\cos\theta & cos^2\theta - sin^2\theta \end{bmatrix} \begin{bmatrix} \sigma_1 \\ \sigma_2 \\ \tau_{12} \end{bmatrix} \qquad (2.15)$$

Similarly, the transformation of the strains between the different coordinates takes the form of Eq.(2.16).

$$\begin{bmatrix} \varepsilon_x \\ \varepsilon_y \\ \dfrac{\gamma_{xy}}{2} \end{bmatrix} = \begin{bmatrix} cos^2\theta & sin^2\theta & -2\sin\theta\cos\theta \\ sin^2\theta & cos^2\theta & 2\sin\theta\cos\theta \\ \sin\theta\cos\theta & -\sin\theta\cos\theta & cos^2\theta - sin^2\theta \end{bmatrix} \begin{bmatrix} \varepsilon_1 \\ \varepsilon_2 \\ \dfrac{\gamma_{12}}{2} \end{bmatrix} \qquad (2.16)$$

By using some mathematical simplifications and matrix concepts the stress-strain relationship in x-y coordinates is given by Eq.(2.17)

$$\begin{bmatrix} \sigma_x \\ \sigma_y \\ \tau_{xy} \end{bmatrix} = \begin{bmatrix} \bar{Q}_{11} & \bar{Q}_{12} & \bar{Q}_{16} \\ \bar{Q}_{12} & \bar{Q}_{22} & \bar{Q}_{26} \\ \bar{Q}_{16} & \bar{Q}_{26} & \bar{Q}_{66} \end{bmatrix} \begin{bmatrix} \varepsilon_x \\ \varepsilon_y \\ \gamma_{xy} \end{bmatrix} \qquad (2.17)$$

Where, $\bar{Q}_{ij}$ are the reduced stiffness matrix of laminate contains fibres in random orientations and can be written as per Eq. (2.18).

$$\bar{Q}_{11} = Q_{11}cos^4\theta + 2(Q_{12} + 2Q_{66})sin^2\theta cos^2\theta + Q_{22}sin^4\theta$$

$$\bar{Q}_{12} = (Q_{11} + Q_{22} - 4Q_{66})sin^2\theta cos^2\theta + Q_{12}(sin^4\theta + cos^4\theta) \qquad (2.18)$$

$$\bar{Q}_{22} = Q_{11}sin^4\theta + 2(Q_{12} + 2Q_{66})sin^2\theta cos^2\theta + Q_{22}sin^4\theta$$

$$\bar{Q}_{16} = (Q_{11} - Q_{12} - 2Q_{22})sin\theta cos^3\theta + (Q_{12} - Q_{22}$$
$$+ 2Q_{66})sin^3\theta cos\theta$$

$$\bar{Q}_{26} = (Q_{11} - Q_{12} - 2Q_{22})sin^3\theta cos\theta + (Q_{12} - Q_{22}$$
$$+ 2Q_{66})sin\theta cos^3\theta$$

$$\bar{Q}_{66} = (Q_{11} + Q_{22} - 2Q_{12} - 2Q_{66})sin^2\theta cos^2\theta + Q_{66}(sin^4\theta$$
$$+ cos^4\theta)$$

2.2.3 Mechanical behaviour of multidirectional laminates

According to the principles of laminated composite structures, the entire strength and stiffness are highly dependent on the fibre orientations in each layer. Otherwise, stiffness may change through the thickness of laminated structure. This explains that the aim of manufacturing laminated structures is to satisfy a high level of bending stiffness [17].

2.2.3.1 Stress-strain variation through a laminate

Knowledge of the change in stress and strain through the laminate is significant to determine the extensional and bending stiffness of laminated structures. To perform this analysis, there are some assumptions that need to be verified, such as perfect bonding between layers, the bond area between laminas must be infinitesimally thin, and there is no shear deformation in this area. These assumptions are important to ensure that the displacement domain will continue through the lamina edges. According to the Kirchhoff theorem, and because the lamina is infinitesimally thin as shown in Fig 2-3, the displacement of point C can be represented as per Eq.(2.19) [1],
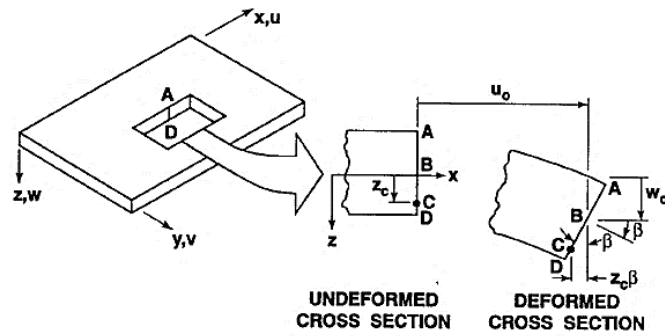
Fig 2-3: Geometry of an element deformation [1].

$$u_c = u_\circ - z_c \beta \qquad (2.19)$$

where β represents the slope of the middle surface of laminate in the x direction. If it is assumed that the displacements u and v are in the x- and y-directions through the laminate thickness, respectively, then the displacement components can be formulated as per Eq. (2.20):

$$u = u_\circ - z \frac{\partial w_\circ}{\partial x}, v = v_\circ - z \frac{\partial w_\circ}{\partial y} \qquad (2.20)$$

From the definition of strain, $\epsilon = \frac{\partial u}{\partial x}$, and by deriving Eq.(2.20), the relationship strain components via laminate thickness can be given as in Eq.(2.21), where ε_x° is the strain of middle surface, and k_x is the curvature in the x-axis.

$$\begin{bmatrix} \varepsilon_x \\ \varepsilon_y \\ \gamma_{xy} \end{bmatrix} = \begin{bmatrix} \varepsilon_x^\circ \\ \varepsilon_y^\circ \\ \gamma_{xy}^\circ \end{bmatrix} + z \begin{bmatrix} k_x \\ k_y \\ k_{xy} \end{bmatrix}, \begin{bmatrix} k_x \\ k_y \\ k_{xy} \end{bmatrix} = \begin{bmatrix} \dfrac{\partial^2 w_\circ}{\partial x^2} \\ \dfrac{\partial^2 w_\circ}{\partial y^2} \\ 2\dfrac{\partial^2 w_\circ}{\partial x \partial y} \end{bmatrix} \qquad (2.21)$$

It is clearly possible to obtain the magnitude of the stress at any given position in laminate by substituting of the corresponding strains shown in Eq.(2.21) into Eq.(2.17).

Another important issue in laminated structures analysis is the relationships between forces and moments across the thickness. Therefore, applying Hooke's law can provide the magnitude of a force through the laminate thickness, as per Eq.(2.22):

$$N_x = \int\limits_{-\frac{t}{2}}^{\frac{t}{2}} \sigma_x z, \ M_x = \int\limits_{-\frac{t}{2}}^{\frac{t}{2}} \sigma_x z dz \qquad (2.22)$$

Moreover, the entire magnitude of force and moment of laminated structure shown in Fig 2-4, can be found by integration the induvial force and moment components for each layer, as formulated by Eq.(2.23).
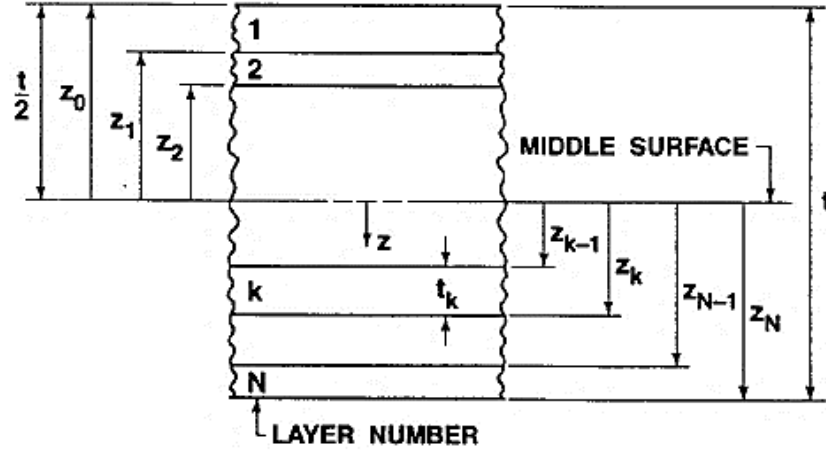
Fig 2-4: Model of Nth layered laminate [1].

$$\begin{bmatrix} N_x \\ N_y \\ N_{xy} \end{bmatrix} = \sum_{k=1}^{N} \begin{bmatrix} \bar{Q}_{11} & \bar{Q}_{12} & \bar{Q}_{16} \\ \bar{Q}_{12} & \bar{Q}_{22} & \bar{Q}_{26} \\ \bar{Q}_{16} & \bar{Q}_{26} & \bar{Q}_{66} \end{bmatrix}_k \left[\int\limits_{z_{k-1}}^{z_k} \begin{bmatrix} \varepsilon_x^\circ \\ \varepsilon_y^\circ \\ \gamma_{xy}^\circ \end{bmatrix} dz + \int\limits_{z_{k-1}}^{z_k} \begin{bmatrix} k_x \\ k_y \\ k_{xy} \end{bmatrix} z dz \right]$$

$$\begin{bmatrix} M_x \\ M_y \\ M_{xy} \end{bmatrix} = \sum_{k=1}^{N} \begin{bmatrix} \bar{Q}_{11} & \bar{Q}_{12} & \bar{Q}_{16} \\ \bar{Q}_{12} & \bar{Q}_{22} & \bar{Q}_{26} \\ \bar{Q}_{16} & \bar{Q}_{26} & \bar{Q}_{66} \end{bmatrix}_k \left[\int\limits_{z_{k-1}}^{z_k} \begin{bmatrix} \varepsilon_x^\circ \\ \varepsilon_y^\circ \\ \gamma_{xy}^\circ \end{bmatrix} z dz + \int\limits_{z_{k-1}}^{z_k} \begin{bmatrix} k_x \\ k_y \\ k_{xy} \end{bmatrix} z^2 dz \right]$$

$$(2.23)$$

Eq.(2.23) can be simplified to a new form, as shown in Eq.(2.24). These equations provide the relationship between the laminated stiffness and their forces and moments.

$$\begin{bmatrix} N_x \\ N_y \\ N_{xy} \end{bmatrix} = \begin{bmatrix} A_{11} & A_{12} & A_{16} \\ A_{12} & A_{22} & A_{26} \\ A_{16} & A_{26} & A_{66} \end{bmatrix} \begin{bmatrix} \varepsilon_x^\circ \\ \varepsilon_y^\circ \\ \gamma_{xy}^\circ \end{bmatrix} + \begin{bmatrix} B_{11} & B_{12} & B_{16} \\ B_{12} & B_{22} & B_{26} \\ B_{16} & B_{26} & B_{66} \end{bmatrix} \begin{bmatrix} k_x \\ k_y \\ k_{xy} \end{bmatrix}$$

$$\begin{bmatrix} M_x \\ M_y \\ M_{xy} \end{bmatrix} = \begin{bmatrix} B_{11} & B_{12} & B_{16} \\ B_{12} & B_{22} & B_{26} \\ B_{16} & B_{26} & B_{66} \end{bmatrix} \begin{bmatrix} \varepsilon_x^\circ \\ \varepsilon_y^\circ \\ \gamma_{xy}^\circ \end{bmatrix} + \begin{bmatrix} D_{11} & D_{12} & D_{16} \\ D_{12} & D_{22} & D_{26} \\ D_{16} & D_{26} & D_{66} \end{bmatrix} \begin{bmatrix} k_x \\ k_y \\ k_{xy} \end{bmatrix}$$

$$(2.24)$$

Where A is an extensional matrix, B is the bending-extension stiffness matrix and D is the bending matrix; each of those elements can be calculated using Eq.(2.25).

$$A_{ij} = \sum_{k=1}^{N} (\bar{Q}_{ij})_k \, (z_k - z_{k-1})$$

$$B_{ij} = \frac{1}{2} \sum_{k=1}^{N} (\bar{Q}_{ij})_k \, (z_k^2 - z_{k-1}^2) \qquad (2.25)$$

$$D_{ij} = \frac{1}{3} \sum_{k=1}^{N} (\bar{Q}_{ij})_k \, (z_k^3 - z_{k-1}^3)$$

2.3   Dynamic analysis of structures

Dynamic analysis has become of particular significance in structural health monitoring. This technique was used in analytical laboratories as well as gaining the attention of researchers as a potentially useful approach in analysing the dynamic behaviour of different mechanical structures. Historically, this method was first utilized to investigate and measure the elasticity of materials in 1909, and subsequently to find the deformation of materials under oscillatory motion in 1926. Thereafter, it reached a considerable level to analyse different mechanical structures [18]. This provides a clear idea about the use of dynamic analysis in different mechanical disciplines.

2.3.1   Free vibration of spring-mass system

Calculating equations of motion is essential to understand the behaviour of any mechanical structure. Calculating the equation of motion for the spring-mass system can be a good example to understand the behaviour of a simple structure vibrates under harmonic motion. The system shown in Fig 2-5 is considered an example through which to determine its equation of motion and natural frequency. It was set up to move in the vertical direction (one degree of freedom) and oscillates at a natural frequency f_n.
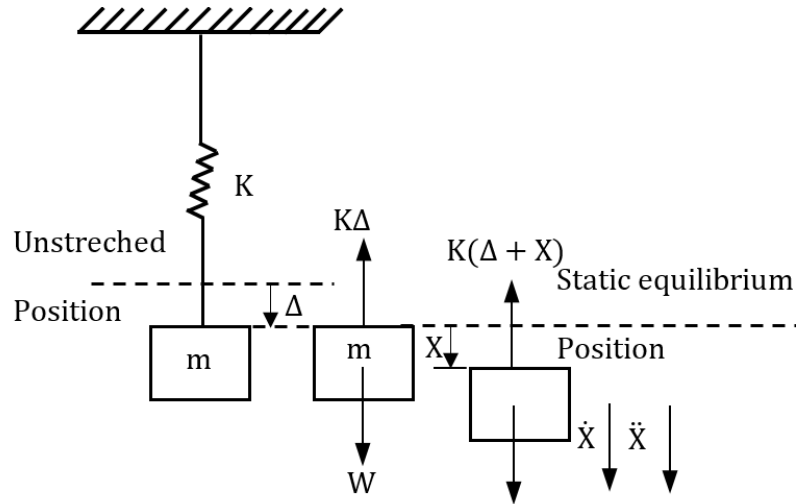
Fig 2-5: The simple oscillation of a mass-spring system [19].

According to Newton's second law, the summation of vertical forces can be calculated as written in Eq.(2.26),

$$m\ddot{x} = \sum F = w - k(\Delta - x)$$ (2.26)

where $k\Delta$ is the force of the spring; if this is equal to the weight then Eq.(2.26), can be simplified to Eq.(2.27).

$$m\ddot{x} = -kx$$ (2.27)

In addition, if angular frequency is defined as $\omega_n^2 = \frac{k}{m}$, then the equation of motion can be represented by Eq.(2.28).

$$m\ddot{x} + \omega^2 x = 0$$ (2.28)

Then by solving the differential equation Eq.(2.28) and applying the boundary condition of free vibration, and where τ is the period of oscillation ($\omega_n \tau = 2\pi$), the natural frequency can be given as per Eq.(2.29) [19].

$$f_n = \frac{1}{\tau} = \frac{1}{2\pi}\sqrt{\frac{k}{m}}$$ (2.29)

2.3.2 **Lagrange equation**

Applying the Lagrange equation in dynamic analysis can provide the equation of motion for any mechanical structure. Calculating equation of motion is the most important step in starting the analysis of a mechanical structure; for instance, Newton's second law is appropriate to finding the equation of motions for a simple mechanism. However, in complex cases, the Lagrange approach is more suited to the derivation of an appropriate equation of motion, and which completely depends on computing the work and the kinetic energy of the object.

To determine the equation of motion, *generalized coordinates* must be defined. This coordinate system is defined as a common coordinate system which used to describe the instantaneous position of any system. q_n is usually used to denote to the set of generalized coordinates that describes the system, and they are represented by $q_1, q_2, ..., q_n$ [20]. Furthermore, if δW refers to the virtual work (work is produces as a result of particles moving and depends on the particles displacement), the work which is produced by the effect of virtual displacement, and where Q_i indicates a force in a translation state and a moment in rotation. Therefore, the virtual work in the equilibrium position is $\delta W = Q_i \delta q_i$.The Lagrangian identifies the difference between the kinetic energy and potential energy for the entire system [L = T - V]. Here, the equation of motion for any system is written as per Eq.(2.30).

$$\frac{d}{dt}\left(\frac{\partial L}{\partial \dot{q}_i}\right) - \frac{\partial L}{\partial q_i} = Q_i, i = 1,2, ..., \text{n} \tag{2.30}$$

By applying this formulation to the energy quantities of any mechanical system and where there is no dissipation of energy (i.e., the system energy is conserved), the right-hand side of Eq.(2.30) is equal to zero, and the Lagrangian can be written as per Eq.(2.31).

$$\frac{d}{dt}\left(\frac{\partial T}{\partial \dot{q}_i}\right) - \frac{\partial T}{\partial q_i} + \frac{\partial V}{\partial q_i} = 0 \tag{2.31}$$

To explain the Lagrange criteria, one can consider the mechanical system shown in Fig 2-6, [21].
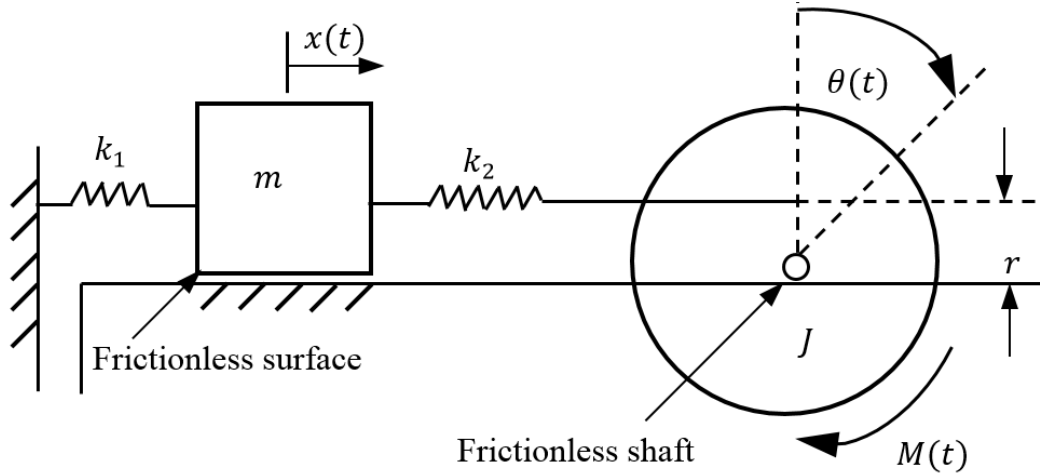
Fig 2-6: Vibration model of the mechanical system [21].

If the generalized coordinates of this system are $q_1(t) = x(t)$ and $q_2(t) = \theta(t)$, then the kinetic energy is

$$T = m\dot{q}_1^2 + \frac{1}{2}J\dot{q}_2^2$$

, the potential energy is

$$V = \frac{1}{2}k_1 q_1^2 + \frac{1}{2}k_2(rq_2 - q_1)^2$$

, and the polar moment of inertia J is

$$J = \frac{\pi r^4}{2}, r \; is \; radius \; of \; shaft$$

Applying the Lagrange theorem for the two coordinate systems, at $i = 1$ and $Q_1 = 0$.

$$\frac{d}{dt}(m\dot{q}_1) + k_1 q_1 - k_2(rq_2 - q_1) = 0$$

For $q_1(t)$ coordinate the Lagrange is given by Eq.(2.32).

$$m\ddot{q}_1 + (k_1 + k_2)q_1 - k_2 rq_2 = 0 \qquad (2.32)$$

, and for the second coordinate $q_2(t)$ the Lagrange becomes as given by Eq.(2.33);

$$J\ddot{q}_2 + k_2 r^2 q_2 - k_2 rq_1 = M(t) \qquad (2.33)$$

, and these two equations represent the equations of motion for the above mechanism.

2.3.3 **Vibration of continuous systems**

This section provides the fundamentals of the dynamic analysis. An example was a beam vibrating laterally to its longitudinal axis. This analysis explains the relationship between the stiffness of the vibrated structure and its modal characteristics such as natural frequency, mode shape and damping ratio. From this, the effect of damage on the local stiffness and modal characteristics can be understood. Therefore, for the bent beam shown in Fig 2-7 [21], the free body diagram of the element shows the expected forces under vibration state. In fact, the equilibrium equation in the vertical axis of motion is given by Eq.(2.34).
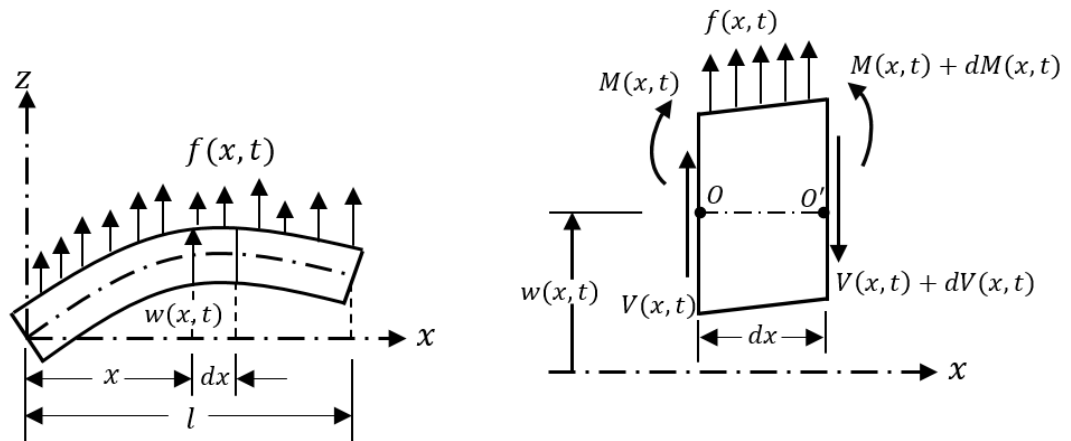
Fig 2-7: Forces and moments diagram of the vibrated beam reported in [21].

$$-(V + dV) + f(x,t)dx + V = \rho A(x)dx \frac{\partial^2 w}{\partial t^2}(x,t) \qquad (2.34)$$

, and the moment about the y-axis can be calculated as per Eq.(2.35)

$$(M + dM) - (V + dV)dx + f(x,t)dx \frac{dx}{2} - M = 0 \qquad (2.35)$$

Then the derivative of force and moment is,

$$dV = \frac{\partial V}{\partial x}dx \ and \ dM = \frac{\partial M}{\partial x}dx$$

, and simplifying the above equations, then the final equation of motion of the uniform beam can be written as per Eq.(2.36). With free vibration condition, the right-hand side is equal to zero.

$$c = \sqrt{\frac{EI}{\rho A}}$$

$$EI\frac{\partial^4 w}{\partial x^4}(x,t) + \rho A(x)dx\frac{\partial^2 w}{\partial t^2}(x,t) = f(x,t)$$

$$c^2\frac{\partial^4 w}{\partial x^4}(x,t) + \frac{\partial^2 w}{\partial t^2}(x,t) = 0, free\ vibration$$

(2.36)

Moreover, the solution of this differential equation under simple harmonic motion shows that the natural frequency of the vibrating system can be formulated as per Eq.(2.37).

$$\omega = \beta^2\sqrt{\frac{EI}{\rho A}} = (\beta l)^2\sqrt{\frac{EI}{\rho A l^4}}, \beta^4 = \frac{\omega^2}{c^2}$$

(2.37)

2.3.4 Dynamic response of a structure

This section provides a simple demonstration of the vibration mechanism of the body shown in Fig 2-8 under simple harmonic motion. Harmonic motion refers to an oscillatory motion that repeats itself on a regular time base. In this figure, the instantaneous position of particle A, shown in Fig 2-8a (which vibrates at angular frequencyω), can be determined at any time as per Eq.(2.41). Fig 2-8b shows clearly the similarity between harmonic motion and sinusoidal motion after t time. Fig 2-8c shows the amplitude and velocity of the vibrated body.

To analyse the above mechanism, the general solution of differential equation Eq.(2.27) can be formulated as per Eq.(2.38), where A_1 and A_2 are constants to be determined depending on the initial conditions of the system. Two conditions that can be used to evaluate this equation as written in Eq.(2.39), where $x(t)$ and $\dot{x}(t)$ are the displacement and velocity components [21].

$$x(t) = A_1\ \cos \omega_n t + A_2\ \sin \omega_n t$$

(2.38)

$$x(t = 0) = A_1 = x_0$$

$$\dot{x}(t = 0) = \omega_n A_2 = \dot{x_0}$$

(2.39)

Appling these conditions to Eq.(2.38), the displacement component can be written as per Eq.(2.40).

$$x(t) = x_0 \cos \omega_n t + \frac{\dot{x_0}}{\omega_n} \sin \omega_n t$$

(2.40)

The other important concept in vibrational analysis of mechanical structures is decomposition the dynamic response into components. This concept demonstrates the idea behind the use of mode shape, where according to the above equations, the instantaneous position and velocity of the vibrated particle can be predicted. This criteria can be applied to systems with multiple degrees of freedom to find their conditions of motion.

Then, the same simple harmonic motion described by Eq.(2.38) can be formulated in an alternative form by applying the notations in Eq.(2.41), where A and Ø are new constants as represented in Eq.(2.42). According to the initial conditions and these new constants, the dynamic of response of this mechanism can be expressed as per Eq.(2.43).

$$A_1 = A \cos\emptyset$$

$$A_2 = A \sin\emptyset$$

(2.41)

$$A = (A_1^2 + A_2^2)^{\frac{1}{2}} = \left[x_0^2 + \left(\frac{\dot{x_0}}{\omega_n} \right)^2 \right]^{\frac{1}{2}} = amplitude$$

(2.42)

$$\emptyset = \tan^{-1} \left(\frac{A_1}{A_2} \right) = \tan^{-1} \left(\frac{\dot{x_0}}{x_0 \ \omega_n} \right) = phase \ angle$$

$$x(t) = A_0 \sin(\omega_n t - \emptyset_0)$$

(2.43)
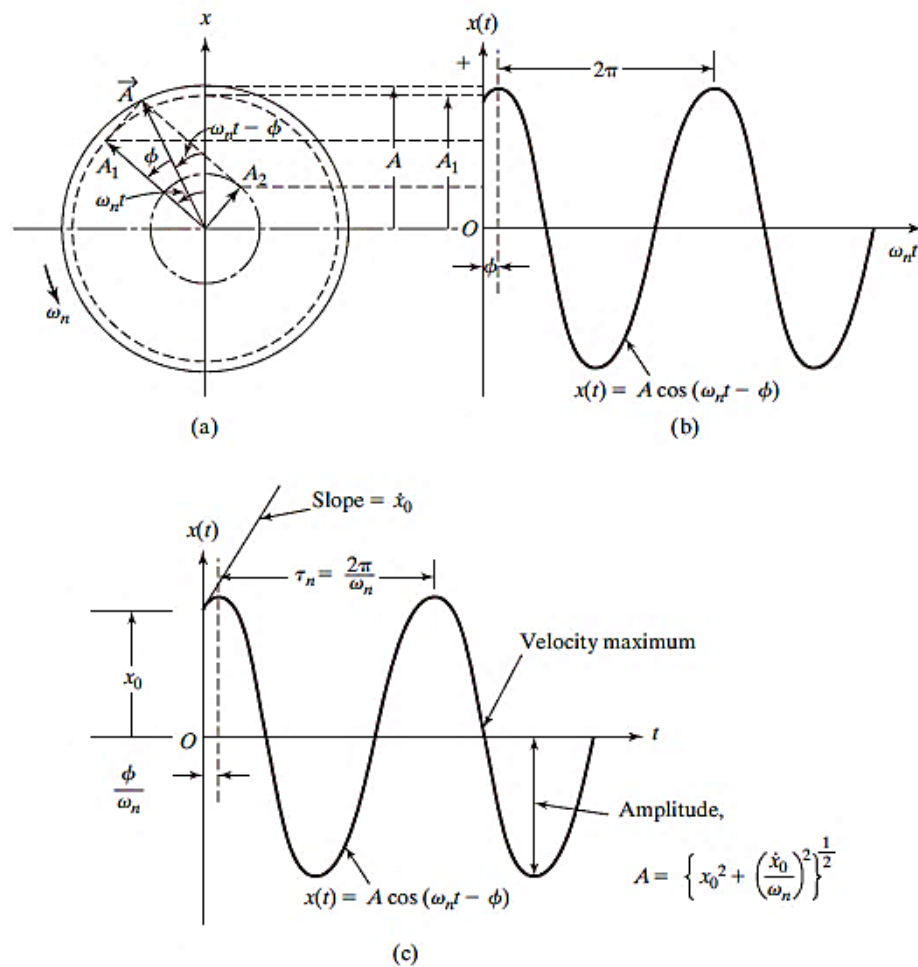
Fig 2-8: Graphical description of a vibrating mechanism undergoing simple harmonic motion [21].

2.3.5 Introduction to use of the Finite Element Method in modelling engineering structures

Developing the Finite Element Method (FEM) helps the modern computing technology to model and simulate both simple and advanced types of engineering structures. The defined keys (refer to GUI "graphical user interface" used in the modelling process) is one of the excellent features in the developed finite element software programs. As engineers and designers go through an extensive amount of work in the process of designing, modelling, simulating, analysis and visualization before the final step of manufacturing a given component. In complex structures an approximate understanding of their analysis through FEM is extremely needed. In modelling of complex engineering and mechanical structures, it is often difficult to model all the

surrounding conditions perfectly. However using FEM can save the costs of unsuccessful experimental trials and provide more information about the given structure without the requirement for physical testing [22].

In general, FEM in engineering studies is the process by which the given object, such as a gas, liquid or solid, is simulated as an ensemble of sub-elements called finite elements. These elements are related to each other by inter-connections at certain points called nodes, as per Fig 2-9. Although the actual variation of the parameters such as stress, displacement, temperature or velocity of the continuum inside the body are not defined, the underlying assumption to FEM is that variation can be assumed in an approximate manner by a simple function, where these relations are called interpolation models. From this principle, the entire solution can be found depending on the boundary conditions and applied loads for each case study [23].
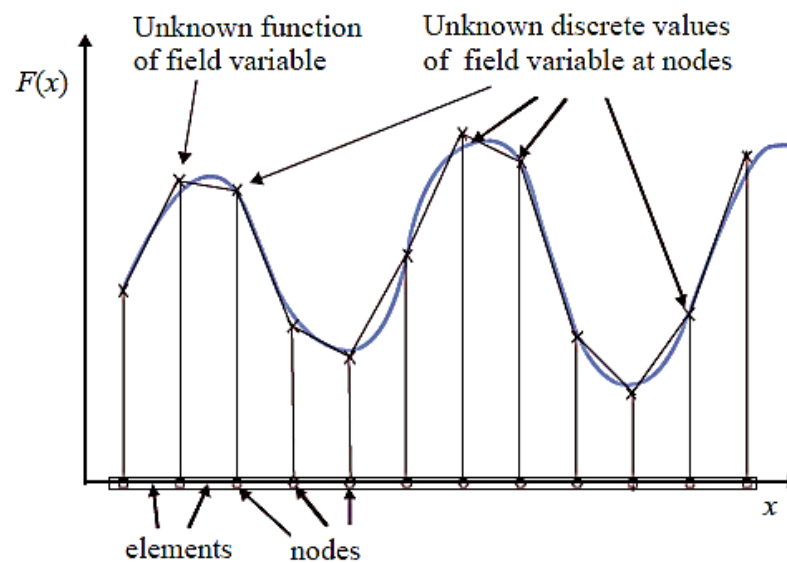
Fig 2-9: Finite element description of a one-dimensional structure [22].

In FEM, the general solution for a continuum body generally follows the following steps:

Step 1: Any given structure is divided into a number of elements, which means number, type and size of elements must be taken into consideration.

Step2:   The interpolation or the displacement model should be selected properly. Normally, the displacement solution for complex structures is not known, so the start

point for the use of FEM assumes some approximations to the actual solution. The approximated solution must come from solid-point (defined point) and satisfy the convergence rules.

Step 3: Derive the stiffness matrix elements and the load vector

According to the principles of the displacement model, the stiffness matrix can be in terms of $[K]$ and the load vector $\vec{P}$.

Step 4: Assemble equations for the individual elements to find the solution of the entire body equations. If it is assumed that a body consists of a number of elements, and nodal displacement $\vec{\phi}$, then the overall equilibrium equations is written as per Eq.(2.44),

$$[K]\,[\vec{\phi}]=[\vec{P}] \tag{2.44}$$

Step 5: Solve for the non-defined nodal displacement.

Starting by the defined points (boundary conditions are given) to calculate the overall model displacement; subsequently, calculating stresses and strains for the given problem [22].

2.3.5.1 Analysis of free vibration using FEM

The same criteria is the finite element method illustrated in section 2.3.5 is applied to simulate and analyse the free vibration of mechanical structures. The modelling procedure can be summarized as below:

- Modelling and design the required geometry or case study;
- Implement the material properties;
- Fulfil the meshing for the entire structure;
- Apply the boundary conditions, and any external loads if required;
- Run the job analysis and then visualize the results produced.

In this section, it is important to explain the principles of calculating mode shape using dynamic analysis. For a solid structure system with N degrees of freedom, the global equation for all individual elements are shown in Eq.(2.45),

$$KD + M\ddot{D} = F \qquad (2.45)$$

where K is the stiffness matrix, M the mass matrix, D the displacement vector and F the external load. Under free vibration, the external load is given by $F = 0$, and this equation of motion can be formulated as per Eq.(2.46).

$$KD + M\ddot{D} = 0 \qquad (2.46)$$

If the nodal displacement $D = \phi \exp(it\omega)$, where ϕ is the amplitude, ω is the natural frequency and t is the time, the solution of differential equation Eq.(2.46) can be written as per Eq. (2.47):

$$[K - \omega^2 M]\phi = 0 \qquad (2.47)$$

If it is assumed that $\lambda = \omega^2$, the eigenvalue equation can be represented by Eq.(2.48),

$$[K - \lambda M]\phi = 0 \qquad (2.48)$$

Accordingly, the overall eigenvalue equation for the entire continuum problem is formulated as per Eq.(2.49),

$$[K - \lambda_i M]\phi_i = 0 \qquad (2.49)$$

where eigenvector ϕ_i is related to vibrational mode $i,$ and from this, each structure may vibrate in a number of ith mode shapes. The above equations show the mathematical basis by which the mode shape is calculated in the dynamic analysis. The same criteria is used by finite element software programs to calculate the modal characteristic. An example of the above analysis, the first three numerical modes of the cantilever beam shown in Fig 2-10 were determined. The cantilever beam was analysed analytically, and the first three bending modes were determined as shown in Fig 2-11under two boundary conditions. First of all, mode shapes were calculated in vibrated beam without rotation [beam did not rotate], and then they calculated for beam rotated at an angular velocity Ω with respect to the normal axis to study the effect of different conditions on the calculation of mode shapes [24].
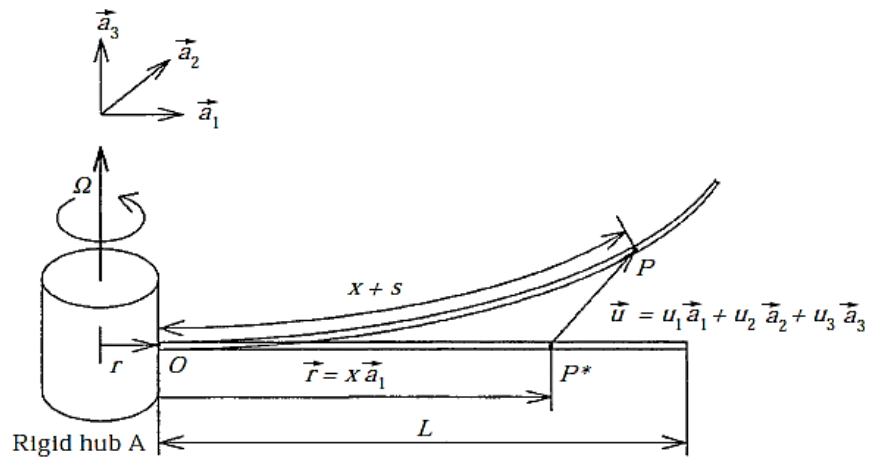
Fig 2-10: Schematic of rotating beam used in [24].
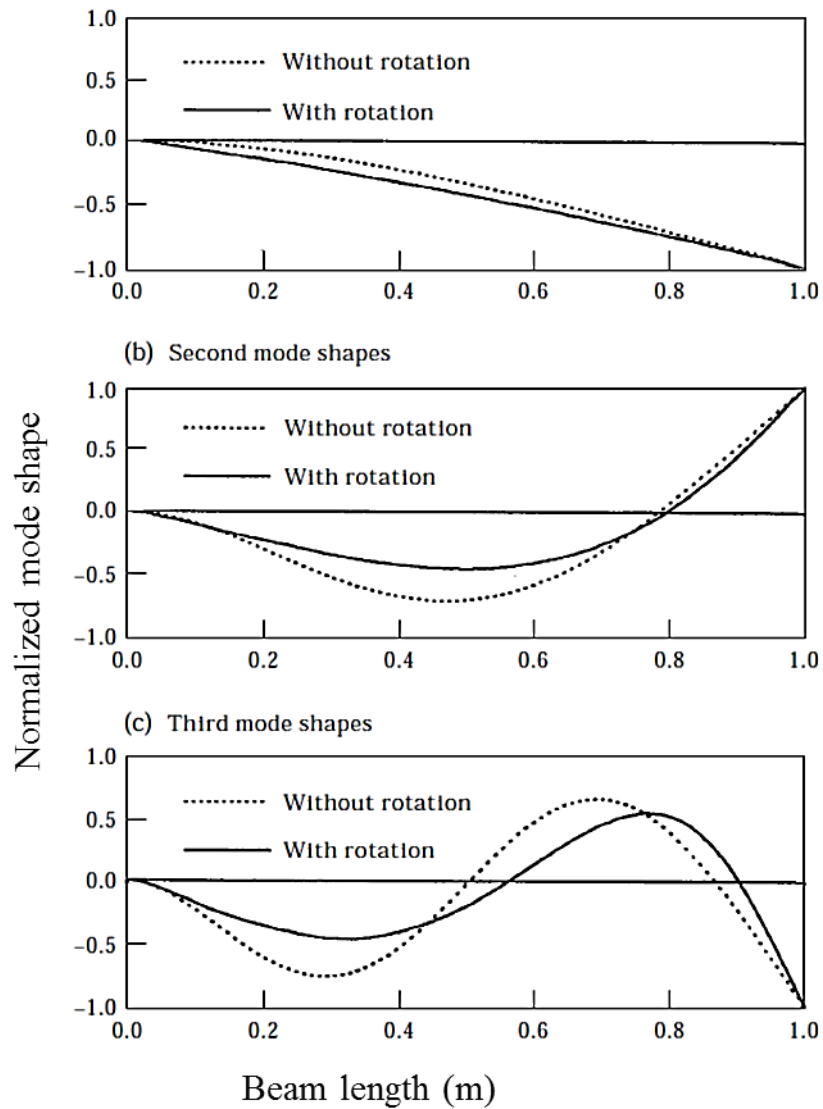
Fig 2-11: The first three modes of a cantilever beam [24].

2.4 Concluding remarks

A detailed introduction to the mechanics of laminated structures and the principles of dynamic analysis of mechanical structures were presented in this chapter. An introduction to the stress-strain relationship has been demonstrated to provide a clear understanding of these relationships. The variation of stiffness over the entire laminate thickness was presented to explain the effect of damage in laminated structures. This introduction represents an important start-point to an understanding of modelling the damaged elements and in order to provide a comprehensive overview of mechanics of laminated structures.

The second objective of this chapter was to present a review of principles of dynamic analysis. The definition of free vibration, equation of motion, vibration of continuous systems and the dynamic response of vibrating structures were discussed. Additionally, an introduction into the use of the finite element method to calculate mode shape was given. In summary, this chapter clarified the criteria behind the mechanics of laminated materials and the principles of dynamic response analysis.

Chapter 3: A literature review of vibration-based damage detection methods

This chapter covers an overview of different techniques used in damage detection, and discusses the knowledge gap in damage detection subject. Various techniques have been investigated and practiced in the field of Structural Health Monitoring (SHM) depending on the efficiency, cost and ease of use. In general, these method can be divided into two groups; first is vibration-based damage techniques that are used to detect damaged sections in mechanical structures. The second is non-destructive testing (NDT) techniques which are a range of analysis methods used in the evaluation of structure functionality without causing damage. Both of these groups will be reviewed in sections 3.1 and 3.2 in this chapter [25].

3.1 Vibration-based damage detection methods

Vibration-based damage detection is based on the analysis of dynamic characteristics such as natural frequency and mode shape in different mechanical structures. Quantify damages can be accomplished via the analysis of the dynamic responses of the damaged structures and compare them with the analysis of intact data [26]. This method is frequently used to quantify and localize the damaged areas and is considered to be one of the most practical techniques in damage detection. Practically, this means any effect on, or change to the structural characteristics, such as losing of mass or stiffness in any given element, will have a clear effect on the dynamic modal parameters [27]. The following sections explain this method.

3.1.1 Method based on the change of natural frequency

For a number of reasons, the measurement of natural frequency in mechanical structures considers easy to use for more than one aspects. For example, it is not affected excessively by noisy conditions. It is a global technique, which means the measured data does not depend on the location (same damage in different locations may provide the same data). However, the data are measured in this technique require accuracy level much more than determining the mode shape or the damping

characteristics. Salawu [28] presented a comprehensive review that included most of the publications presented before 1997 and used natural frequency technique to detect the damaged areas. Ultimately, it should be noted that a natural frequency change might not be sufficiently accurate to localize damaged regions, according to the view that the same damage in different locations results in the same frequency change in a given structure. To overcome the challenge of damage localisation, Messina and Williams [29] suggested the localisation of damaged sections by a correlation coefficient termed the Multiple Damage Location Assurance Criterion (MDLAC). This method depends entirely on the sensitivity of the natural frequency in each mode to the damaged regions. MDLAC is essentially a statistical correlation between the analytical and experimental frequency change. The analytical frequency change (the magnitude of the frequency change, which is calculated analytically) is given by δf and the measured frequency is Δf. The change in analytical frequency can be formulated as a function of the damage vector, δD, as shown in Eq.(3.1). So when damage occurs the magnitude of MDLAC index will increase. Here, δD refers to the stiffness reduction factor D_f for the element. In this regard, the value for the undamaged element is $D_f = 1$, and for 100% damage, $D_f = 0$. Although the authors mentioned the validity of this index to detect damage in truss structures. However, the biggest challenge that calculating this index needs a number of accurate mode shapes, and this is not easy in experiment.

$$\text{MDLAC}(\{\delta D\}) = \frac{\left| \Delta f^T . \{\delta f(\{\delta D\})\} \right|^2}{(\{\Delta f\}^2 . \{\Delta f\}) . (\{\delta f(\{\delta D\})\}^T . \{\delta f(\{\delta D\})\})} \tag{3.1}$$

Chinchalkar [30] developed a finite element method to detect cracks in a stepped beam, as per Fig 3-1, using the first three natural frequencies under a free vibration condition. Cracks were modelled by reducing the stiffness of the element at four locations, 0.05, 0.2, 0.4, 0.45, to the fixed edge, as shown in Fig 3-1. The material data used in this study are Young's modulus = 210 GPa, density = 7800 kg/m^3, ν = 0.3 and $\beta = \frac{x}{L}$. The authors reported that calculating the non-dimensional stiffness $\left(K = \frac{kL}{EI} \right)$, for the first three natural frequencies allowed the detection of the damaged section, where the intersection points of these frequencies showed the exact location of the crack, as shown in Fig 3-2.
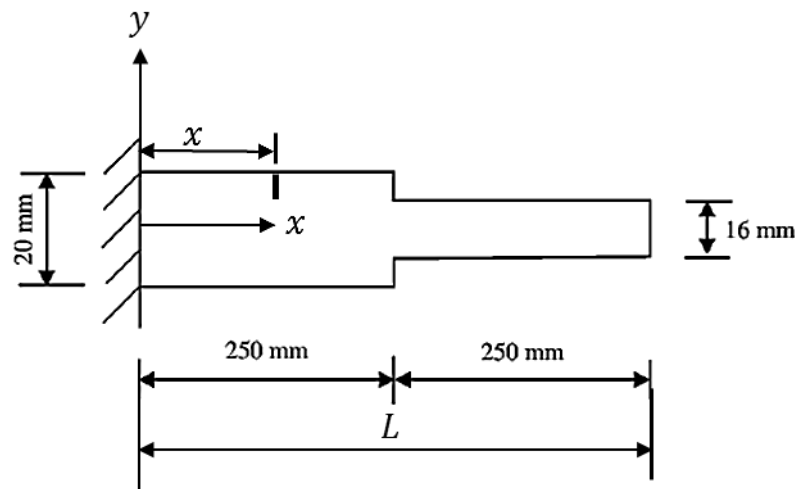
Fig 3-1: The cracked beam used in the numerical analysis performed in [30].
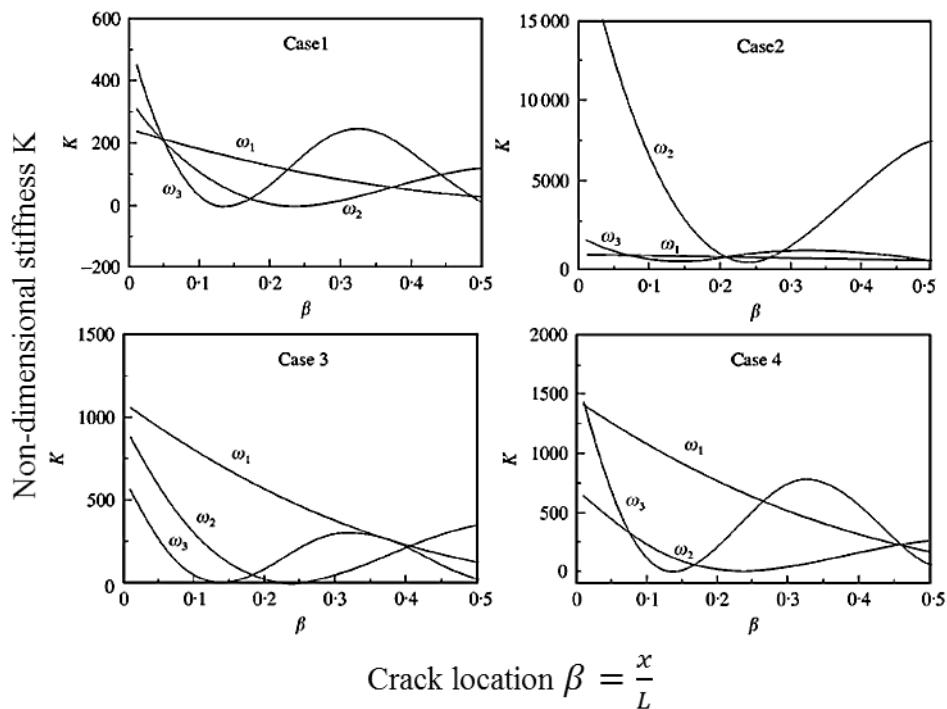
Crack location $\beta = \dfrac{x}{L}$

Fig 3-2: The change of the first three natural frequencies of a cracked beam at different locations. The intersection points of these modes show the crack location [30].

Patil [31] used Euler-Bernoulli theory to detect multiple open cracks in a beam using frequency-based damage detection method. To model cracks, the beam was divided into a number of equal segments, as per Fig 3-3. In this analysis, a rotational spring (in this spring, the applied torque is proportional to the angular displacement of one end with respect to the other) was used to implement the reduction in stiffness at the cracked sections. The stiffness was reduced across this spring, which is how the

modelling of cracks can be accomplished. The crack detection procedure was dependent on calculating the change in natural frequency due to the existence of cracks. This calculation can be performed by computing the strain and kinetic energies, U and V, as shown in Eq.(3.2). Then, the change in natural frequency can be obtained as per Eq.(3.3). The material properties are Young's modulus = 28 GPa, and density = 2350 kg/m3. The final step in this method was to calculate the stiffness K of the first three modes and plot these magnitudes versus the crack location, as shown in Fig 3-4. The intersection points were associated with crack locations, β. However, the authors noted certain limitations to this procedure, which are; that it cannot be applied to beams with rotational inertia, or where there is shear deformation or a damping effect.

$$\omega^2 = \frac{\frac{1}{2}\int_0^L EI(x)\left(\frac{d^2 Z}{dx^2}\right)^2 dx}{\frac{1}{2}\int_0^L \rho A Z^2 \, dx} = \frac{U}{V} \tag{3.2}$$

$$\frac{\Delta \omega}{\omega} = \frac{\Delta U}{U} - \frac{\Delta V}{V} \tag{3.3}$$
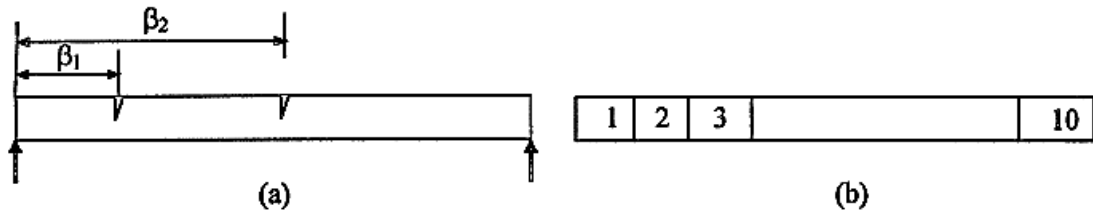
Fig 3-3: Simply supported cracked beam and its segments, as investigated by [31].
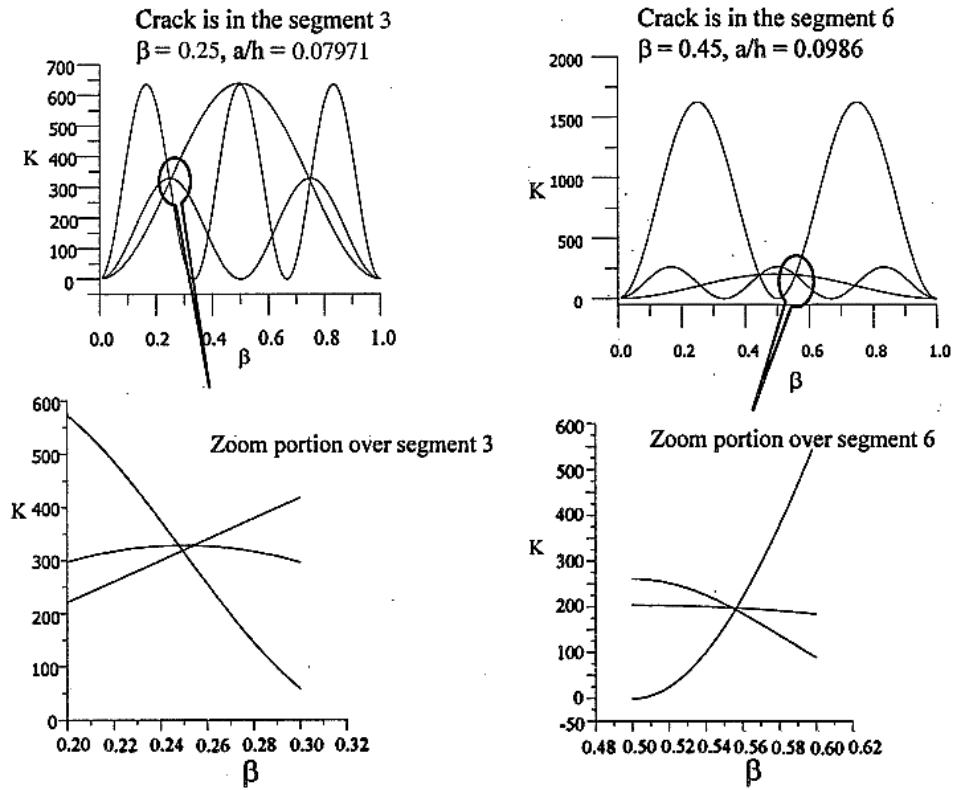
Fig 3-4: The relationship between variation of stiffness and crack location, β [31].

Kim et al. [32] proposed a new damage index to detect and quantify the damaged sections in structures for which a few mode shapes or natural frequencies are available. In this study, a damage-localization algorithm, a damage-sizing algorithm and a damage indictor were investigated. The damage indictor DI_j was calculated as a single index for a number of available modes as shown in Eq.(3.4). In this equation e_{ij} represents the magnitude of error localization for ith mode and jth location, where NM indicates that this index can use a number of mode shapes. The peak of this indictor, as shown in Fig 3-5, was entirely associated with the location of the crack in the beam. However, no experiments were performed in this study to demonstrate the practical application of this approach.

$$DI_j = \left[\sum_{i=1}^{NM} e_{ij}^2 \right]^{-\frac{1}{2}} \qquad (3.4)$$
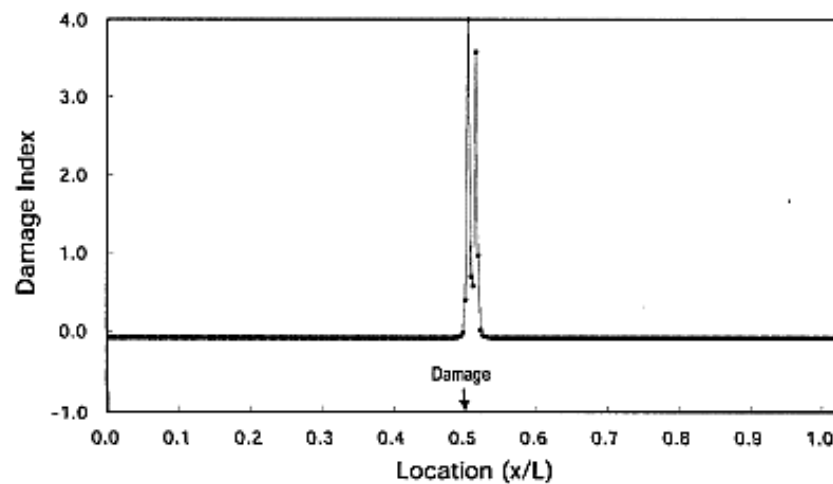
Fig 3-5: The damage index of the cracked beam investigated in [32].

Lee [33] reported a simple approach to detect multiple notches in the vibrating beam demonstrated in Fig 3-6, where the damaged sections were modelled in terms of rotational springs to apply the stiffness reduction. The numerical solution was calculated using MATLAB program to calculate the few first natural frequencies. One of the main conclusions of this research was that damaged sections reduce the magnitude of the natural frequency.
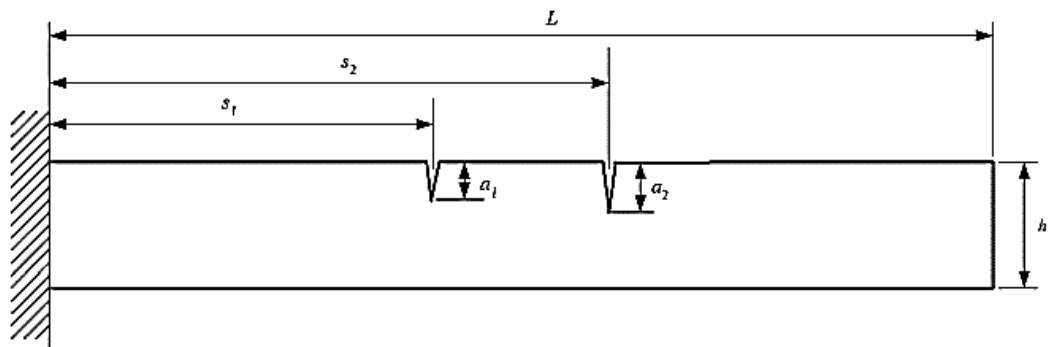
Fig 3-6: The multiple cantilever notched beam analysed in [33].

Although frequency-based damage detection has been investigated by a number of researchers for damage detection, it still has a number of limitations. One of the common fundamental drawbacks is modelling damage, where the mathematical basis of most approaches in modelling cracks depends on the Euler-Bernoulli beam theory. In this theory, cracks can be modelled as part of a rotational spring system to show the reduction of local stiffness. It is common, when using this approach, to lose accuracy

when modelling the cracked section at high frequencies or there are deep cracks. So, this method is most applicable for detecting damage in simple structures, for example thin beam with small cracks [34]. Further, the same authors reported that similar forms of damage might cause similar reduction in natural frequency, even they are located in different regions. Additionally, when using frequency-based damage detection at low frequencies levels, the small changes in frequency might be swamped by high levels of noise.

3.1.2 **Mode shape-based damage detection**

There a number of advantages to damage detection methods that use mode shape compared to natural frequency-based damage detection. Firstly, mode shape can provide more local information than natural frequencies, this make mode shape more sensitive to damage localization. Secondly, mode shape is less sensitive to environmental conditions than natural frequency [35]. Mode shape-based damage detection depends on the assessment of the change between damaged and intact modes. The intact data is considered to be a baseline measurement, and can be determined either by experimental examination of the healthy structure or accurate numerical modelling of the same.

Ostachowicz et al. [36] investigated the effects of a transverse crack in a cantilever beam, as per Fig 3-7, on the measured dynamic response. The authors emphasized the fact that the existence of damage such as transverse cracks along beams causes a reduction in local stiffness. The cracked beam was analysed under condition of forced vibration. Then the analysis of dynamic response was utilized to quantify the damaged section in this beam. Using the subroutine of a program written in Fortran77, researchers were able to study the effect of cracks by calculating the global stiffness matrix for the structure. The dynamic amplitude of the cracked beam (crack ratio $\frac{L_1}{L} = 0.3$), was calculated at different crack sizes, as per Fig 3-8, under harmonic excitation. The crack size in this research had a ratio in terms of $\left(\frac{A}{H}\right)$, where A is the crack height, and H is beam height and it was implemented at different values 0, 0.125, 0.250, 0.375, 0.500, and 0.600. Obviously, from Fig 3-8, increasing the crack size decreases the local stiffness and this results in an increase in the dynamic amplitudes. Calculating the angle

of the dynamic response at these sizes clearly showed the cracked section, as per Fig 3-9. The sudden change in the angle deflection was associated with the location of the crack.
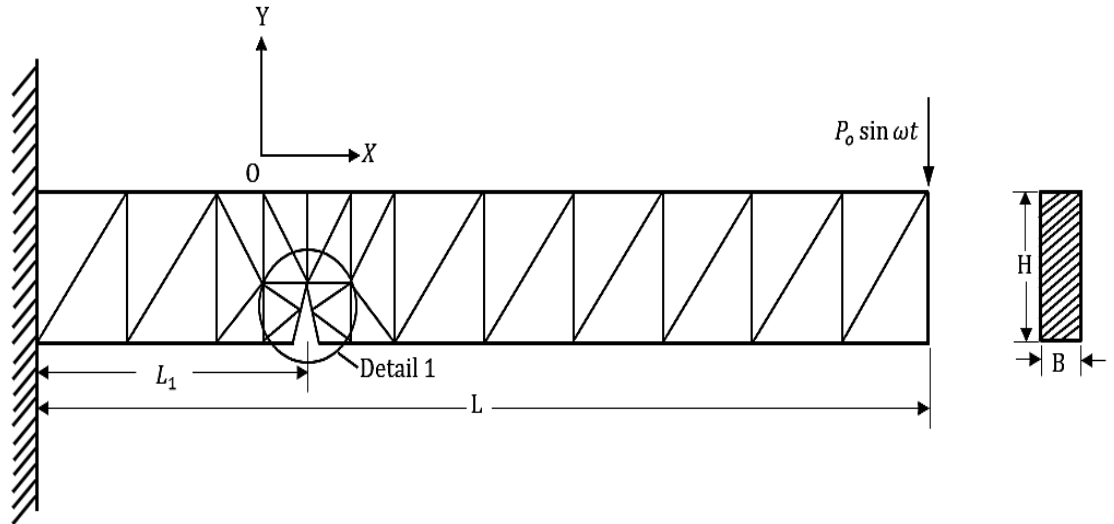
Fig 3-7: Notched cantilever beam as reported in [36].
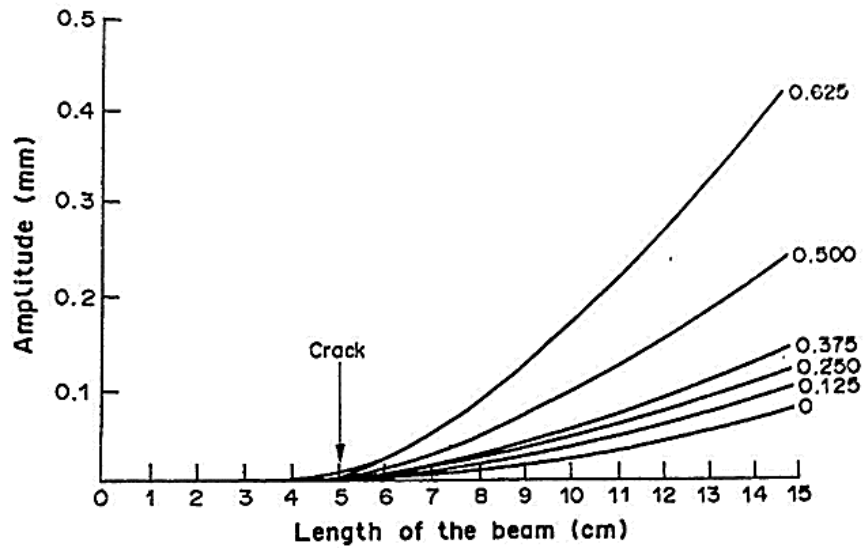
Fig 3-8: The dynamic amplitude of different notches size in a cantilever beam [36].
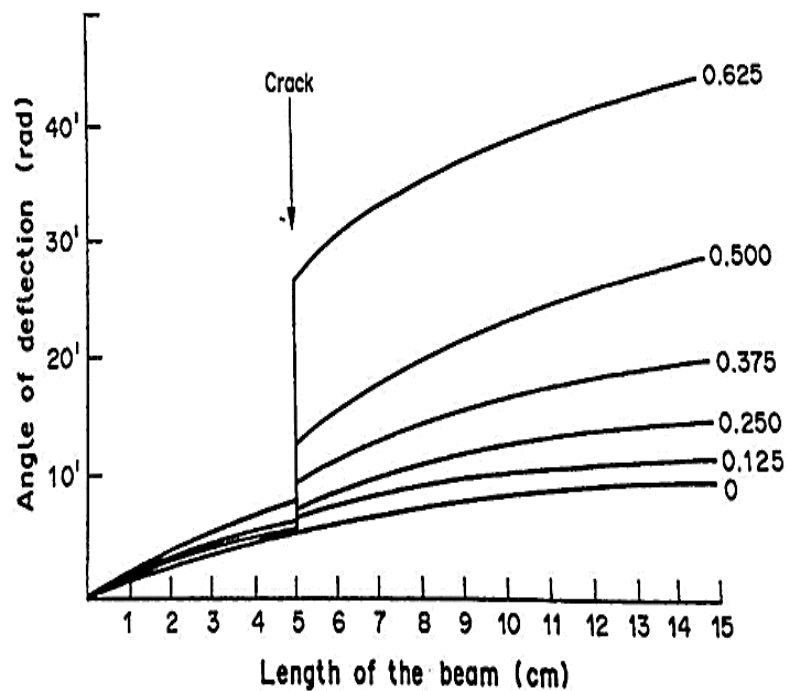
Fig 3-9: Angle of deflection for the notched cantilever beam [36].

Abdo et al. [37] investigated the rotation in mode shape as a technique to define damaged regions in structures. Here, the first four modes were calculated numerically for damaged beam and plate structures. The damaged sections were modelled at 0.5 and 0.6 to the supported edges, by reducing the value of Young's modulus, ΔE, of a simply supported bar. Calculating the damaged modes and their derivatives, as per Fig 3-10 and Fig 3-11, clearly showed that the slope of mode shape could capture the damaged sections, even with only a small change in stiffness of 5% E. The peak or spike associated with slope of the damaged modes showed the location of the damage. This study added further evidence in support of the use of vibration techniques in damage detection, even though an experiment study was not reported in this research.
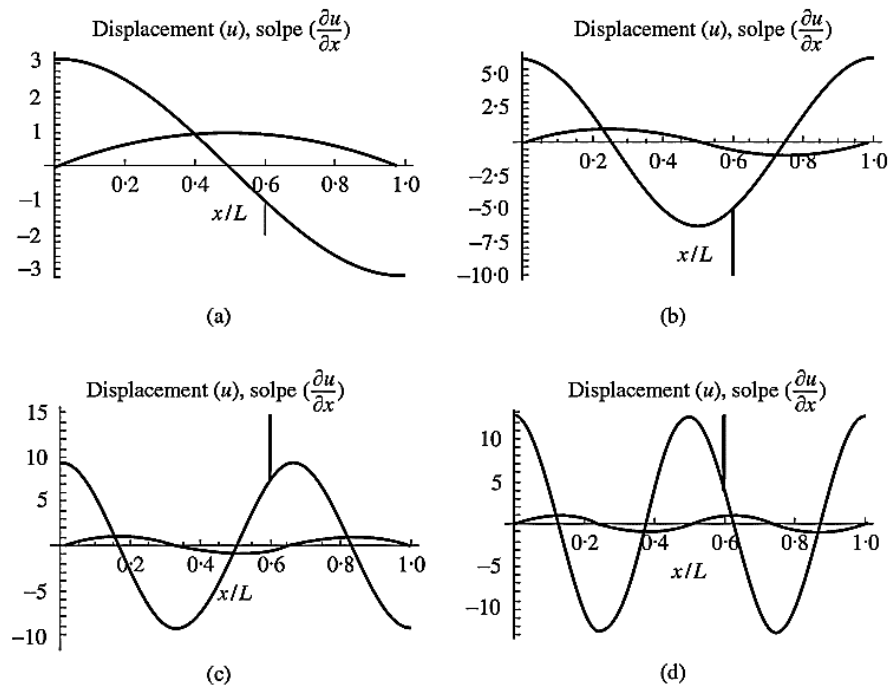
Fig 3-10: Mode shape and its derivative for a steel bar with damage at 0.6 L: (a) first mode; (b) second mode; (c) third mode; (d) fourth mode [37].
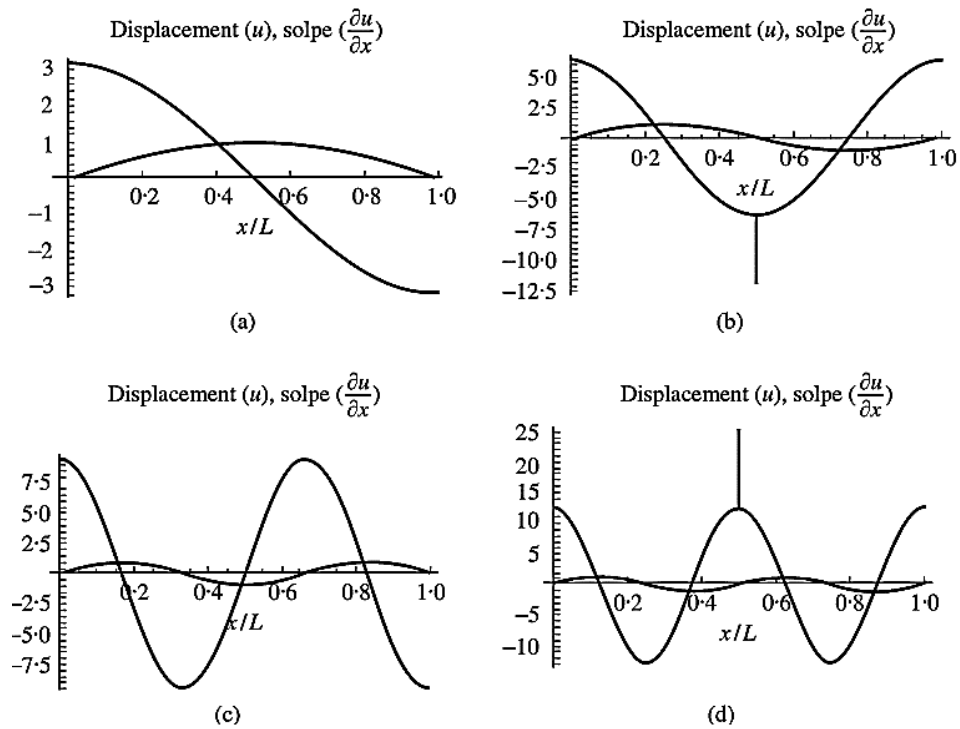
Fig 3-11: Mode shape and its derivative of a steel bar with damage at 0.5 L: (a) first mode; (b) second mode; (c) third mode; (d) fourth mode [37].

Ghoshal et al. [38] reported the use of Vibration Deflection Shapes (VDS) to detect the delaminated areas in composite structures. Delamination was artificially created in different sizes and locations. Piezoelectric actuator patches were embedded in the plate samples, and a laser scanning Doppler vibrometer was used to measure the vibrational modes of the delaminated sample under steady-state condition. The test procedure required are scanning the damaged structure at different frequencies to identify the resonant frequencies, and then exciting these frequencies using a sine wave. The sine excitation adds the maximum energy to the sample at resonance, whereby the peak point of the VDS can then identify the location of the damage. The planar location shown in Fig 3-12b, d shows the delaminated area.
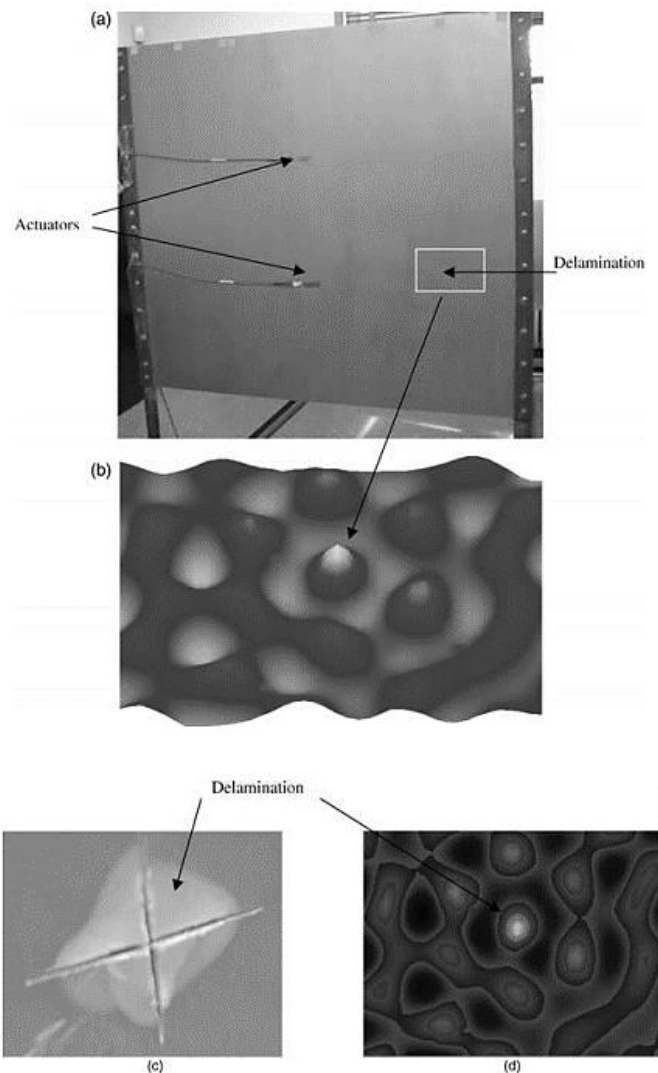
Fig 3-12: Delaminated fibreglass plate with its vibration deflection shapes (a) – (d), as measured by a laser scanning Doppler vibrometer [38].

A damaged multi-girder bridge was investigated by Lee et al. [39]. In this research, neural network-based damaged identification was utilized to detect the damaged sections. The difference between the intact and damaged modes was used as input to the neural network. By analysing two numerical examples for a simple beam model and the multi-girder bridge, the proposed method showed the applicability of mode analysis as a basis for damage identification. In a different study, the damaged carbon fibre-reinforced epoxy plate samples were utilized to detect the damaged areas using vibration-based damage detection techniques [40]. The change in the dynamic characteristics was used as a basis to determine the damaged areas. Double-pulse TV holography with acoustic excitation was employed to measure mode shape translation, rotation and curvature differences due to impact damage in laminated plates. Calculating the curvature difference index using the measured signals showed the ability of this method to detect the damaged area, although the actual type of damage was not noted.
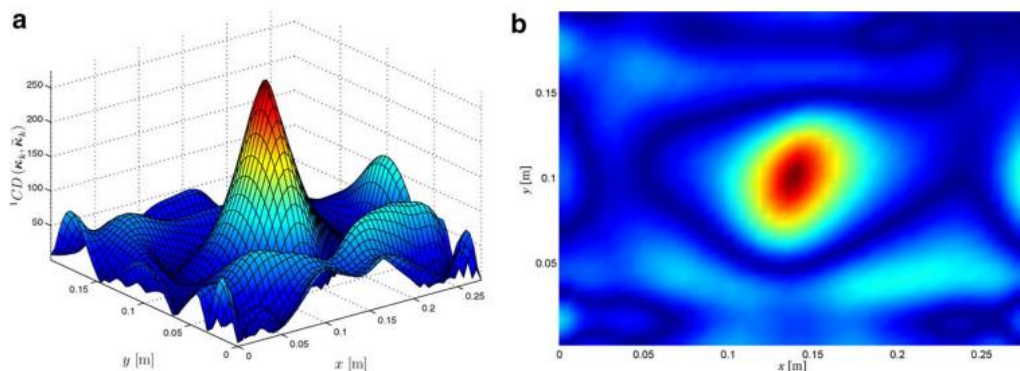
Fig 3-13: Curvature differences method for a damaged plate for the third mode (a) 3D plot of curvature index, (b) contour plot [40].

An excellent review of the development of vibration-based damage detection techniques was given by Yan et al. [41]. The details of these methods were explained in addition to potential trends in their future development. Furthermore, this article explains why vibration-based damage detection is utilized for damage detection purposes. Qiao et al. [42] studied the combination of static and dynamic methods to identify the delaminated areas in E-glass epoxy laminated composite specimens. Whereas, the pre-set of composite samples with static compressive force showed that as static force goes up, damage detection via the analysis of dynamic signals becomes

increasingly clear. Experimental work was completed in this regard, while numerical analysis was performed using the ANSYS software to allow for identification of the delaminated sections. Notched steel beams were investigated to demonstrate the possibility of using vibration-based damage detection methods in the practical applications [43]. The structural irregularity index (SSI) was calculated to determine the damaged sections. The irregularity of dynamic responses was shown by calculating the curvature index of the contact and damaged modes. Mode shape was less sensitive than curvature for localization damaged sections. This paper again confirms the utility of vibration-based techniques in damage detection. Roy et al. [44] investigated the mathematical criteria for the correlation between the damage and the fundamentals of mode shape. This was achieved by mathematically deriving an expression for the damaged mode shape. The numerical example was a cantilever beam divided into a number of elements to study the effects of damaged sections on the dynamic responses at different positions, as per Fig 3-14, where the discontinuities in beam can be localised by calculating the mode shape and its derivatives, as per Fig 3-15.
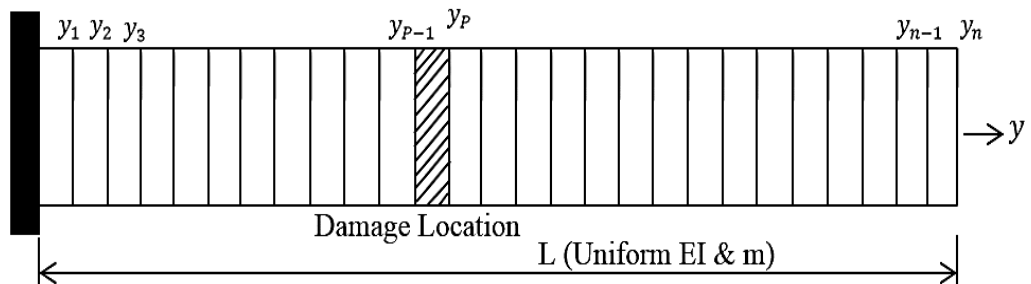
Fig 3-14: Schematic of the cantilever beam used in [44].
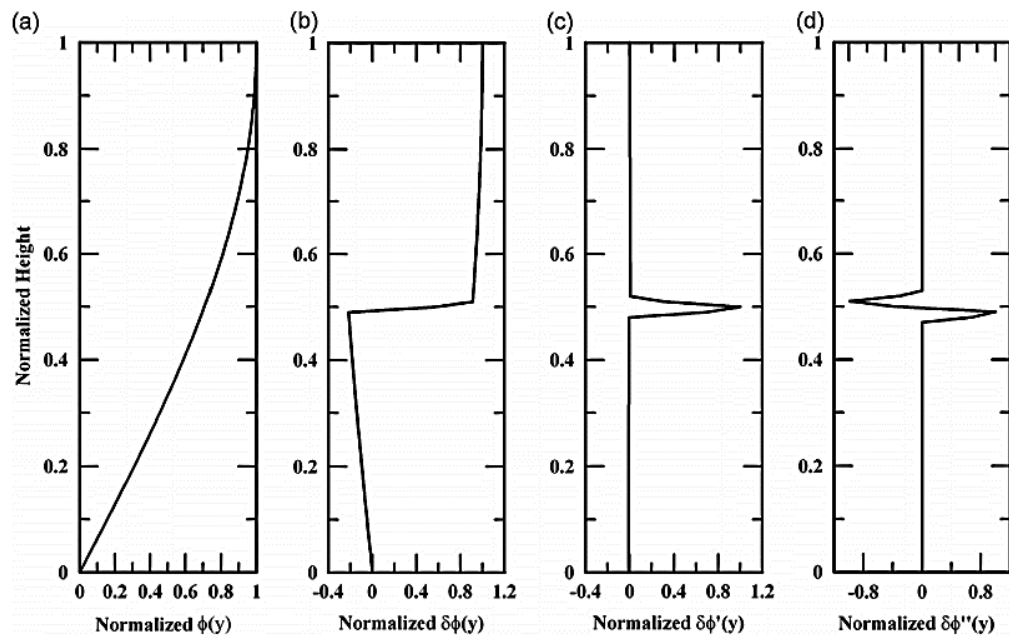
Fig 3-15: The sensitivity of mode shape and its derivatives for the damage to the beam shown in Fig 3-14 [44].

3.1.3 Analysing mode shape using modern signal processing methods

To develop the damage detection using the change in mode shape, extensive research has been completed into damage detection using modern signal processing methods. In most cases, the intact data-baseline is not available, so the numerical model should be created carefully [45]. To avoid a lack of intact data and difficulty in modelling the accurate numerical model, modern signal processing can detect the damaged sections without the intact data being required. Hadjileontiadis et al. [46], [47] proposed a beam and plate index called a fractal dimension (FD) to detect the notched sections in the beam and plate structures. Fractal dimension is an index proposed to analyse waveform points for more mathematical details about this index, see chapter four section 4.2.4. Hadjileontiadis et al. [46] used FD to localize the notched section in beam structures, as shown in Fig 3-16. As it is clear from Fig 3-17, that this index can detect the damaged section by the peak associated with the location of the damaged region, where the FD was calculated directly using mode shape data.
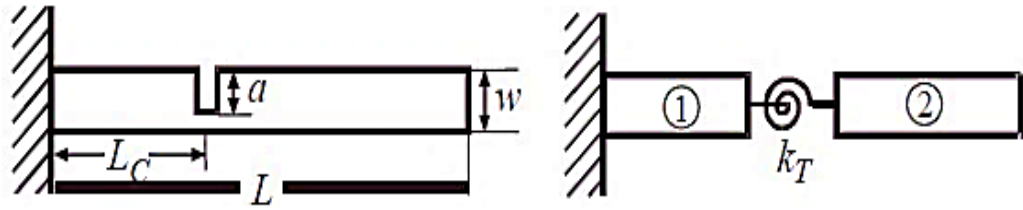
Fig 3-16: Cantilever beams with transverse notches [46].
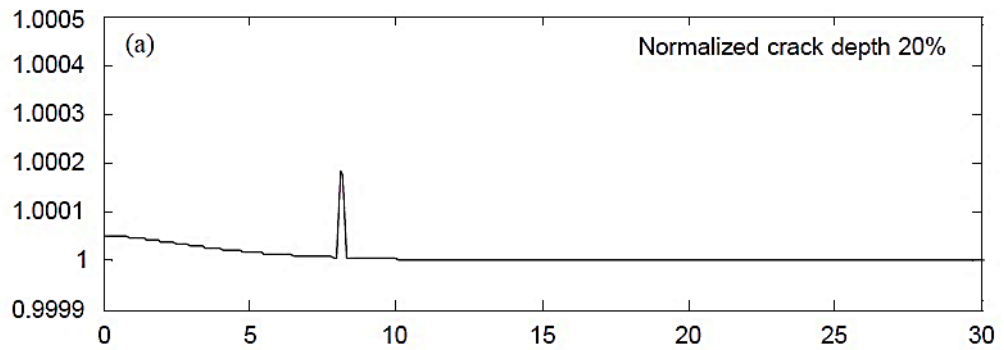
Fig 3-17: Fractal dimension calculated for the notched beam [46].

FD is sufficient to detect damage using lower-frequency modes; however, for higher-frequency modes, FD might give misleading information about the damaged area. For this, Wang et al. [48] proposed a modifications to FD, referred to as a "generalized fractal dimension" (GFD) by implementing a scale factor, $S,$ to the FD equation, as shown in Eq.(3.5). The authors noted that the choice of S is vital to accurate detection. Theoretically, S is a scale and it is used to increase the index peak. According to Wang et al. [48], S can be increased till the data over the curves begins to oscillate. After this step, increasing S might result in the disappearance of the peak in the curve used to detect damaged sections.

$$GFD = \frac{log_{10}(n)}{log_{10}(n)\left(\frac{d_s}{L_s}\right) + log_{10}(n)}$$

(3.5)

$$d_s = \max_{1<j\leq M} \sqrt{\left(y_{i+j} - y_i\right)^2 + S^2\left(x_{i+j} - x_i\right)^2},$$

$$L_s = \sum_{j=1}^{M} \sqrt{\left(y_{i+j} - y_{i+j-1}\right)^2 + S^2\left(x_{i+j} - x_{i+j-1a}\right)^2}$$

Qiao et al. [49] confirmed the advantages of using GFD in detecting delaminated areas in laminated E-glass composite plates, as shown in Fig 3-18. Both numerical and experimental results showed the delaminated area as per the GFD peaks shown in Fig 3-19 and Fig 3-20. The same criteria of damage detection were applied, where the mode shapes of delaminated samples were obtained and then GFD was calculated to show the damaged areas.
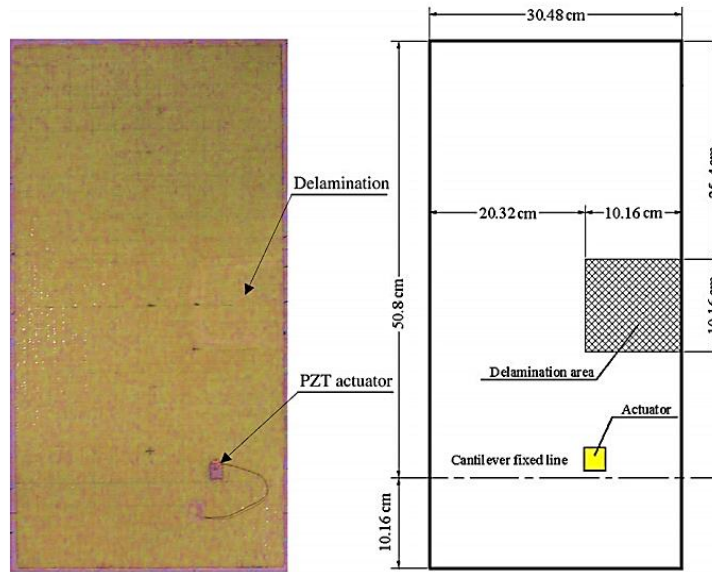
Fig 3-18: E-glass epoxy delaminated plate investigated by [49].
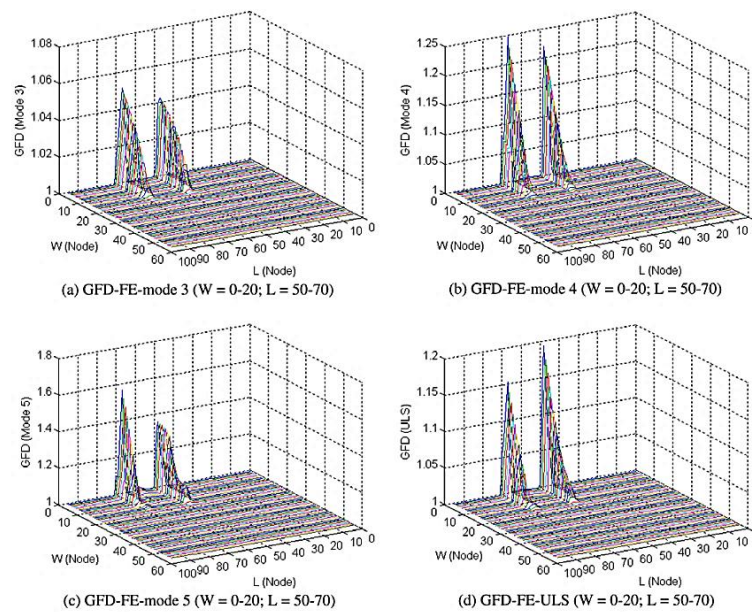
Fig 3-19: Numerical GFD index of E-glass epoxy delaminated plate as investigated in [49].
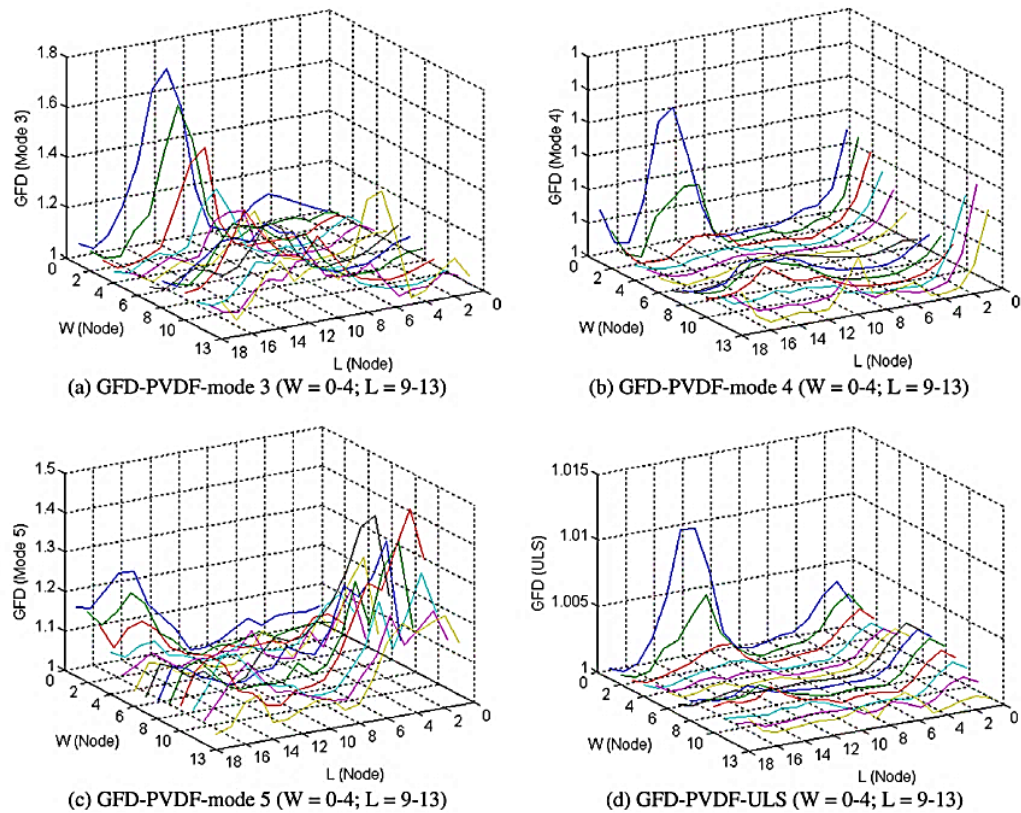
Fig 3-20: Experimental GFD index of E-glass epoxy delaminated plate as investigated in [49].

Qiao et al. [50] suggested a novel fractal dimension–based damage detection method by which to detect the location of damage in a notched cantilever beam. Mode shape was calculated, and the new algorithm applied to identify the location of the damage. The approximated waveform capacity dimension (AWCD) was then derived, as well as formulating the modal abnormality algorithm to determine the damage location. Another approach to damage identification was described by Hadjileontiadis et al. [51]. The proposed kurtosis crack detector (KCD) was a new algorithm to analyse the dynamic response of damaged specimens. The crack is modelled in terms of a spring to represent the reduction in stiffness due to the presence of cracks in the damaged beams. The use of this indicator showed that an analysing dynamic responses is applicable to localize cracks at different locations in beam structures. Li et al. [52] suggested the use of FD-based index to formulate a new index called FD-based index for damage localization (FDIDL). The key idea to this index was to show the deviation between any two sequence points along the displacement mode shape. Numerical and experimental analysis were achieved to test the efficiency of this index. A cracked beam

was used, where the numerical analysis showed the damaged location, while analysis of the experimental data was not sensitive to damaged regions, as numerical analysis subsequently showed. More recently, Jiang et al. [53] provided further evidence that the analysis of the damaged mode shape of cracked beam structures using FD index provides a good index by which to define damaged areas. By contrast, a double-cracked beam model is used to calculate the first three mode shapes, and then, by determining the FD indicator for the damaged modes, two clear peaks were found that indicated the presence of two damage regions. Both numerical and experimental analysis were accomplished to show the applicability of FD in damage detection purpose. According to the features of FD index, for instance, localization, identification severity of damage and ease of calculation have resulted in a number of researchers considering this index to be one of the proposed techniques in use. However, there is no evidence about the efficiency of using FD with noisy data.

3.1.4 Analysing mode shape using wavelet transform method

The Wavelet Transform Method (WTM) is another significant approach that has received considerable attention due to its ability to show damage information via analysis of modal characteristics. Liew and Wang [54] were amongst the first researchers to use wavelet theory to detect edge-cracks in beam structures, as shown in Fig 3-21. Numerical study presented the damage model, where eigenvalues were analysed using wavelet theory to determine the crack locations. In this study, damage locations were accurately determined. In utilizing wavelet transform analysis, Wang and Deng [55] reported the detection of tip cracks in beam structures using Gabor wavelets, Eq.(3.6), under static and dynamic loads. This formula can be used to detect damage locations in terms of displacement or strain data, as per Eq.(3.7). One of the selected results, that shown in Fig 3-22, illustrates the damage location in the proposed beam.

Here, $\omega_\circ$ and γ are positive constants $\omega_\circ = 2\pi$ and $\gamma = \pi \sqrt{\frac{2}{ln2}}$

$$\psi(t) = \frac{1}{\sqrt[4]{\pi}} \sqrt{\frac{\omega_\circ}{\gamma}} \exp \left[-\frac{\left(\frac{\omega_\circ}{\gamma}\right)^2}{2} t^2 + i\omega_\circ t \right] \tag{3.6}$$

$$C_{j,k} = \int_0^1 f(x)\, \overline{\psi_{J,k}(x)}\, dx \qquad\qquad (3.7)$$
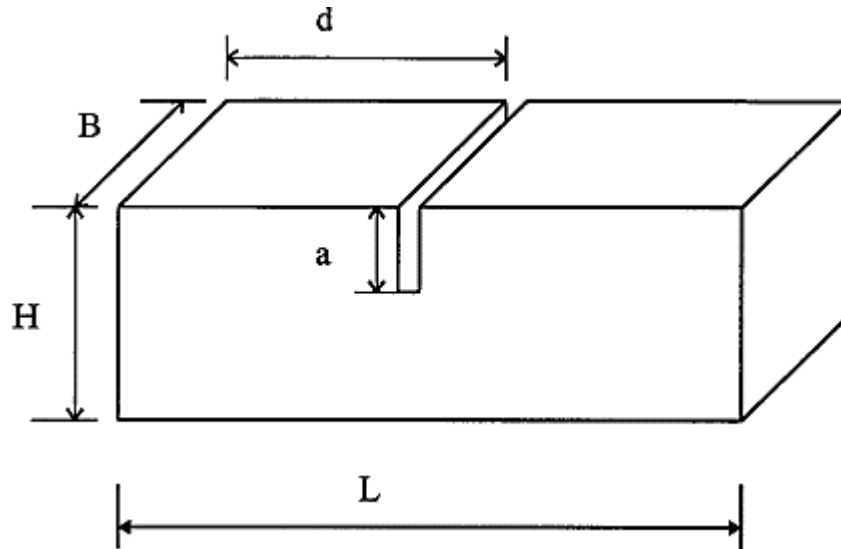
Fig 3-21: Schematic of the cracked beam utilized in [55].
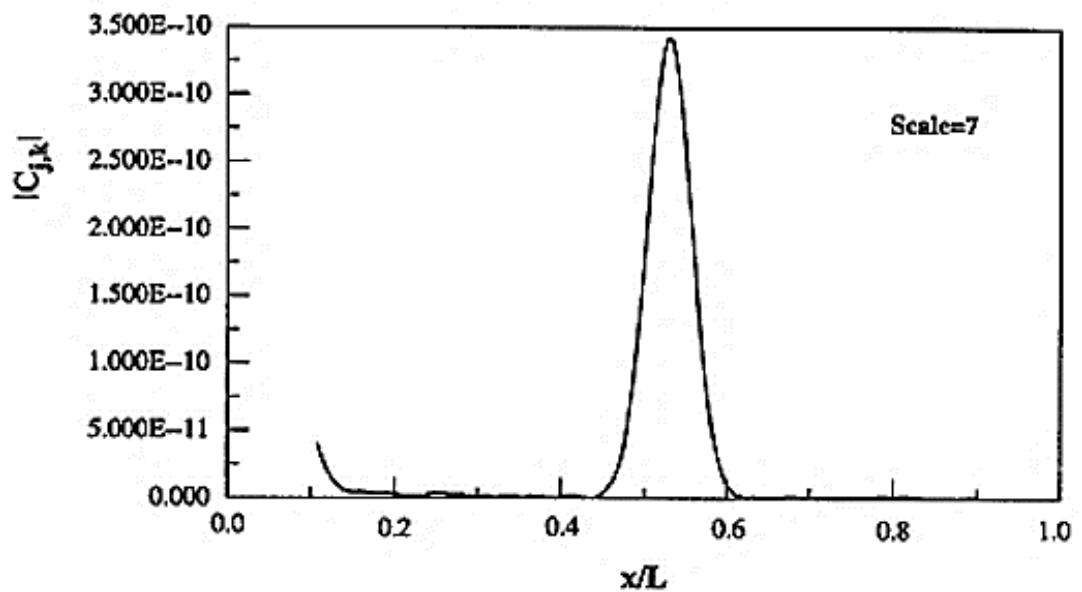
Fig 3-22: Gabor index distribution of the cracked beam investigated in [55].

Quek et al. [56] reported the sensitivity of using the wavelet transforms in damage identification in beam structures. Static and impact loads were used in this study. One of the most significant contributions the authors made via their research was that signal processing analysis is effective in analysing mode shape and consequently

detecting damaged areas. Douka et al. [57] and [58] studied the use of wavelet transforms to analyse changes in mode shape to detect damaged regions, where the use of continuous wavelet transform (CWT) in detecting damaged sections for the damaged steel beam was investigated by [57]. In [58], the authors reported one-dimensional damage detection using CWT on plate structures. To estimate the severity of such damage, an intensity factor was calculated as a reflection of crack depth. In both articles, a sudden change in wavelet transform index was associated with the damaged regions. The use of wavelet transforms in detecting transverse open cracks in beam structures was demonstrated by [59]. Extensive work was undertaken to simulate the cracked location, and different wavelet families were used in damage detection. Classical Gaussian wavelets were used to analyse mode shape and define damaged sections. The Gabor index as shown in Eq.(3.6) was calculated to show the damaged sections. The authors suggested, as shown in Fig 3-23, that scaling the damage index provides clear damage index peaks. Also, Chang et al. [60] used the same technique reported in [59] to detect the damaged sections in plate structures.
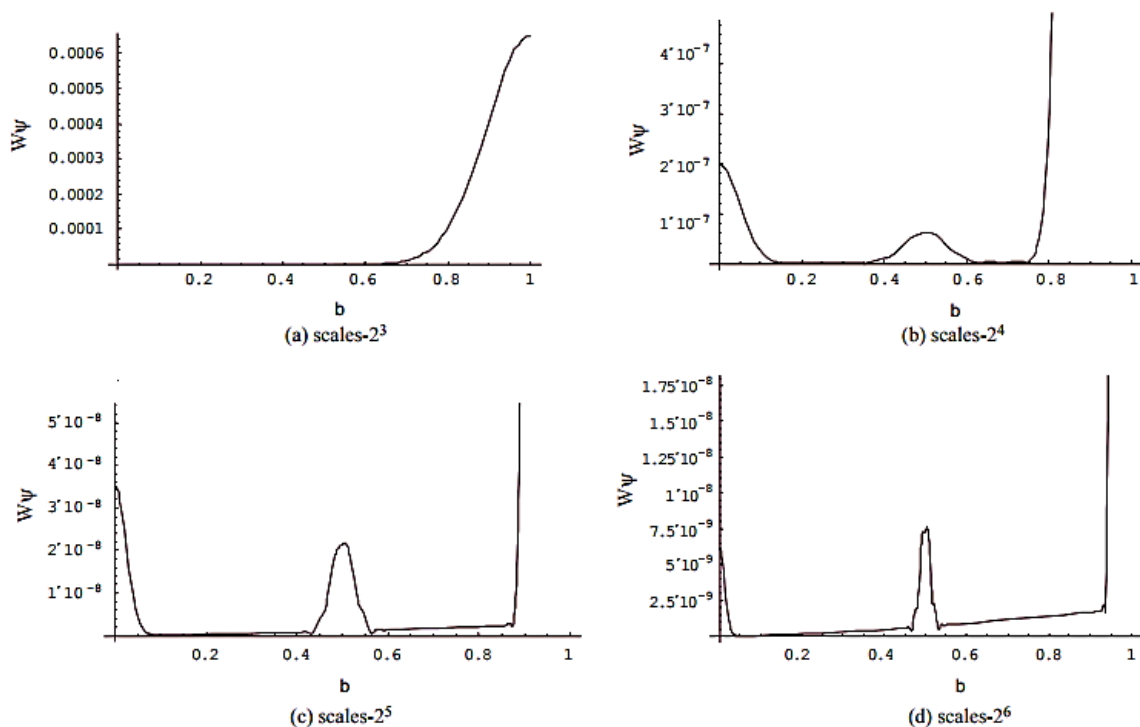
Fig 3-23: Calculated first-mode Gabor index for a notched cantilever beam using different scales [59].

Rucka et al. [61] applied both respective and biorthogonal wavelet criteria on the fundamental mode shape to detect damaged sections, where the fundamentals of 1D analysis were extended to 2D. The sudden change in wavelet distribution provided a tip identical with the location damage. One of the studies focused on using a 2D CWT-based algorithm detection to detect damage in plate and shell structures was introduced by Khan et al. [62]. The use of this technique was reported as being an effective method of analysing damaged modes. Shahsavari et al. [63] studied the application of wavelet transform-based damage detection in localizing damage sections in beam structures. According to the fundamentals of CWT, authors proposed a new indicator called the Likelihood ratio, as per Eq.(3.8), where, σ_i is standard deviation, μ_i the mean, m, n are the numbers of observations, and S_i is a vector generated by the original wave. One of the selected results shown in Fig 3-24 explains a possible way in which wavelet transform signal processing could be improved. The damage was detected by analysing the measured mode shape.

$$L(S_i \backslash \mu_i, \sigma_i) = \left\{ \sum_{j=N_1+1}^{m} (2\pi\sigma_i^2)^{\frac{1}{2}} e^{\frac{-(S_i(j)-\mu_i)^2}{2\sigma_i^2}} \right\}_i ; (i = 1,2,3,\ldots,n) \quad (3.8)$$
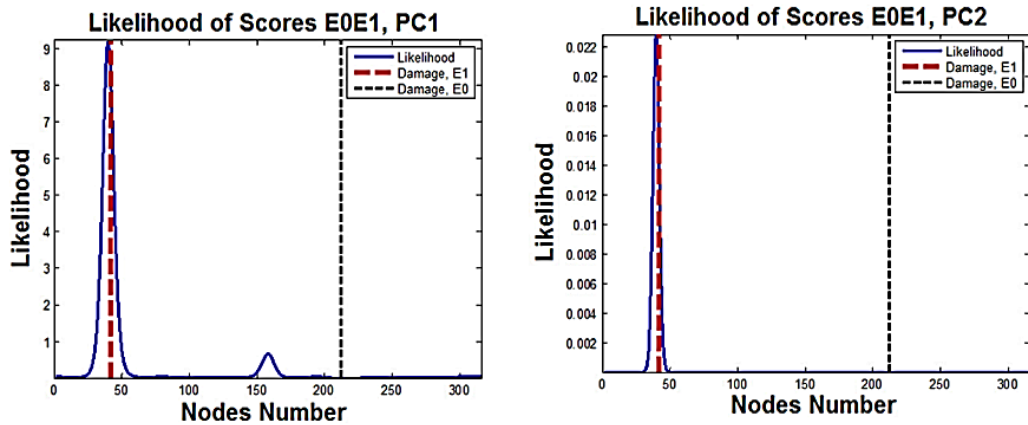
Fig 3-24: Calculated likelihood ratio using wavelet transform criteria of a steel beam with damage at $0.17\ L$ [63].

3.1.5 **Curvature-based damage detection**

The main purpose of using any method in damage detection is to quantify and localize damaged areas. In the last few decades, most researchers in this subject have noticed that using displacement mode is not effective to detect simple damages even with using higher modes [64]. An extensive effort was made to develop the sensitivity of mode shape in damage detection.

Pandey et al. [65] was one of the first research groups to investigate the relationship between the change in dynamic characteristics and physical properties. The authors proposed the possibility of using the second derivative of mode shape in damage detection. This derivative was called curvature index as per Eq.(3.9), where v_i'' is the curvature, v_{i+1} displacement of mode shape and h element length. The numerical analysis of a cantilever beam was proposed, and the damaged sections were modelled in terms of reducing the local stiffness, as per Fig 3-25. In this figure the cantilever beam model was divided into 20 equal elements. Then damage was modelled by reducing the modulus of elasticity; according to this, damage can be modelled at any location along the beam. As demonstrated, calculating the curvature of the intact for the first five modes did not show any sudden change or jump, as seen in Fig 3-26, while calculating the difference between the damaged and intact curvatures for the first mode, Fig 3-27, showed a clear peak at the damage location. This difference was calculated for different damage locations, where the modulus of the elasticity of the damaged section E' was reduced to different values ($0.1\,E$, $0.1\,E$, $0.3\,E$, $0.3\,E$, $0.5\,E$, $0.7\,E$ and $0.9\,E$). Each damage provided a unique peak due to the change in mode shape amplitude. A larger reduction in local stiffness showed a larger curvature index peak.

$$v_i'' = \frac{(v_{i+1} - 2v_i + v_{i-1})}{h^2} \tag{3.9}$$
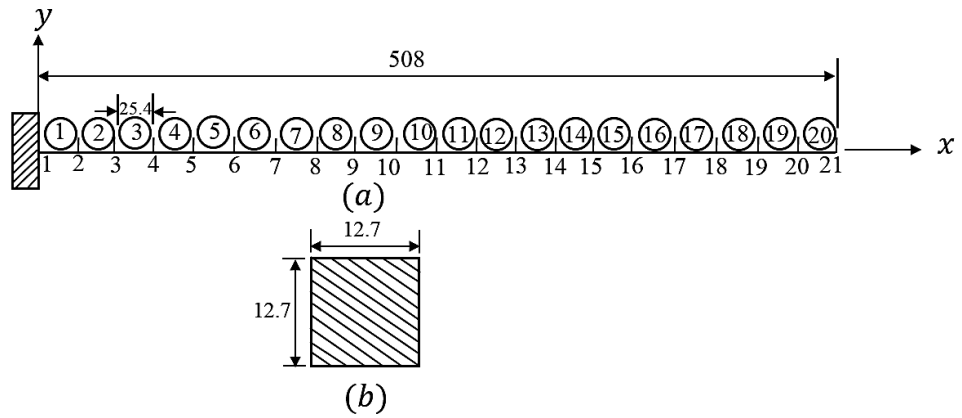
Fig 3-25: Numerical cantilever beam model: (a) finite element model; (b) cross-sectional area of beam [65].
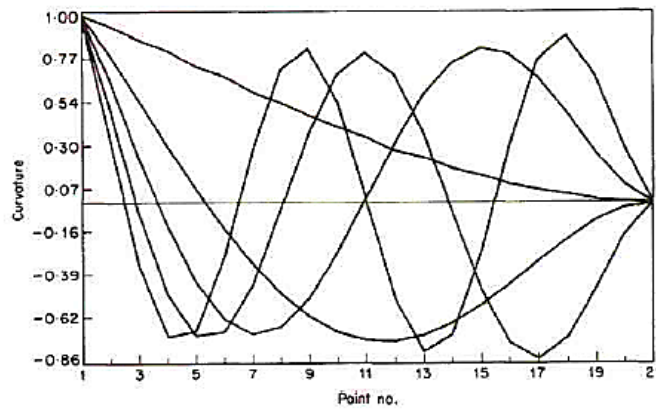
Fig 3-26:The first five curvatures mode shapes for an intact cantilever beam, as per [65].
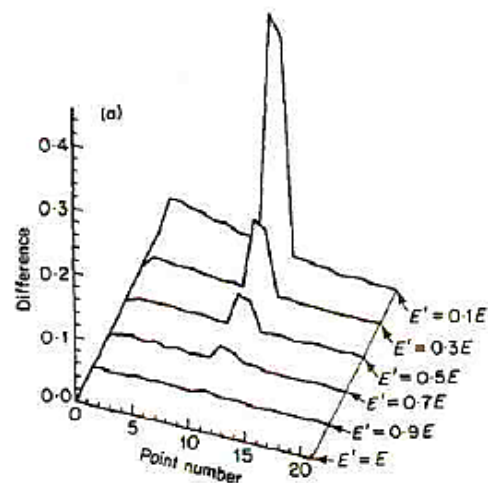
Fig 3-27: Numerical absolute difference between the damaged and intact first mode with different local stiffness at element 10 [65].

Salawu et al. [66] confirmed the same point investigated in [65], namely that calculating the displacement of mode shapes numerically or measuring them experimentally is not an effective approach in identifying discontinuity in mode shape. This contribution urged researchers to research and modify the dynamic analysis process in order to use in damage detection for different mechanical structures. Swamidas and Chen [67] performed a finite element study on notched structures. This study showed that notches had a clear effect on modal parameters. Also, the authors reported that cracks can be quantified via the analysis of measured mode shapes. The difference between the intact and damaged data was used for this purpose. Further, they reported that using the accurate instruments in experiment have potential role to reduce the noise problems.

Ratcliffe [68] proposed the use of modified Laplacian operator to analyse mode shape and localize damaged sections, where it was reported that in cases of severe damage the local thickness reduces to more than 10%. Here, a finite difference approximation of Laplace's differential operator was applied to the damaged mode to identify the damaged elements. It was found that the magnitude of the difference function using the Laplace criteria was able to localize damaged sections, as per Fig 3-28.
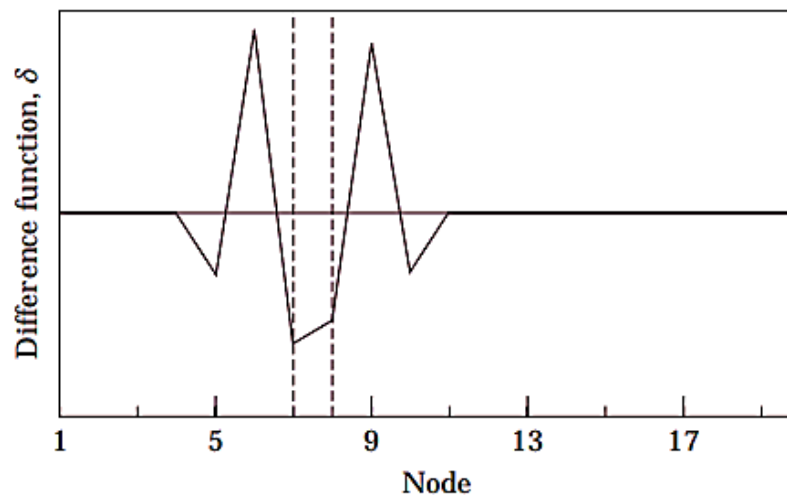
Fig 3-28: Calculating the difference function using Laplace criteria of a damaged cantilever beam [68].

The experimental study completed by Ratcliffe and Bagaria [69] demonstrated the localization of delaminated areas in a composite beam. Vibration-based damage

detection was implemented through the measurement of dynamic modes. Then, to determine the damaged area, the curvature index was calculated; to improve this damage index, the algorithm from the gapped smoothing method (GSM) was implemented to help reduce the effects of noise. The authors reported that the intact data baseline was not required for damage detection. Sampaio et al. [70] discussed the effectiveness of using the curvature of frequency response function (FRF) in damage detection. The difference between the intact and damaged FRF curvature index was clearly show the damage location. Local stiffness was reduced at different values to evaluate the efficiency of this method. The author concluded that higher reduction in stiffness causes higher curvature peaks.
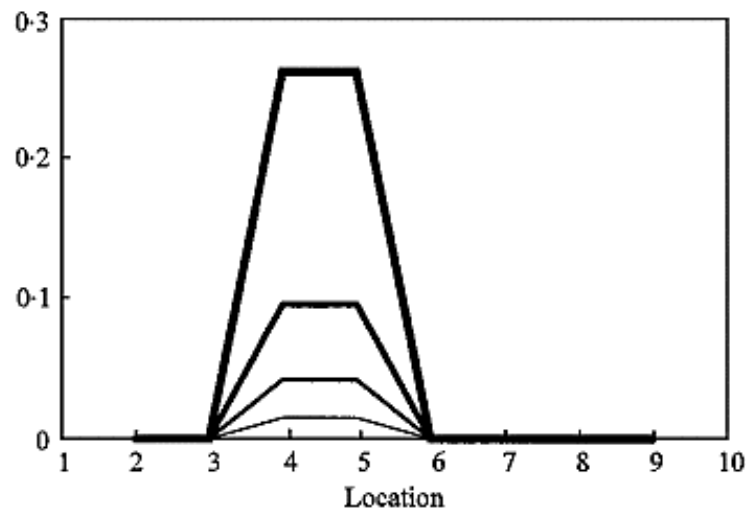
Fig 3-29: FRF$_s$ curvature difference index for a frequency between 0-10 rad/s, damaged located between points 4 and 5 and peaks representative of different damage levels of 20, 40, 60 and 80% from the low to the high peak [70].

Within the frame-work of damage detection development, Wahab et al. [71] presented a numerical study to develop the curvature damage index. This development was accomplished by calculating the curvature damage factor, Eq.(3.10). Damage in this numerical study was modelled by reducing local stiffness to 90% *EI* (*EI* Intact stiffness). This reduction was used to represent the stiffness of a damaged section in a simply supported beam. This factor was calculated by using the average of the absolute difference between intact and damaged data for the first four modes. In this equation, v_{oi}'' and v_{di}'' are the intact and damaged curvatures, respectively and N is number of modes. The authors reported that calculating this index showed the damaged

location (node 11) precisely, as shown in Fig 3-30. This factor was applied to detect damage in real bridge with damaged sections. According to their research, as per Fig 3-31, curvature damage factor can be more accurate than just calculate curvature. However, this factor depends on more than one mode and in dynamic analysis it is not easy to measure the higher modes accurately.

$$CDF = \frac{1}{N} \sum_{n=1}^{N} |v''_{oi} - v''_{di}| \qquad (3.10)$$
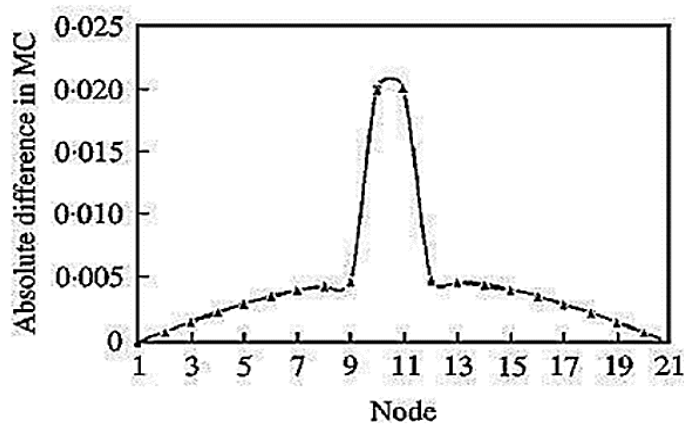
Fig 3-30: The effect of the damaged element on the curvature difference index of simply supported beam [71].
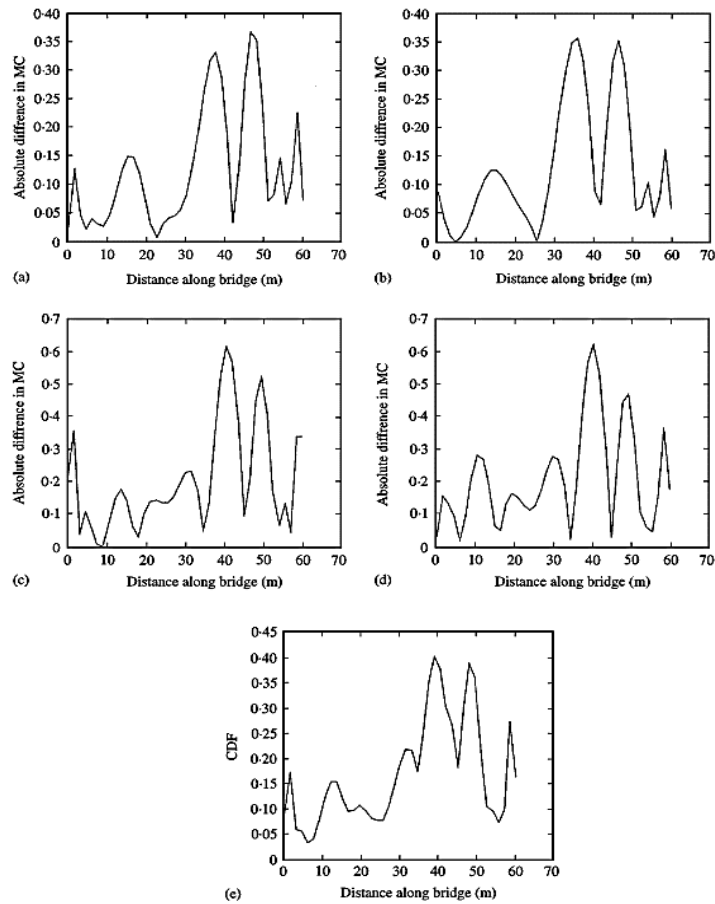
Fig 3-31: Calculated curvature index and CDF of the real bridge; (a-d) are absolute curvature index for mode 1-4 and (e) is the curvature damage factor calculated by [71].

Ratcliffe [72] used vibration-based damage detection to identify the notched sections in steel beam structure. Experimental results included measuring the frequency response functions for the damaged beam to determine the displacement as a function of the measured frequency. Then displacement functions were converted to curvature indexes. To improve the damage detection process, the damage index was calculated according to the formula shown in Eq.(3.11), where δ_i is the damage index for the ith grid in the curvature curve, p_0, p_2, and p_3 are coefficients calculated using curvature points, C_i. The difference shown between Fig 3-32 and Fig 3-33 explains the upgrading of curvature (using curvature as a basis to calculate another damage index) to detect damaged sections efficiently.

$$\delta_i = (p_0 + p_1 x_i + p_2 x_i^2 + p_3 x_i^3 - C_i)^2 \qquad (3.11)$$
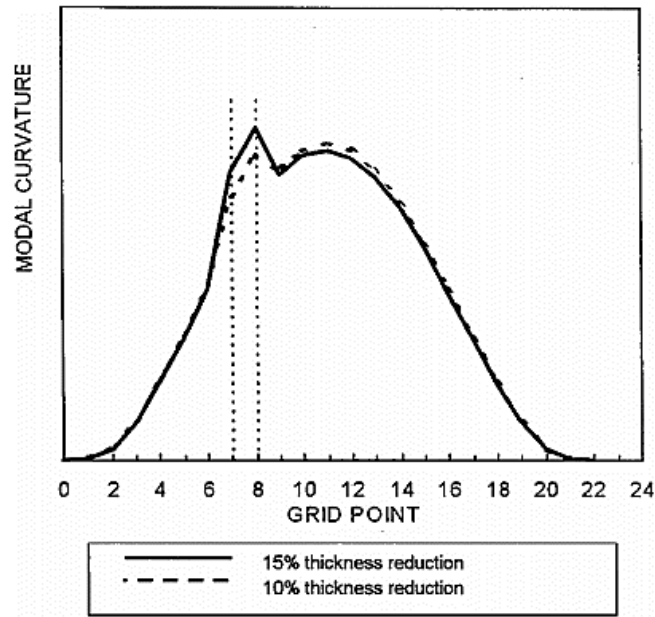
Fig 3-32: Curvature index with two thickness reduction percent, 10% and 15% between points 7 and 8 of a notched steel beam [72].
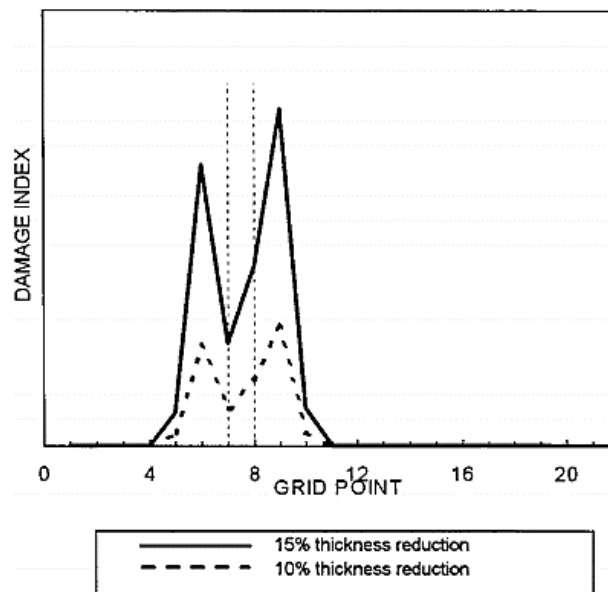
Fig 3-33: Damage index with two thickness reduction percent, 10% and 15% between points 7 and 8 of a notched steel beam [72].

Hamey et al. [73] addressed the use of vibration techniques in delamination detection for carbon/epoxy composite beams. In this study, piezoelectric detectors were used as a sensor to capture the curvature of the laminated beams. Measuring the frequency and mode shape of the vibrating beams were considered the basis for subsequent damage detection. The Absolute Difference Method (ADM) was found to be

a simple approach of damage localization. The difference between the intact and damage curvatures was calculated. In this method, each mode shape was tested individually and then analysed as a single signal. They determined that the careful setting of experimental procedures increased the efficiency to detect the damaged regions. One of the most significant algorithms which involves the same criteria of absolute difference method is Curvature Damage Factor (CDF). Calculating CDF is more accurate than ADM. The third algorithm investigated in this research was Damage Index Method (DIM). It was reported that this technique provides a high level of sensitivity compared to CDF, although it was not as easy to calculate as other methods. Finally, they examined the Frequency Curvature Method (FCM) for the Frequency Response Function (FRF), which was considered to be of particular importance to experimental work. In this method, there is no need for a database of intact structures to perform damage detection. Lestari and Qiao [74] reported damage detection in sandwich E-glass fibre composite beams. Artificial damage was created within the core of these structures and smart piezoelectric detectors were used to measure the dynamic response of the vibrating samples. Calculating curvature damage factor (CDT), as per Eq.(3.10), and damage index, Eq.(3.12), demonstrates that this approach was useful in detecting the damaged areas in sandwich structures. Fig 3-34 can confirm that the CDF and damage index method are useful in damage detection.

$$\beta_{i,j} = \frac{(\{\phi_d''\}_{i,j}^2 + \sum_{i=1}^{i\,max}\{\phi_d''\}_{i,j}^2)\,\sum_{i=1}^{i\,max}\{\phi_d''\}_{i,j}^2}{(\{\phi_h''\}_{i,j}^2 + \sum_{i=1}^{i\,max}\{\phi_d''\}_{i,j}^2)\,\sum_{i=1}^{i\,max}\{\phi_d''\}_{i,j}^2} \qquad (3.12)$$
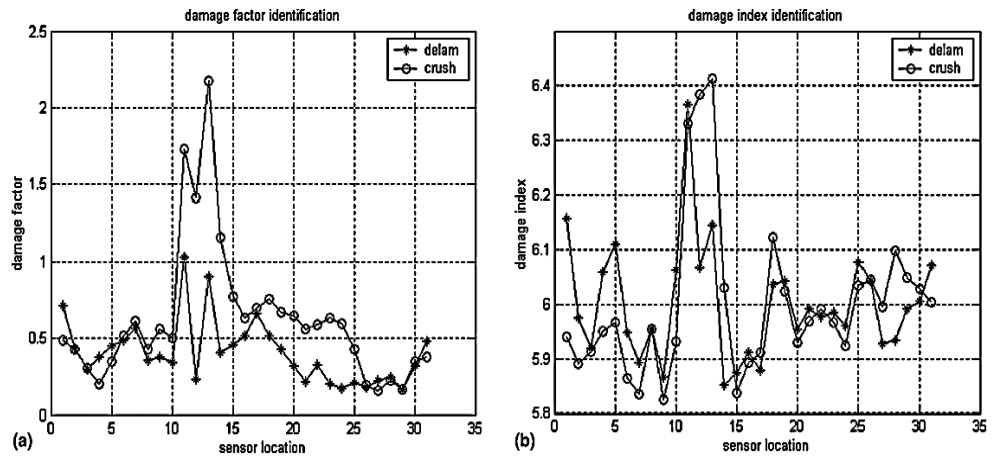
Fig 3-34: Comparison between curvature index (a) and damage index (b) in damage detection in a sandwich beam with delamination and crush damage [74].

A beam subjected to an axial load was investigated by Kim et al. [75]. In this study, the curvature of the damaged and intact modes was calculated to quantify the damaged regions. The authors reported that analysis of dynamic responses clearly showed the damaged regions. Vibration-based damage detection was used to identify the damaged area in wooden beam structures [76], whereas a novel statistical method was proposed to calculate the damage index, DI_{ij}, as shown in Fig 3-35. Calculation of this index depends on the difference between the intact and damaged data, as implemented for a small number of mode shapes in this calculation.
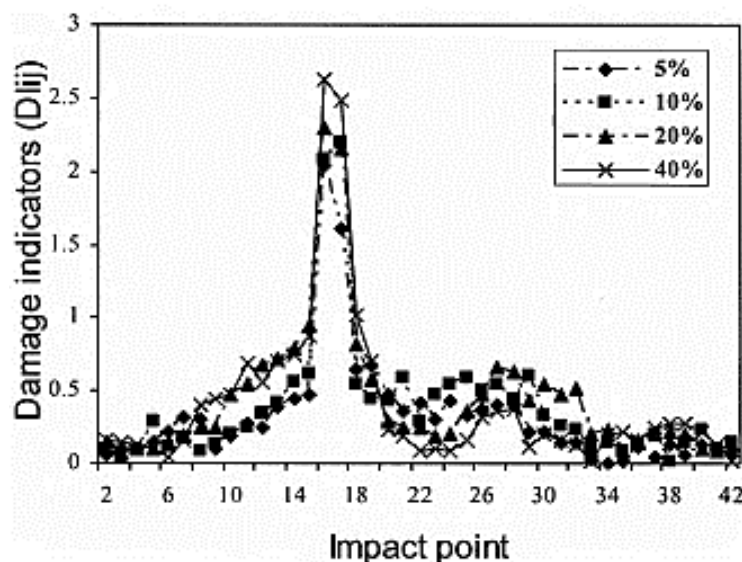
Fig 3-35: Damage detection index for the damaged wooden plate considered in [76].

By contrast, the passive method depends on signal processing analysis to identify the damaged regions, as investigated by a number of researchers. In this regard, numerical and experimental study was investigated by Mosti et al. [77]. The authors demonstrated that dynamic techniques are useful to detect damage in composite structures. The numerical approach involved simulating damage in isotropic laminated composite plates using the FE COMSOL Multiphysics. Calculating the curvature of mode shapes for both damaged and intact data used to detect the damaged area. In experimental work, a numerical filter was combined with the unit of data measurement in order to eliminate the effects of noise. Damage detection using vibration-based techniques was reviewed by Dessi and Camerlengo [78]. This article compared two groups of vibration-based damage detection methods. The first group includes methods require to baseline data, while the second group methods used modified techniques to avoid the intact baseline. In this article the authors reported that the limitations of each technique should be understood. Which means that in practical applications, some techniques are able to localize damaged areas while failing to quantify the severity of the associated damage. More recently, damage detection in delaminated composite plates was reported by Chandrashekhar and Ganguli [79]. The delaminated area (2.5 cm *5 cm) in their study was located at different locations (inboard, centre and outboard) in carbon cyanate laminated plate as shown in Fig 3-36. In this article, a Fuzzy Logic Systems (FLS) was used to calculate the probability densities Eq.(3.13), (Gaussian distribution function), for both damaged and intact plates. In this equation m is the midpoint of fuzzy set and σ is the standard deviation. In this method the change in natural frequency due to different damage locations was used to calculate this index. It is clear from Fig 3-37 that the probability density wave location moves forward depending on the location of the delaminated area. This change in location can be considered an indicator of the existence of damage. The second contribution in this article was calculating CDF as per Eq.(3.10) for a few mode shapes. The peak of this factor was obvious, showing the delaminated area at different levels (slight, moderate and severe) as per Fig 3-38; though for severe damage the distortion at the damaged area become larger.

$$P(\Delta\omega) = \frac{1}{\sqrt{2\pi}\bar{\sigma}} e^{-0.5\left(\frac{(\Delta\omega - \bar{m})}{\bar{\sigma}}\right)^2} \tag{3.13}$$
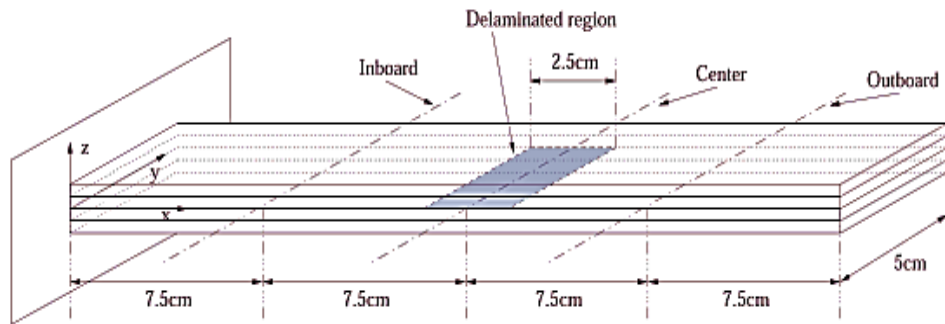
Fig 3-36: Schematic of delaminated composite plate investigated in [79].
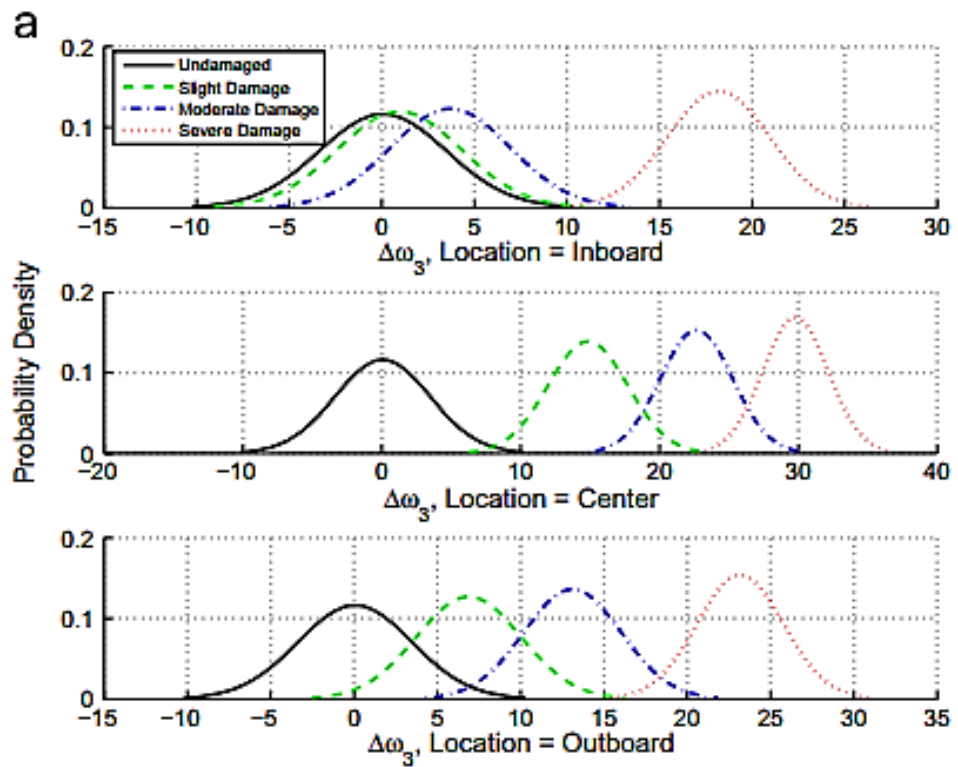
Fig 3-37: Calculating the probability density index for intact and damaged plates using fuzzy logic system for the third vibrational mode [79].

a

Severe Damage

b

Moderate Damage

c

Slight Damage
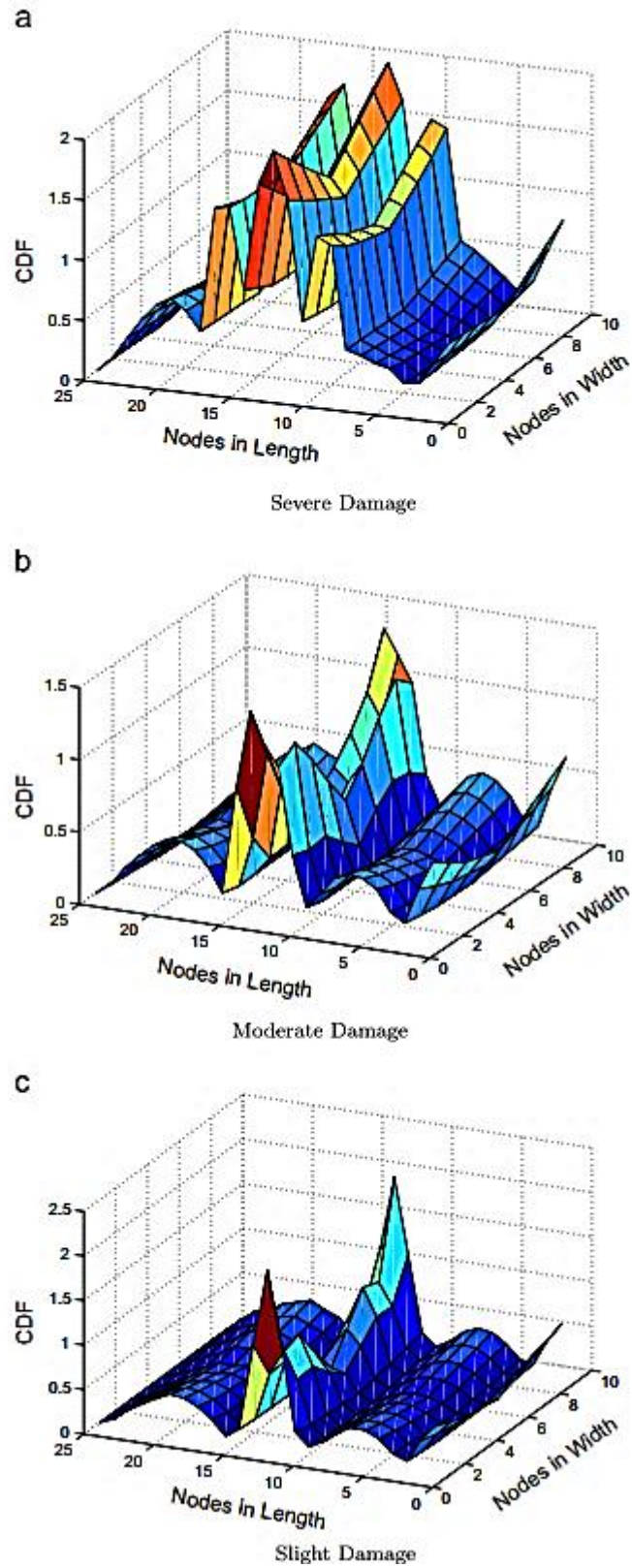
Fig 3-38: Calculating the curvature damage index for different damage levels in delaminated composite plates [79].

3.1.6 **Modal flexibility-based methods damage identification**

Using the flexibility parameter of mechanical structures in damage detection has been investigated by a number of researchers. Pandey et al. [80] proposed a numerical study whereby the variation in flexibility and its curvature were calculated as indexes to detect the damaged regions. The authors showed that this method works better with severe damage than simple damage. Zhang et al. [81] discussed the use of modal flexibility and its derivative, uniform load surface (ULS), Eq.(3.14), where $\emptyset_r$ is the normalized mass mode, n the degree of freedom, ω_r the natural frequency of rth mode. The authors concluded that ULS was less sensitive to the noise data than the mode shape. ULS curvature was used to determine damaged areas in plate structures, as investigated by Wu and Law [82] and [83]. The ULS curvature shown in Fig 3-39 emphasizes the use of this technique as a useful method in the detection of damaged areas. To improve the use of ULS method, Wang [48] proposed the application of a new filter called Simplified Gapped-Smoothing (SGS), as shown in Eq.(3.15), where $(C_0 - C_4)$ are constants that can be calculated by regression analysis. According to the definition of SGS, this index is based on a polynomial equation, as shown in Eq.(3.15), so squaring the entire equation can increase the index peak.

$$u_k = \sum_{r=1}^{m} \frac{\emptyset_r(k) \sum_{l=1}^{n} \emptyset_r(l)}{\omega_r^2} \tag{3.14}$$

$$SGS(x) = (y_{measured}(x) - C_0 - C_1 x - C_2 x^2 - C_3 x^3 - C_4 x^4)^2 \tag{3.15}$$
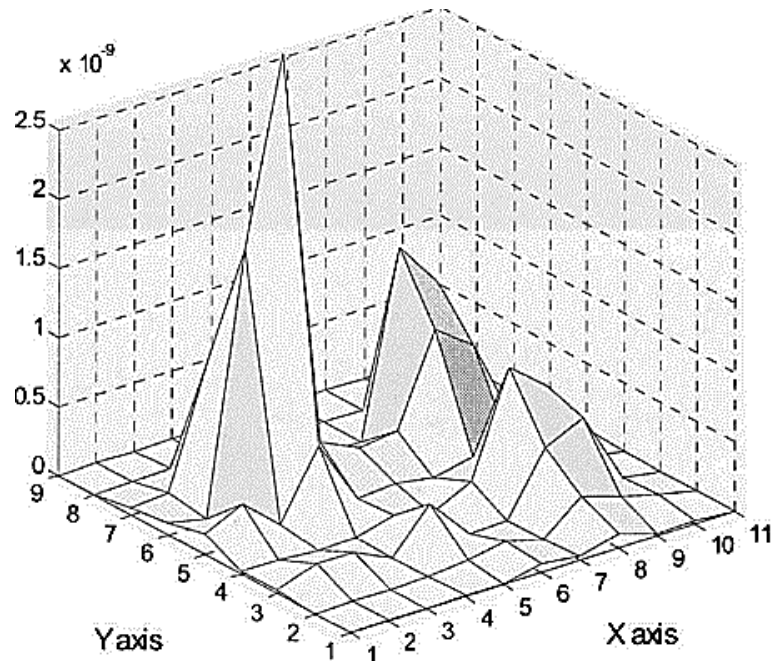
Fig 3-39: Calculated ULS curvature index map of the damaged plate discussed in [83].

Bernagozzi et al. [84] investigated the use of modal flexibility-based damage identification to detect the damage in truss steel structures. This technique can be used in structural health monitoring of generic buildings. This study added another evidence that studying the flexibility behaviour of mechanical structures might be useful in damage detection purpose.

3.2 Non-destructive testing (NDT) techniques

In general, composite structures are inspected for the existence of damage that is commonly caused by the continuous use of these structures in different applications. In composite structures, visual inspection is considered among the easiest and most common methods used in monitoring subject. Techniques similar to radiography are employed to test and analyse bond-line defects. Thermography and shearography NDT methods are generally used to diagnose fibre discontinuity, or where defects occur in honeycomb core and adhesive voids. Acoustic emissions are another NDT techniques utilized to detect damage in thin structures. Ultrasonic methods are another important NDT technique that can be used to macerate the energy of a sound wave to identify damaged regions in composite structures [85]. According to this explanation, the most common NDT methods are:

3.2.1 **Thermal NDT**

Thermography method can be used in health monitoring of composite structures as reported by Dutton [86]. In this research Dutton [86] utilized infrared thermography in addition to external radiation source in order to induce differences in temperature at the surface of composite samples. These differences in temperature were used to detect air voids and other foreign bodies in the samples, as shown in Fig 3-40, whereas the recorded data could be analysed to clarify the nature of any internal damage. Genest et al. [87] investigated detection of disbands in composite structures. To detect the damaged areas, pulse thermography (PT) was used. Then a thermographic signal processing (TSP) and derivative processing were employed to analyse the received signals. Using transient thermal NDT to assess damage in aircraft structures was investigated by Avdelidis et al. [88]. In this research, the authors used this technique to detect different types of damages in composite samples. It was found that this method could detect damage in large structures with considerable efficiency. However, this method has limitation to a certain amount of size and depth of damage after that damaged areas cannot be detected. So, this method is not useful in the detection of small regions of delamination in composite structures. Meola et al.[89] reported the use of optical lock-in to detect the manufactured damages (artificial damages) in carbon fibre reinforced polymer (CFRP) samples. Fig 3-41 demonstrates the set-up of this method that used in the experiment work. It is worth noting that thermographic techniques can be not useful in testing the sensitive surface and are not valid for online health monitoring.
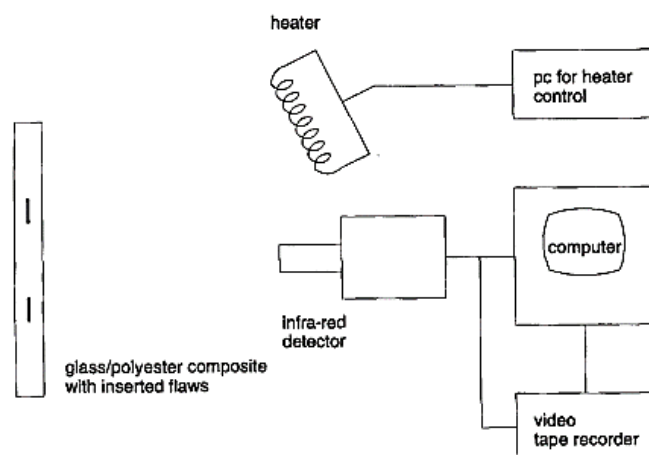
Fig 3-40: Experimental schematic of thermography[86].
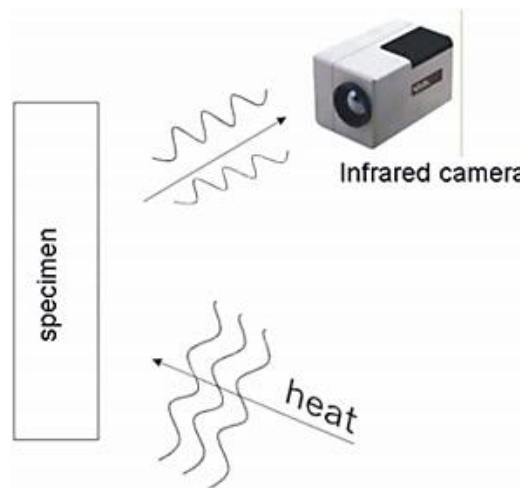
Fig 3-41:Look-in thermography pattern [88].

3.2.2 **Radiography**

Radiographic techniques, practically X-ray, are considered among the most important non-destructive methods. These methods can be applied to all materials and can be used to examine the internal parts of an object. X-rays are electromagnetic waves at wavelengths ranging between 0.01 and 10 nanometres. X-rays have a high energy level according to the inverse relationship between wavelength and energy. This enables them to pass through materials and examine their internal parts. This feature of X-rays can be utilized to detect damage, cracks, voids and any fault in the material. Different parameters are related to the use of these waves, such as the density and thickness of the material to be examined, the density and energy of the X-rays, and the required amount of X-rays to pass through the material. Also X-rays can be collected in 1D, 2D and even in 3D [90].

Fiori et al. [91] conducted an experiment using phase-contrast neutron tomography to examine the ability of this technique to identify cracks in samples of aluminium alloy. In this study, the authors used 2024 fatigued Al alloy samples. They reported that using this experimental method detected cracks and provided an estimate as to some of the cracks' parameters, such as thickness and length. Xu et al. [92] investigated an automatic-X-ray approach to identify radial and circular cracks in wing structures. To this end, the authors used a robotic X-ray imaging system provided with a sophisticated detector to collect high-resolution photographs. These images have been

taken for fastener holes at different locations in the wing of aircraft. Both of radial and circular scanning on this structure was accomplished to detect the crack location, as per Fig 3-42. Finally, to reduce the effect of noise in the captured images, three crack filters were employed. Albuquerque et al. [93] presented a successful identification of delaminated areas in laminated plates utilizing radiographic technique. Here, the authors used an artificial network to divide the captured images and analyse them efficiently.

The advantages of using radiographic technique that can be applied to all types of materials, allows rapid examination, and provides efficient visual of interior parts. However, there are a few limitations of this technique, such as it being expensive, potentially unsafe, and extensive user training is required.
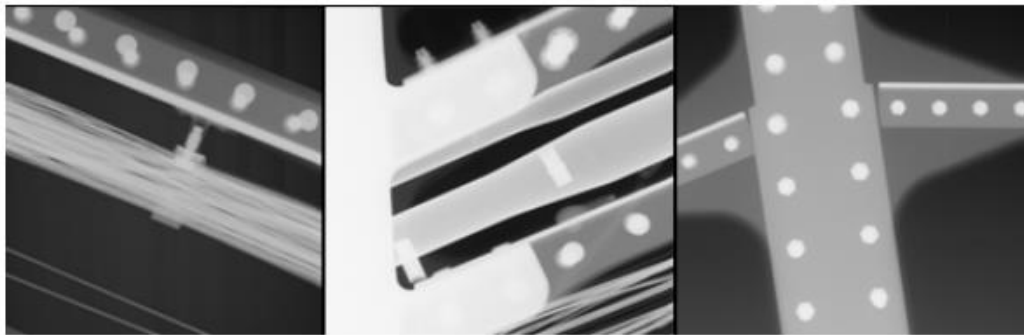
Fig 3-42: Photo of X-ray scanning of an aircraft wing structure [92].

3.2.3 **Acoustic emissions**

Acoustic emissions (AE) can be defined as the process by which transient elastic waves are generated at high speed and energy at a source and are directed into the material. In this process, waves are created inside the material. Thus, external excitation is required to encourage the source sending acoustic waves out. This feature is the key idea to the use of this technique. In addition, in the AE method any change in the applied load, temperature, pressure or strain can be considered as a type of external excitation.

Holford et al. [94] investigated damage detection in bridges using acoustic emission. The authors identified damage in steel-concert bridge by applying time-of-arrival location methods. Local and global attempts were used. The local monitoring was achieved on a 12 m I-beam at the same laboratory conditions. In addition, finite element included modelling a component of bridge was presented and results compared

with the experiment work. The acoustic emission signals were analysed and modes are filtered. It was reported that the use of this technique could successfully detect damage in steel-concert composite bridge. Hatta et al. [95] presented the using of AE to detect cracks in carbon composite samples. Notched composite samples subjected to compact tension load were utilized. To detect the notches, Electronic Speckle Pattern Interferometry (ESPI), as per Fig 3-43, and a Super Conducting Quantum Interference Device (SQUID), as seen in Fig 3-44, were employed. In this study, the authors found that delaminated areas were detected efficiently, where ESPI detected the delamination in this structure and it proved to diagnose failure in fibres.

Elforjani and Mba [96] researched the use of acoustic emission technique in detection and localization natural damages in rolling element bearing and test its ability to assess initiation and propagation cracks in bearing races during their operation. Many data analysis sets were recorded, such as spectrum wave analysis and characteristics of entropy, to detect the existence of cracks. They reported that using the AE technique efficiently provided information about natural crack sizes in bearings. As demonstrated by Fig 3-45, a typical acoustic emission has various waveform amplitudes at different working hours.

One of the most significant drawbacks to use acoustic emission is that this technique is not useful in noisy environments, as it is difficult to filter the measured signal from the noise. Also, it is not useful for online structural health monitoring [97].
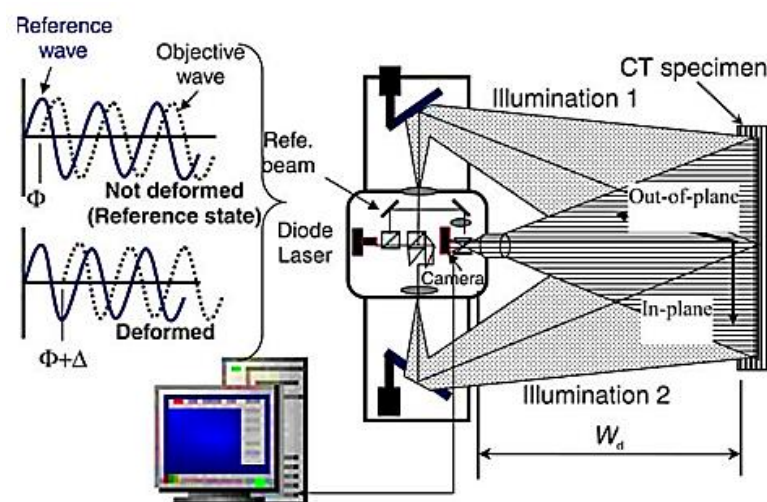
Fig 3-43: Schematic 3D-ESPI system used in [95].
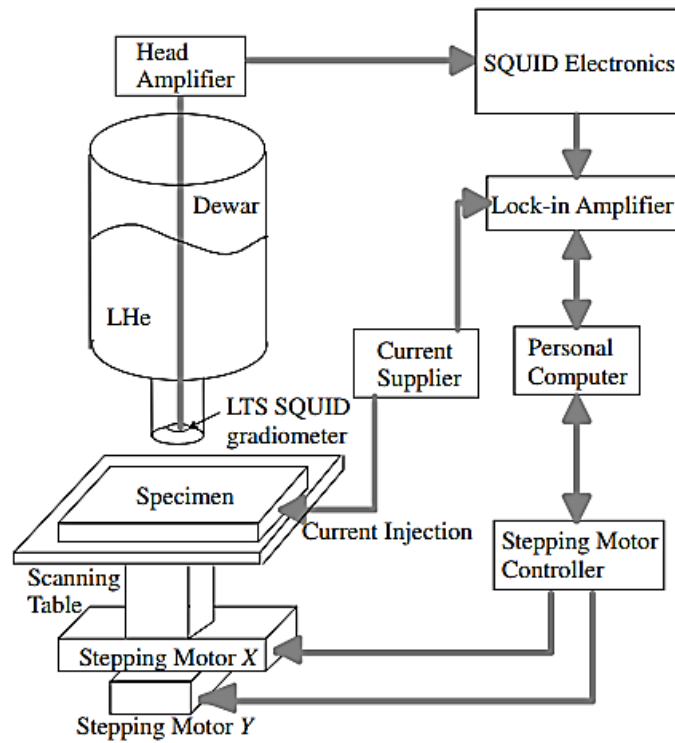
Fig 3-44: Schematic of SQUID system and terminal setting used in [95].
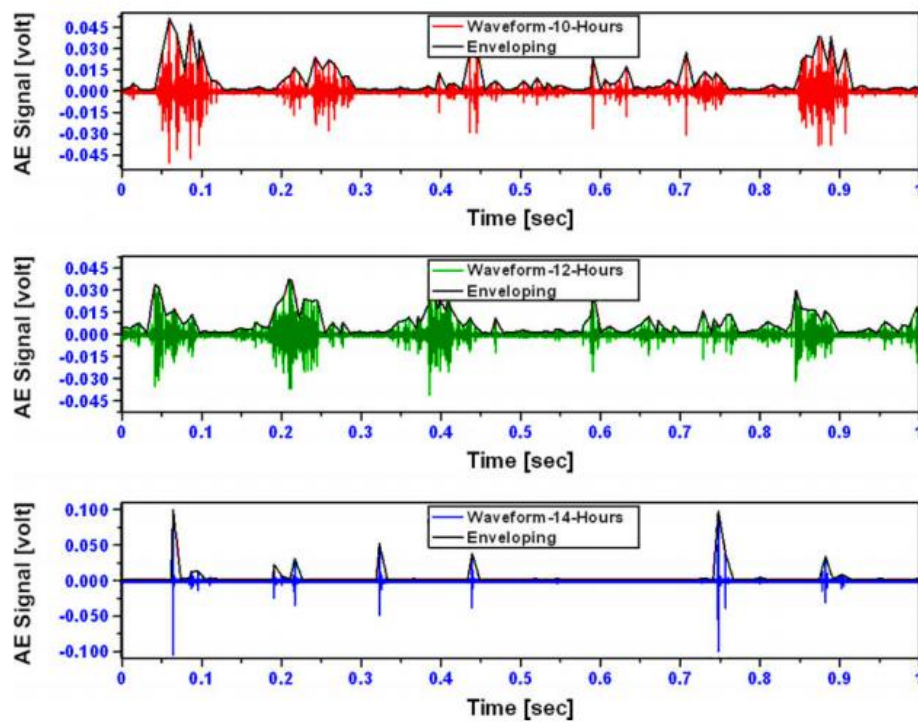
Fig 3-45: Acoustic emission waveforms record during different times of operation [96].

3.2.4   Ultrasonic waves

Ultrasonic waves can be defined as high-frequency sound waves vibrating at frequency of more than 20,000 Hz. This higher frequency makes these waves are not heard by humans who are generally restricted to a frequency range of $20 - 17,000$ Hz. In non-destructive evaluation (NDE), ultrasonic frequencies are higher than 50 kHz [90]. These waves can be used to assess a material in terms of geometry, density, configuration, mechanical properties and even to detect damage in the material. The key feature is that this technique depends on the scattering of ultrasonic waves due to damages. Analysis of echo properties can be used to quantify damage characteristics such as location, size and shape.

Guta et al. [97] improved the statistical methods used to detect fatigue damage in polycrystalline alloy structures. This statistical method can be used to analyse ultrasonic waves and then applied in the online monitoring of these structures. The authors reported that a simple change found to this statistical due to the growth of simple crack inside the material. They concluded their study by noting that data analysed using this statistical analysis can provide an early warning to the next failure.

Harri et al. [98] investigated an online method to quantify the surface cracks in wing structures under loading. Their method involved passing a continuous multi-sine ultrasonic wave and then measuring the variance in the received signal. The method was reported as a useful approach where cracks had not yet attained a critical length (start fracture). In addition to this, this method is applicable to structures under tensile or compressive load in order to verify the opening and closing in cracks. However, the challenge to this method is that crack detection depends on analysing characteristics of ultrasonic waves that should pass through more than one transducers.

In summary, there are a number of advantages of using ultrasonic waves in damage detection. This method was shown to be highly efficient in noisy conditions, even when excited at high frequencies. However, ultrasonic waves have some limitations, where they can fail to scan damage parallel to the wave direction. It has also been reported that this method is not always useful in online structural health monitoring.

3.3 Application of damage detection methods on different structures

Over the last few decades, the analysis of modal characteristics such as mode shape and natural frequency have become considered to be reliable techniques to detect the damaged areas. Valdes et al. [99] reported the analysis of natural frequency response to detect delaminated areas in composite beams. A piezoceramic was utilized to vibrate the structure, with the subsequent dynamic responses measured using piezoelectric film sensors. Resonant ultrasound spectroscopy was applied to determine the modal frequencies. Comparison of intact and damaged data clearly showed the delaminated area via the associated change in modal frequencies. Moreover, the effect of delaminated area size on the natural frequency was examined. The influence of a delaminated area in a honeycomb beam on natural frequency was investigated by Kim et al. [100]. The effect of delamination on flexural stiffness and natural frequency was computed theoretically and compared with experimental results. This study showed that the reduction of the natural frequency was proportional to the increase in the length of the delamination in a composite beam. The authors also reported that calculating the difference between the intact and damaged frequency response function showed that increasing the delaminated area reduces the peak in the natural frequency response.

Lestari et al. [101] investigated the experimental and theoretical analysis of mode shape and its curvature. They mentioned that calculating the curvature can be considered as a sensitive index to assess damaged regions. Different types of damages were created to test the validity of using this technique in damage detection. A new approach to detect cracks in beam structures was investigated in [102]. The key feature of this was calculating the irregularity index of mode shapes. In this study, the mode shape of cracked beam was calculated analytically. Then, numerically, the intact and damaged mode shapes were calculated and filtered at different frequencies. This filtration was able to separate the fluctuating part in the damaged data and use this to identify the position and severity of any crack. Another study was proposed by Cao et al.[103], who explained the validity of using the mode shape approach and static deflection to detect damaged section in cantilever beam structures. Another contribution to the subject of damage detection was the proposal presented by Wang et al. [102].

The authors investigated and extended what achieved by Bazardehi et al. [104] to detect the delamination in laminated plate structures under different boundary conditions. It was found that mode shapes contain sufficient information about any change in the physical characteristics of the vibrated structures to be useful as a detection technique. To improve the detection process, two new indexes 'slope of the smooth part', and 'irregularities in the slope of smooth part' were calculated to show the damaged areas. The limitations to this method were the lack of detection of deep delamination through thicknesses and the inability to detect delaminated areas near edges.

Delamination in laminated composite structures using vibration-based damage detection was investigated by Ullah and Sinha [105]. The lower few modes were utilized and the harmonic response was calculated and measured to show the nonlinear interaction of delamination in laminated structures. The finite element analysis available in ABAQUS was used to model the delaminated areas and calculate the amplitude of dynamic velocity components. Then, an experiment was implemented to compare to the numerical analysis. In this study the novel index called "Cumulative of Normalize Summation Harmonic" (CNSH) was proposed to detect the delaminated area. Different damage regions in a metal beam and plate structures were detected by using the damage index method (DIM), as proposed by Eraky et al. [106]. A numerical model was developed to study the effect of different parameters, such as the orientation and location of damage on the dynamic response. Experimental work was undertaken to compare with the numerical analysis. The authors concluded that analysing modal strain energy and calculating the damage index was sufficient to detect damaged sections.

Ghosh et al. [107] researched the higher derivatives of mode shape and their sensitives in damage detection. They reported that the higher modes were more sensitive in the detection of damaged areas than lower ones. Theoretical analysis concentrated on the mathematical formulation to derive the changes in mode shapes. Additionally, experimental work was performed on steel frame structures to detect damaged regions. The authors concluded that although the higher modes and their derivatives provide significant damage indicators, they are significantly affected by damage location. Which means that the detection of damage near the fixed edges is easier than damage located nearer the free edges.

There are a number of studies that have attempted to compare experimental and numerical analysis using vibration-based damage detection techniques, whereas in [108] and [109], the authors reported a number of damage indexes used in damage detection for both numerical and experimental work. For example, curvature of mode shape index, and change in flexibility and stiffness, were calculated to identify the location and severity of damage in a three-span bridge structure. Ndambi et al. [110] studied damage detection in concrete beams by utilizing the analysis of the intact and damaged dynamic characteristics. According to this study, the severity of damaged sections has a potential effect on the magnitudes of indexes.

3.4 Unresolved issues on damage detection of composite structures

Vibration-based damage detection techniques are still one of the most important methods by which to assess and monitor the development of damage in mechanical structures. Modal parameter-based damage detection techniques have been used to detect damaged areas in different applications. These techniques can include analysis of mode shape, natural frequency, and damping ratio.

Intensive research has been conducted into the use and development of vibration-based damage detection methods. According to the literature review in this research, each method has advantages and disadvantages, where some can detect but not localize, some require a number of mode shapes, etc. Also, there are a number of limitations to NDT methods, such as being expensive, requiring high levels of training, and some are not useful for online monitoring, etc. In this regard, the most important issue in damage detection processes is to select the perfect method, one which is sufficiently sensitive to detect any damaged areas and save both time and money.

Frequency change-based techniques can be applied to detect and quantify damaged regions in simple structures. Due to its limitations, this method is not sufficient to detect damage in complex structures, although it can be considered a global damage detection method. Using mode shape is useful for detecting severe damage. To improve mode shape-based damage detection, the curvature index was formulated. This index was found to be more sensitive than mode shape.

The aim of comparative studies was to evaluate the dynamic damage indicators used in damage identification. This was one of the motivations to apply and discuss this

method in chapter four of this thesis. The second point is that damages in laminated structures tend to be complicated. According to the literature review, there is a knowledge gap in detecting different types of damage in laminated composite structures and the comparison between them. Additionally, there is a general lack of research into local damage detection. This was the main motivation to investigate the detection of damage in linear patterns and to attempt to report the severity of the damage in laminated structures.

Part 2

Finite Element Study in Damage Detection Methods

Chapter 4: A comparative study of the damage detection methods

The main purpose of this chapter is to evaluate a number of dynamic indexes in damage detection subject. This evaluation started with numerical analysis, by modelling a cracked cantilever beam using FE COMSOL Multiphysics 5.1 software, where the variation of the first natural frequency at different crack sizes was computed. Then, a simple cantilever beam with and without damage was simulated using COMSOL to test the sensitivity of slope of mode shape, curvature, fractal dimension and irregularity indexes. This analysis was accomplished under a free vibration condition, where the few first mode shapes were calculated and used to detect the damaged sections. Also, the effect of noise on the dynamic response analysis was examined.

4.1 Validation case study

The aim of this section was to study the effect of a cracked section on the natural frequency of the beam structure using finite element analysis. To this end, COMSOL 5.1 software was employed to calculate the dynamic response of this model and to allow comparison with the analysis investigated by Chati et al. [111]. Here, cracked cantilever beams were investigated by Chati et al. [111] and Barad et al. [112] modelled as a validation case study. Moreover, the variation of natural frequency was calculated for different crack depths. Natural frequency, according to the literature review, is considered to be a global index, whereas a reduction in natural frequency indicates the existence of damage.

The numerical solution was determined via simulation of a cantilever beam using the COMSOL Multiphysics 5.1. All dimensions of the model were identical to those reported in [111], where L represents the length of the beam = 10 m, A is the cross-sectional area = 1 m^2, b is the location of crack relative to the fixed end and a is the crack length. Also, the mechanical properties of steel, as listed in Table 4-1, were used in the FE analysis. Moreover, Fig 4-2 illustrates the simulated model of a cracked beam. To achieve the numerical analysis, a solid mechanics interface was employed to identify the boundary conditions of the cracked beam, and an eigenfrequency study was utilized

to find the associated eigenmodes and natural frequencies. A free triangular mesh type with extremely fine size was utilized to create the unstructured, triangular mesh in the 2D domain.

Table 4-1: Mechanical properties of steel, as reported in [111].

Property	Magnitude
Modulus of elasticity (GPa)	210
Poisson's ratio	0.3
Density $\left(\frac{kg}{m^3}\right)$	7850
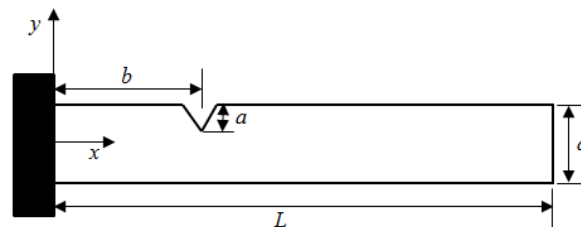
Fig 4-1: Schematic of cracked cantilever beam used in the validation case study [111].
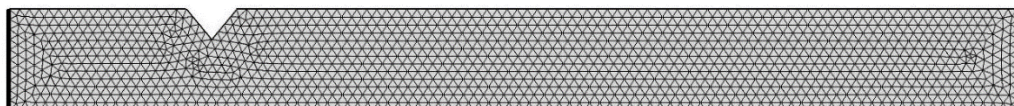
Fig 4-2: Numerical model of the cracked cantilever beam as represented in the FE software COMSOL Multiphysics 5.1.

The numerical analysis for this case study showed the relationship between the variations in natural frequency of a cracked beam for different crack sizes. The normalized natural frequency was calculated for this model by dividing each value of damaged natural frequency (ω_c) by the undamaged value (ω), (normalized natural frequency = ω_c/ω). In this analysis, the crack reduces the local stiffness and the higher crack size causes higher reduction in the local stiffness. To explain this, Fig 4-3 was the best demonstration of the common relationship between crack size and natural frequency, with cracks located at different positions along the beam.
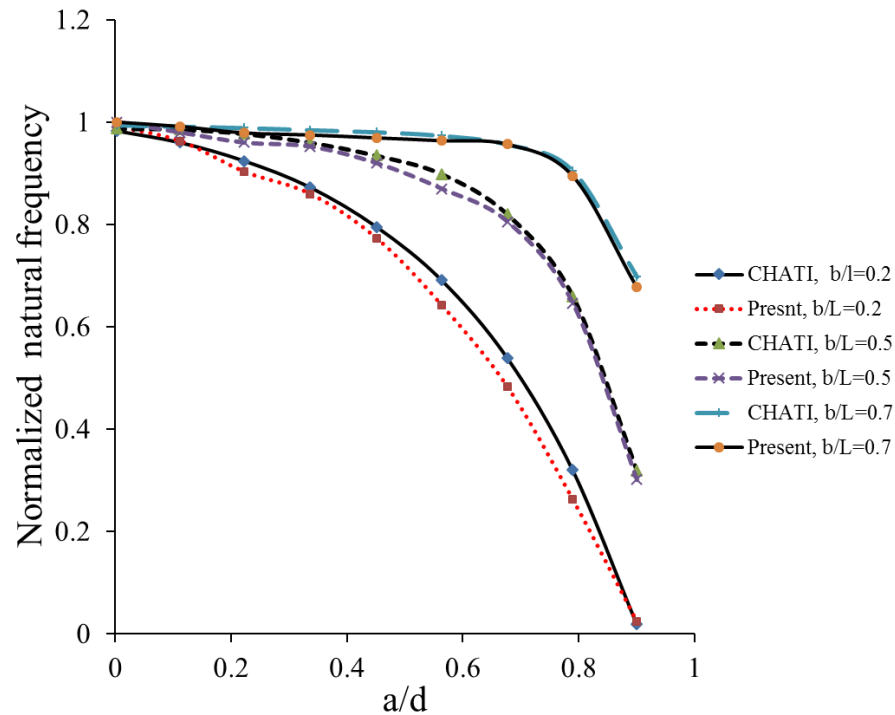
Fig 4-3: The variation of first normalized natural frequency ω_c/ω with a different crack ratio for the cantilever beam shown in Fig 4-1[111].

According to the principles of the vibration of a continuous system, as discussed in section 2.3.3, the mathematical basis for the relationship between natural frequency and the stiffness of a vibrating beam is clear. Two important issues can be seen in Fig 4-3: firstly, that increasing crack depth decreases the natural frequency, and that normalized value consequently reduces, where at a crack depth approximately equal beam height, the normalized value roughly will be equal to zero. Secondly, natural frequency is affected by a crack that is close to the fixed end to a much greater extent than a crack near to the free edge. As is clear in this figure, a crack at 0.2 has a greater influence than a crack at 0.5 and 0.7 L (beam length) because the local bending moment of beam is variable along its length.

4.2   Results of comparative study

This section involves the evaluation of dynamic indicators via the analysis of the dynamic response for the damaged cantilever beam, where the variation of natural frequency, mode shape and its slope, curvature, fractal dimension and irregularity indexes were calculated for both intact and damaged beams. The dimensions used in the

numerical model, as simulated by COMSOL Multiphysics 5.1, are listed in Table 4-2. To clarify, Fig 4-4 describes the schematic of damaged beam used in the current study. The mechanical properties shown in Table 4-1 were also used for the vibrating beam in this section. Furthermore, to simulate this model, the beam element type, a cantilever beam as boundary conditions, mechanical properties of steel and the eigenfrequency were utilized to calculate the modal characteristics. A 1D beam element type was selected for the simulation.

Table 4-2: Details of the cantilever beam used in the comparative study.

Part	Symbol	Magnitude (Unit)
Beam length	L	$1\ (m)$
Position of damaged section to the fixed edge	L_1	Different values (m)
Length of damaged section	L_2	$0.03\ (m)$
Position of damaged section to the free edge	L_3	Different values (m)
Cross-sectional area	A	$0.0025\ (m^2)$
Width and thickness	b, b	$0.05\ (m)$
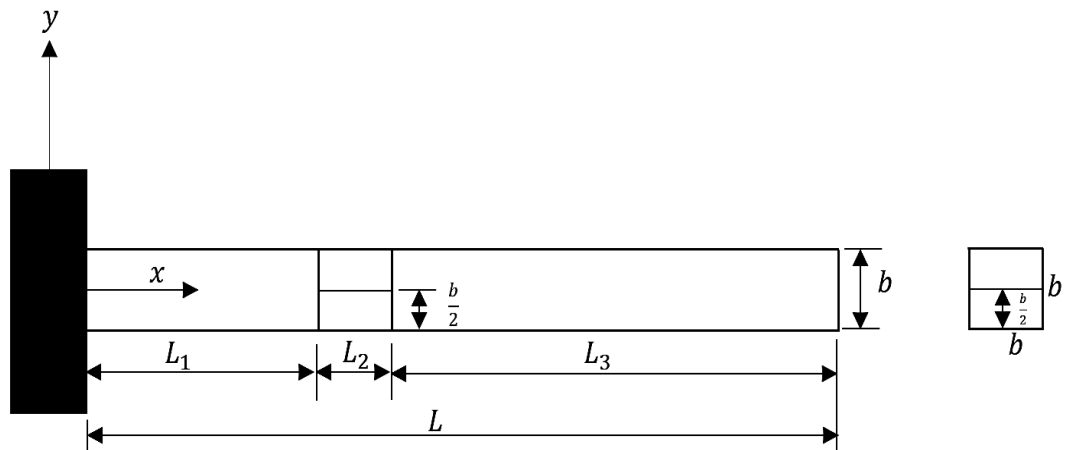
Fig 4-4: Schematic of the damaged cantilever beam used in the numerical analysis. The total length = 1 m, cross-sectional area = 0.0025 m^2 and damage is located at L_1.

4.2.1 Frequency-based damage detection in a simple cantilever beam

The motivation for this section is that damage detection in complicated structures is not in any way straightforward. For this, an evaluation of different indicators is of particular important to improve the damage identification process. There has been intensive work, as reported in the literature, into testing the modal characteristics and improving them to better analyse dynamic signals.

The cantilever beam in Fig 4-4 has been simulated to detect the damaged sections. Within this analysis, a few first natural frequencies were calculated. The key idea of this study was to determine the relationship between natural frequency and variation of beam stiffness(EI). To model damage in this beam, the stiffness was reduced in terms of change the moment of inertia (I) at the damaged section. This reduction occurs due to the change of coordinate point of neutral axis, which means there will be a new area moment of inertia for the damaged section. As demonstrated by Fig 4-5, the area moment of inertia for both circular and rectangular areas are entirely different and depends on the coordinates of the neutral axis. For a rectangular area, this is:

$$I_x = \frac{1}{3}bh^3 \text{ and } \bar{I}_{\acute{x}} = \frac{1}{12}bh^3, \ \bar{I}_{\acute{y}} = \frac{1}{12}hb^3.$$

While for a semi-circular area this is:

$$I_x = \bar{I}_y = \frac{1}{8}\pi r^4 \quad \bar{I}_{\acute{x}} = \left(\frac{\pi}{8} - \frac{8}{9\pi}\right)r^4.$$

In the current study, the reduction in moment of inertia can be understood by considering Fig 4-6, where I_h, I_d are the area moments of inertia for the intact and damaged beams, respectively. The reduction of moment of inertia means a reduction in the local stiffness of the damaged sections.
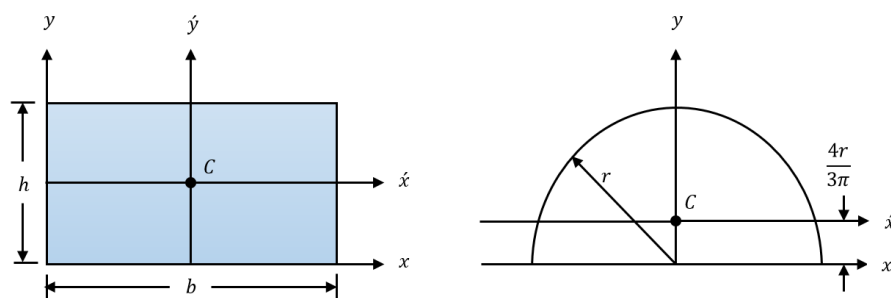
Fig 4-5: The effect of coordinate location on the moment of inertia.

$$I_h = \frac{b^4}{12}$$

$$I_d = \frac{b^4}{48}$$
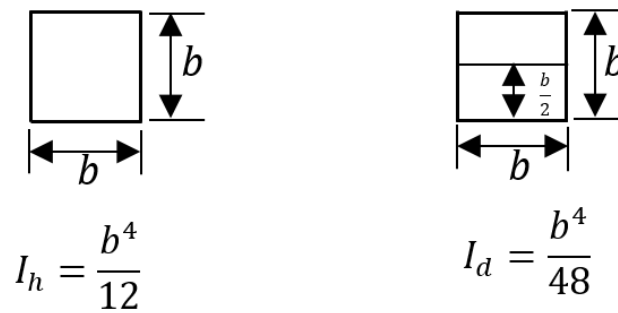
Fig 4-6: The moment of inertia for both the intact and a damaged square area.

The damaged section has been simulated with different moments of inertia, and this is in fact the same idea as when damage occurs in laminated structures. According to the delamination mechanism discussed in chapter one, delamination causes the debonding of adjacent plies and this divides the damaged section into more than one area, and this was the same idea assumed here to model the damaged section. Furthermore, the first three natural frequencies have been calculated. To demonstrate this more clearly, Fig 4-7, Fig 4-8 and Fig 4-9 show the decreasing value of the first three natural frequencies with the associated reduction in moment of inertia (the initial value of the moment of inertia for the damaged section is 0.52 e-6 m4). It is obvious from these figures that frequency-stiffness variation is not smooth, so these curves show greater stability at damaged stiffness larger than 0.2, while from damaged stiffness less 0.2, the reduction in natural frequency increases sharply. This variation in natural frequency can add another evidence to explain the relationship between natural frequency and the reduction in local stiffness. Also, in the dynamic analysis each mode shape vibrates at a certain natural frequency, which explains why each curve in the above figures show their own unique frequency- stiffness curve.
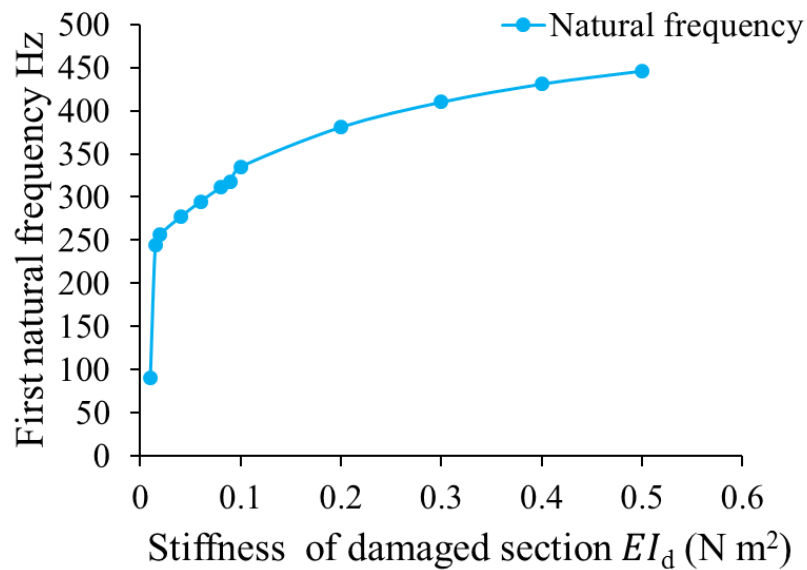
Fig 4-7: The variation of first natural frequency of the damaged cantilever beam at different local stiffnesses, $L = 1$ m, $L_1 = 0.5$ m, $L_2 = 0.03$ m and cross-sectional area $= 0.0025$ m^2.
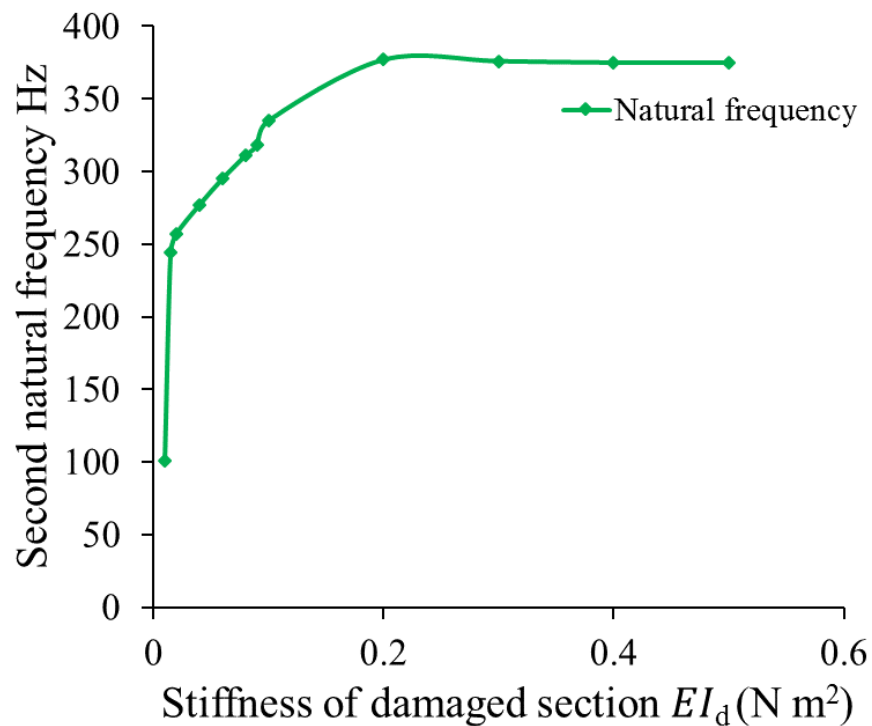
Fig 4-8: The variation of the second natural frequency of the damaged cantilever beam at different local stiffnesses, $L = 1$ m, $L_1 = 0.5$ m, $L_2 = 0.03$ m and cross-sectional area $= 0.0025$ m^2.
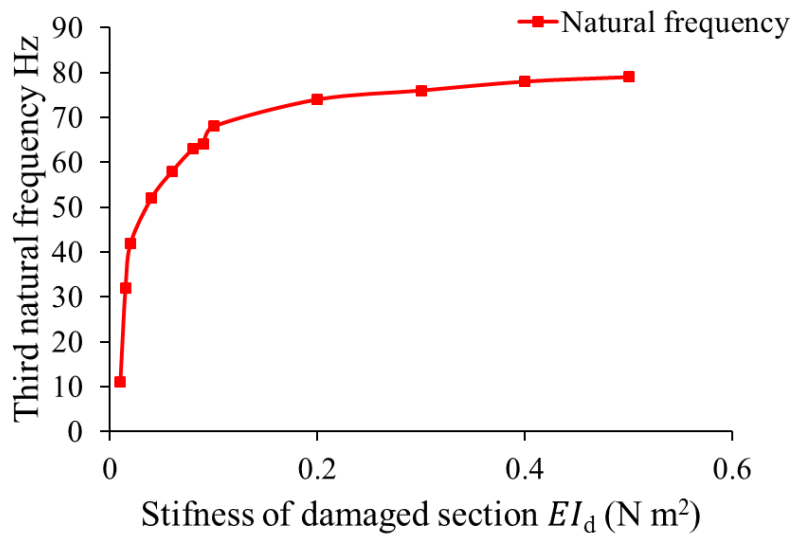
Fig 4-9: The variation of the third natural frequency of the damaged cantilever beam at different local stiffnesses, $L = 1$ m, $L_1 = 0.5$ m, $L_2 = 0.03$ m and cross-sectional area = 0.0025 m^2.

4.2.2 Mode shape damage index

This section demonstrates the effect of the reduction in local stiffness on the displacement mode shape in the beam structures shown in Fig 4-4, where the first two modes were calculated using COMSOL 5.1. This case study assumes that the drop in stiffness occurs at different ratios in order to represent the reality of severe damage. The mathematical basis of this approach is that clear from Eq.(2.37) and Eq.(2.38). According to the relationship between the dynamic amplitude of mode shape, natural frequency and stiffness, the decrease in natural frequency is the real indicator of any reduction in local stiffness. To this end, local stiffness at the damaged section (refers to the length in which stiffness is reduced to EI_d) was reduced by sequentially by 10%, 20% and 30% (i.e., 0.1, 0.2 and 0.3 EI_d) to study the change in stiffness, as seen in Table 4-3. The first two mode shapes with 10%, 20% and 30% and without these percentages under condition of free vibration were calculated. The normalized first intact and damaged modes are presented in Fig 4-10. In this figure, it can be seen there is no significant difference between the intact and damaged modes, because reducing stiffness for example 0.3 or 0.2 EI_d has invisible effect on the mode shape. Which means it is not easy to see the effects of simple damage [damage was modelled by

reducing the local stiffness] by mode shape itself. However, it is not surprising to see the effect of damage that mode shape can be affected by severe reductions in local stiffness, and that the local disturbance associated with the damage location can be noticed when the reduced stiffness value is equal to $0.1\ EI_d$. The second issue that should be demonstrated is that modelling the damaged section at different positions relative to the fixed edge (0.4 and 0.6 m) may result in different local disturbances, whereas in Fig 4-11, reducing the stiffness to $0.1\ EI_d$ resulted in a clear local distortion in mode shape, with the same occurring at a damage location of 0.6 m, as per Fig 4-12. The same criteria were applied to the second mode, as shown in Fig 4-13, Fig 4-14 and Fig 4-15. The intact mode was quite close to the profile of the damaged modes as seen by Fig 4-13. The same discussion is equally valid for the second mode, the only difference being that reducing the local stiffness to greater than $0.3\ EI_d$ showed a clear local perturbation at the damaged section. Also, damage at different locations had different influences on the amplitude of the damaged modes and this due to the varying of local bending moment of the beam along its length, as seen in Fig 4-13 and Fig 4-14, where the variation of damaged modes due the damaged sections at 0.2 and 0.4 m showed different local distortions. The most important point in mode shape analysis is that the mode shape itself can be sensitive to cases of severe damage.

Table 4-3: Details of stiffness parameters used in this chapter.

Stiffens	Magnitude
Intact stiffness	(EI_h)
Damaged stiffness	(EI_d)
Intact moment of inertia	$I_h = \dfrac{b^4}{12}$
Damaged moment of inertia	$I_d = \dfrac{b^4}{48}$
Reduced stiffness	$N\% * (EI_d), N > 0$
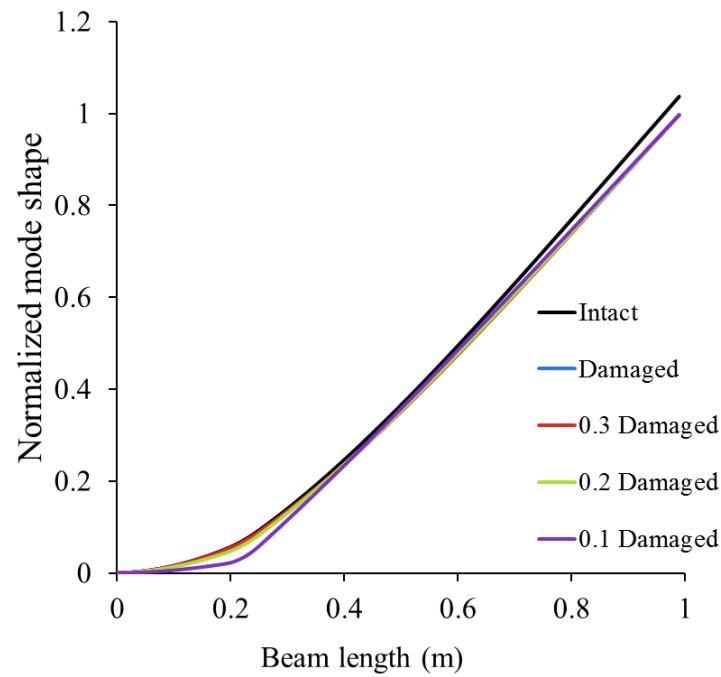
Fig 4-10: Numerical first mode shape of the intact and damaged cantilever beam, $L = 1$ m, $L_1 = 0.2$ m, $L_2 = 0.03$ m, cross-sectional area = 0.0025 m² at different local stiffness.
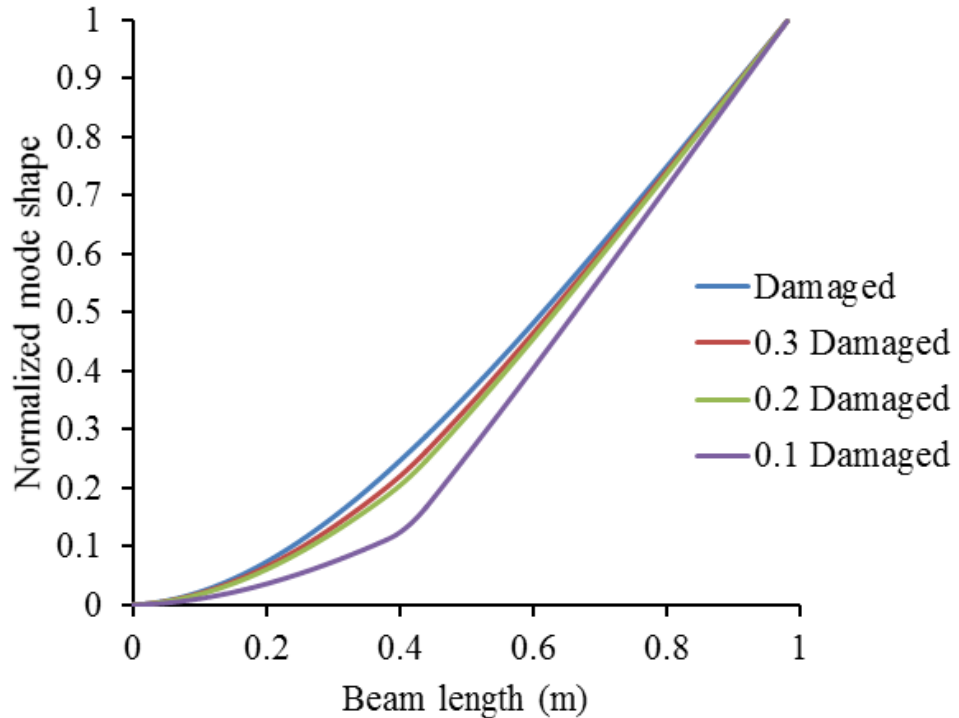
Fig 4-11: Numerical first mode shape of the damaged cantilever beam, $L = 1$ m, $L_1 = 0.4$ m, $L_2 = 0.03$ m, cross-sectional area = 0.0025 m² at different local stiffness.
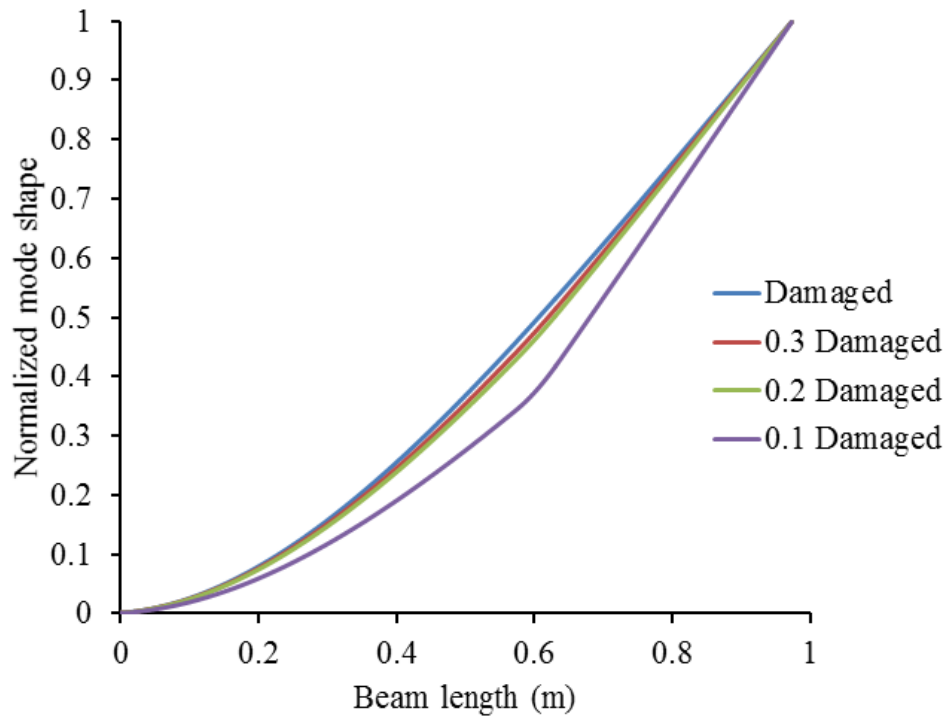
Fig 4-12: Numerical first mode shape of the damaged cantilever beam, $L = 1$ m, $L_1 = 0.6$ m, $L_2 = 0.03$ m, cross-sectional area $= 0.0025$ m^2 at different local stiffness.
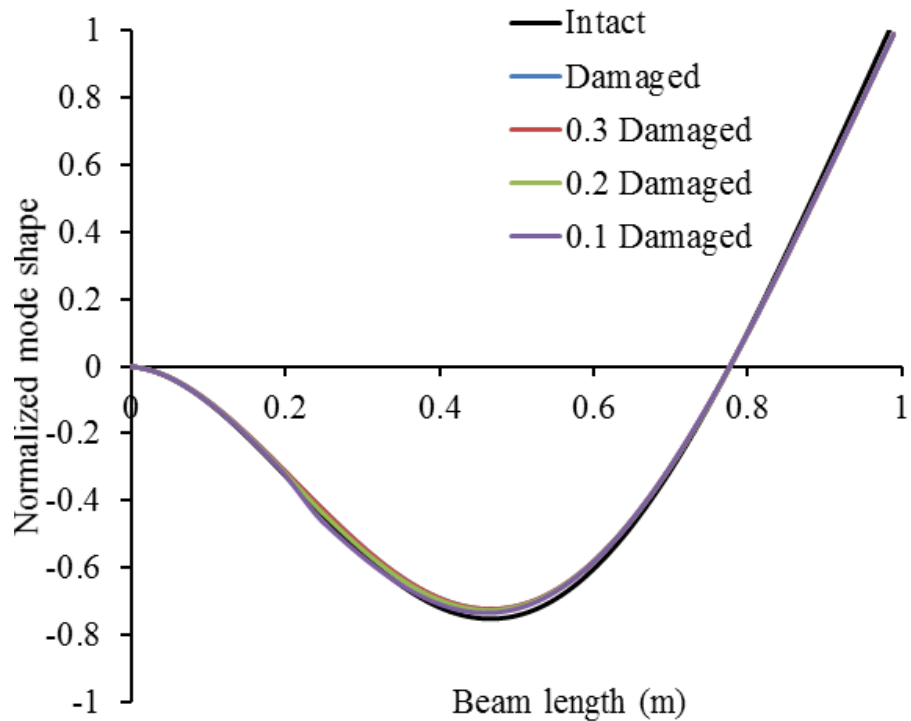
Fig 4-13: Numerical second mode shape of the intact and damaged cantilever beam, $L = 1$ m, $L_1 = 0.2$ m, $L_2 = 0.03$ m, cross-sectional area $= 0.0025$ m^2 at different local stiffness.
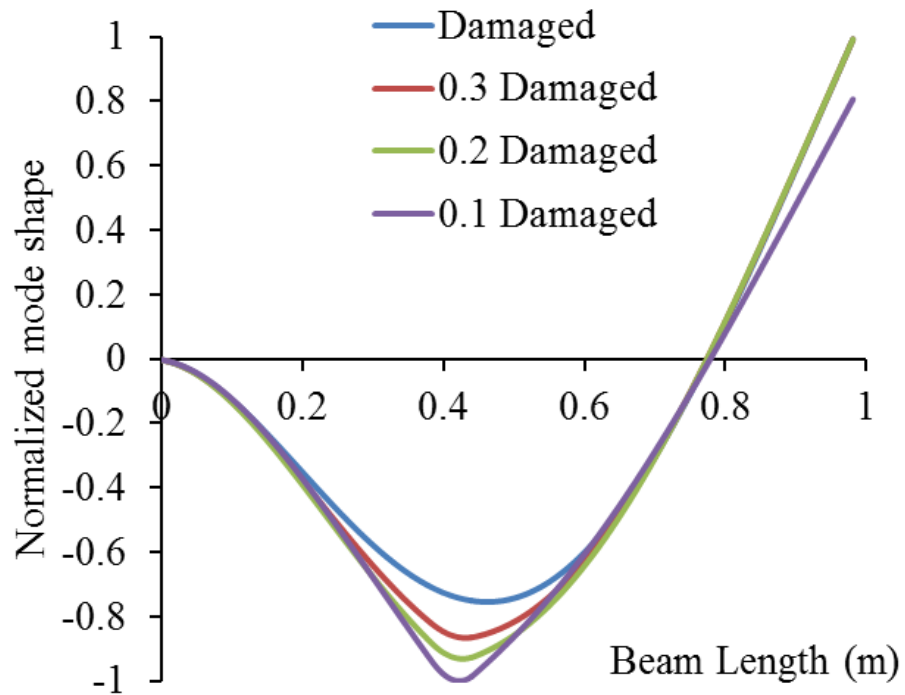
Fig 4-14: Numerical second mode shape of the damaged cantilever beam, $L = 1$ m, $L_1 = 0.4$ m, $L_2 = 0.03$ m, cross-sectional area $= 0.0025$ m^2 at different local stiffness.
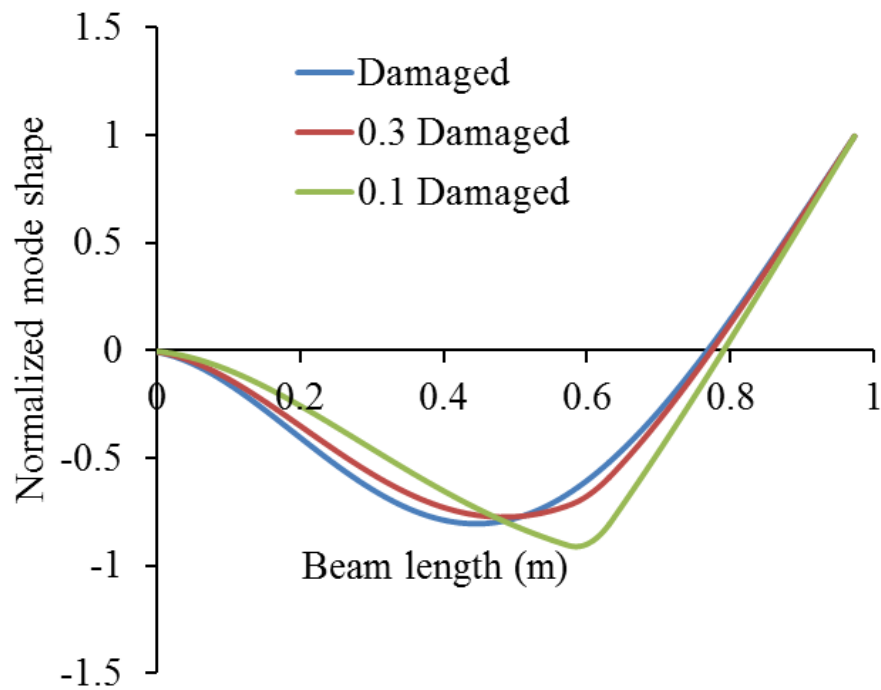
Fig 4-15: Numerical second mode shape of the damaged cantilever beam, $L = 1$ m, $L_1 = 0.6$ m, $L_2 = 0.03$ m, cross-sectional area $= 0.0025$ m^2 at different local stiffness.

4.2.3   Slope of mode shape damage index

In this section, the slope of the damaged modes was evaluated in terms of the identification the damaged sections in the simple cantilever beam shown in Fig 4-4. The forward finite difference in the *x*-direction was utilized to determine the slope of mode shape as shown in Eq.(4.1), where $\frac{\partial \phi}{\partial x}|_{i,j}$ is the first derivative, ϕ_{ij} is the mode shape and Δx the element length for the sequence points over the calculated mode. The most important issue in analysing mode shape is to test its efficiency in detecting damaged sections. Some of the earliest articles in this subject, as investigated by Ostachowicz et al. [36] and Cao et al. [103], reported that the slope of the mode shape might be suitable for identifying the cracked sections. To test the efficiency of this index, the slope of the first two modes was calculated.

$$\frac{\partial \phi}{\partial x}|_{i,j} = \frac{\phi_{(i+1)j} - \phi_{ij}}{\Delta x} \qquad (4.1)$$

It is clear from Fig 4-16 that any reduction in the local stiffness of the damaged section at 0.2 m has a noticeable effect on the continuity of the slope index. This means that the slope can show any hidden information in the displacement mode shape due to the influence of damaged section. In this figure, there was no significant difference between slope indexes for both damaged stiffness (EI_d) and $(0.3\ EI_d)$ value, while, once the stiffness reduces further, the local distortion to the mode shape becomes more obvious, for example at $(0.2\ EI_d)$, a clear jump can be seen. For this case, the local stiffness was reduced by 10%, 20% and 30% to determine the influence of this parameter on the dynamic signal. Furthermore, this reduction was applied to different locations (0.4, and 0.6 m) as per Fig 4-17 and Fig 4-18 . Both of these figures show that the slope index allows detection of the damaged sections at these locations. However, this index showed that the detection of low stiffnesses is more difficult than an equivalent value near the fixed edge, as can be seen in Fig 4-17 and Fig 4-18. The same concept was applied to the second mode shapes, as shown in Fig 4-19, Fig 4-20 and Fig 4-21. The variation in slope index still indicates a distortion at all three different stiffnesses and locations, also the slope of the second mode showed that the detection of any damage that is distance from fixed end is easier than damage close to the fixed edge. This can occur because each mode has a certain profile due to the change in local

bending moment. In brief, the slope of the mode shape is more effective than the mode shape itself in terms of detection of damaged regions. However, it still detects severe damages more efficiently than the detection of simple damage [in FEA simple damage means small reduction in local stiffness].
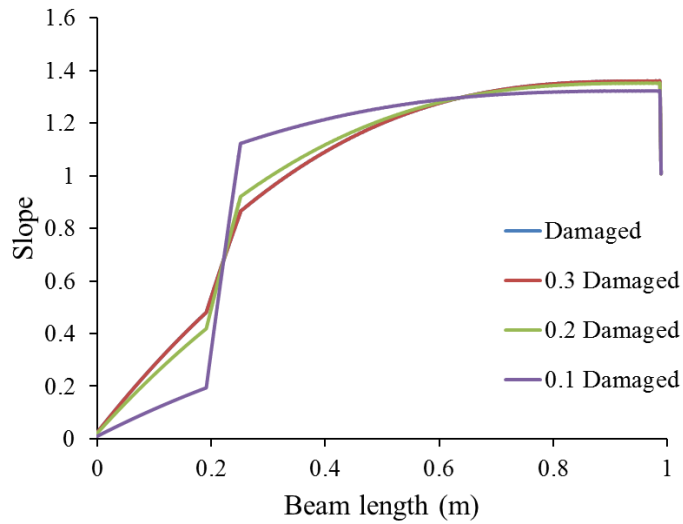
Fig 4-16: Slope index of numerical first mode shape of the damaged cantilever beam, $L = 1$ m, $L_1 = 0.2$ m, $L_2 = 0.03$ m, cross-sectional area = 0.0025 m^2, at different local stiffnesses.
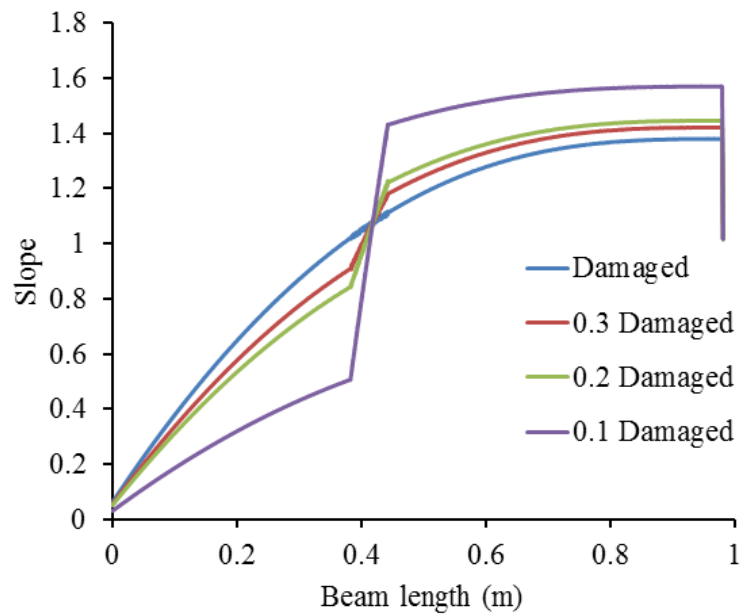
Fig 4-17: Slope index of numerical first mode shape of a damaged cantilever beam, $L = 1$ m, $L_1 = 0.4$ m, $L_2 = 0.03$ m, cross-sectional area = 0.0025 m^2, at different local stiffnesses.
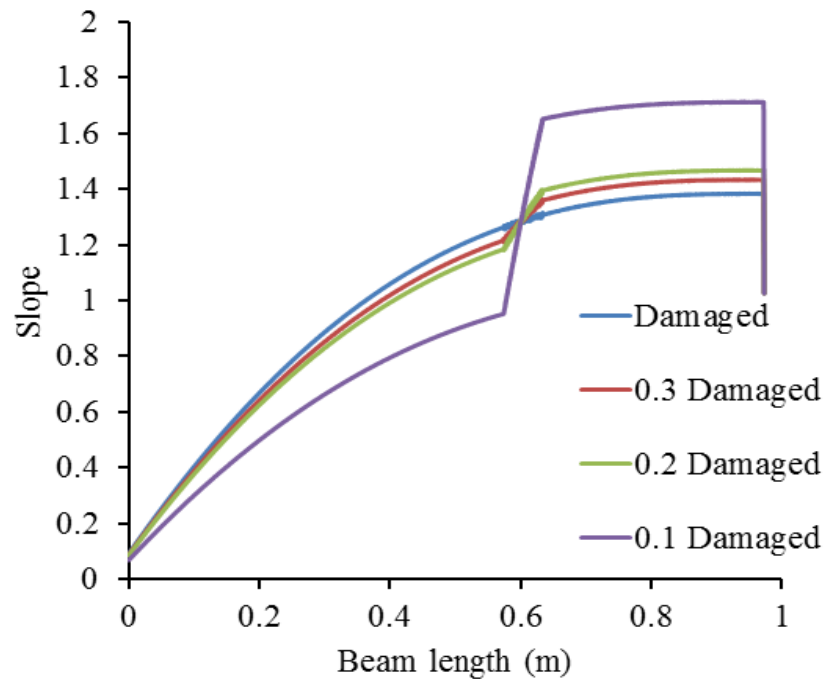
Fig 4-18: Slope index of numerical first mode shape of a damaged cantilever beam, $L = 1$ m, $L_1 = 0.6$ m, $L_2 = 0.03$ m, cross-sectional area $= 0.0025$ m^2, at different local stiffnesses.
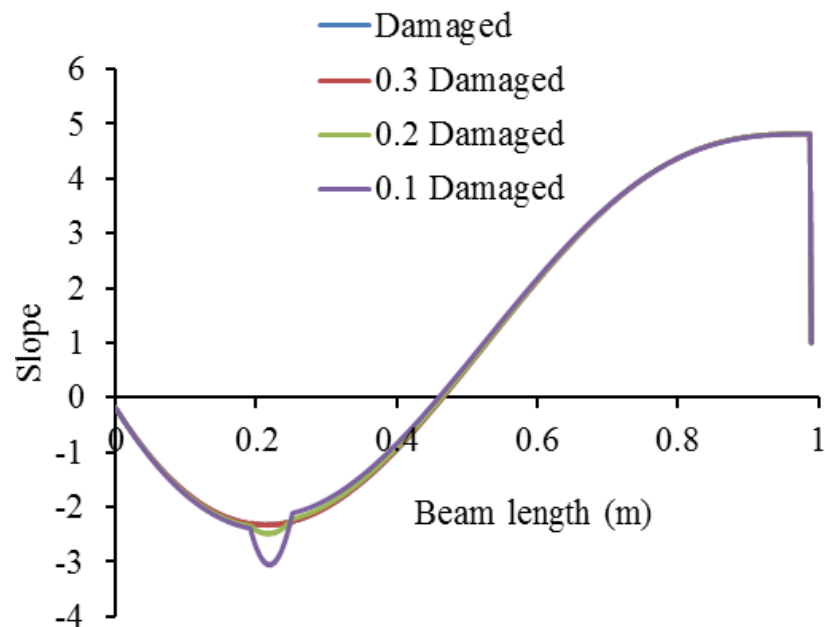
Fig 4-19: Slope index of numerical second mode shape of a damaged cantilever beam, $L = 1$ m, $L_1 = 0.2$ m, $L_2 = 0.03$ m, cross-sectional area $= 0.0025$ m^2, at different local stiffnesses.
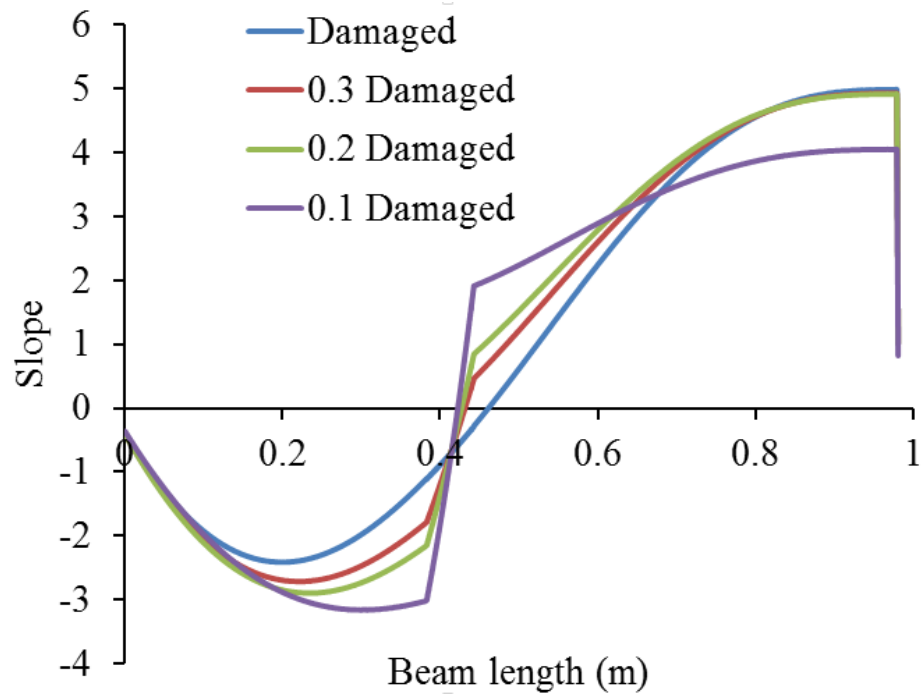
Fig 4-20: Slope index of numerical second mode shape of a damaged cantilever beam, $L = 1$ m, $L_1 = 0.4$ m, $L_2 = 0.03$ m, cross-sectional area $= 0.0025$ m^2, at different local stiffnesses.
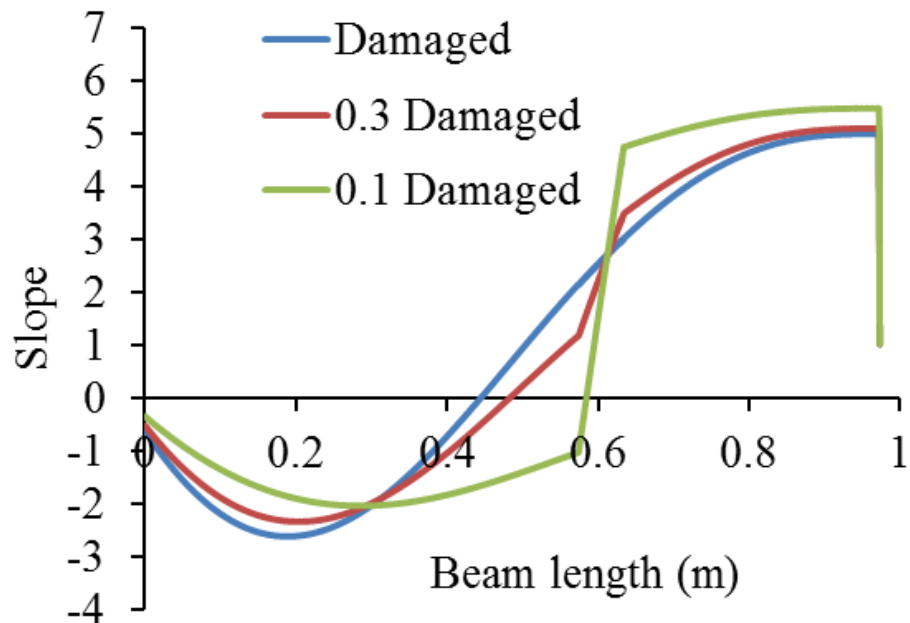
Fig 4-21: Slope index of numerical second mode shape of a damaged cantilever beam, $L = 1$ m, $L_1 = 0.6$ m, $L_2 = 0.03$ m, cross-sectional area $= 0.0025$ m^2, at different local stiffnesses.

4.2.4 Curvature and fractal dimension indexes

The purpose of this section is to explain the calculation and evaluation of curvature and fractal dimension indexes. Both of these indicators were used to quantify the damaged sections using vibration-based damage detection.

The curvature of the mode shape is the second derivative of the curve. The central difference method was employed to formulate the curvature index Eq.(4.2), as reported by Chandrashekhar and Ganguli [113].

$$v''_{i,j} = \frac{\phi_{(i+1)j} - 2\phi_{i,j} + \phi_{(i-1)j}}{\Delta x^2} \tag{4.2}$$

Where $v''_{i,j}$ is the modal curvature and i represents node number, j is the mode number and Δx is the element length. $\phi_{i,j}$ is the modal value of the ith node and the jth mode.

Fractal dimension index is another damage detection index, as per Eq.(4.3), as proposed by Katz [114]. This index was used in the detection of cracked sections of a rectangular plate [47]. This index was proposed to improve damage detection analysis by revealing the hidden information in dynamic signals. Fig 4-22 shows the application of the fractal dimension to the 1D signal analysis.

$$FD = \frac{log_{10}(n)}{log_{10}\left(\frac{d}{L}\right) + Log_{10}(n)} \tag{4.3}$$

Where n represents the number of steps over the curve $= \frac{L}{\bar{a}}$, $\bar{a}$ is the average distance between the successive points over the curve, $d = \max \text{ dist } (1, i)$ is the max estimated diameter between the first point and the ith point over the curve and L is the total length of the curve or the summation of the distance between successive points.
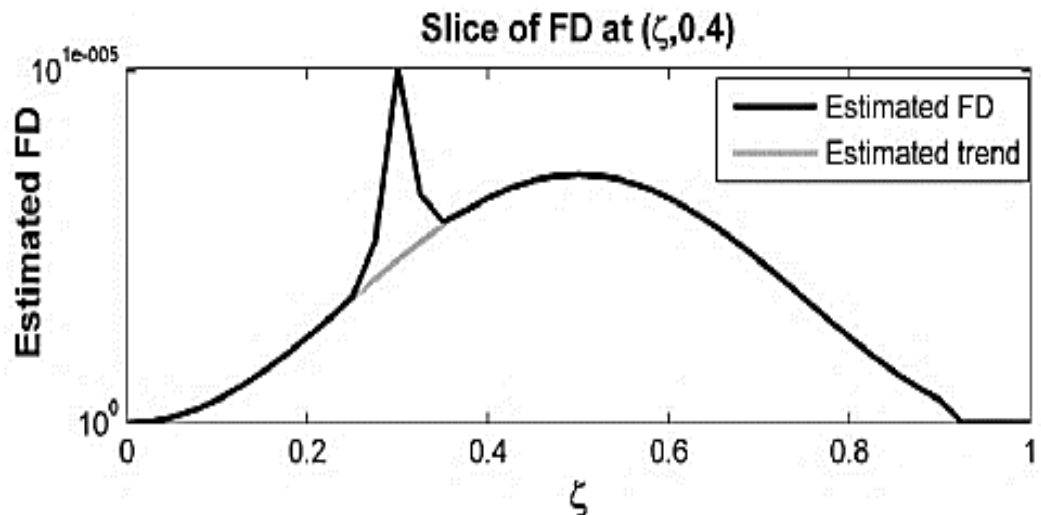
Fig 4-22: Numerical 1D estimated fractal dimension index of a rectangular plate with a surface crack, where the FD peak shows the exact notch location [47].

Numerically, the intact and damaged cantilever beams shown in Fig 4-4 were simulated using COMSOL Multiphysics 5.1 with different local stiffnesses. Both the intact mode shape and its curvature index do not show any significant change as per Fig 4-23 and Fig 4-24. This means there is no change in the physical properties that can affect the continuity of the dynamic response for the vibrated object. By contrast, Fig 4-25 shows an extreme jump in the curvature index of the first mode shapes for damage modelled at 0.2 m. The peaks of curvature index associated with damage sections (EI_d) and $(0.3\ EI_d)$ were approximately equal to -7000. Different curvature indexes were seen depending on the reduction of local stiffness. By contrast, Fig 4-26 and Fig 4-27 introduce the curvature index of the damaged beam at different locations, namely 0.4 and 0.6 m. Both figures showed that a significant reduction in local stiffness shows a low curvature index peak. For example, a peak of $(0.3\ EI_d)$ is higher than peak of $(0.1\ EI_d)$. In addition, damage that is distance from the fixed edge has curvature index peak values that are greater than similar damage close to the fixed end, for example the numerical values for curvature peak with damaged stiffness (EI_d) at 0.6 m equal to -70000 Fig 4-27 , while -6800 for the same damaged stiffness at 0.2 m Fig 4-25 . These three figures show that curvature can effectively detect damage at different positions due to the ability of the curvature correlation to show any minor change between adjacent points along the calculated dynamic response.

The performance of the fractal dimension on the same cantilever beam model discussed in the above paragraphs was tested. Calculating fractal dimension index using the intact mode data did not show any change, as seen in Fig 4-28. On the other hand, calculating this index using the first damaged mode showed a sudden jump associated with the damaged sections, as per Fig 4-29. However, it is clear from this figure whether the magnitude of the fractal dimension peak in the damaged section is significantly lower than the curvature peak for the same damage (Fig 4-25), where the fractal dimension peak = 0.6 while curvature = -6800. According to this analysis, the expected peak in the curvature index is more visible than fractal dimension in a real-world applications.
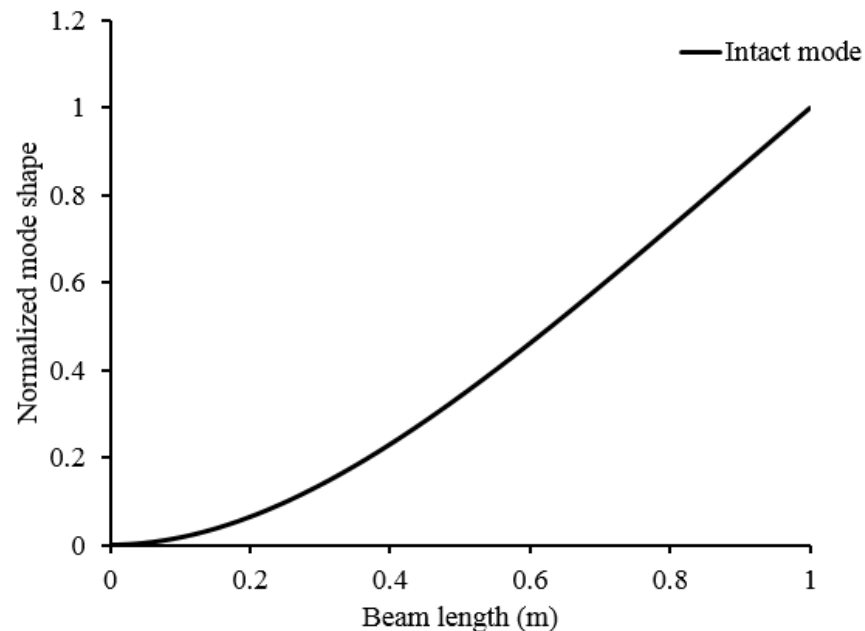
Fig 4-23: Numerical first intact mode shape of the cantilever beam, $L = 1$ m, cross-sectional area $= 0.0025$ m^2.
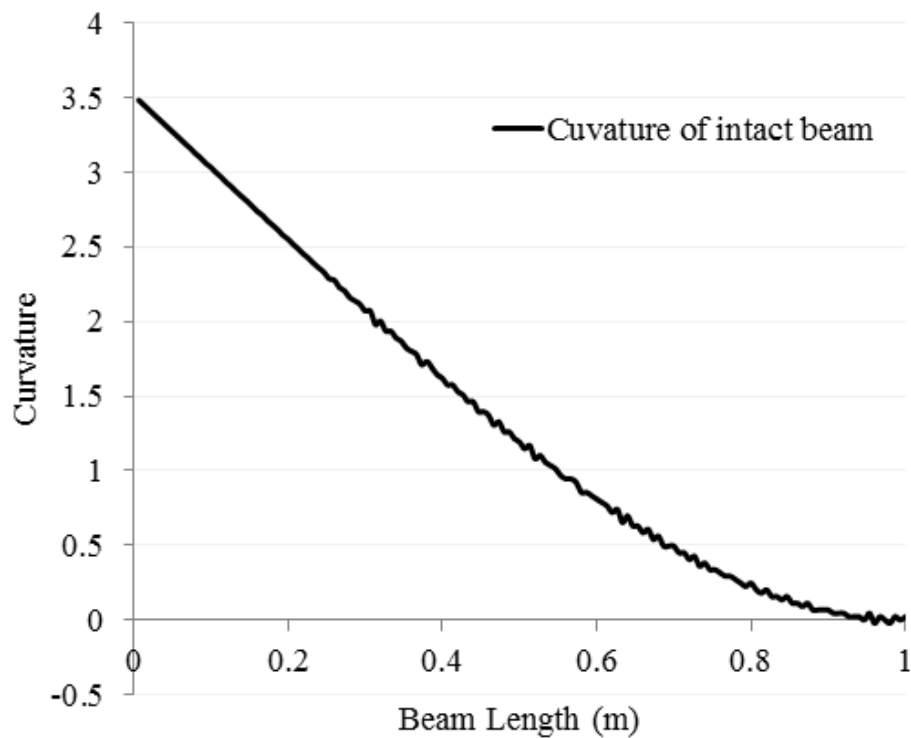
Fig 4-24: Numerical curvature index of first intact mode shape of a cantilever beam, L = 1 m, cross-sectional area = 0.0025 m^2; no change can be seen.
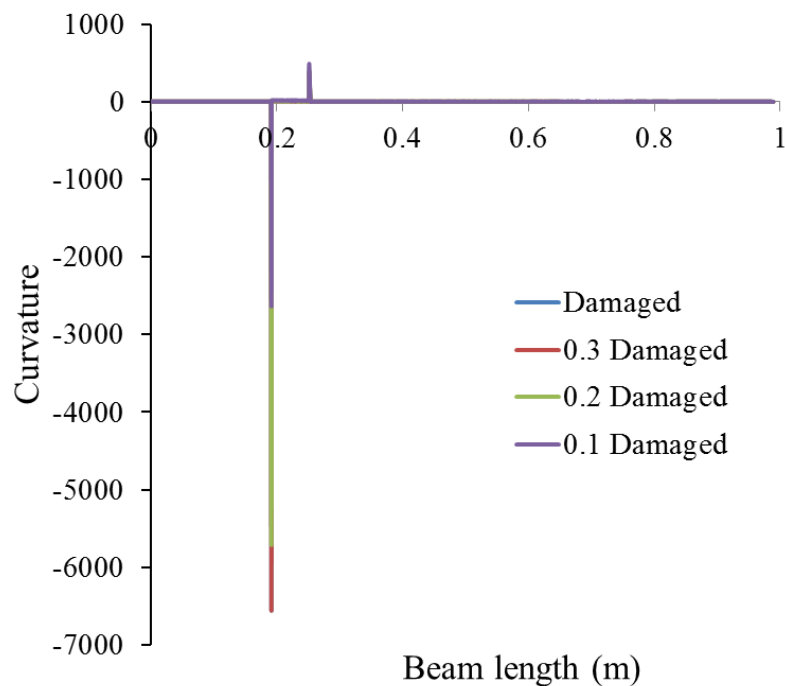
Fig 4-25: Numerical curvature index for first mode shape of a damaged cantilever beam, L = 1 m, L_1 = 0.2 m, L_2 = 0.03 m, cross-sectional area = 0.0025 m^2, for different local stiffnesses; curvature peaks show the damaged elements.
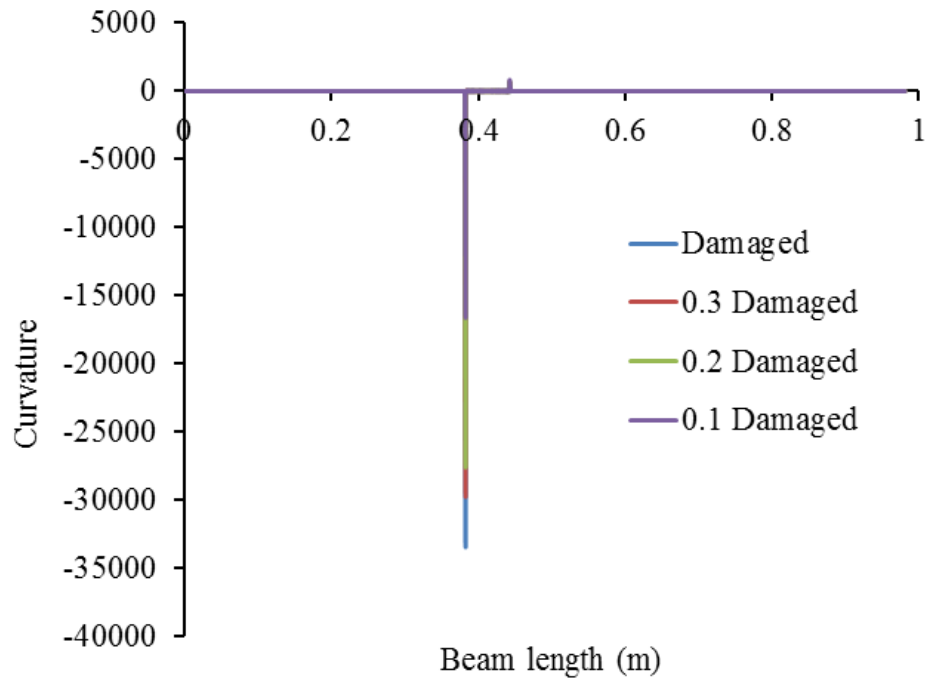
Fig 4-26: Numerical curvature index for first mode shape of a damaged cantilever beam, $L = 1$ m, $L_1 = 0.4$ m, $L_2 = 0.03$ m, cross-sectional area $= 0.0025$ m^2, at different local stiffnesses; curvature peaks show the damaged elements.
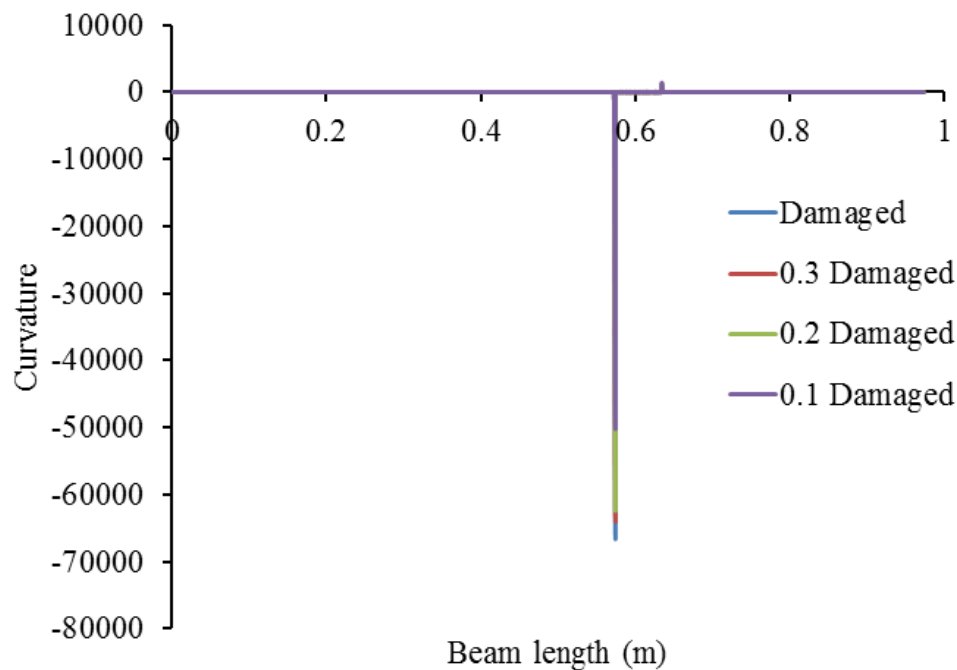
Fig 4-27: Numerical curvature index for first mode shape of a damaged cantilever beam, $L = 1$ m, $L_1 = 0.6$ m, $L_2 = 0.03$ m, cross-sectional area $= 0.0025$ m^2 at different local stiffnesses; curvature peaks show the damaged elements.
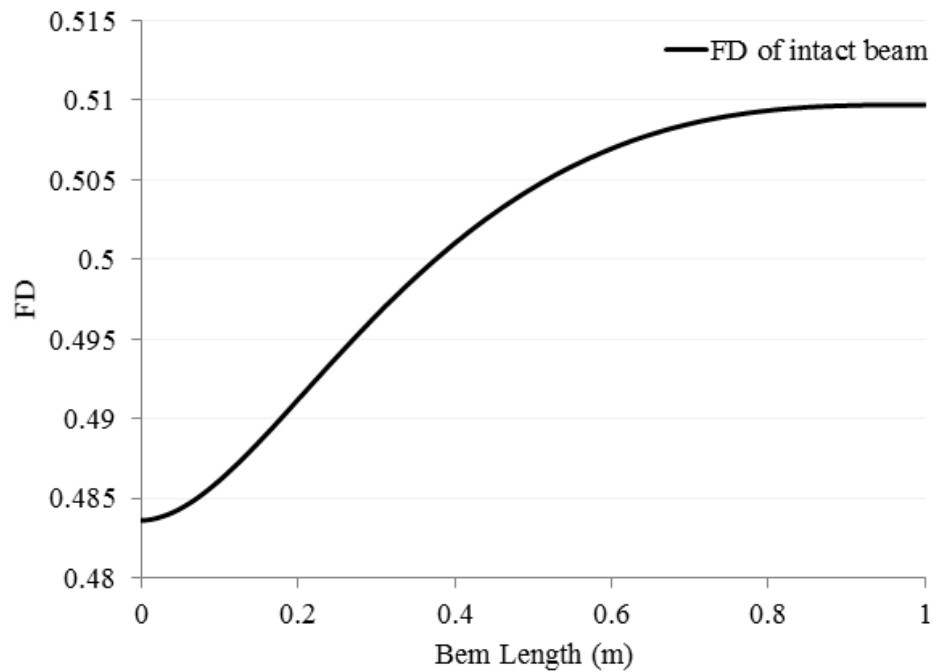
Fig 4-28: Numerical fractal dimension index of first intact mode shape of the cantilever beam, $L = 1$ m, cross-sectional area $= 0.0025$ m^2. There is no obvious change to be seen.
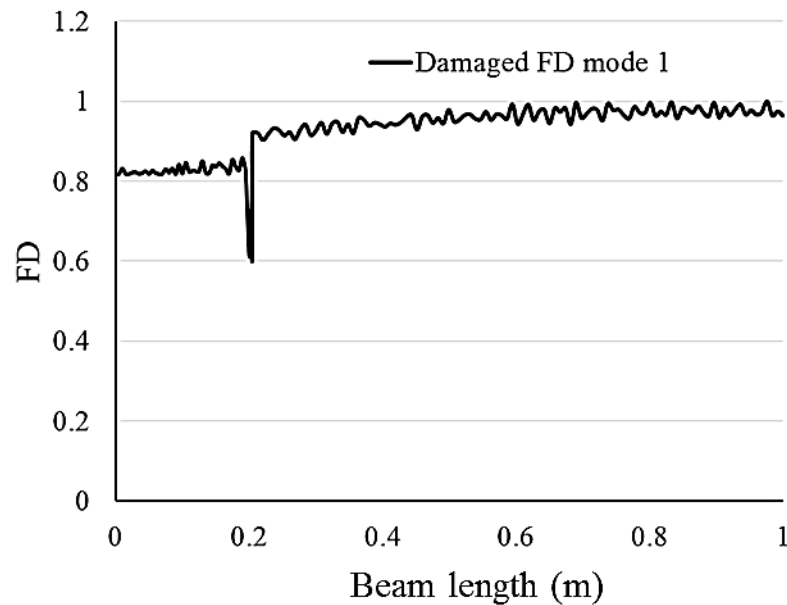
Fig 4-29: Numerical fractal dimension index for first mode shape of a damaged cantilever beam, $L = 1$ m, $L_1 = 0.2$ m, $L_2 = 0.03$ m, cross-sectional area $= 0.0025$ m^2. The peak shows the damaged elements.

4.2.5 **Damage detection at different noise levels using curvature and fractal dimension indicators**

4.2.5.1 Testing with noisy modes

From a practical perspective, noise is one of the most important issues to control due to its effect on the measured data. To study this parameter, a theoretical analysis was proposed. To explain this analysis, consider that e represents the fluctuation in the mode shape across the damaged section, as seen in Fig 4-30. Then numerically adding this magnitude to the intact mode to create noisy mode shape. Providing for the analysis of noisy data can help to evaluate the efficiency of both curvature and fractal dimension in damage detection within a noisy environment. Random values were created depending on the magnitude of e and then added to the mode shape to simulate the effect of noise. To test the noisy modes, Fig 4-31 demonstrates the noisy first mode with 10% e and with damage at 0.2 m. Then, the curvature index of this mode was calculated, as seen in Fig 4-32. The peak of the curvature clearly indicates the damage location, as created at 0.2 m. The same noisy mode was used to calculate the fractal dimension index, as seen in Fig 4-33, where its peak still shows the exact location of the damage. However, even though the same mode shape was used, the curvature peak is higher than fractal dimension peak for example curvature peak is roughly -19000, while fractal dimension is 3.3. With this amount of noise, although fractal dimension still showed the damaged sections, the curvature peak was the more visible of the two.
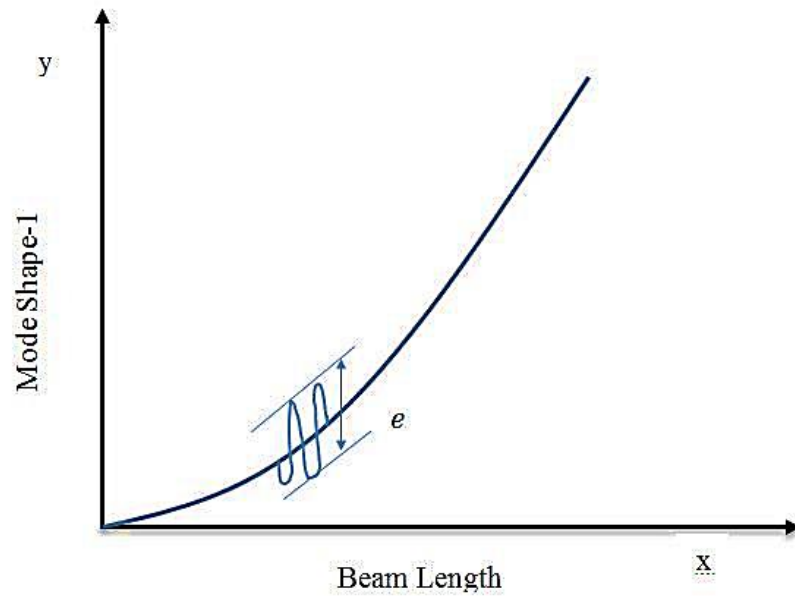
Fig 4-30: Expanding the mode shape at the damaged section of the damaged cantilever beam, $L = 1$ m, $L_1 = 0.2$ m, $L_2 = 0.03$ m, cross-sectional area $= 0.0025$ m^2.
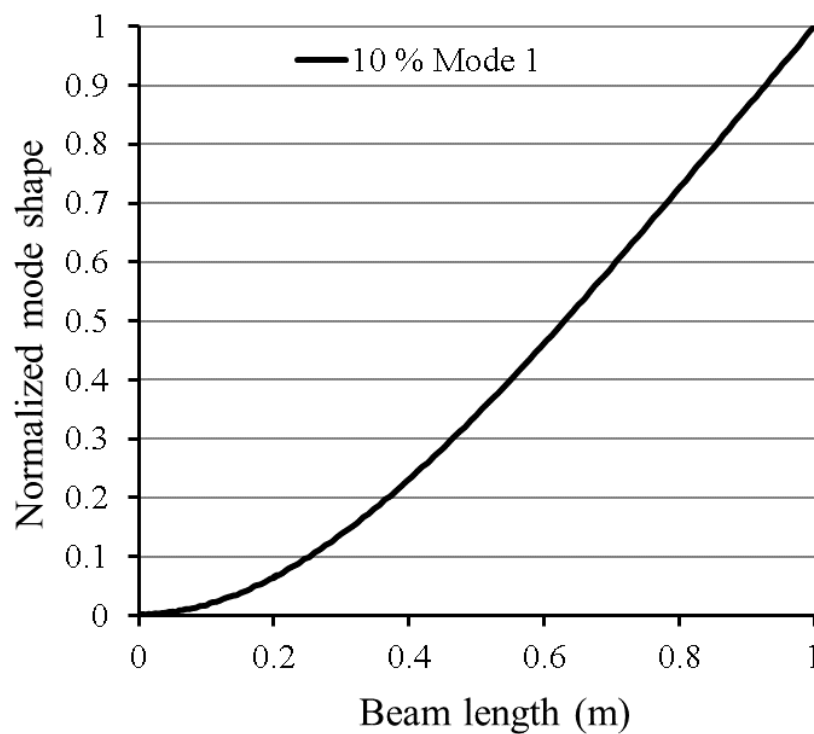

Fig 4-31: Non-dimensional first mode shape of the damaged cantilever beam, $L = 1$ m, $L_1 = 0.2$ m, $L_2 = 0.03$ m, cross-sectional area $= 0.0025$ m^2. Noise level is 10%.
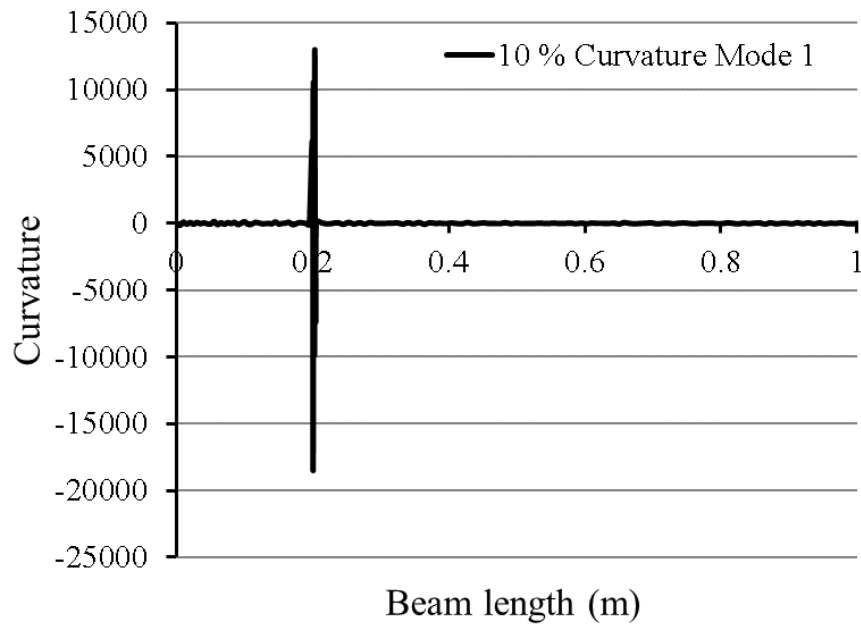
Fig 4-32: Curvature index of first mode shape of the damaged cantilever beam, $L = 1$ m, $L_1 = 0.2$ m, $L_2 = 0.03$ m, cross-sectional area = 0.0025 m^2, noise 10%. Curvature shows the damaged elements.
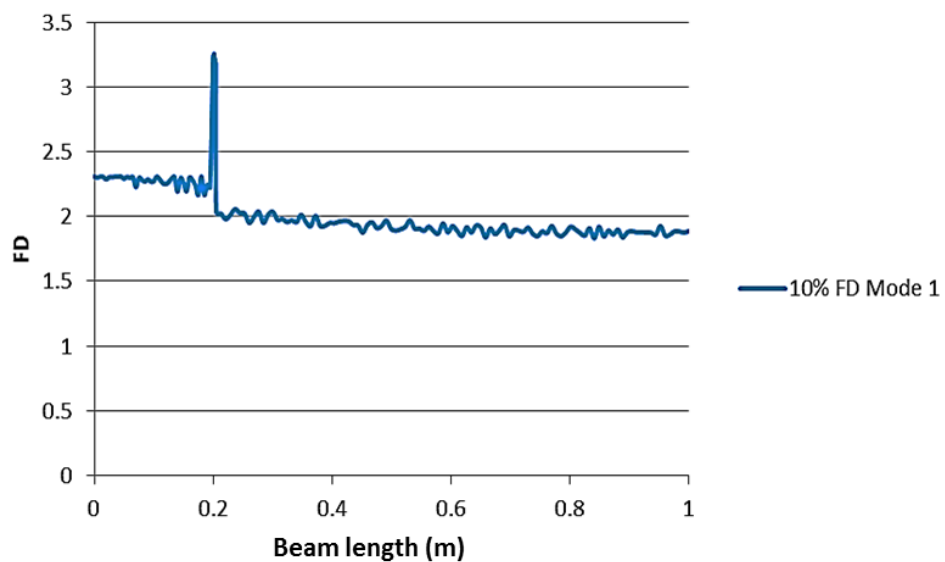
Fig 4-33: Fractal dimension index of first mode shape of the damaged cantilever beam, $L = 1$ m, $L_1 = 0.2$ m, $L_2 = 0.03$ m, cross-sectional area = 0.0025 m^2, noise 10%. The fractal dimension peak is less sensitive than curvature, but still shows the damaged elements.

4.2.5.2   Test them at different noise levels

The purpose of this section was to discuss and evaluate the curvature and fractal dimension indexes at different noise levels. Noise effect is considered one of the main challenges associated with experimental work. Ideally, any index that might be used in damage detection should be sensitive to damaged regions, even with noisy data.

Within this analysis, different levels of noise, at 20%, 40%, and 60% e, were added to mode shape, as shown in Fig 4-34 and Fig 4-35. It was obvious from these figures that as the level of noise increases, the mode begins to assume a non-smooth profile. This fluctuation in mode shape has a significant influence on the analysis of dynamic responses. The calculated curvature peak was tested at the above noise levels, as shown in Fig 4-36, Fig 4-37 and Fig 4-38, respectively. According to these figures, curvature gives different peaks values, it is easy to demonstrate that curvature peak increases with increasing noise value, thus at 20%, e = -29000, 40%, e = 39000 and 60%, e = 90000 (approximately). It should be noted that curvature index still allows for the detection of damaged sections, even with high noise. The same concept of damage detection at different noise percentages was applied to calculate fractal dimension index, as shown in Fig 4-39, Fig 4-40, and Fig 4-41. It is clear from Fig 4-39 and Fig 4-40 that increasing the noise from 20% e to 40% e does not effect peak value, which is 3.3; however, at 40% e the rest of the FD profile begins to fluctuate. On raising this percentage to 60% e, as per Fig 4-41, a dramatic change was seen in the FD by reducing the peak to 0.7, whereby a messy FD profile was generated. In brief, according to the trend found for the peaks, the curvature index would be expected to detect the damaged area more efficiently than FD in real-world applications. However, FD may be useful for the detection of severe damages and dynamic responses are accurately measured.
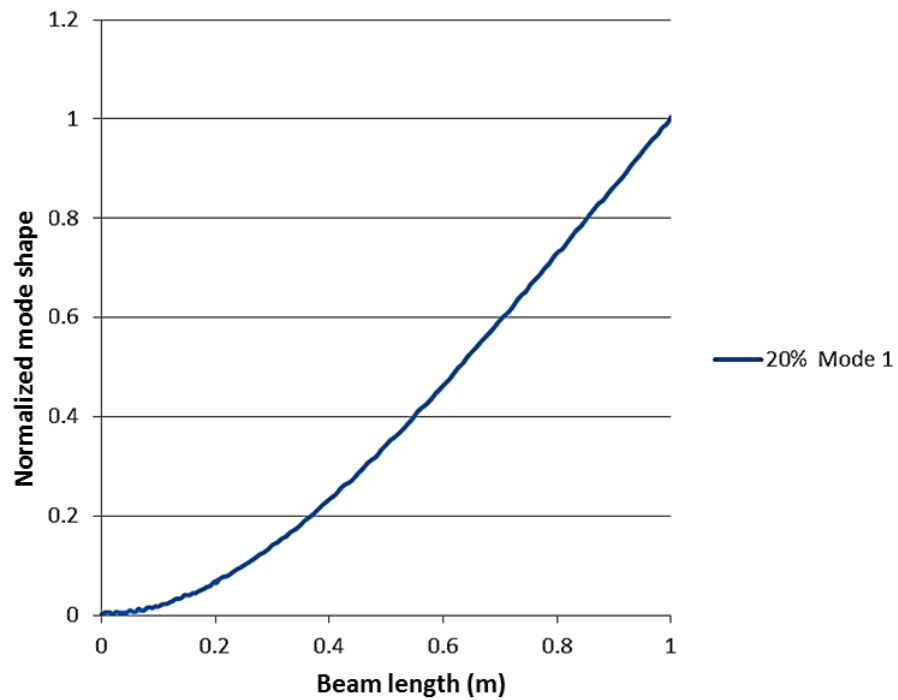
Fig 4-34: Non-dimensional first mode shape of the damaged cantilever beam, $L = 1$ m, $L_1 = 0.2$ m, $L_2 = 0.03$ m, cross-sectional area = 0.0025 m^2, noise 20%.
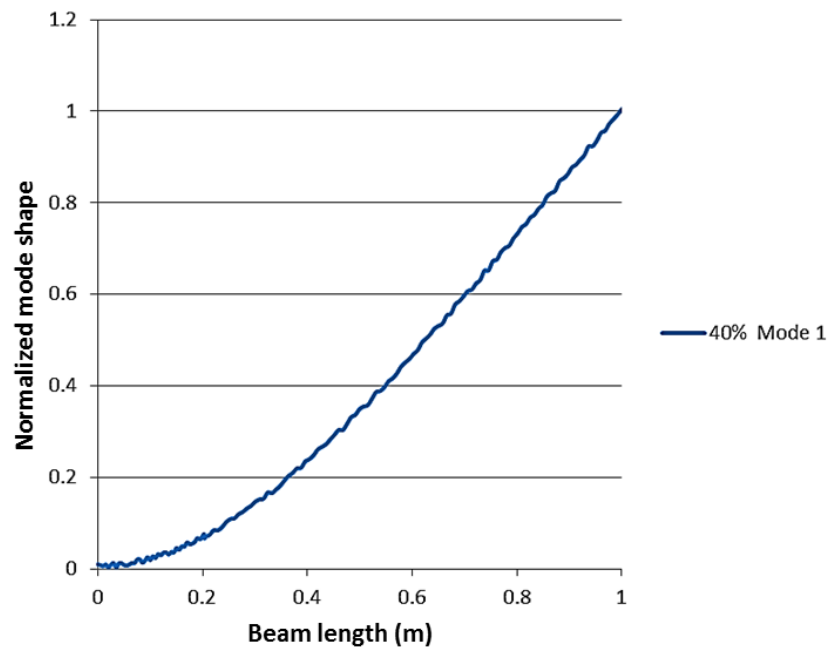

Fig 4-35: Non-dimensional first mode shape of the damaged cantilever beam, $L = 1$ m, $L_1 = 0.2$ m, $L_2 = 0.03$ m, cross-sectional area = 0.0025 m^2, noise 40%.
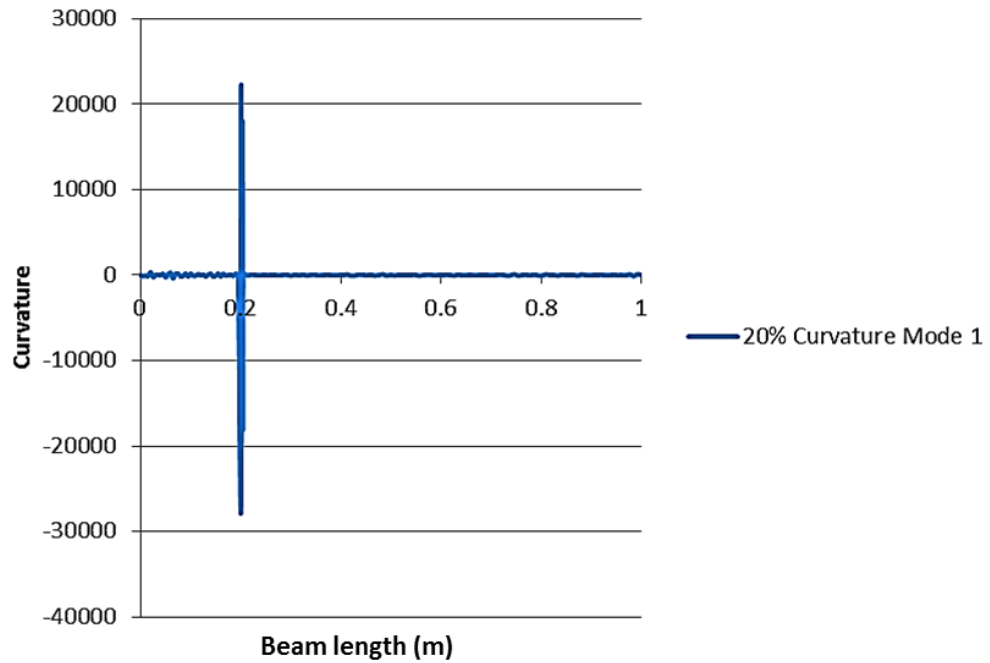
Fig 4-36: Curvature index of the first mode shape of the damaged cantilever beam, $L = 1$ m, $L_1 = 0.2$ m, $L_2 = 0.03$ m, cross-sectional area $= 0.0025$ m^2, noise 20%. Curvature clearly shows the damaged elements.
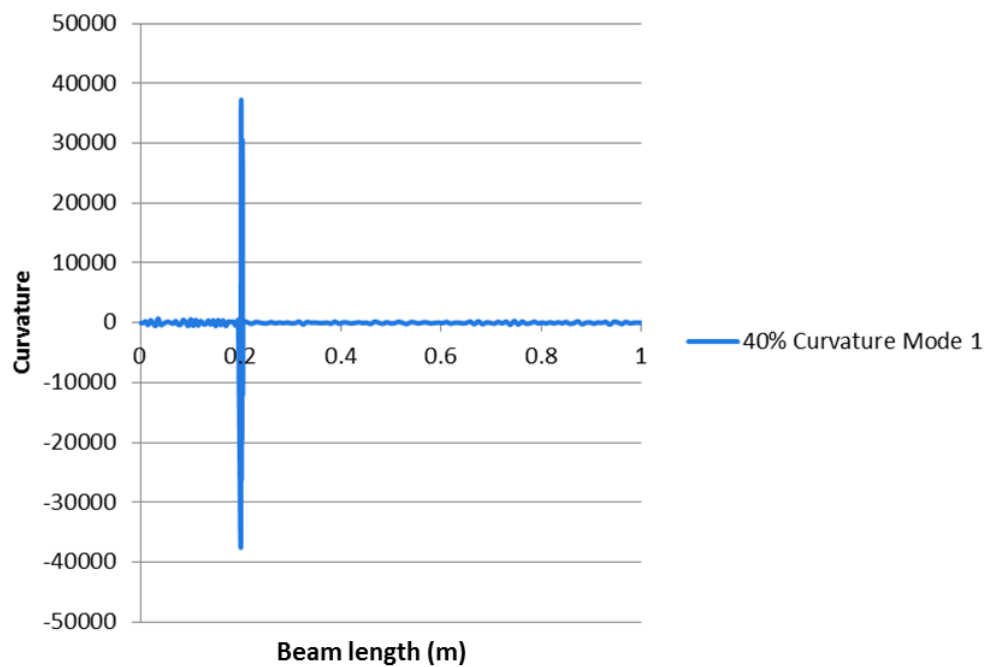

Fig 4-37: Curvature index of first mode shape of a damaged cantilever beam, $L = 1$ m, $L_1 = 0.2$ m, $L_2 = 0.03$ m, cross-sectional area $= 0.0025$ m^2, noise 40%. Curvature shows the damaged elements.
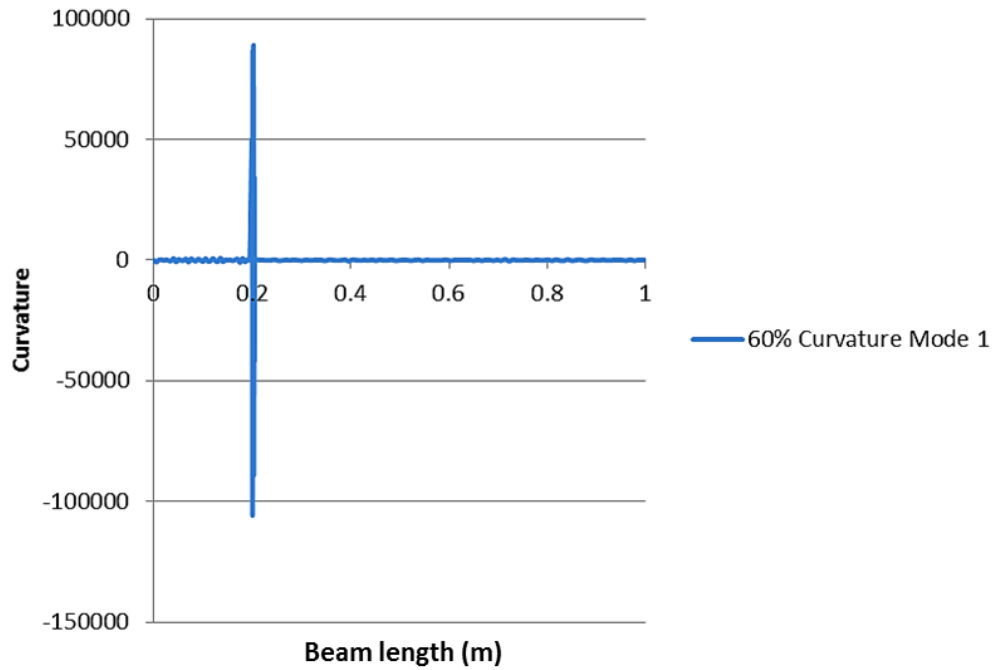
Fig 4-38: Curvature index of first mode shape of a damaged cantilever beam, $L = 1$ m, $L_1 = 0.2$ m, $L_2 = 0.03$ m, cross-sectional area $= 0.0025$ m^2, noise 60%. Curvature shows the damaged elements.
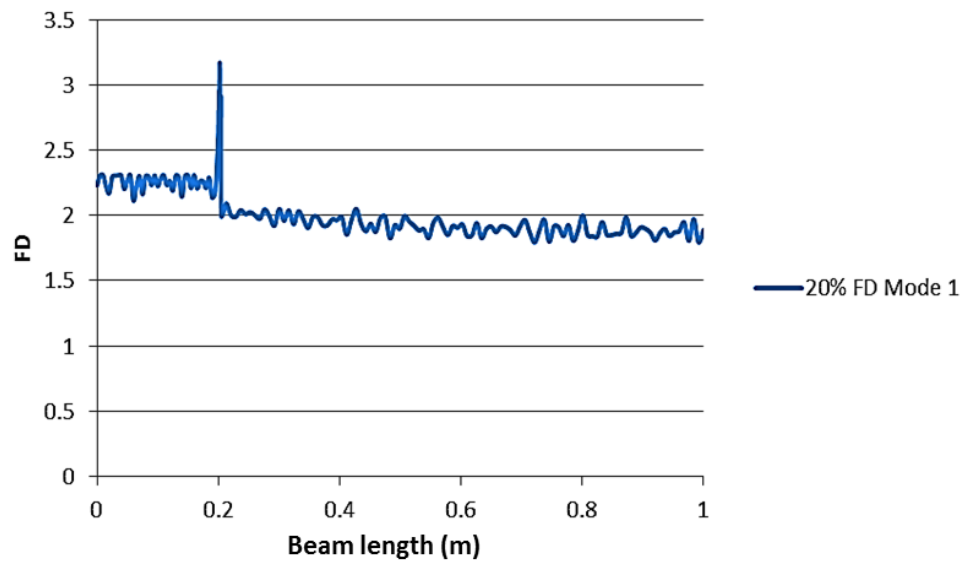
Fig 4-39: Fractal dimension index of first mode shape of the damaged cantilever beam, $L = 1$ m, $L_1 = 0.2$ m, $L_2 = 0.03$ m, cross-sectional area $= 0.0025$ m^2, noise 20%. The fractal dimension peak can still be seen.
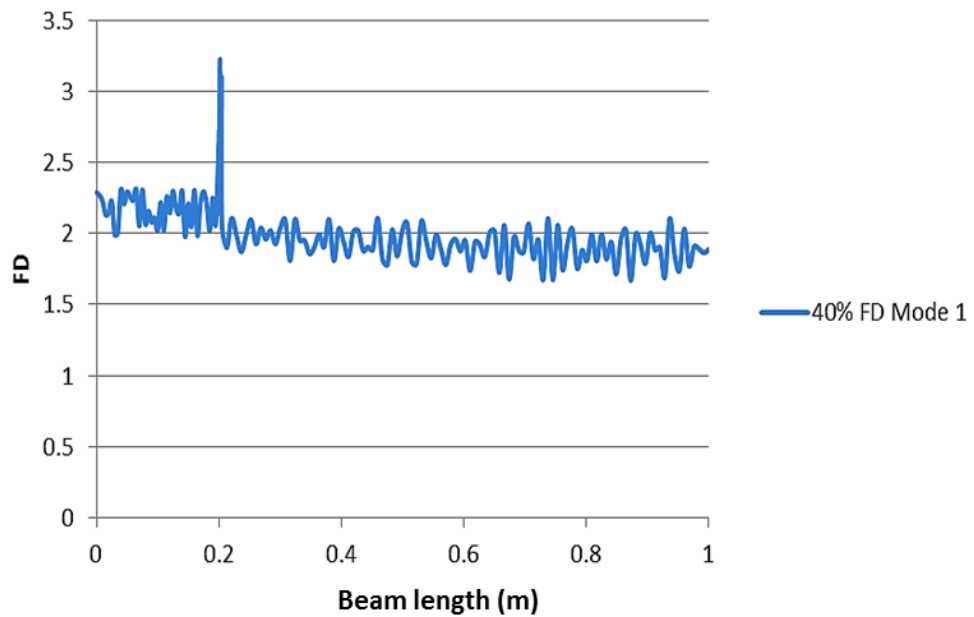
Fig 4-40: Fractal dimension index of first mode shape of a damaged cantilever beam, L = 1 m, L_1 = 0.2 m, L_2 = 0.03 m, cross-sectional area = 0.0025 m^2, noise 40%. The fractal dimension can be seen to begin fluctuating at this level of noise.
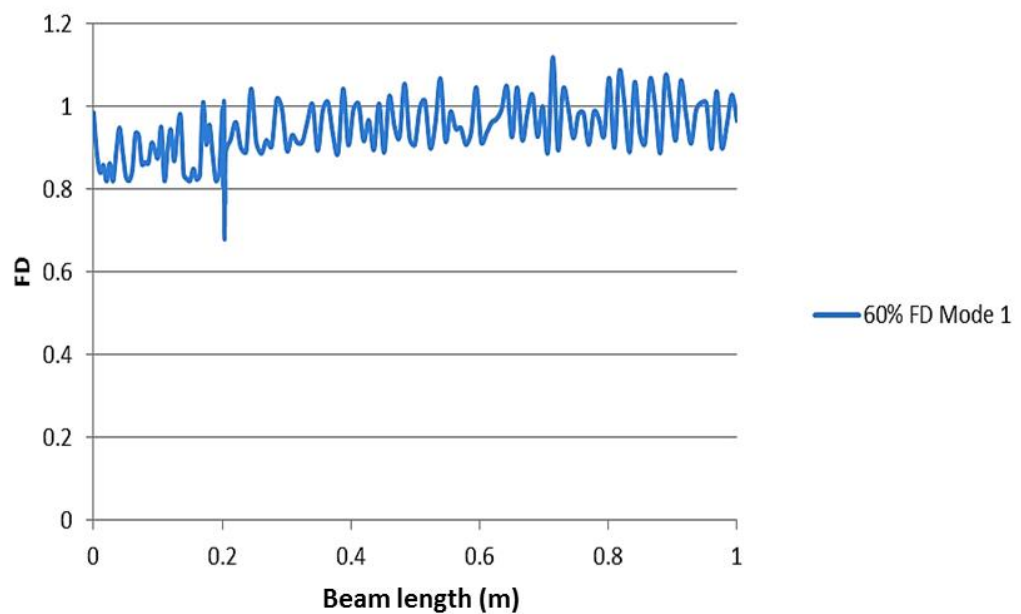
Fig 4-41: Fractal dimension index of first mode shape of a damaged cantilever beam, L = 1 m, L_1 = 0.2 m, L_2 = 0.03 m, cross-sectional area = 0.0025 m^2, noise 60%. The fractal dimension peak has essentially disappeared in the noise.

4.2.6 Irregularity damage index

The last part of this chapter presents an assessment of the irregularity index. This concept was originally proposed by Wang and Qiao [102], where the "waviness" of the damaged mode was extracted numerically. They used Eq.(4.4) to smooth the mode shape, upon which the smooth part is subtracted from the entire mode to provide the irregularity index, R, as formulated in Eq.(4.5). Within these equations, z is the amplitude of mode shape, $h(x)$ is the weighted function used to provide the smooth part of mode shape, and w refers to the waviness of the mode shape (as defined mathematically below).

In the current study, the concept discussed above was determined by calculating the numerical irregularity index (R^2) as per Eq.(4.6), where $\left(\emptyset_{ij}\right)_D$ and $\left(\emptyset_{ij}\right)_H$ are the damaged and intact modes respectively. Both the damaged and intact mode shapes are calculated using the FE analysis, from which the square of their difference defines the irregularity index, as shown in Eq.(4.6).

$$w(x_o) = \int_{-\infty}^{\infty} z(x_o + x)h(x)dx \tag{4.4}$$

$$R(x_o) = z(x_o) - w(x_o). \tag{4.5}$$

$$Irregularity\ Index\ (R^2) = \left(\left(\emptyset_{ij}\right)_D - \left(\emptyset_{ij}\right)_H\right)^2 \tag{4.6}$$

The cantilever beam shown in Fig 4-4 was analysed using COMSOL 5.1 to detect the damaged sections by calculating the irregularity index, Eq.(4.6). The first and second modes were calculated for intact and damaged beams. In this section, damaged regions were located at 0.4, 0.5 and 0.65 m from the fixed edge using the same stiffness reduction criteria. As can be seen from the irregularity index for mode one, as shown in Fig 4-42, Fig 4-43 and Fig 4-44, this index can effectively detect the damaged sections, where the index peak was associated with damage at different locations. In all these figures, the peak value of the irregularity index was 2.2e-28, which means that damage at different locations provides the same peak. The same analysis was applied to the

second mode, as can be seen in Fig 4-45, Fig 4-46 and Fig 4-47; the same peak trend was found as for the first mode, where the peak was localized at the damaged location. The only difference was that the second mode peak is larger in magnitude than the first mode peak at 1.2e-25. This difference makes using second mode data is more applicable in damage detection than using first mode shape. In summary, testing the irregularity index provides another efficient way to precisely detect the damaged sections.
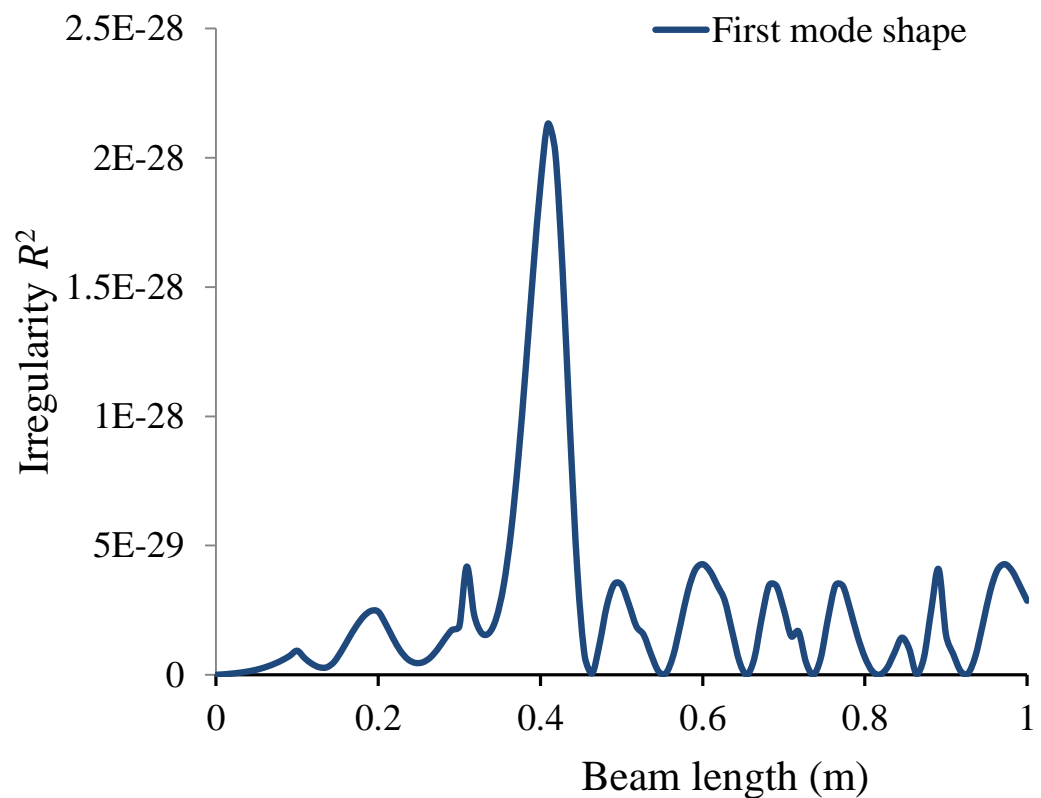
Fig 4-42: Irregularity index of the first mode shape of a damaged cantilever beam, $L = 1$ m, $L_1 = 0.4$ m, $L_2 = 0.03$ m, cross-sectional area = 0.0025 m^2. Damage was located 0.4 m from the fixed end of the beam.
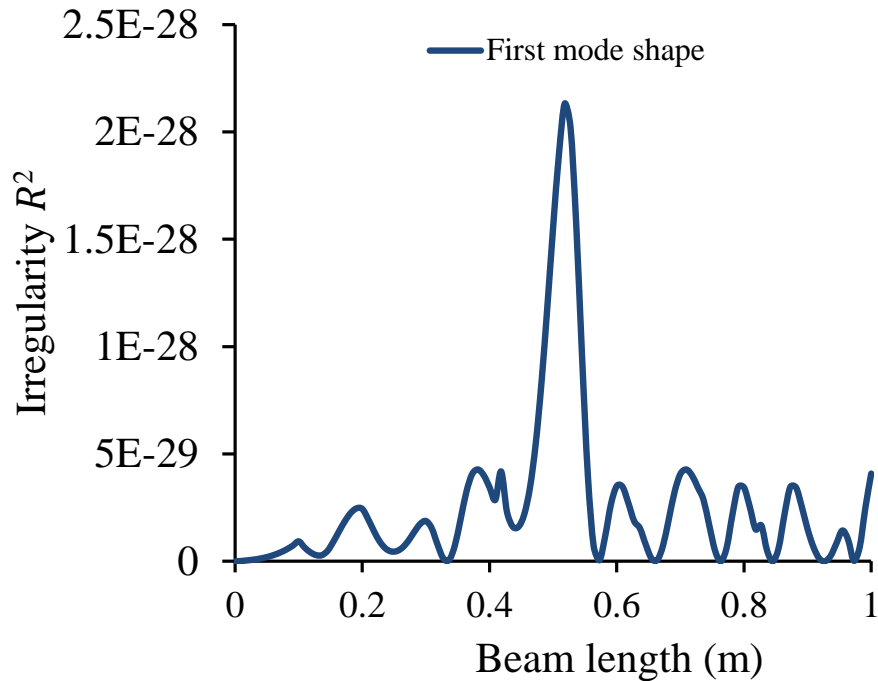
Fig 4-43: Irregularity index of the first mode shape of a damaged cantilever beam, $L = 1$ m, $L_1 = 0.5$ m, $L_2 = 0.03$ m, cross-sectional area = 0.0025 m^2. Damage was located 0.5 m from the fixed end of the beam.
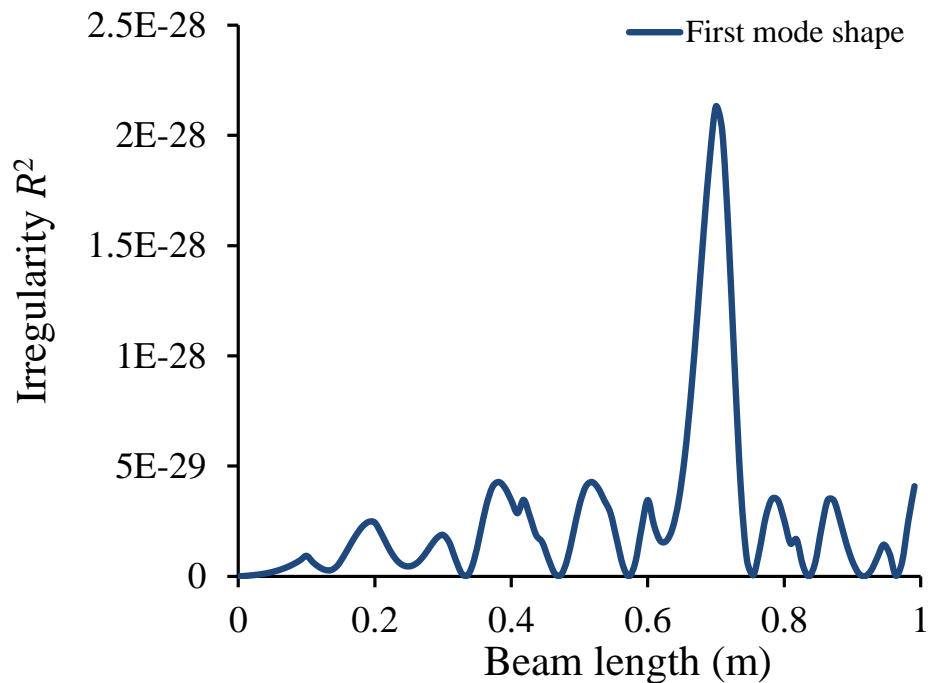
Fig 4-44: Irregularity index of the first mode shape of a damaged cantilever beam, $L = 1$ m, $L_1 = 0.65$ m, $L_2 = 0.03$ m, cross-sectional area = 0.0025 m^2. Damage was located 0.65 m from the fixed end of the beam.
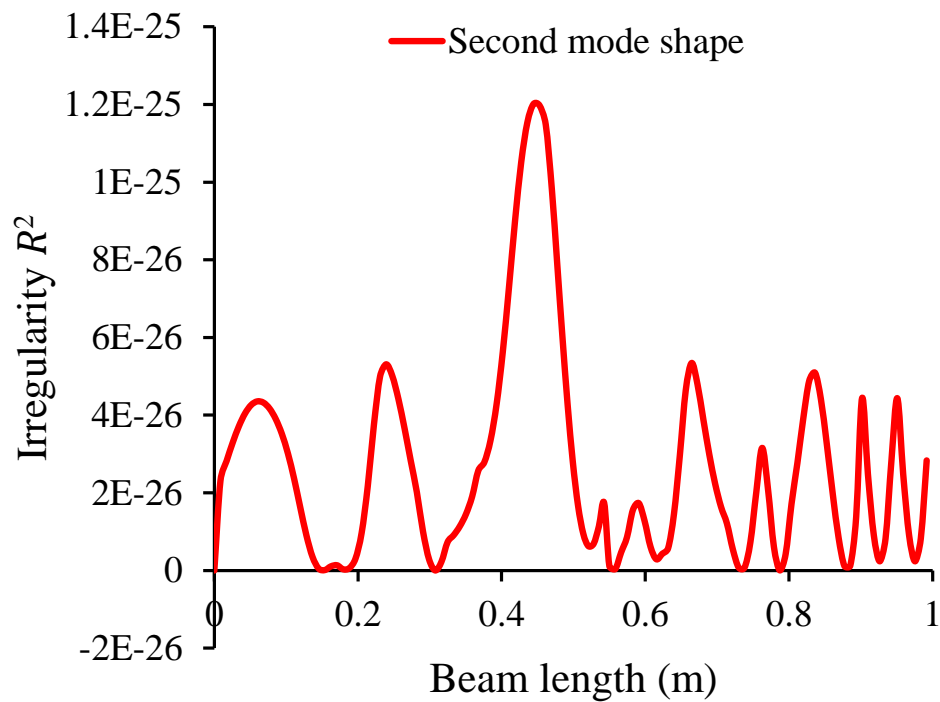
Fig 4-45: Irregularity index of the second mode shape of a damaged cantilever beam, $L = 1$ m, $L_1 = 0.4$ m, $L_2 = 0.03$ m, cross-sectional area $= 0.0025$ m^2. Damage was located 0.5 m from the fixed end of the beam
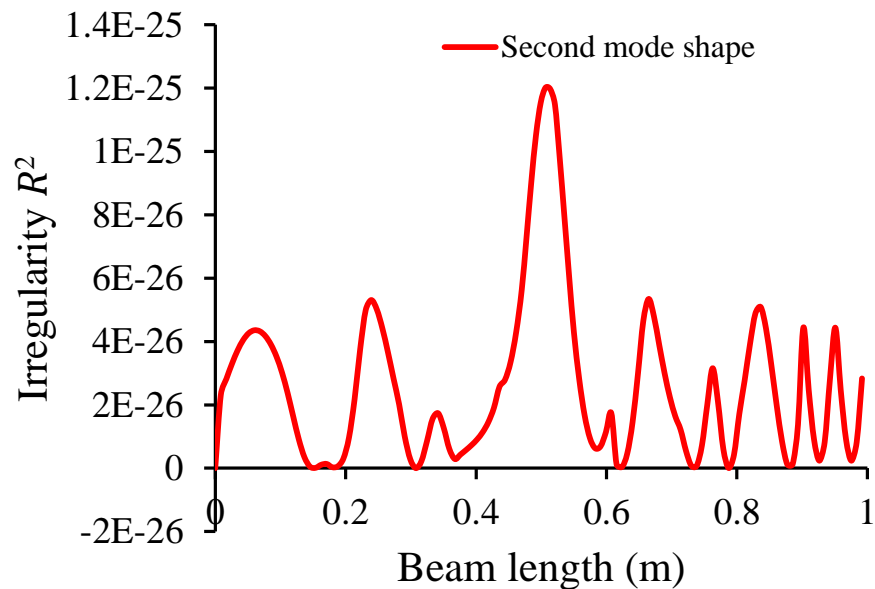
Fig 4-46: Irregularity index of the second mode shape of a damaged cantilever beam, $L = 1$ m, $L_1 = 0.5$ m, $L_2 = 0.03$ m, cross-sectional area $= 0.0025$ m^2. Damage was located 0.5 m from the fixed end of the beam.
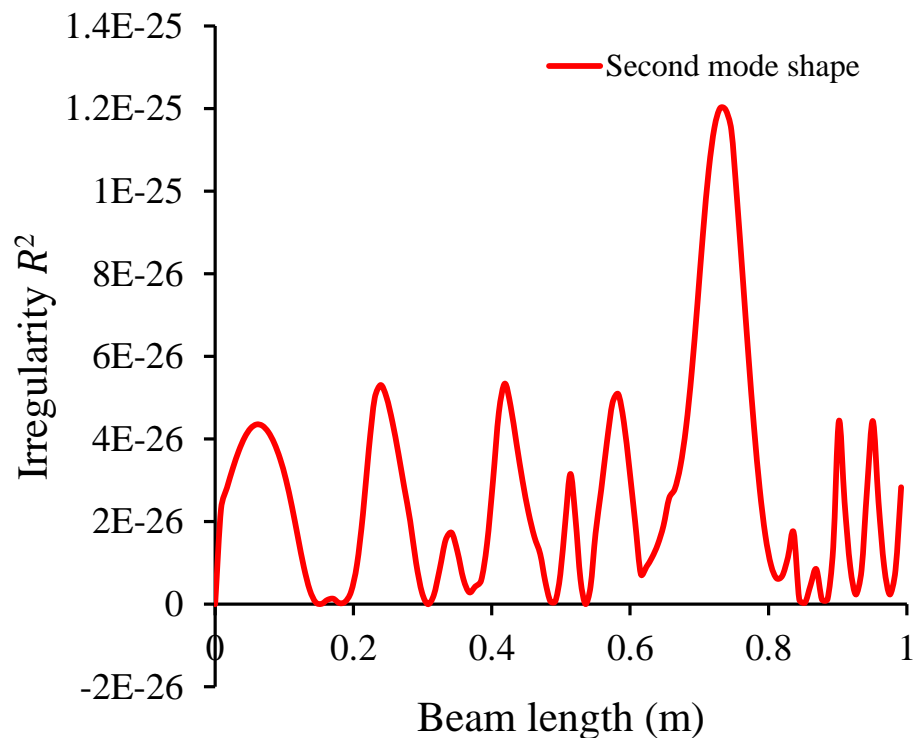
Fig 4-47: Irregularity index of the second mode shape of a damaged cantilever beam, $L = 1$ m, $L_1 = 0.65$ m, $L_2 = 0.03$ m, cross-sectional area = 0.0025 m^2. Damage was located 0.65 m from the fixed end of the beam.

4.3 Conclusion

This chapter concludes the evaluation of vibration-based damage detection using different damage indicators. COMSOL Multiphysics 5.1 was used to run finite element analysis (FEA) on the cantilever beam models. The damaged sections were modelled by calculating the reduction in local stiffness (EI). It has been assumed that damage produces new local cross-section coordinates. The validation case study was undertaken by simulation of a cracked cantilever beam, upon which the subsequent effects on variation of natural frequency were investigated. The use of area moment of inertia to reduce the local stiffness was proposed as an approach to evaluating a number of dynamic indexes.

A comparative case study was run to evaluate a number of dynamic indicators, where mode shape, slope of mode shape, curvature, fractal dimension and irregularity indexes were calculated. These indicators were evaluated at different local stiffnesses, different locations, and some were further assessed in terms of the influence of different

noise levels. All the indicators were found to be sensitive to severe cases of damage. The higher derivatives of mode shape and filtration of the damaged data showed greater efficiency with regards to damage detection and localization than using the mode shape itself. Fractal dimension showed a lower peak magnitude and lower sensitivity to the noisy data.

Using the beam structure in this analysis provides a clear idea about the evaluation of different dynamic indexes. As is already known, the detection of damage in laminated structures is more complicated than in metal structures due to the complexity of these structures [laminated structure consists at least of two materials]. This feature can effectively influence their dynamic responses such as mode shape, natural frequency and damping ratio. This analysis suggests curvature index as a recommended approach of damage detection in laminated composite structures due to its efficiency and sensitivity to the existence of damage.

Part 3

Experimental and Numerical FEA Study on Damage Detection Methods

Chapter 5: Experimental setup

This chapter discusses the manufacture of the laminated composite samples used in the experimental work. Also, the fundamentals of using laser Doppler vibrometer (LDV) in measuring dynamic responses are demonstrated. In this research, carbon fibre-reinforced polymer (CFRP) was used to produce the laminated composite plate structures. Two different sized lay-ups of CFRP plates were used. The first set was a narrow four-layer laminated plate with and without damage, while the second setup had two styles (A and B) of eight-layer CFRP laminated plate structures which were prepared in order to investigate the damage detection process. Here, A and B refer to different lay-up orientations.

The intact and damaged mode shapes and frequency response functions (FRF) were measured using a laser Doppler 3D vibrometer. This tool was employed to overcome the noise challenge associated with dynamic tests.

5.1 Damage detection in CFRP using a laser vibrometer scanning system

For the past few decades, vibration-based damage detection has remained one of the most important techniques used to quantify the damaged areas in different mechanical structures. Damage detection in composite structures, in particular, has gained the attention of a number of researchers. The high strength relationship between physical characteristics such as stiffness, mass, and damping and dynamic parameters such as mode shapes, natural frequencies, and damping ratio enhance the use of this technique for damage detection purposes.

A Laser Doppler Vibrometer (LDV) is a non-perturbing measurement tool (for continuous measurement of dynamic response) was used to precisely measure the dynamic signal of the vibrated surfaces via the laser scanning technique [115]. The process of data acquisition using LDV is shown schematically in Fig 5-1. It is clear from this figure that the measurement hardware requires the following:

    i.   Scanning laser vibrometer head
    ii. Custom cable used to control the scan-mirror servo motors

iii.   Dual channel with arbitrary function generator

iv.   Impact hammer to excite the object to be vibrated

Where in simple way that scanning laser Doppler vibrometer can obtain non-contact vibrational data from a vibrated structures. The hammer, for example, in this figure was used to excite the object at different frequencies. Then the collected data is computerized in order to be separated into different mode shapes [115].

As reported by Stanbridge and Ewins [116], LDV can be considered a diagnostic-quality tool for damage detection due to its ability to scan a dense set of points and provide non-contact data for the vibrated structure. If v_z represents the sinusoidal velocity of any point in the z-direction, which is perpendicular to surface in the x, y plane, with an angular frequency ω, then mathematically this can be formulated as per Eq.(5.1)

$$v_z(s,t) = V_a(s)cos\omega t + V_b(s)sin\omega t \qquad (5.1)$$

where s is the distance between point a and b, and V_a and V_b are velocities of these points. The operating deflection shape (ODS) can be found if the laser scan is performed continuously by demodulating the dynamic signal. The mathematical basis for demodulation is represented by Eqs.(5.2) and (5.3). Then, the imaginary and real ODS shown in Fig 5-2 give the dynamic output signal that can be used to gauge the performance of the final vibrational modes [116].

$$v_a(t)cos^2\omega t + V_b(t)sin\omega t \ cos\omega t = \frac{1}{2}V_a(t) + \frac{1}{2}V_b \ cos2\omega t + \frac{1}{2}V_b(t)sin2\omega t \qquad (5.2)$$

$$v_a(t) \ sin\omega t \ cos\omega t + V_b(t)sin^2\omega t = \frac{1}{2}V_b(t) + \frac{1}{2}V_a \ sin2\omega t - \frac{1}{2}V_b(t)cos2\omega t \qquad (5.3)$$
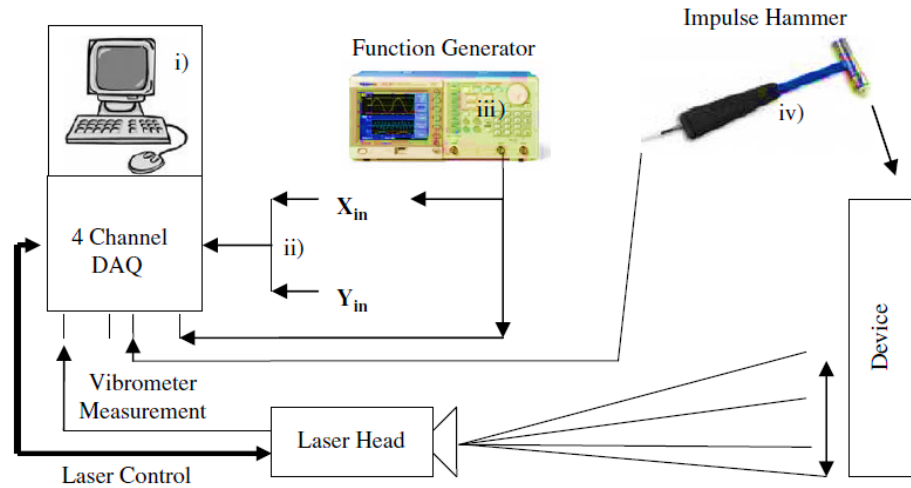
Fig 5-1: Schematic explanation of data measurement [115].
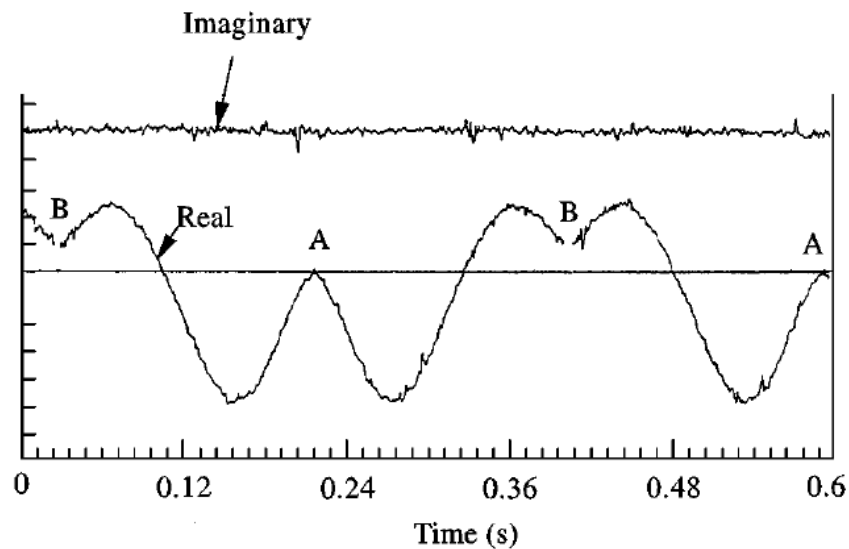
Fig 5-2: The imaginary and real operational deflection shape of a cantilever beam
     [116].

The experimental results can be collected over linear path or in any selected
pattern [117]. One of the limitations to LDV tools is that the point-by-point collection
by this method needs a very long time to complete, especially when the number of
required points is large. Sriram et al. [118] [119] suggested a new method to improve
the scanning of surfaces through the use of a continuous laser scan over the required
area. A sinusoidal excitation was used in this instance to vibrate the damaged structure.
Also, researchers built a prototype to modify the measurement of the dynamic response.

Here, the velocity of the surface was recorded and then processed to gain an accurate signal.

Another suggestion was proposed by Stanbridge and Ewins [116] [120], to improve the continuous scan by scanning different patterns such as circular and scans of the entire area. They investigated the application of filters to the output signal to increase damage detection efficiency. The continuous laser scan method has been used with impact testing, as discussed by Stanbridge et al. [121], and with different excitation modes, as reported by Maio and Ewins [122]. Laser vibrometer scanning has further been extended to include the measurement of the modal response of civil structures, as reported by Bougard and Ellis [123] and Kaito and Fujino [124]. The "lifting" method was suggested by [115] to improve the dynamic response measured by laser scanning, where curve fitting was used to modify and smooth the output signal. This method has been further modified to identify the modal characteristics of structures under random excitations [125]. Yang and Allen [126] proposed the harmonic transfer function to treat the dynamic output signal of laser scanning. This method was utilized to calculate the translational and rotational velocities of surfaces using a circular scan pattern. Fig 5-3 shows additional evidence for the advantage of using LDV to scan light structures and its ability to show their 3D excitations [127]. This is a practical example of using LDV to measure the second mode shape of a tennis racket. It is clear that this figure presents the second bending mode of this racket under free vibration. One of the important feature of using LDV that even racket was thin, LDV can successfully measure the vibrational modes. Also, the latest generation of development in LDV offers automatic control over the scanning of mechanical structures. It is clear from Fig 5-4 that a laser scan of the entire body of vehicle by a robotic system indicates the extent to which LDV can be used in damage detection, even with complex structures [128].
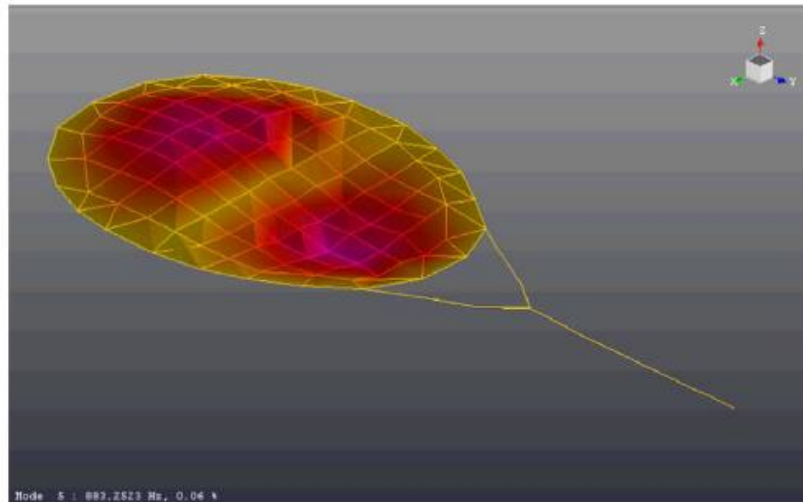
Fig 5-3: The second mode shape of tennis racket strings was determined using LDV [127].
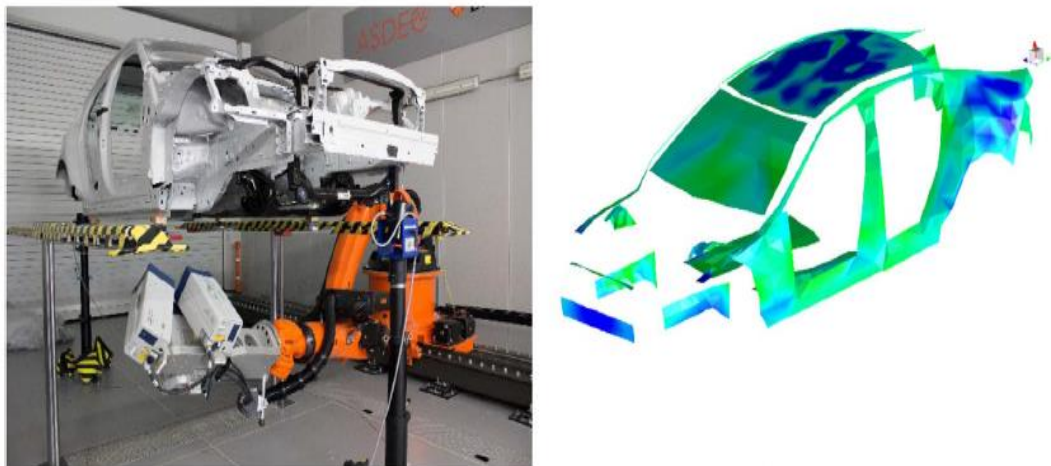
Fig 5-4: 3D laser Doppler scanning vibrometer and the typical mode shape of an entire vehicle body in the ASDEC lab [128].

5.2   Experimental setup for CFRP plate structures

5.2.1   Curing conditions for carbon laminated samples

Unidirectional carbon fibre reinforced polymers (CFRP), M55J with epoxy, were utilized to manufacture the laminated plate structures. A frozen roll of carbon fibre / epoxy was utilized to prepare experimental samples in the required dimensions. The first step was to leave a roll of the raw material for 12 hours at room temperature before starting sample preparation. Then, the fibres were cut into rectangular pieces (each piece

represents a layer with a certain fibre orientation) according to the required size for each set. These layers were then stacked together to produce the laminated plate structures required. These samples were then covered with unperforated film and a layer of breather cloth on both sides, and then isolated with bagging film and tacky tape. To produce the final laminated structures, the laminated sample needed to be heated. This process is quite important in terms of increasing the interfacial adhesion of surfaces between carbon fibres and matrix, where interfacial adhesion plays an important role in transferring stresses from the matrix to fibres.

5.2.2 Laminated narrow plate structures

Three groups of narrow laminated plates were manufactured using the high modulus M55J unidirectional CFRP prepreg, as provided by the Cytec group, following the procedure recommended by the manufacturer. All symmetric plates consist of four layers of CFRP with orientations of $0^0, 90^0, 90^0, 0^0$ with identical layer thicknesses. The dimensions of the intact plate are represented by L (plate length) = 0.25 m, W (plate width) = 0.02 m, A-A (selected path to measure the mode shape), D = 0.01m (the distance between the free edge and A-A), and t (layer thickness) = 0.125 x 10^{-3} m, as shown in Fig 5-5.
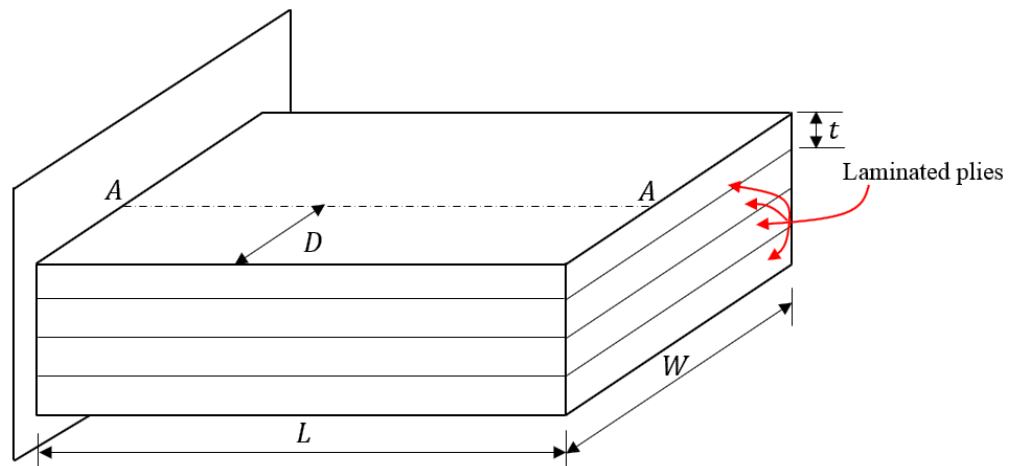
Fig 5-5: Schematic of the intact narrow laminated cantilevered rectangular carbon-epoxy plate, length = 0.25 m, width = 0.02 m and total thickness = 0.5 x 10^{-3} m.

The damaged plates, with artificial delamination and fibre breakage damage at $L_1 = 0.1\ m$ to the fixed edge were manufactured. The delamination was created by adding a thin layer of 15 μm R_{250} unperforated release film to separate the top two layers, as shown in Fig 5-6. The dimensions of the delaminated area, b* W, are W plate width, and b = 0.01 m. In this research, fibre breakage was created by cutting the fibre on the top surface of plate in the same area as the delamination located at L_1, as per Fig 5-7. The actual shape of the laminated samples used in the experimental work is shown in Fig 5-8.
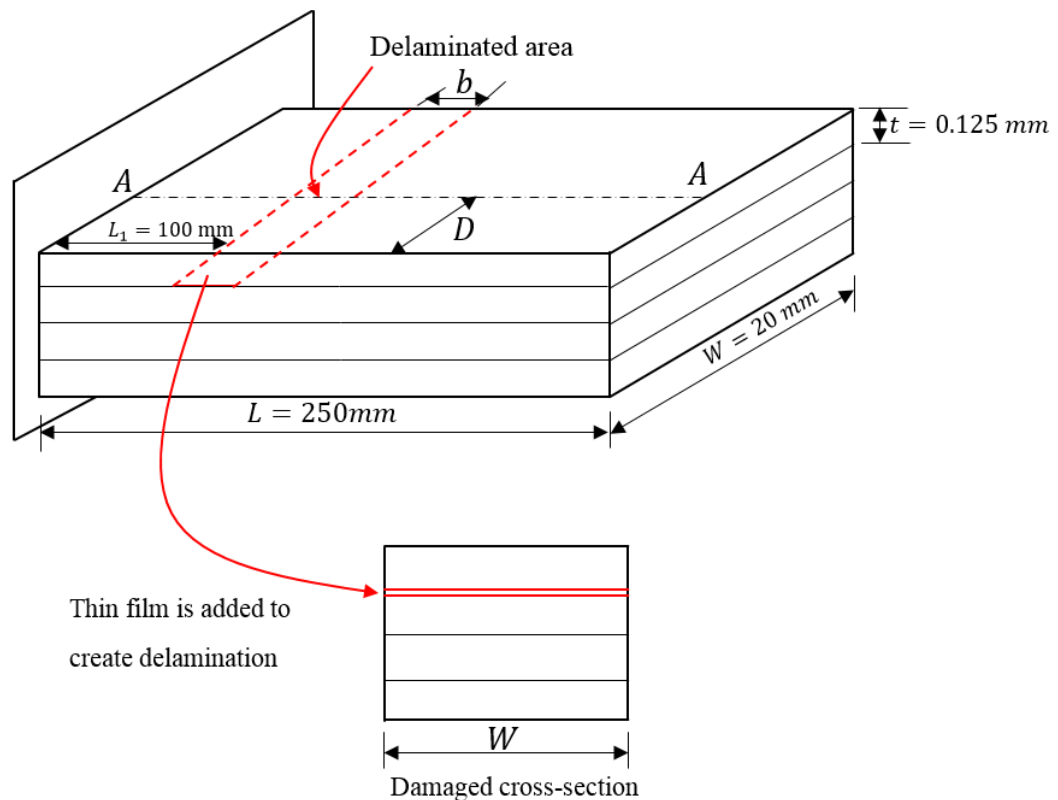
Fig 5-6: Schematic of the delaminated a narrow laminated cantilevered rectangular carbon-epoxy plate, length = 0.25 m, width = 0.02 m, total thickness = 0.5 x 10^{-3} m and the delaminated area (0.01 m * 0.02 m) at L_1 = 0.1 m between the top two layers.
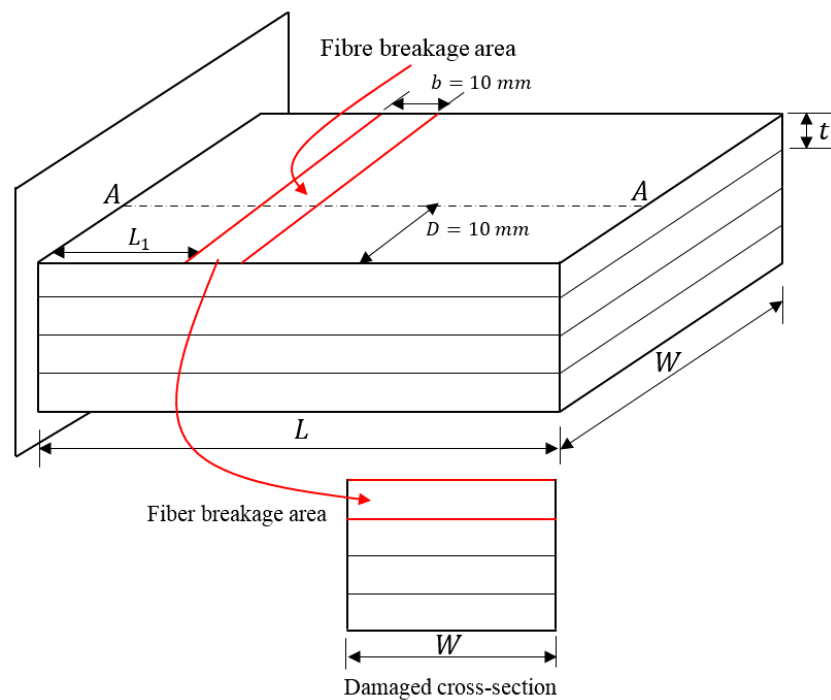
Fig 5-7: Schematic of fibre breakage in a narrow laminated cantilevered rectangular plate with four plies of carbon-epoxy, length = 0.25 m, width = 0.02 m, total thickness = 0.5 x 10^{-3} m and fibre breakage area (0.01 m * 0.02 m) at L_1 = 0.1 m on the top surface.

Fig 5-8: Actual shape of intact, delaminated and fibre breakage narrow laminated plate structures.

The manufacture for the experimental samples was performed in the Mechanics of Materials (MoM) lab. The first step was to cut the unidirectional fibre mat to match the required direction and size of each sample, as shown in Fig 5-9. Then, these individual layers were stacked together according to the required thickness. A double layer of

unperforated release film was used to separate the samples from the aluminium mould and the top layer covering them. Another breather cloth was placed over the release film, and the entire structure was isolated by vacuum bagging film, after which the bagging film was stuck to the mould using the tacky tape, as per Fig 5-10. When the samples were ready to cure, they were heated in the automatic oven, Fig 5-11, at two continuous temperature steps under vacuum condition; for the first two hours, the samples were heated at $130^0 C$, while for the second two hours the temperature was set to $180^0 C$. Finally, samples were ready to be tested and their dynamic responses measured.
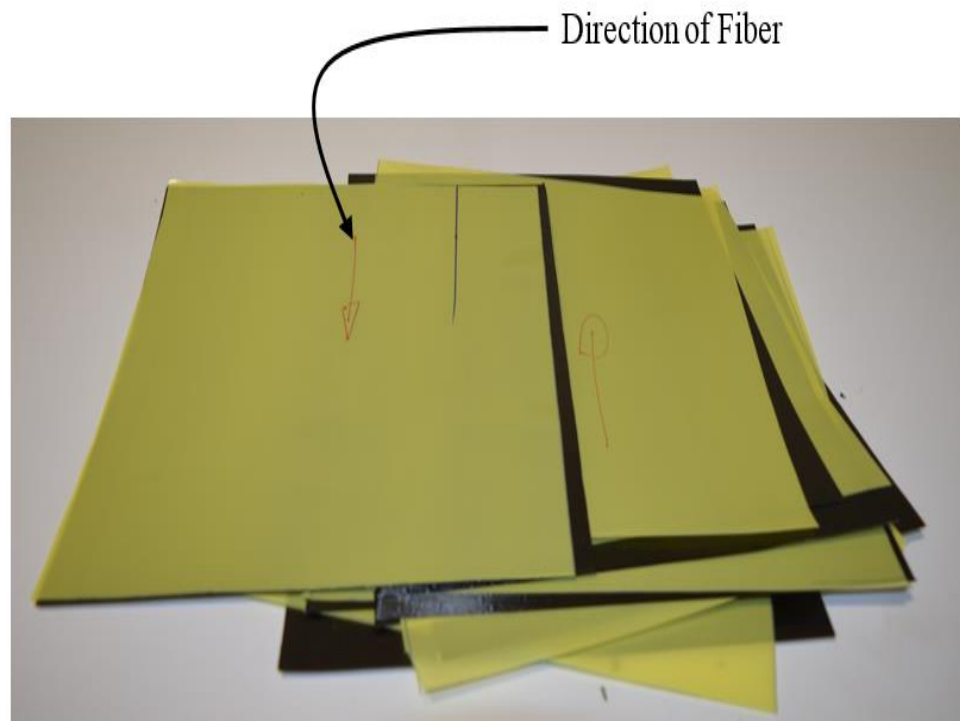
Fig 5-9: Unidirectional carbon fibre reinforced polymer CFRP–epoxy when cutting the first layer's shape.
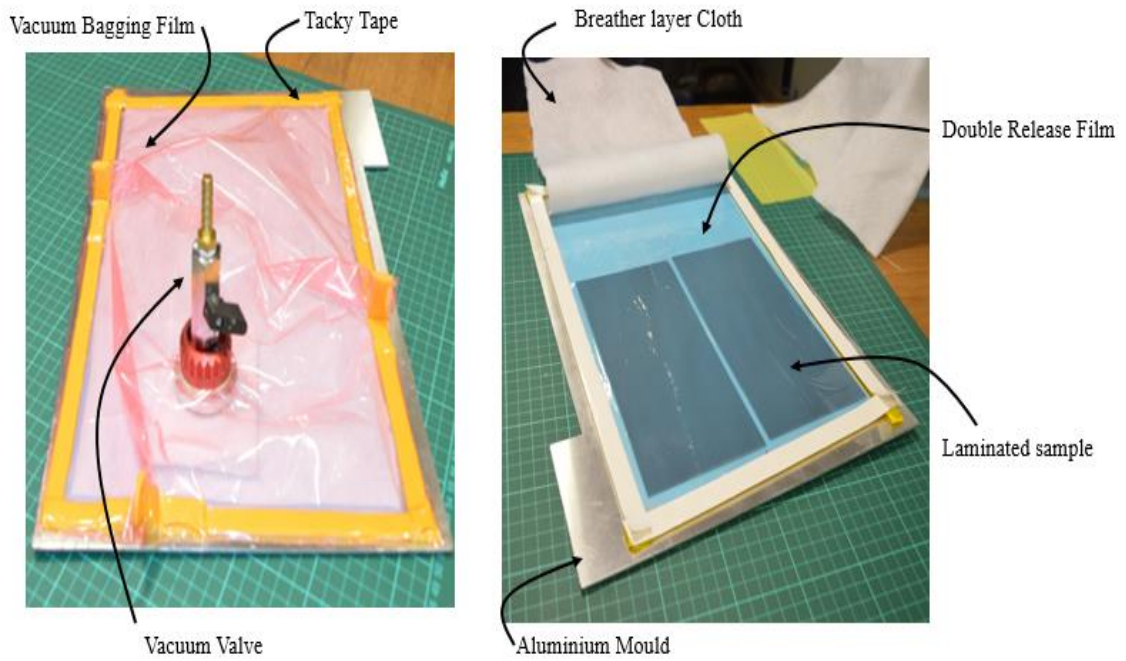
Fig 5-10: Fabricated laminated samples in their final shape, at Mechanics of Materials (MoM) lab.

Fig 5-11: Automatic oven with vacuum pump.

5.2.3 Laminated plate structures

5.2.3.1 Laminated plates with artificial damage

The same narrow plate structure procedures were used to produce the laminated composite plate structures. Two lay-up sequences were prepared to study the effects of fibre orientation on damage identification. The first sequence, style A, consisted of eight symmetric layers with identical layer thicknesses and with orientations of $0^0, 90^0, 0^0, 90^0, 90^0, 0^0, 90^0, 0^0$, whilst the second, style B, had orientations of $0^0, 45^0, 90^0, -45^0, -45^0, 90^0, 45^0, 0^0$. The dimensions of the intact plate are plate length, L = 0.2 m, width, W = 0.1 m, distance between the free edge and the measurement line, D = 0.01 m, A-A measurement line and layer thickness, and t = 0.125 x 10^{-3} m, as shown in Fig 5-12. The artificial damage was manufactured in both the A and B plate sample styles. The side square delamination area (b = 0.02 m) was placed at L_1 = 0.1 m to the fixed edge, using the unperforated film to produce the delamination damage, as seen in Fig 5-13, while, fibre breakage was created by cutting a narrow strip of fibre from the structure with dimensions of l = 0.001 m, b = 0.02 m at L_1, as seen in Fig 5-14. To clarify the description, Fig 5-15 shows the actual intact and damaged plate samples.
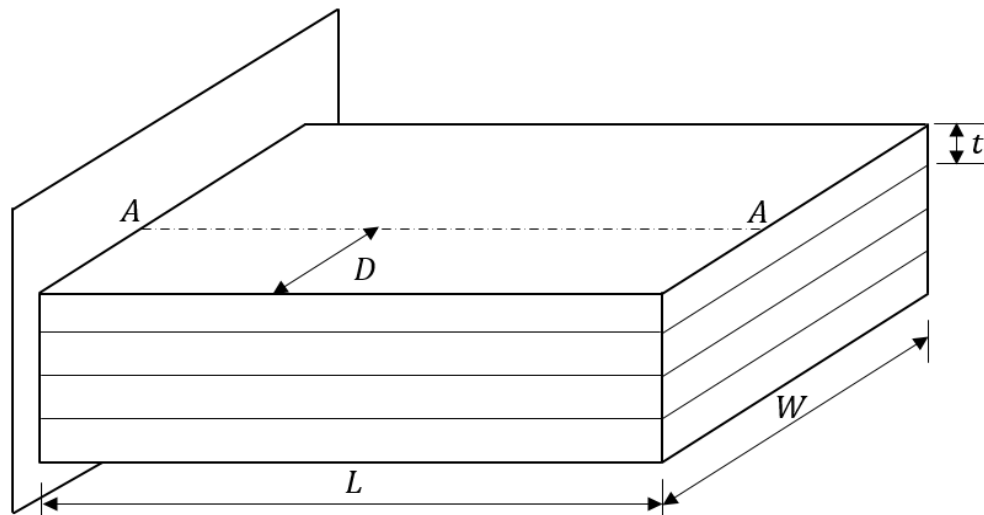
Fig 5-12: Schematic of the intact laminated cantilever rectangular plate with eight plies of carbon fibre -epoxy, length = 0.2 m, width = 0.1 m and total thickness = 1 x 10^{-3} m.
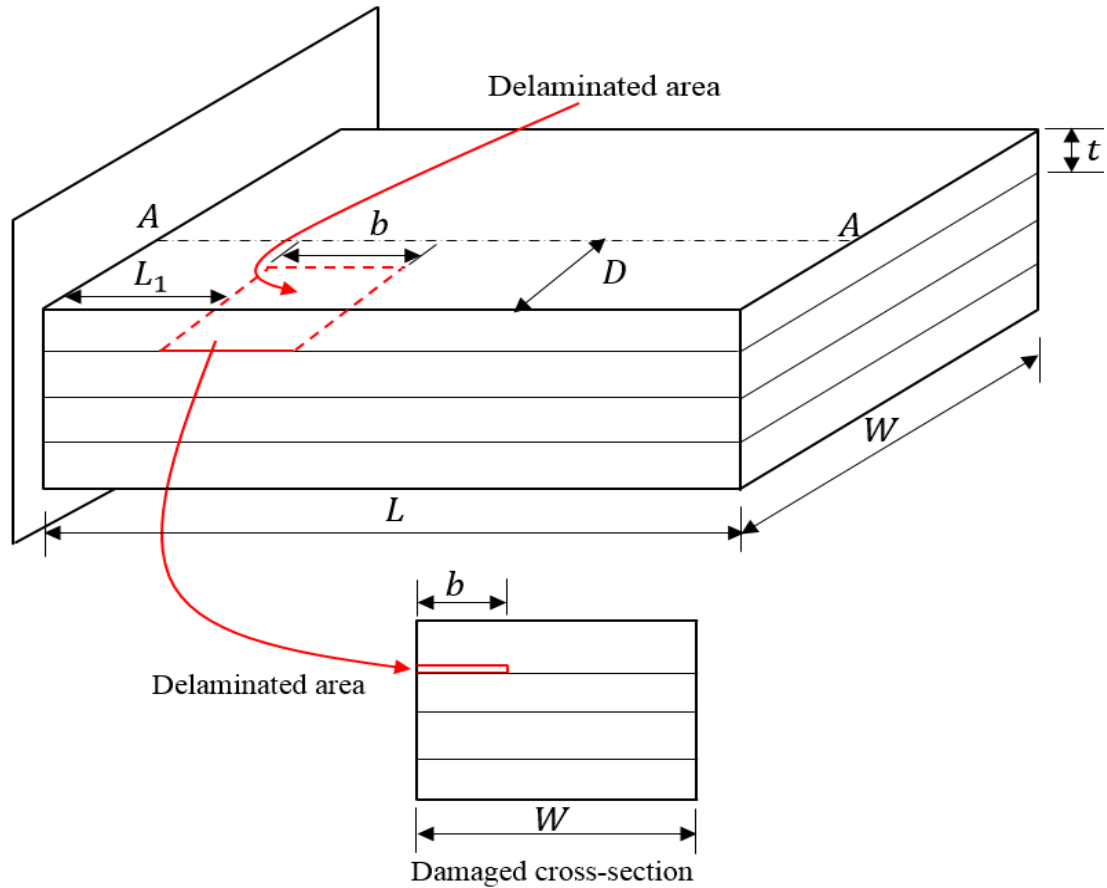
Fig 5-13: Schematic of the delaminated laminated cantilevered rectangular plate with eight plies of carbon fibre-epoxy, length = 0.2 m, width = 0.1 m, total thickness = 1 x 10^{-3} m and delaminated area b^2 (0.02 m * 0.02 m) at L_1 = 0.1 m between the top two layers.
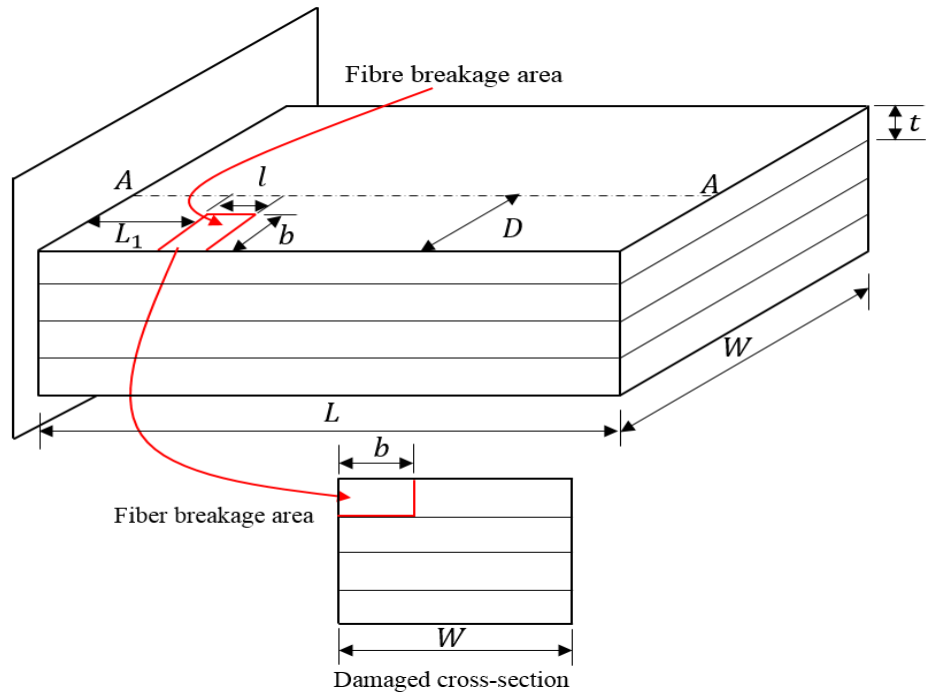
Fig 5-14: Schematic of the fibre breakage in the cantilevered rectangular plate with eight plies of carbon fibre-epoxy, length = 0.2 m, width = 0.1 m, total thickness = 1 x 10^{-3} m and fibre breakage area (0.001 m * 0.02 m) at L_1 = 0.1 m on the top surface.
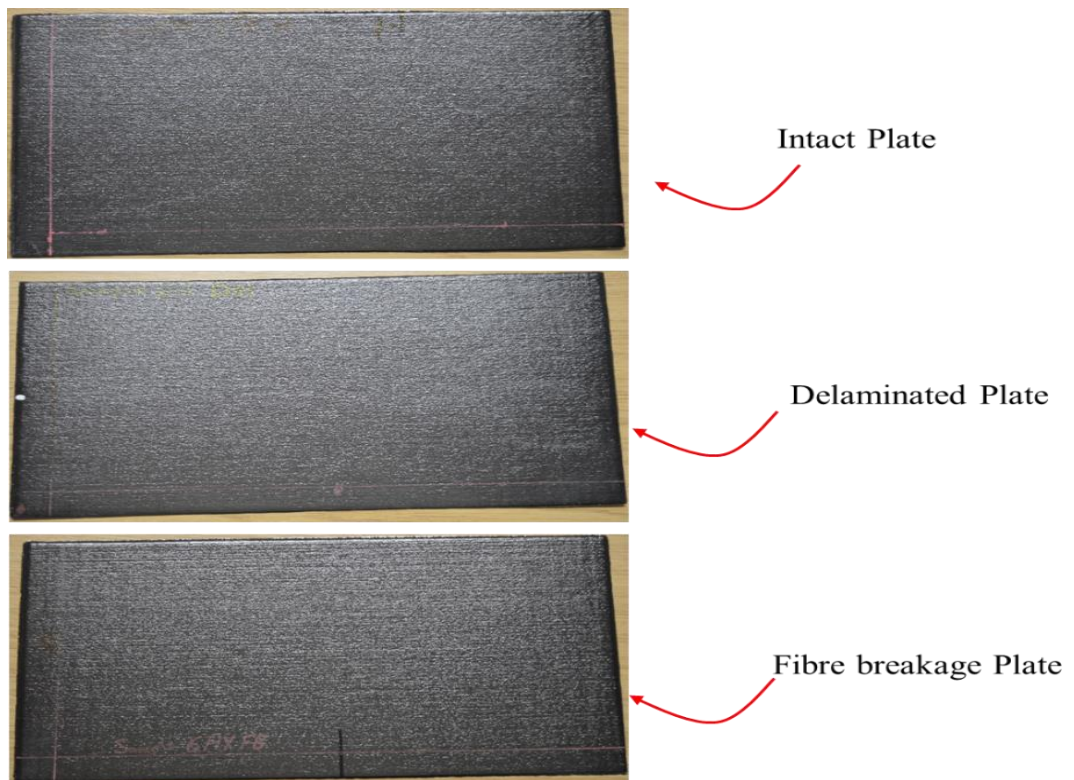
Fig 5-15: Actual intact, delaminated and fibre breakage eight-ply laminate plate samples.

5.2.3.2   Laminated plates with real impact damage

Laminated plate samples A and B lay-up sets were tested using impact load tests to match the reality of laminated structure damage. The impact test achieved in the MaTIC (Lab Materials Technology Integration Centre) at the Engineering Department, University of Leicester, as shown in Fig 5-16. Fibre breakage and delamination were produced by dropping the impact load at L_1 (the same location as the artificial damage). Two steel indenters, 2 and 10 mm in diameter, were used to produce damage in the laminated sample, as seen in Fig 5-17. In this study, the delaminated area was created by dropping a 0.363 kg weight from a 0.26 m height using a 10 mm indenter. Fibre breakage was produced by a 0.362 kg, 0.26 m height and 2 mm diameter indenter. The front and back sides of the damaged specimens are shown in Fig 5-18 and Fig 5-19, respectively, which also show the differences between these two damage modes. In Fig 5-18, it is clear that fibre breakage dominated the damage mode and the penetration of the indenter is quite visible. In contrast, in Fig 5-19 the damaged area could not be identified with the naked eye, which means the main damage in this case was delamination (although there may be some damaged fibres but this was not significant in this case). In fact, as the diameter of the indenter used becomes smaller, the fibre breakage becomes more visible, and the opposite state (using large indenter diameter) produces the delamination [129].
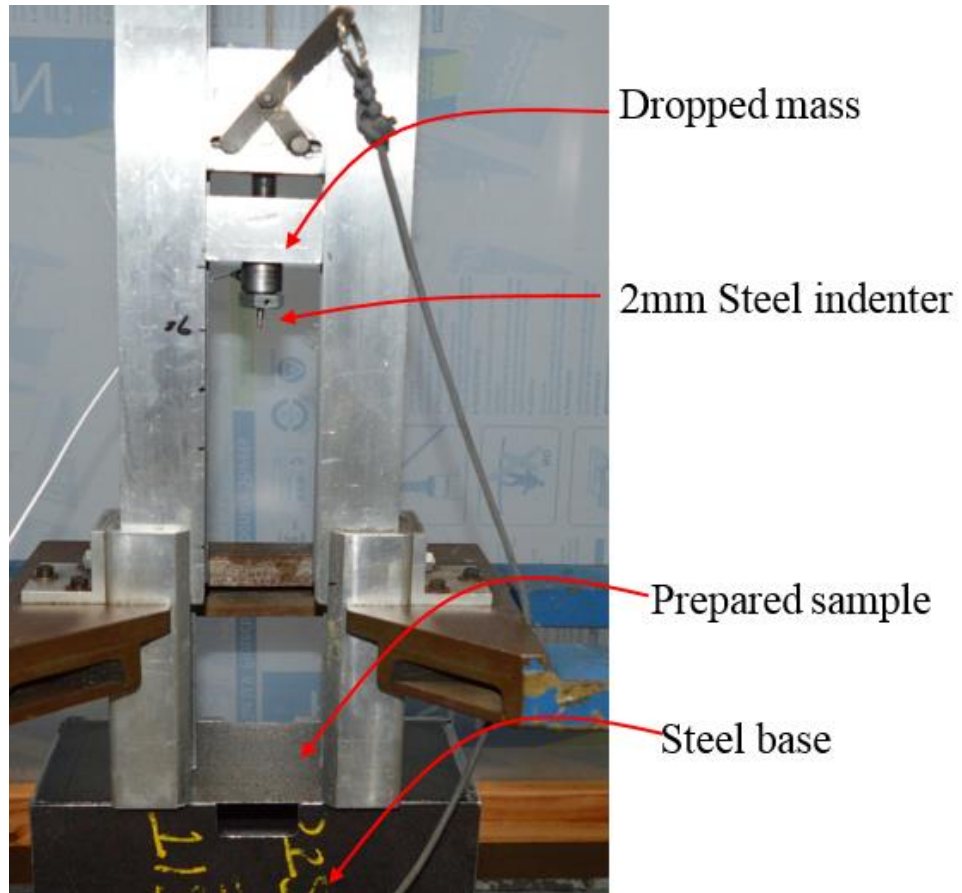
Fig 5-16: Impact test apparatus in the Materials Technology Integration Centre lab.
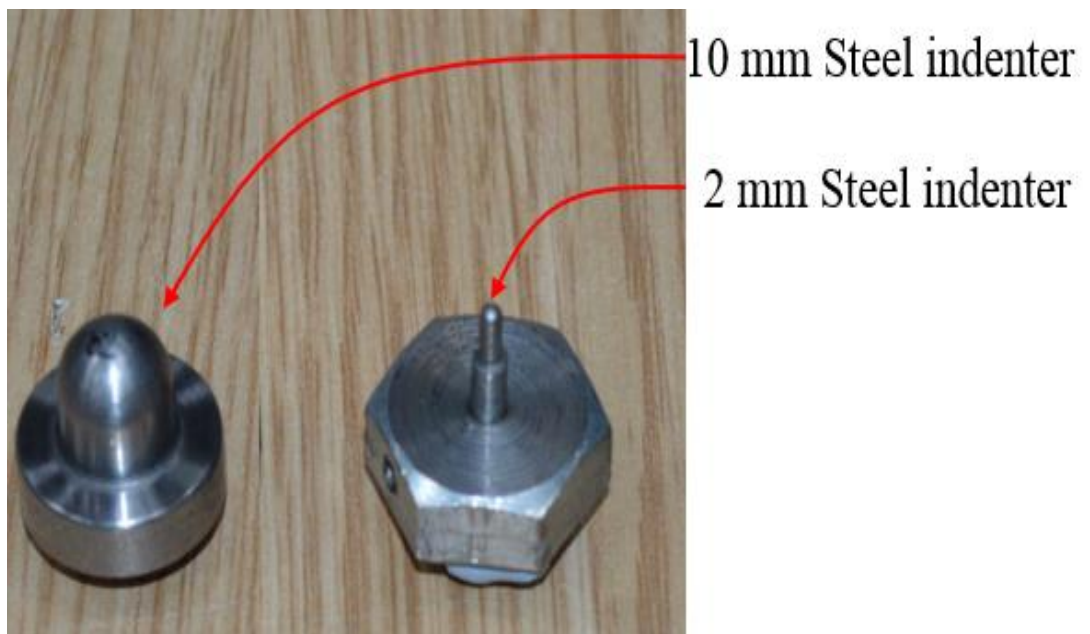
Fig 5-17: Two different steel indenter diameters.
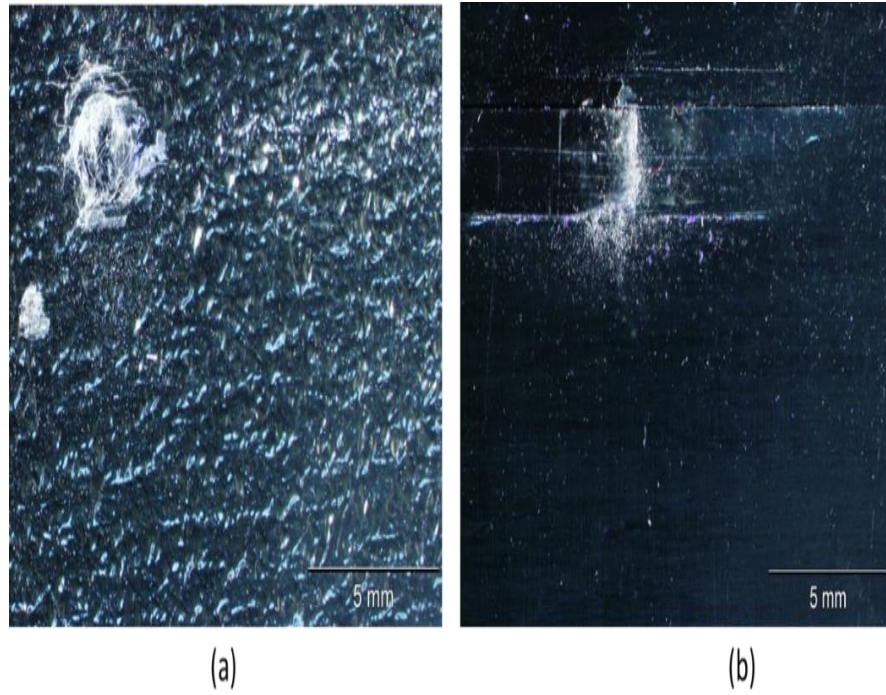
Fig 5-18: Microscope photos of fibre breakage for (a) the front side and (b) back side of the impact test.
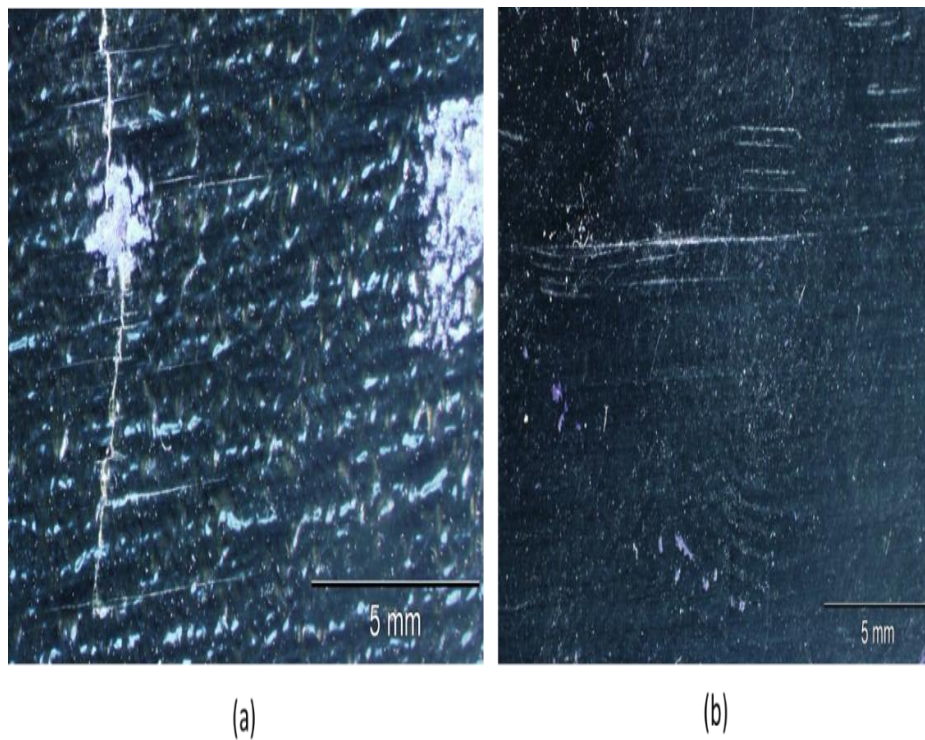
Fig 5-19: Microscope photos of delamination for (a) the front side and (b) back side of the impact test.

5.2.4   Experimental modal analysis (EMA)

A free vibration analysis test was run to measure the first three frequencies and mode shapes for all types of laminated plate structure (i.e., with both artificial and impact damage). These tests were performed using the laser vibrometer in the Advanced Structural Dynamic Evolution Centre (ASDEC). One of the advantages of this technology is the accuracy of the results collected and the availability of the non-contact vibration technique.

5.2.4.1   Electrodynamic shaker and force gauge

The laminated cantilever plate configurations are set up as per Fig 5-20 for all experimental tests. An Electrodynamic Modal Shaker (model number K2004E01, serial number 1476) was utilized to provide the free vibration condition by shaking the clamped edge, as per Fig 5-21. In addition, the force gauge (model number 208C02, serial number LW39159) was set up to satisfy the equivalent force in the free vibration test. The free vibration condition was achieved by applying a micro-vibration to the clamped jaws, so a 'non-touch' force was provided.
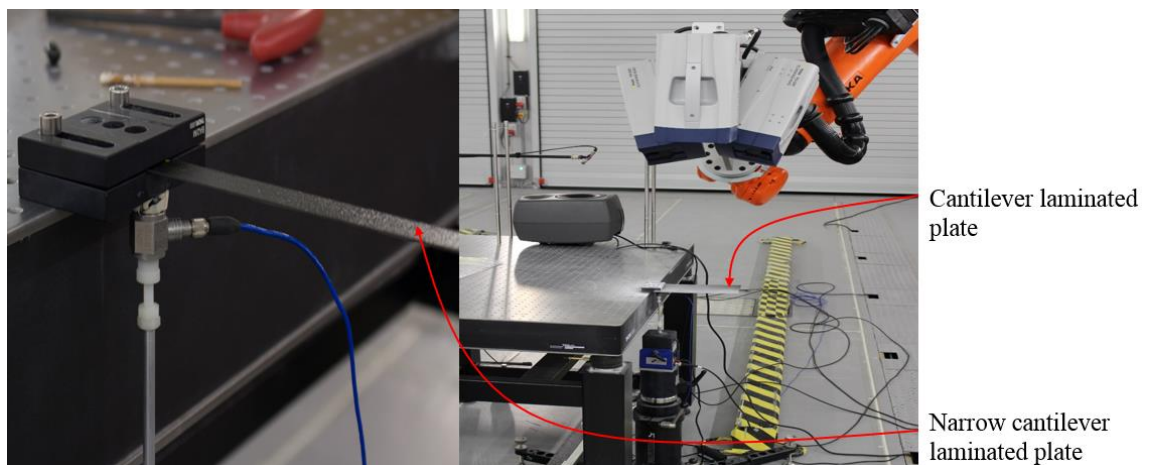
Fig 5-20: Experimental setup for the laminated cantilever plates in ASDEC lab.
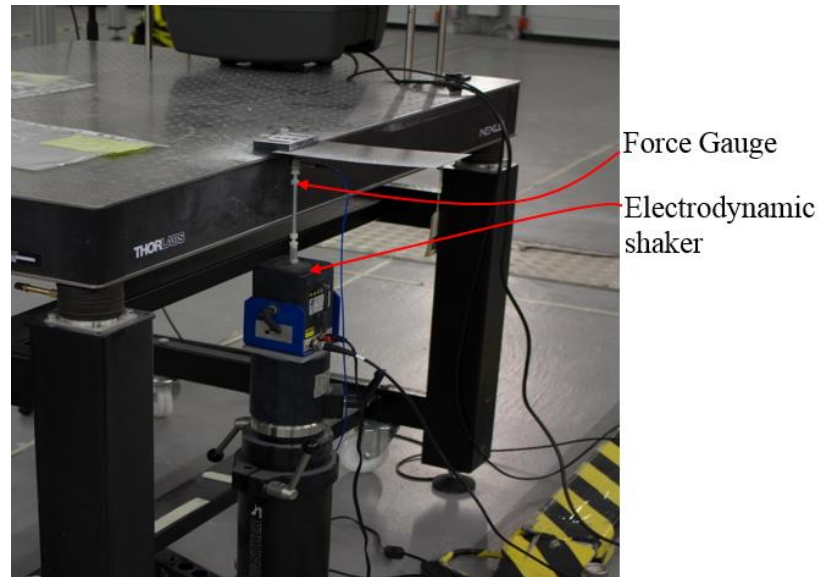
Fig 5-21: Electrodynamic and force gauge.

5.2.4.2 Robotic laser Doppler vibrometer

The dynamic response was measured using 3D laser vibrometer heads, so this technology can be used to measure mode shapes with highly accurate results, as per Fig 5-22, where the noise associated with dynamic response measurement is one of the most important challenges that needs to overcome. In the present research, a 1D mode shape was used to identify the damaged area. The laminated specimens were clamped at one end and the movable robotic laser vibrometer was able to examine any required point.
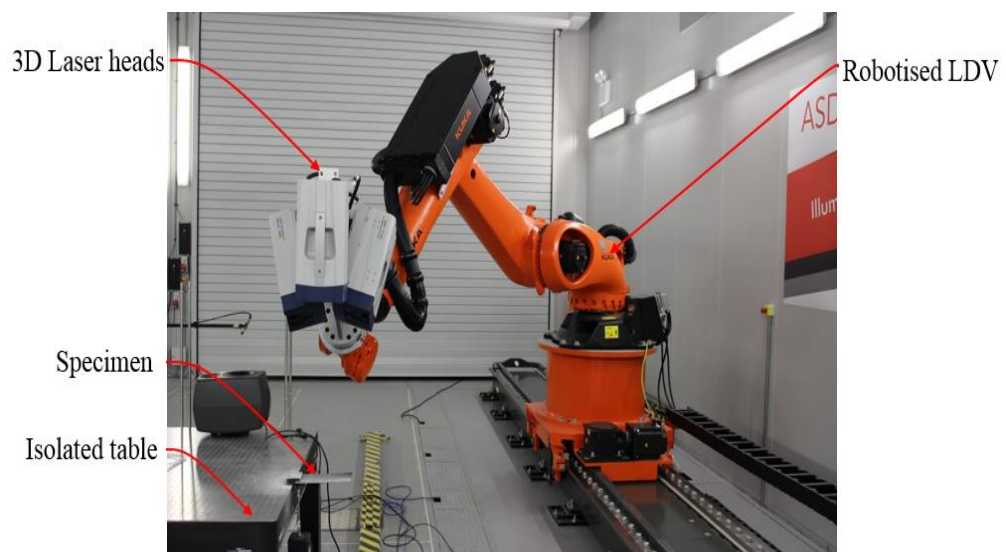
Fig 5-22: Robotic laser Doppler vibrometer in ASDEC.

5.3 Principles of laser Doppler vibrometer

The Laser Doppler Vibrometer (LDV) is a laser-based, non-contact measurement system used to measure the vibrational characteristics (mode shape and frequency). The operational principle behind the LDV system is the Doppler effect concept. As seen in Fig 5-22, the system consists of three measuring units (scanning heads). These heads provide information about the movement of vibrated objects in three orthogonal directions.

The principles of the Doppler effect a change in the frequency or wavelength of released waves occurs when the source of the waves approaches or moves further away from the observed object as seen in Fig 5-23 [130]. This means the effect of the laser wave can be seen twice, primarily, before hitting the particle (denoted any point within the vibrated object), and secondly after impinging the vibrated particle. If it is assumed that subscripts b, r, p represent laser beam, receiver and particle, respectively, in Fig 5-23, then f, V, c, and e are frequency, velocity, velocity of light in the measurement medium and a unit vector. To calculate the frequency of received signal Eq.(5.4) can be used, where f_r, f_p are frequency of receiver and particle respectively, e_{pr} is the unit vector of the particle received by receiver, and λ_b wavelength of laser beam (other symbols can be defined according to their subscripts) . In case of dual scattering as shown in Fig 5-24, the difference in frequency f_D (denoted as the difference between two scattered waves) can be computed as per the formula in Eq.(5.5) [130]. In brief, in an LDV system the vibrometer receives the scattered laser light and compares this with the frequency of a reference beam. It then creates a voltage signal compatible to the shift in frequency. This signal represents the velocity of the vibrated object. The entire process of calculating mode shape is discussed in section 7.3.

$$f_r = f_p \frac{1}{1 - \frac{e_{pr}.V_p}{c}} = f_b \frac{1 - \frac{e_b.V_p}{c}}{1 - \frac{e_{pr}.V_p}{c}} \tag{5.4}$$

$$\approx f_b + f_b \frac{V_p(e_{pr} - e_b)}{c} = f_b \frac{V_p(e_{pr} - e_b)}{\lambda_b}, \left(|V_p| \ll c, \ c = f_b\lambda_b\right)$$

$$f_D = \frac{V_p\,(e_{p2} - e_{p1})}{\lambda_b} \tag{5.5}$$
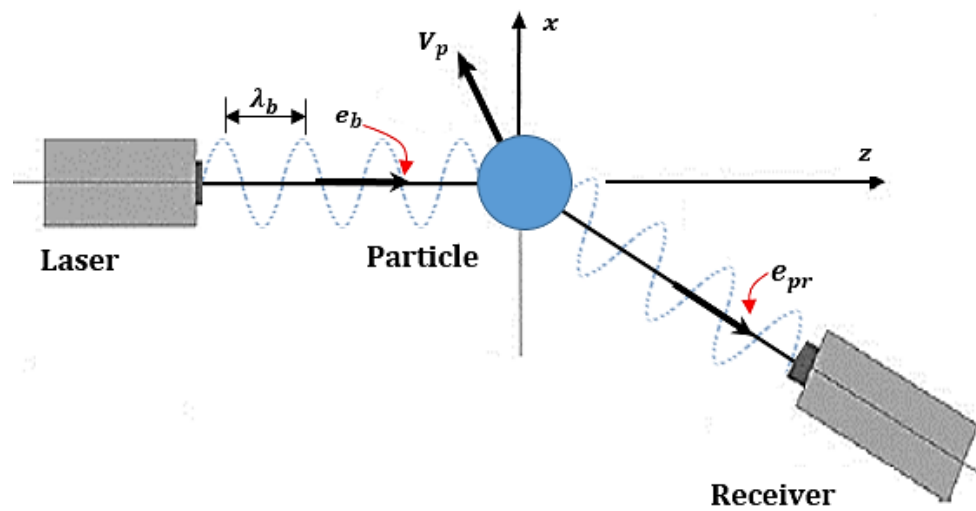
Fig 5-23: Explanation as to how the Doppler effect is used to measure velocity in the laser Doppler technique [130].
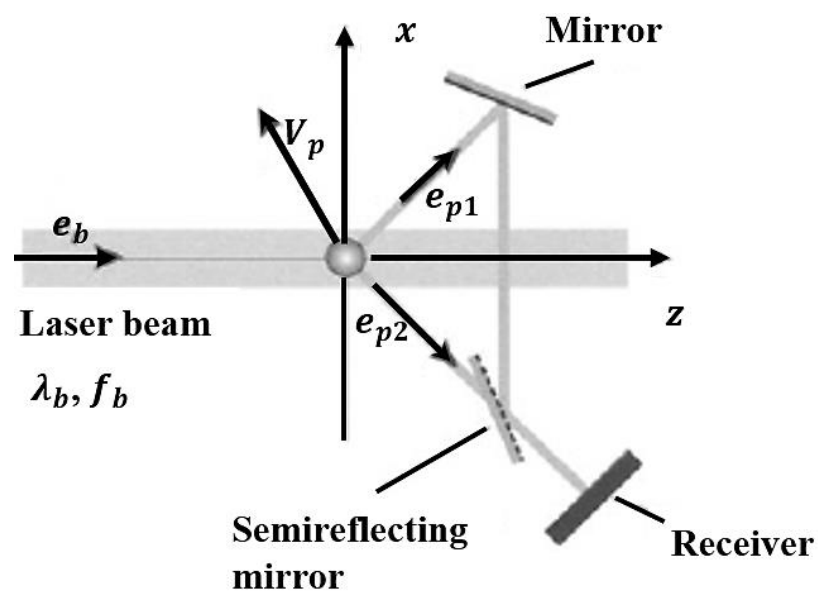
Fig 5-24: Optical configuration of dual-beam scattering of a single incident beam [130].

5.4   Data collection

Free vibration-based conditions were used to determine the performance of the materials in the experimental work. In this study, the first three modes for each sample were collected by laser vibrometers along the lengths of the laminated structures, as shown in Fig 5-25

In terms of calculating the mode shape, an experimental modal analysis with the samples in a fixed-free cantilever plate configurations were used. The samples were excited with a broadband white noise signal delivered via an electrodynamic shaker at the fixed end. The input signal was quantified with a force gauge, through which the force was applied, and the response signal was measured using a scanning laser Doppler vibrometer. The frequency response function (FRF) for each point was exported, and the displacement of each node from the natural frequency was reported via Excel. Natural frequencies were assumed to be the peaks in the FRF.
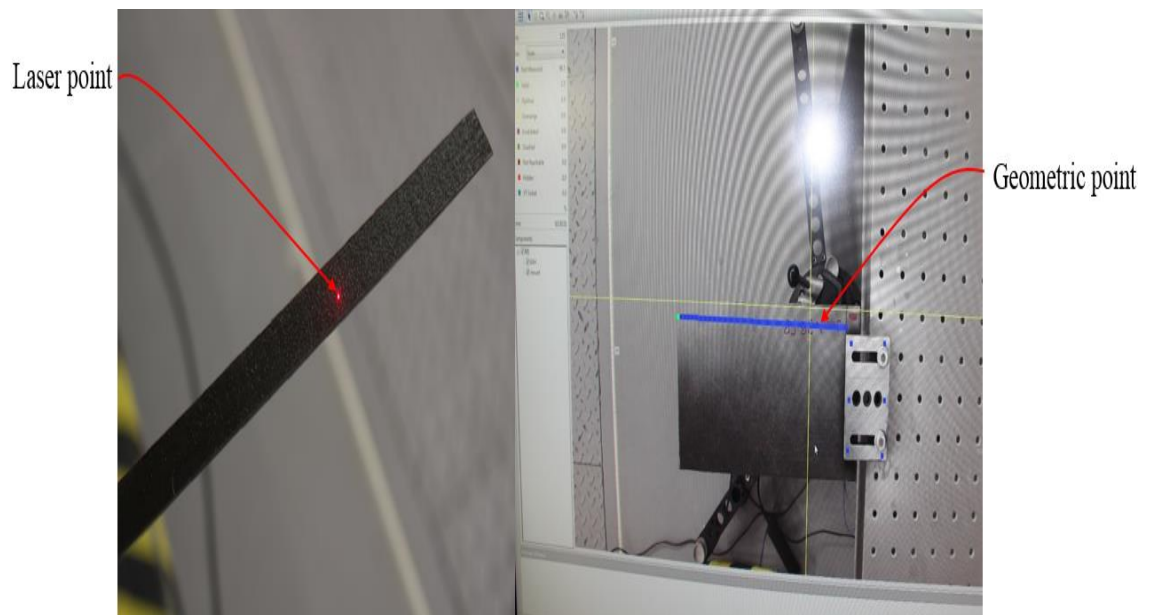
Fig 5-25: Laser geometric points used to measure the modal characteristics.

5.5 Conclusion

This chapter describers the experimental procedures utilized in preparing and measuring the dynamic response of laminated composite plate structures. The principles of using a laser vibrometer (LDV) and its advantages are also briefly described. Furthermore, the practical steps utilised to manufacture the composite samples are explained. Curing of carbon-epoxy fibre to produce the laminated plate structures of the required dimensions was illustrated in this chapter. Narrow plates, and two types of laminated plates, A and B, including intact and damaged samples were prepared to being tested in experimental work. Procedures for creating artificial and impact damage were demonstrated. The setup of the cantilevered laminated samples under free vibration conditions were explained and the principles of the Doppler effect were discussed. Finally, calculating the mode shape using laser vibrometer scanning techniques was illustrated.

Chapter 6: FEA damage detection of laminated composite plates

6.1 Introduction

This chapter presents the finite element analysis of damage detection in laminated carbon fibre-reinforced polymer (CFRP) plate structures using vibration-based damage detection techniques. A detailed discussion for delamination and fibre breakage analysis was presented. Also in this chapter, laminated plates with and without damage are simulated using ABAQUS software (version 6.14-1). The first two mode shapes were calculated and analysed to show the effect of damaged areas on the dynamic signals. One of the novelty points in this research is that the irregularity of curvature was calculated to quantify the damaged areas. Narrow laminated plates in addition to two styles of eight-layer A and B plates were analysed in this chapter. The comparison between fibre breakage and delamination have not been previously reported to the best of our knowledge.

6.2 Shell finite elements

This section explains the principles of sell finite elements used by finite element software programs to simulate thin plate structures. According to the terminology of plate structures, a plate is a thin, flat, structural element. Within this topic/structure, thin refers to the ratio of transverse dimensions (thickness) and are smaller than the minimum length or width of plate. If it is assumed that t is the plate thickness and L it's smallest lateral dimension (either length or width), then thickness can be described as L/t, and demonstrated as in Table 6-1.

Table 6-1: Classification of plate structure according to its thickness

Plate thickness	L/t
Very thin	> 100
Moderately thin	$20 - 100$
Thick	$3 - 20$

For this, the classical theory can be applied to analyse both very thin and moderately thin structures [131].

Using finite element analysis, flat shell elements are used to represent thin plate structures. These type of shell elements can be either triangles or quadrilaterals. A flat element is based on the combination of the plate membrane element (plane stress) and plate element (bending), as shown in Fig 6-1. As illustrated by Fig 6-2 each node in flat shell element has five degrees of freedom, the plate element has three degrees of freedom, while the plane stress elements has two degrees. Within this figure $\widetilde{u_1}$ is the displacement component, $\widetilde{\beta_1}$ is the component of rotational displacement, and $\widetilde{e_1}$ is the local base vector along the 1-axis.

As discussed, flat shell elements can efficiently model thin structures, for example the cylindrical shell seen in Fig 6-3. This only requires a quarter of the sample and can be modelled according to the symmetry condition. The mesh size can significantly affect the accuracy of results, ie. Increasing the quantity of flat elements significantly improves quality of surface approximation.
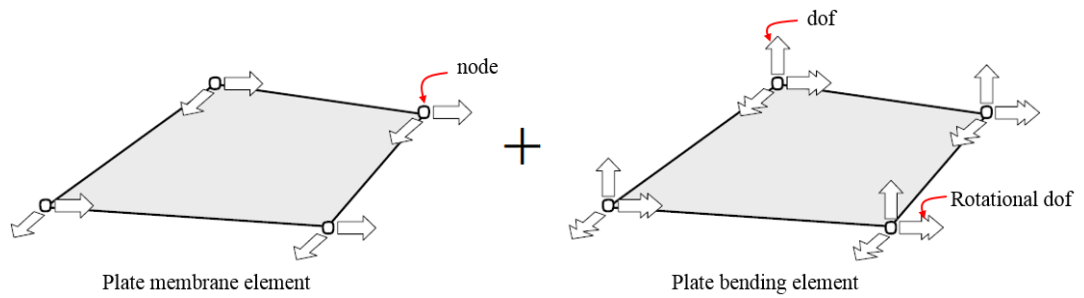
Fig 6-1: A flat element used to represent thin plate structures [131].
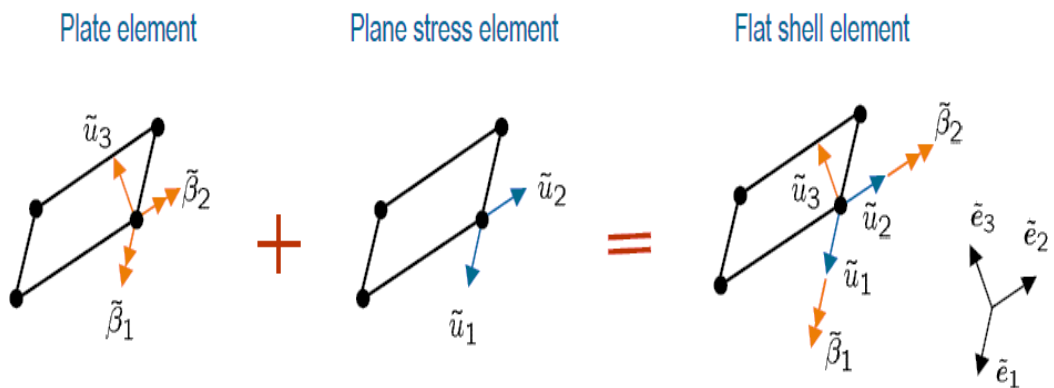
Fig 6-2: Degrees of freedom for each node in the flat shell element [131].
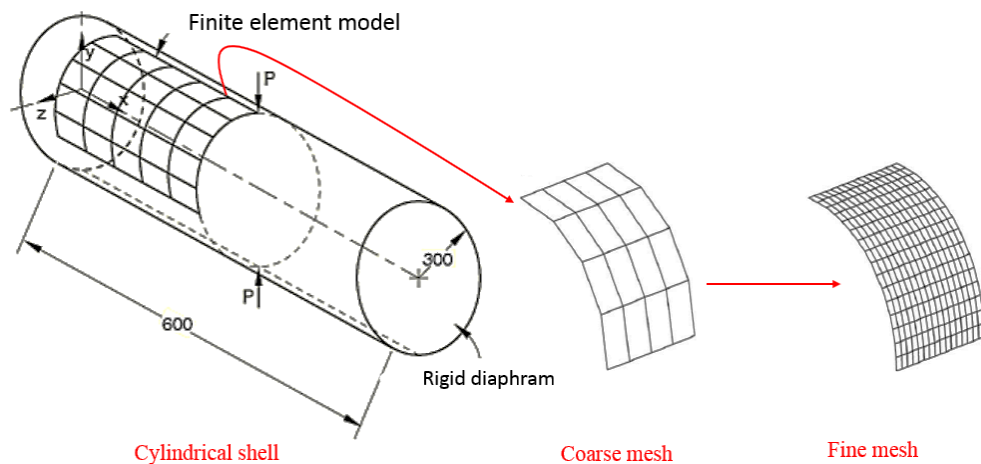
Fig 6-3: Schematic of modelling the cylindrical shell using flat shell element with two coarse and fin mesh [131].

According to the above paragraphs, to model the laminated composite materials, 3D shell-planar (supported by ABAQUS) was used. In this scenario, both narrow and plate structures are considered moderately thin because for both $\frac{L}{t} > 20$, where L is width of plates and t is their thickness. As illustrated in Fig 6-4, flat shell element was used to simulate the intact and damaged (fibre breakage and delamination) laminated

plates. Then, using the shell-planar (mentioned previously) the intact plates are simulated, applying the mechanical properties of carbon fibre reinforced polymer (CFRP) to each layer (each layer may have different orientation). The two modes of breakage were modelled differently. Fibre breakage was modelled by applying the mechanical properties of an epoxy matrix to the top layer in the damage section. For delamination, the mechanical properties of the release film were applied to a thin layer (15 μm) to spread the top layers as demonstrated in Fig 6-4, this will discussed in detail in the next section.
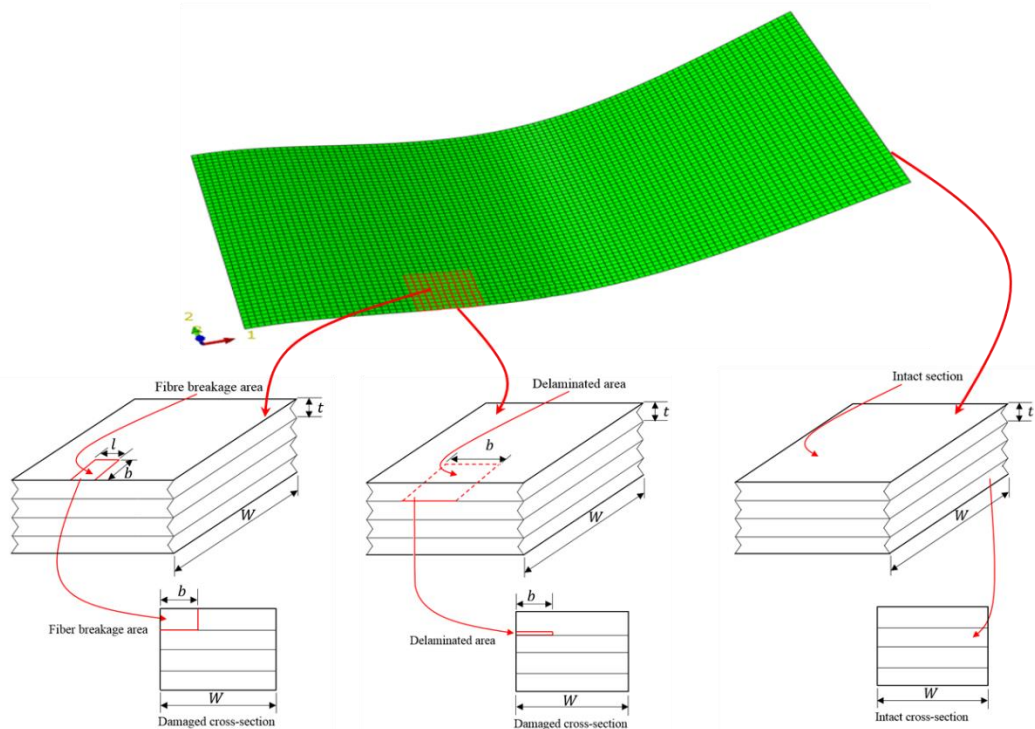
Fig 6-4: Finite element model of laminated palate (as in ABAQUS), with the intact and damaged sections, FB is modelled by applying the mechanical properties to the top layer in the damaged section, whilst delamination is achieved by applying the mechanical properties of the release film to a thin layer between the top two layers in the damaged section.

6.3   Finite Element Model of Laminated Plate Structures

Finite element ABAQUS 6.14-1 software was used to simulate the laminated plate samples. Narrow plate structures in four symmetric layers were modelled using the same dimensions given in section 5.2.2. In this structure, the mechanical properties of the high modulus CFRP M55J unidirectional prepreg provided by the Cytec group were utilized to perform the FE analysis, as shown in Table 6-2. These properties were used to model both the intact and damaged laminated plates by representing the mechanical properties for each lamina. The same dimensions shown in Fig 5-5 are used in the FE analysis to model the intact plate. The delaminated area is modelled by applying the mechanical properties of R250 unperforated release film supplied by Easy Composites Company, as shown in Table 6-3. A thin layer of 15 μm, as shown in Fig 6-5, was added to the damaged section in the FE analysis and is located between the top two layers, while fibre breakage was modelled by adding the mechanical properties of epoxy shown in Table 6-4 to the damaged area on the top surface with the same dimensions seen in Fig 6-6. All models were simulated to match the manufactured samples used in the experiment work (chapter 7).

In ABAQUS software, the 3D-deformable shell was used to model the laminated plates. The procedures of modelling these plates explain as following:

1. Select 3D-deformable shell to create the required dimensions

2. Insert mechanical properties to the model

3. Select shell, then composite section to insert the required layers

4. Section assignment to define the model

5. Select the frequency step to calculate frequency and mode shape

6. Define boundary conditions using load button

7. Add mesh to the model

8. Set up and run a job

9. Finally, select visualization for the calculated results

As demonstrated in Fig 6-7, the second mode is shown with the mesh structure of damaged section. In this study, the sensitivity of the mesh was tested until the calculated results became stable, as per Fig 6-8. A standard linear quad. shell element mesh type with 0.005 m element size was used in the numerical model. The narrow cantilevered

laminated plate was analysed under free vibration conditions. The first two modes are calculated to obtain the dynamic analysis.
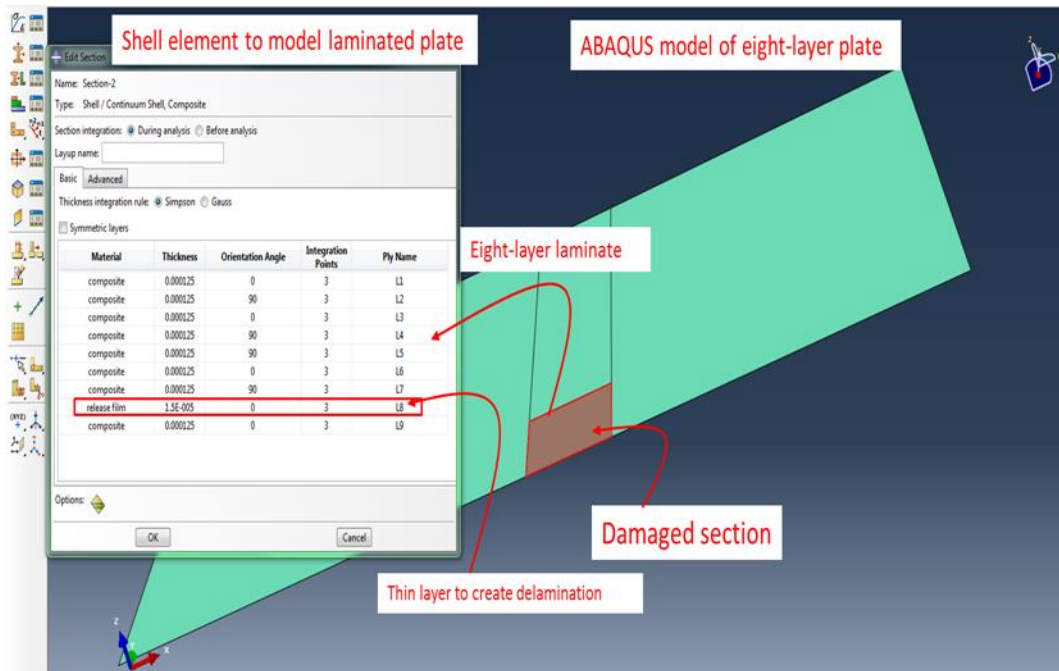
Fig 6-5: ABAQUS model shows modelling of eight-layer laminated plate at different orientations, delamination was simulated by applying a thin layer (layer 8) with mechanical properties of unperforated release film.
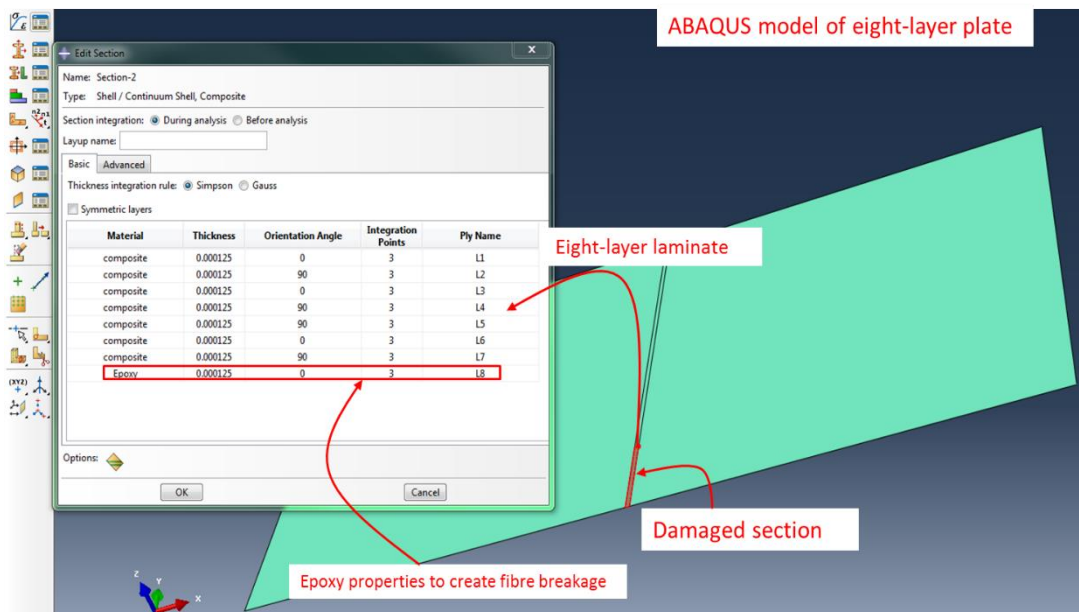
Fig 6-6: ABAQUS model shows modelling of eight-layer laminated plate at different orientations, fibre breakage was simulated by applying the mechanical properties of epoxy to layer 8.

Table 6-2: Mechanical properties of the composite M55J carbon fibre reinforced polymer/ epoxy used in FE analysis.

Tensile modulus 0° E_1 (GPa)	300
Tensile modulus 90° E_2 (GPa)	12
In-plane shear modulus G_{12} (GPa)	5
Density ρ $\left(\frac{kg}{m^3}\right)$	1650
Major Poisson's ratio (ϑ_{12})	0.3
Fibre volume V_f	60 %
Cured temperature	180^0

Table 6-3: Mechanical properties of unperforated film used to create delamination supplied by Easy Composites.

Young's modulus (GPa)	Density $\left(\frac{kg}{m^3}\right)$	Poisson's ratio (ϑ)
0.65	1733.3	0.3

Table 6-4: Mechanical properties of resin epoxy.

Young's modulus (GPa)	Density $\left(\frac{kg}{m^3}\right)$	Poisson's ratio (ϑ)
3.4	1170	0.36
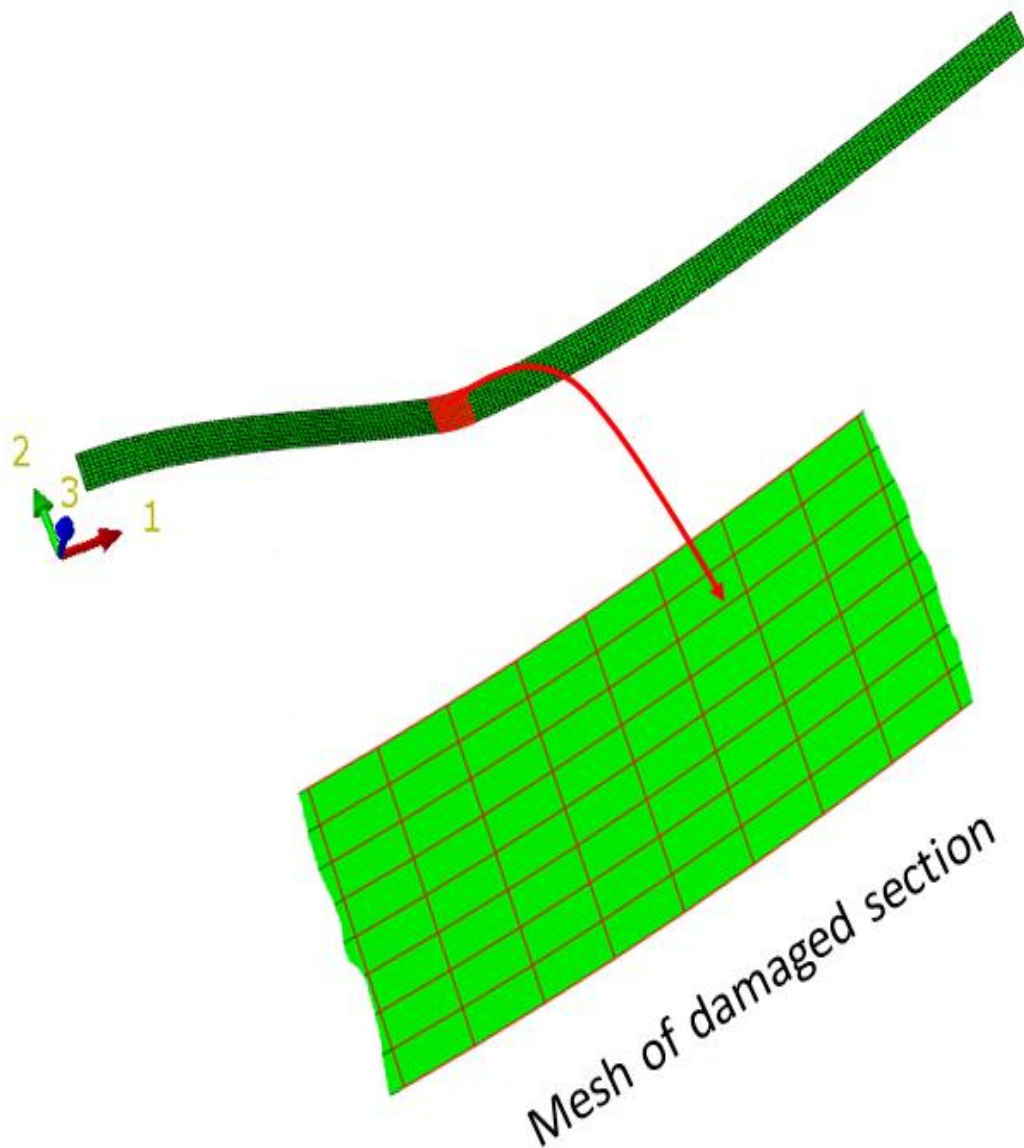
Fig 6-7: The second mode shape and mesh of the damaged section within the four-layer narrow cantilever laminated plates as determined by ABAQUS software.
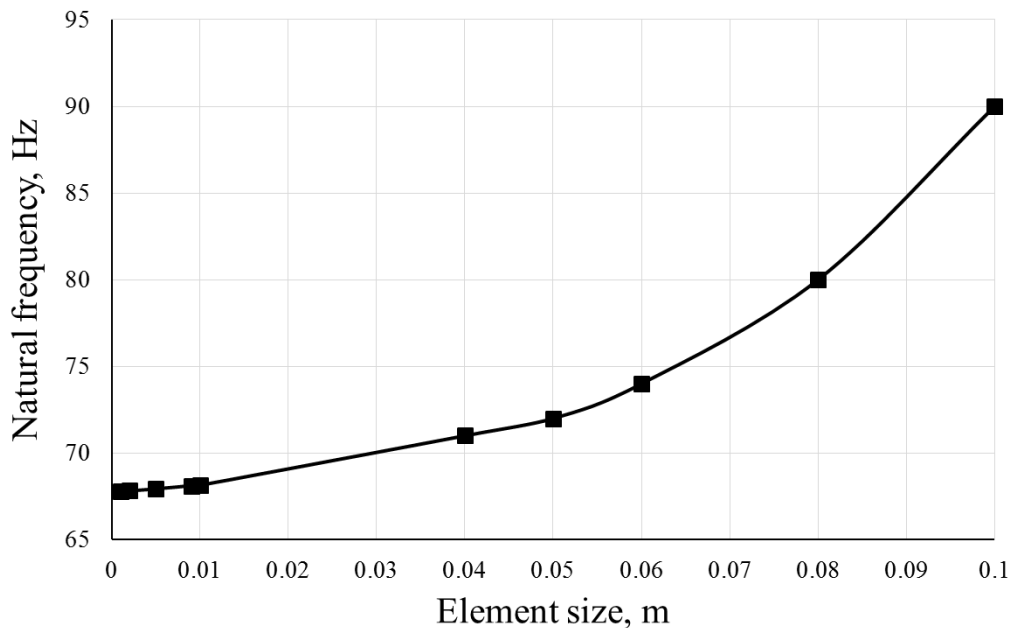
Fig 6-8: Mesh sensitivity was tested for the second mode of the narrow laminated plate. There was no significant change in natural frequency with element sizes less than 0.005 m.

Models of A and B plate sets followed the same numerical steps used to model the narrow plate models in the previous paragraph. The 3D deformable shell in ABAQUS was selected to model the cantilever plate structures, as per Fig 6-9. The same dimensions discussed in section 5.2.3.1, are employed to perform the numerical analysis. The mechanical properties of M55J, as given in Table 6-2, were used in FE analysis. The intact plate is simulated with eight layers and the dimensions identical to those shown in Fig 5-12. Whereas, the mechanical properties of M55J were used as lamina properties. The same concept illustrated in the narrow plates is utilized to model the delamination, where the schematic diagram shown in Fig 5-13 is simulated in ABAQUS. The mechanical properties of the release film were used for the thin layer between the top two layers through the damaged section. Furthermore, fibre breakage was modelled according to the same criteria explained previously with narrow plates. It is accomplished by applying the epoxy properties to the top layer through the damaged section with the same dimensions explained in Fig 5-14 . In terms of the mesh, the standard shell element free medial axis mesh type with an element size of 0.002 m was used. The free vibration condition was selected to analyse the intact and damaged models. To ensure the convergence in the calculated results, the mesh sensitivity was

computed as per Fig 6-10 . According to this figure there is no significant change in the second natural frequency lower than element size 0.002 m. This ensure the viability of this value to mesh these models.
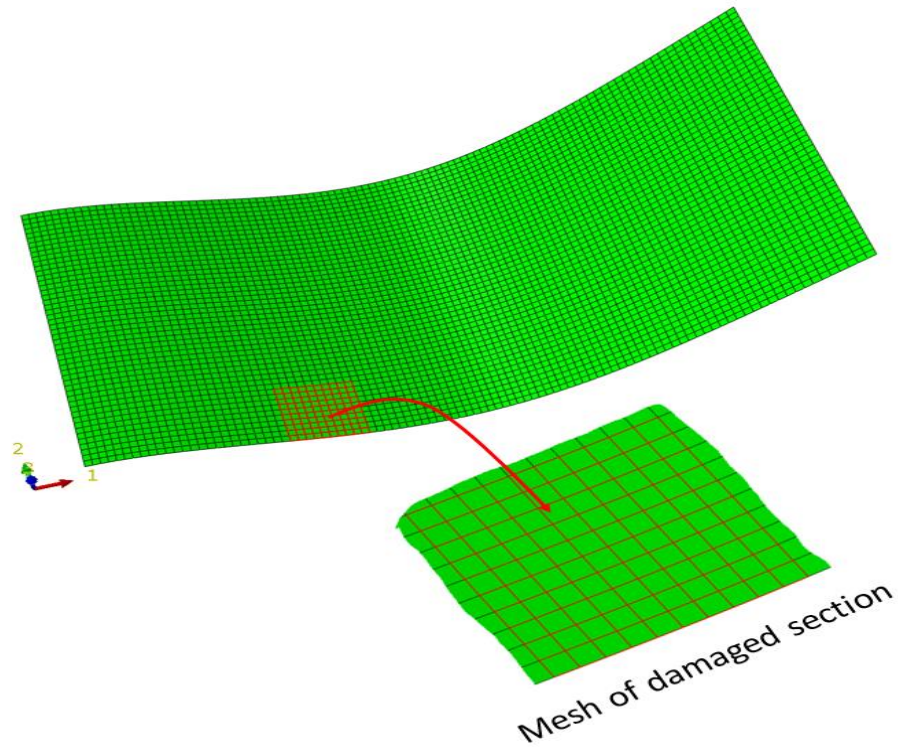
Fig 6-9: The second mode shape of the eight-layer cantilever laminated plates as determined by ABAQUS software.
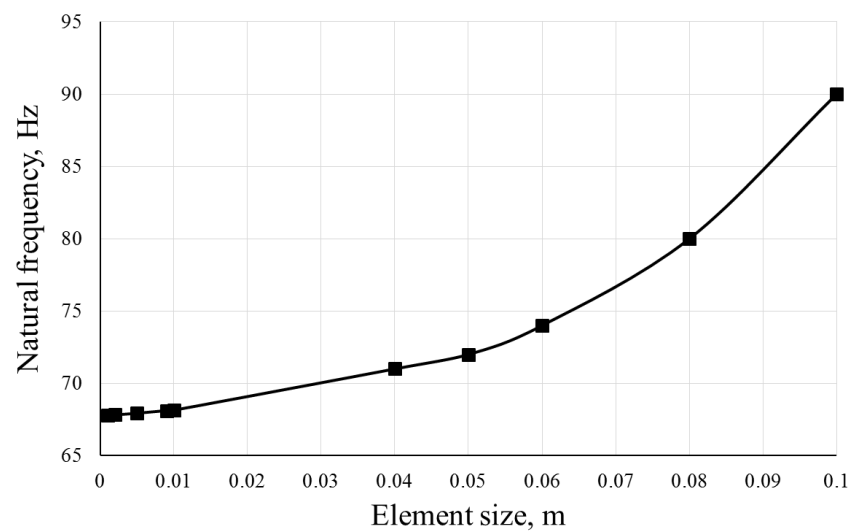
Fig 6-10: Mesh sensitivity was tested for the second mode of laminated composite plate A. There was no significant change in natural frequency with an element size less than 0.002 m.

6.4 Methodology of damage detection in laminated plates

The numerical models discussed in section 6.2 analysed under free vibration conditions. The first two intact and damaged modes of the four-layer narrow and eight-layer laminated plates were calculated. In this chapter, the novel point was to develop the curvature index as a vibration-based damage technique to detect delamination and fibre breakage in laminated composite structures. The curvature index written in Eq.(4.2) was evaluated (chapter 4) as a sensitive index to detect the damaged areas. With laminated plate structures and due to the high strength of these structures, damage detection is expected to be not an easy task. Thus, the curvature was improved by calculating the irregularity curvature index, as can be seen in Eq.(6.1) to be efficient in damage detection purpose. The Irregularity index represents the square difference between the damaged and intact modes, where $\left(\emptyset_{ji}''\right)_H$ is the intact curvature index and $\left(\emptyset_{ji}''\right)_D$ the damaged one. This formula (Eq.(6.1)) has not been reported before.

$$Irregularity\ Index\ (R^2) = \left(\left(\emptyset_{ji}''\right)_D - \left(\emptyset_{ji}''\right)_H\right)^2 \qquad (6.1)$$

6.5 FEA results and discussion of narrow laminated plates

It is important to mention that damage in any structure causes reduction in local stiffness. In this study delamination and fibre breakage reduce the local stiffness at different amounts. This reduction depends on the type of damage and fibre orientations in each lamina through laminated thickness. To start the dynamic analysis of narrow plates, the intact and damaged normalised second mode shapes were calculated as shown in Fig 6-11. It was clear from this figure that there is no significant difference between the intact and delaminated normalised second modes (delamination located at 0.1 m). During calculation, the second mode with fibre breakage showed much more local distribution associated with fibre breakage location (0.1 m). In terms of numerical value, the amplitude of intact and delaminated modes is -0.8, while in fibre breakage is -1. This explains the relationship between physical properties and modal characteristics, where higher stiffness reduction leads to higher amplitude mode shape.

To improve the identification of damaged areas in these structures, the curvature index was calculated. As per Fig 6-12, the curvature index shows a fluctuated profile even when calculated for fibre breakage (the severest damage in laminated structure). The maximum value for this index found is 3.7 at L_1 (location of damaged area), but it is expected to be not effective in practical applications due to the noise effect. The insufficiency of the curvature index suggests further development of this technique is needed. The irregularity index mentioned above was employed to assess the damaged areas. As demonstrated by Fig 6-13 that modelling fibre breakage on the top surface at L_1 can be predicted via the sudden jump in the irregularity index. The main reason for this sudden change is the larger reduction in local stiffness due to fibre breakage, which can affect the calculated mode shape. Mathematically, the irregularity index represents the relationship between the adjacent points along the curve. In other words, the irregularity index can detect any change between neighbouring points along the curve. Fig 6-14 shows the irregularity index of the delaminated area (delamination sets between the top two layers) at L_1 in the narrow plate. The clear flat peak of irregularity index precisely indicates the location of delamination. Numerically, the irregularity index with fibre breakage shows a sharp peak and higher magnitude, while delamination is much lower than the FB damage index magnitude and has a flat peak. For FB, the peak value is 13, and 4.8 for delamination. Also, in FB the irregularity index jumps sharply to hit the peak, while in Del case this increasing observed in two steps. Which means the magnitude and the shape of the irregularity index can be an indicator for damage type. In brief, mode shape and its curvature cannot detect delamination and fibre breakage sufficiently on their own; whilst calculating the irregularity index was shown as a trustworthy method to detect these damages in plate structures.
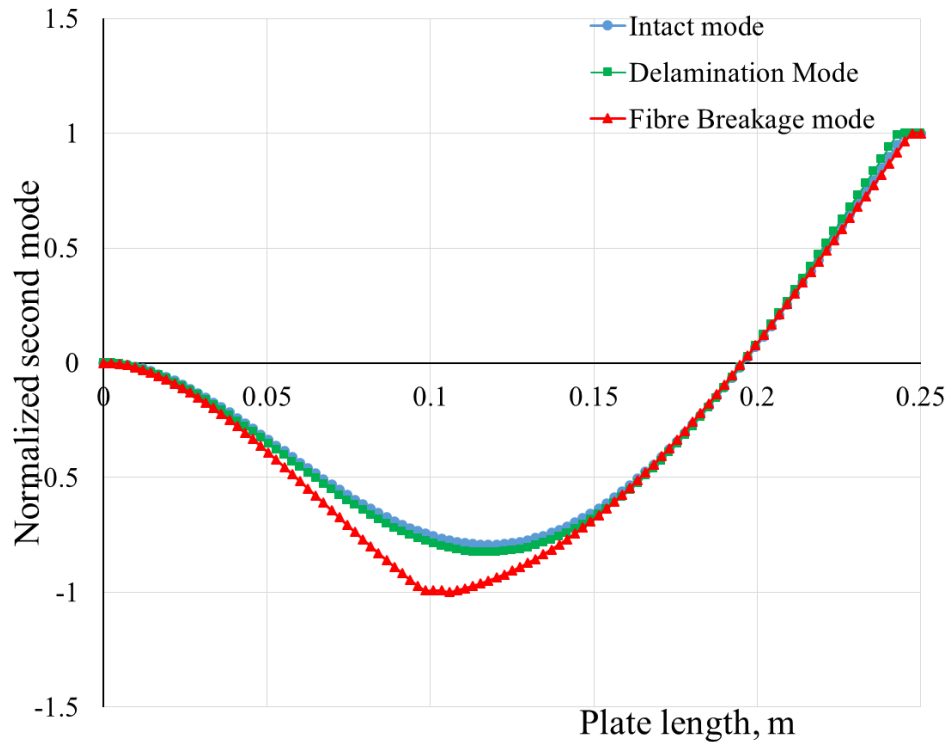
Fig 6-11: Numerical intact and damaged second modes for the four-layer narrow laminated plate, with delamination and fibre breakage located at 0.1 m from the fixed end. There is no visible change between the intact and delamination modes due to the small reduction in stiffness, and damage is not shown.
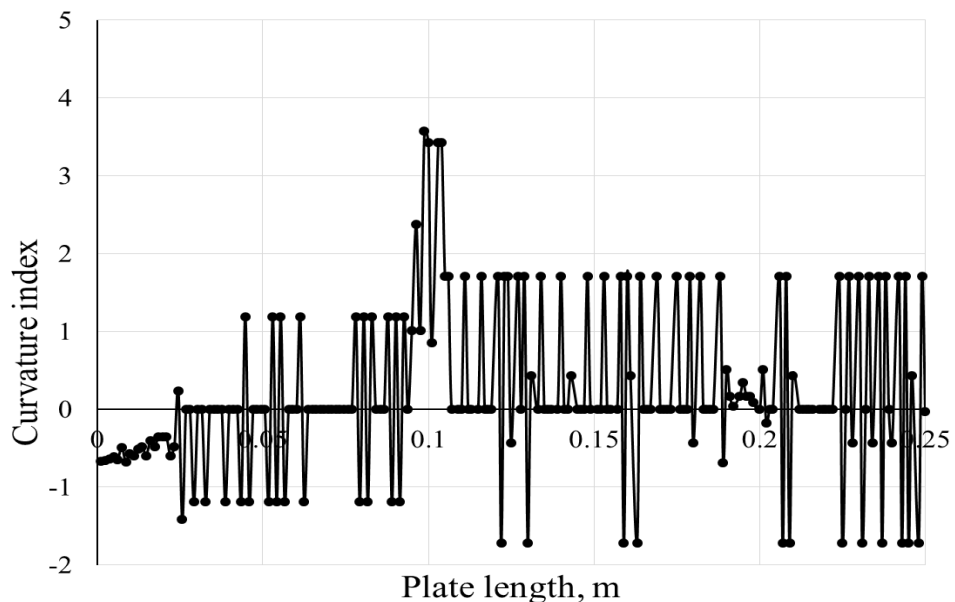
Fig 6-12: Numerical curvature index of the second mode for the narrow laminated plate, fibre breakage at 0.1 m. The curvature does not show the damaged area.
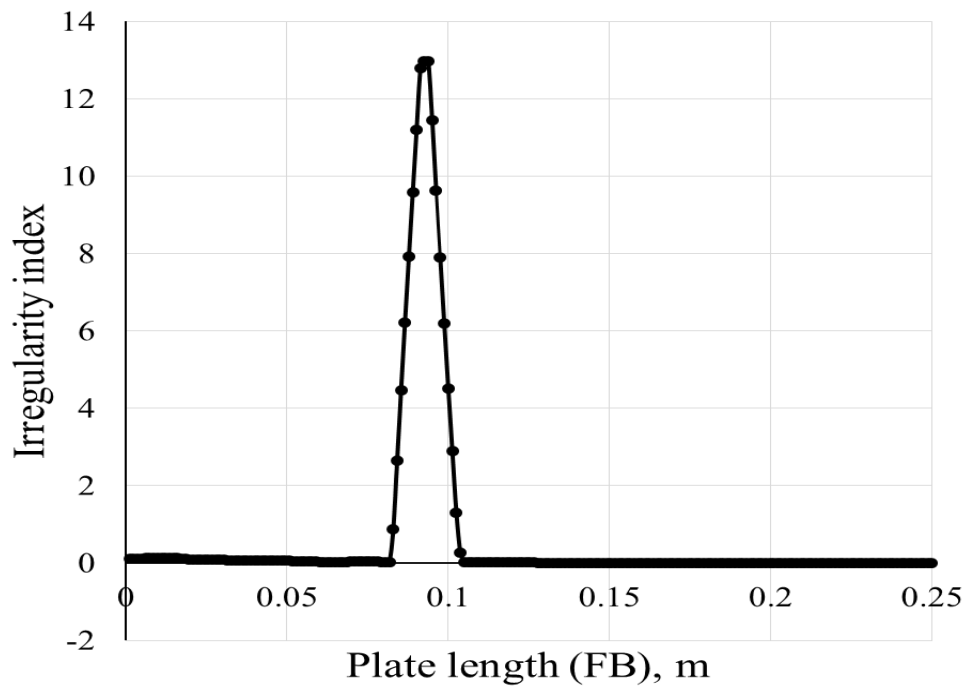
Fig 6-13: Numerical irregularity index for the second mode of the narrow laminated plate, fibre breakage at 0.1 m. The sharp peak shows the damaged section.
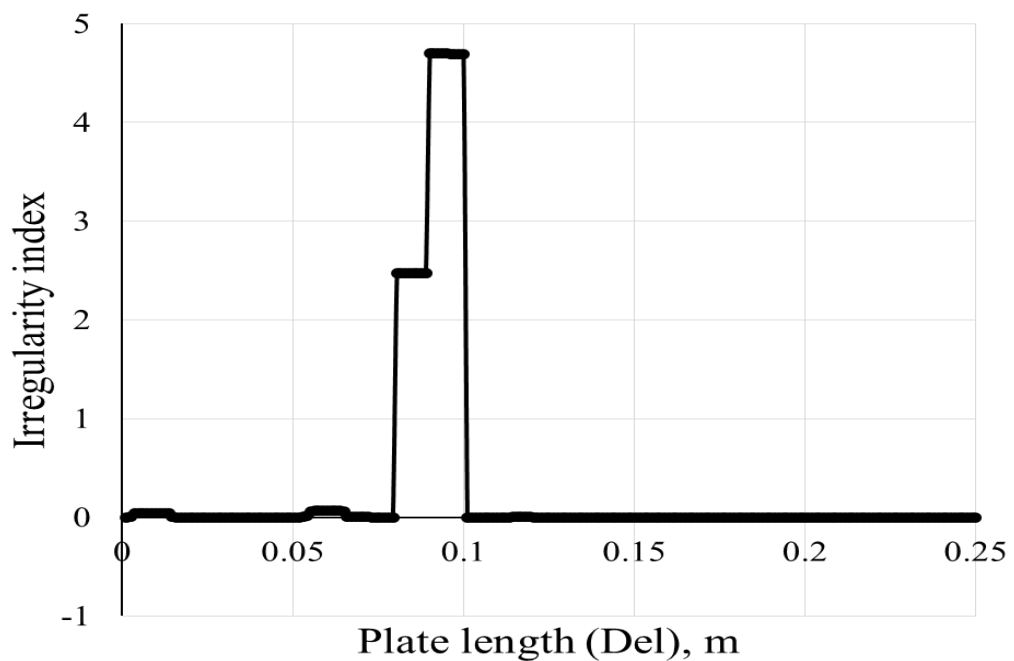
Fig 6-14: Numerical irregularity index of second mode for the narrow laminated plate, delamination at 0.1 m. The flat peak shows the damaged section.

6.6   FEA results and discussion of eight-layer laminated plates

The plate structures discussed in section 5.2.3.1 were used to study the damage detection. Two lay-up sequences, A and B, are utilised to determine if there is any difference between the analysis of intact and damaged dynamic signals for these structures. Mode shape, curvature, and the irregularity index were calculated as a part of damage identification process.

The modelling part achieved using ABAQUS software, where the delamination and fibre breakage are simulated as two types of damage in laminated structures. The same narrow plate analysis procedures were employed to quantify these damages in both styles A and B. Calculating the normalized second intact and damaged modes do not show the damaged sections. As seen in Fig 6-15, although delamination and fibre breakages are modelled at 0.1 m to the fixed edge, there is no that divergence in the mode shape amplitude. The intact amplitude at 0.1 m is - 0.8 and - 0.85 for Del and FB respectively. Which means reduction in local stiffness is not shown by mode shape. In the same regards, calculating curvature index in plate structures still do not provide the solution to quantify the damaged sections. It is obvious from Fig 6-16 that there is no difference between the amplitude of intact and delaminated curvatures at maximum value, approximately 420 at 0.1 m. This suggests no or small change in the local stiffness, which cannot be detected easily. A small jump can be seen in the curvature with fibre breakage, as seen in the red curve. This spike is associated with the damaged section (FB at 0.1 m), but it is expected to be not valid in the real applications with noisy environment.

The irregularity index again was computed to assess the damaged areas in these structures. In style A Fig 6-17 clearly shows a sharp peak completely at the fibre breakage area at 0.1 m, while the flat peak seen in Fig 6-18 suggests the existence of the delaminated area. In those two figures Del and FB can be clearly detected. Further, the reduction in stiffness caused by fibre breakage has a mathematical explanation, where losing fibres means higher reduction in local stiffness [within laminated structures, Young's modulus of fibre is the main parameter in calculating the laminate stiffness]. This can explain the higher effect of FB which is seen in the irregularity index. Furthermore, there is a difference between Del and FB, where FB has sharper and

higher peak than Del. The magnitude of FB is 0.23 while Del is 0.14. In both FB and Del irregularity indexes had sharp increasing close the damaged area (increasing in Del starts early, because the width of delaminated area is greater than FB).The same criteria are applied to style B, as seen in Fig 6-19 and Fig 6-20, where the irregularity index behaves in a similar manner to style A with an obvious variation in the shape and magnitude. However, the only difference between them is that the peak in both FB and Del for style B is higher than the peak of same damage in style A, where the peak magnitudes are 6.5 FB and 0.65 for Del. This is because style B has higher stiffness than style A.
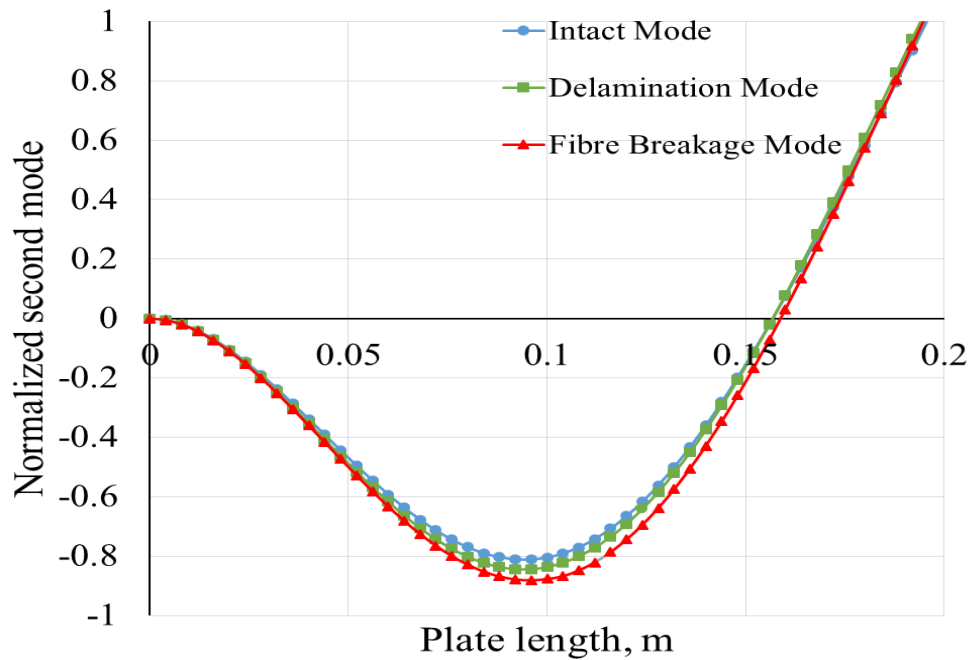
Fig 6-15: Numerical intact and damaged second modes for the laminated plate A, with delamination and fibre breakage located at 0.1 m from the fixed end. There is no visible difference between the intact and damaged modes and damage cannot be localized.
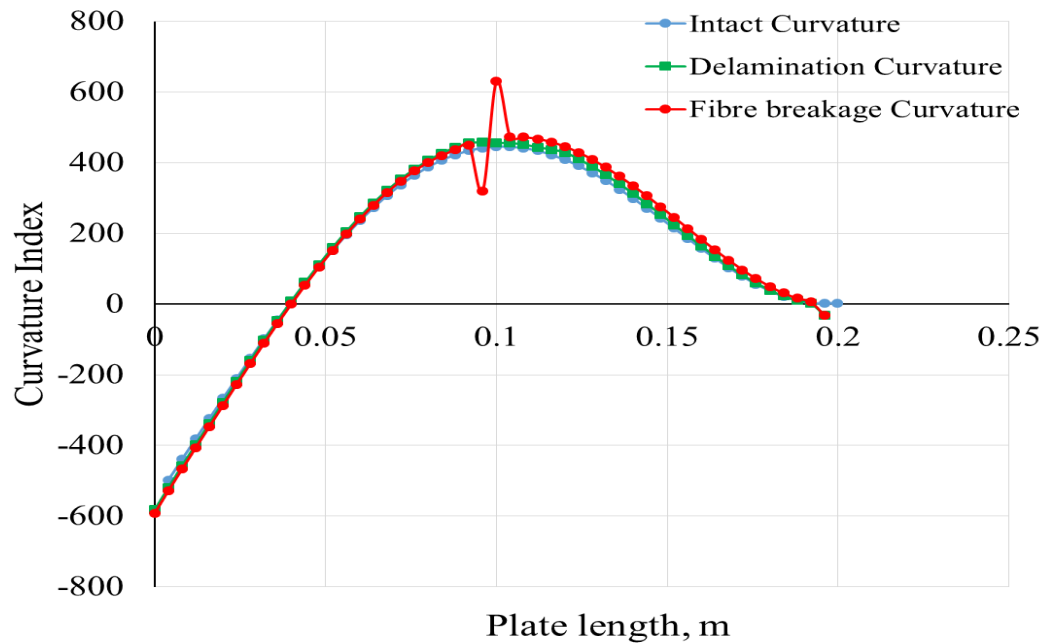
Fig 6-16: Numerical curvature index for intact and damaged second modes for laminated plate A, where delamination and fibre breakage are located 0.1 m from the fixed end. The damaged area is still unpredictable, although there is a little change in the curve for the fibre breakage mode in the relevant location.
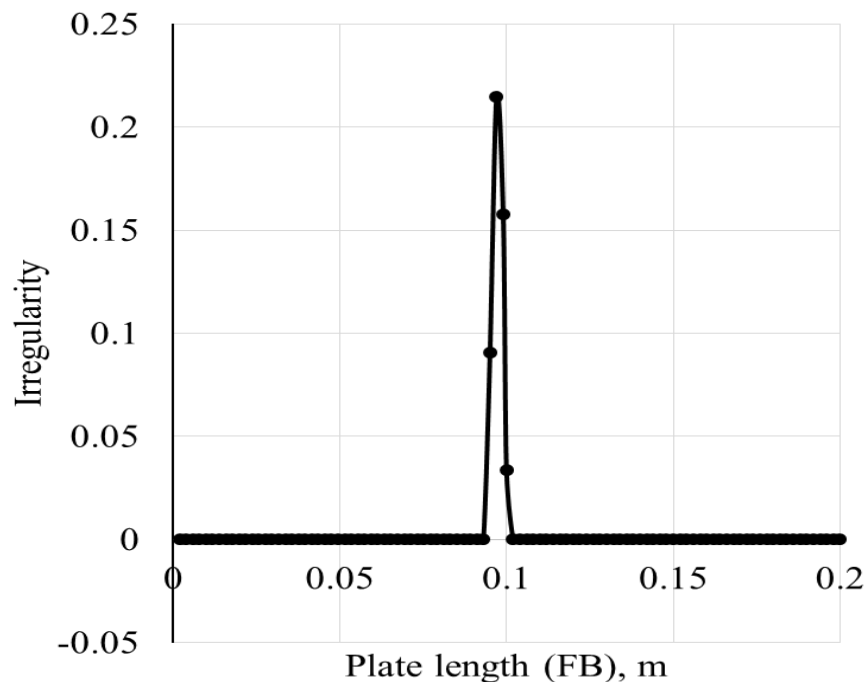
Fig 6-17: Numerical irregularity index for fibre breakage 0.1 m from the fixed end of laminated plate A. The sharp peak with the high magnitude can be consider an indicator of damaged sections.
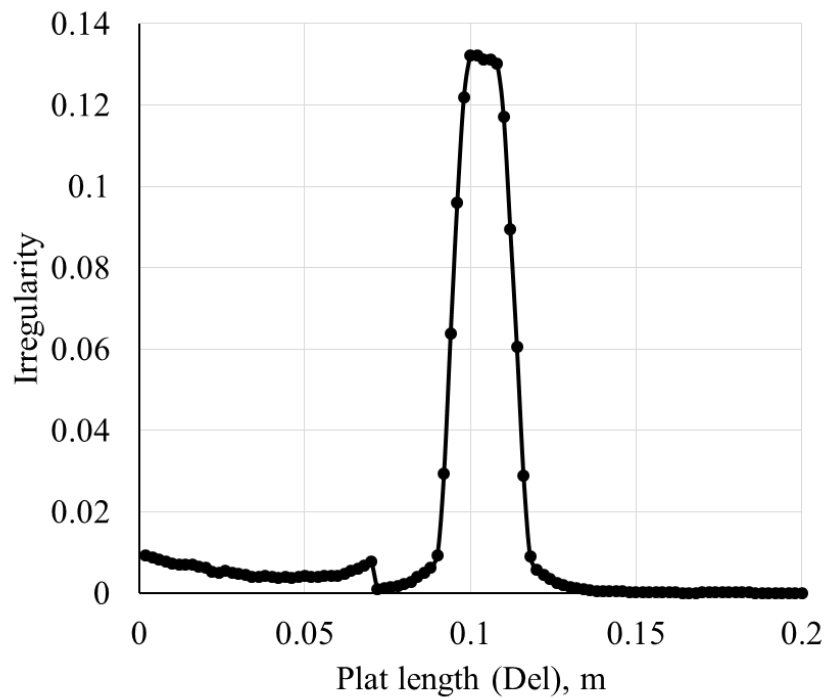
Fig 6-18: Numerical irregularity index of delamination 0.1 m from the fixed end of laminated plate A. The flat peak confirms that damage is not severe.
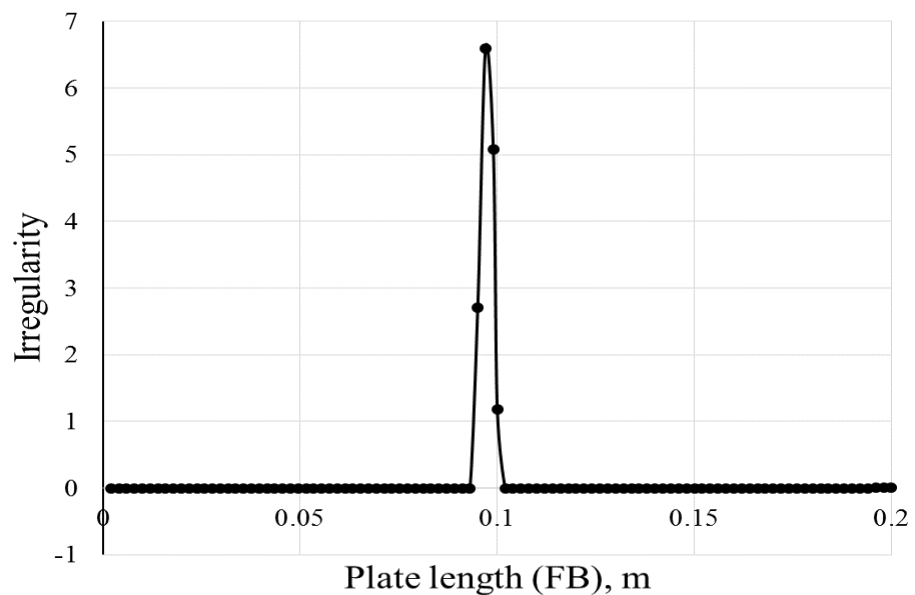
Fig 6-19: Numerical irregularity index of fibre breakage 0.1 m from the fixed end of laminated plate B. The sharp peak with the high magnitude indicates the location of the damaged sections.
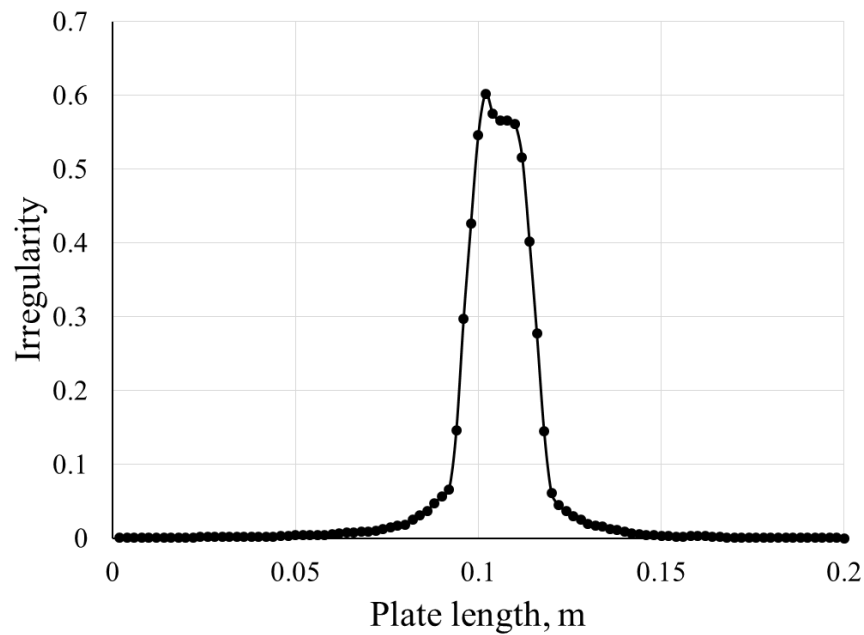
Fig 6-20: Numerical irregularity index for delamination 0.1m from the fixed end of laminated plate B. The flat peak confirms that damage is not severe.

6.7 Summary

To summarise, this chapter has shown the numerical damage detection analysis of laminated CFRP composite plate structures using vibration-based damage detection techniques. Two types of narrow and laminated plates were used in this study. The narrow plates consist of four symmetric layers, while the other samples consist of eight symmetric layers. The numerical analysis was completed using the ABAQUS 6.14-1 software to model both intact and damaged plates. Fibre breakage is modelled by using the mechanical properties of epoxy in the damage area while the mechanical properties of the release film is used to model in the delamination. In this analysis, the first two mode shapes were calculated. The second mode was used for detection purposes. The second conclusion in this chapter is that the damaged modes and curvature index do not detect the damaged sections. The improved irregularity curvature index provided a clear peak for both fibre breakage and delamination. Also, this index showed that fibre breakage has sharper and higher peaks than delamination in all these cases; the discrimination between FB and Del was the main point of this research. This difference occurs due to the considerably greater reduction in local stiffness due to fibre breakage than delamination.

Chapter 7: Experimental damage detection of laminated composite plates

7.1 Introduction

Damage detection in laminated carbon fibre-reinforced polymer (CFRP) plate structures based on experimental analysis is presented in this chapter. Vibration-based damage detection techniques are used to compare between delamination and fibre breakage. The experimental data are presented and explained for the intact and damaged laminated plate samples explained in chapter 5. The first three mode shapes were measured using laser Doppler vibrometer (LDV), where the second mode is analysed to detect the damaged areas. One of the novel points in this chapter calculating the Haar index using the MATLAB R2017$_a$ software. No previous comparison between these two types of damage has been reported to the best of our knowledge.

7.2 Calculating mode shape using laser Doppler vibrometer

This section presents the calculation of the bending modes for the vibrating laminated composite plates. Normally, modal testing or accelerometers are employed to measure the structural dynamic response which is exported and processed to determine the modal characteristics such as natural frequencies, damping and mode shapes of the vibrated objects. The laser Doppler vibrometer, as an optical instruments it can be used to measure the response data, of light weight samples such as composites. With the accessibility of real time scanning, a number of measurement possibilities become available [132].

To demonstrate the process of calculating mode shape, vibrating cantilever beam is assumed, as shown in Fig 7-1. If the structure is excited at one of its resonance frequency, (ω_b), then the formula of velocity distribution in the space-time domain can be written as per Eq.(7.1) [133],

$$v(x,t) = \emptyset(x)\,sin\,\omega_b t + \psi(x)\,sin\,\omega_b t \qquad (7.1)$$

where $\emptyset(x)$ and $\psi(x)$ are reciprocally orthogonal components of the vibrational velocity distribution. Within LDV scanning technique, structures such as beam or plate are supposed to be scanned under controlled way using a normalized scan function formula, as shown in Eq.(7.2),

$$x = \cos \omega_m t \qquad (7.2)$$

where ω_m is the scan rate. According to this, the response measured by LDV $V(t)$ at any time t, and position x can be formulated as per Eq.(7.3).

$$V(t) = \emptyset(\cos \omega_m t) \sin \omega_b t + \psi(\cos \omega_m t) \cos \omega_b t \qquad (7.3)$$

Both functional $\emptyset$ and ψ in the above equation are even and periodic according to assumption of Eq.(7.2).Thus, these quantities can be simplified in the Fourier cosine series as per Eq.(7.4) and Eq.(7.5).

$$\emptyset(\cos \omega_m t) = A_0 + \sum_{k=1}^{\infty} A_k \cos k\omega_m t \qquad (7.4)$$

$$\psi(\cos \omega_m t) = B_0 + \sum_{k=1}^{\infty} B_k \cos k\omega_m t \qquad (7.5)$$

Then, the velocity distribution $V(t)$ is

$$V(t) = \{ A_0 + \sum_{k=1}^{\infty} A_k \cos k\omega_m t\} \sin \omega_b t + \{ B_0 + \sum_{k=1}^{\infty} B_k \cos k\omega_m t\} \cos \omega_b t \qquad (7.6)$$

Eq.(7.6) can be written according to the trigonometric products as

$$V(t) = A_0 \sin \omega_b t + \sum_{k=1}^{\infty} \frac{A_k}{2} \sin(\omega_b + k\omega_m) t + \sum_{k=1}^{\infty} \frac{A_k}{2} \sin(\omega_b - k\omega_m) t + B_0 \cos \omega_b t + \sum_{k=1}^{\infty} \frac{B_k}{2} \cos(\omega_b + k\omega_m) t + B_0 \cos \omega_b t + \sum_{k=1}^{\infty} \frac{B_k}{2} \cos(\omega_b - k\omega_m) t \qquad (7.7)$$

Using the definition of the Chebyshev polynomials T_k which is

$$T_k = \cos(k \cos^{-1}x)$$

Equations (7.4) and (7.5) can be written as

$$\emptyset(x) = A_0 + \sum_{k=1}^{\infty} A_k \; cos \; (k \; cos^{-1}x) \qquad (7.8)$$

$$\psi(x) = B_0 + \sum_{k=1}^{\infty} B_k \; cos \; (k \; cos^{-1}x) \qquad (7.9)$$

It is clear that equations (7.8) and (7.9) represent the expansion of Chebyshev series for $\emptyset(x)$ and $\psi(x)$. A_k and B_k are the coefficients for these series. As demonstrated in Fig 7-2, the frequency at each point along the vibrated beam has two components. According to the above equations, mode shape can be calculated for any frequency. As an example, theoretical and experimental normalized second mode for the cantilever beam is calculated, as shown in Fig 7-3.

The same principle is used in the current research to perform the calculation of the experimental mode shapes, where the LDV was used to measure the frequency response function (FRF) for all samples, then the measured data were processed to calculate the vibrational modes of the laminated CFRP plates.
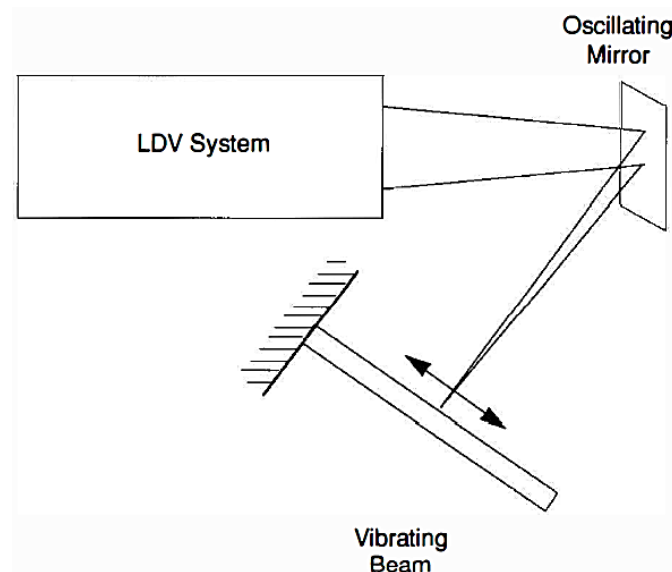
Fig 7-1: Schematic of LDV scanning [133].
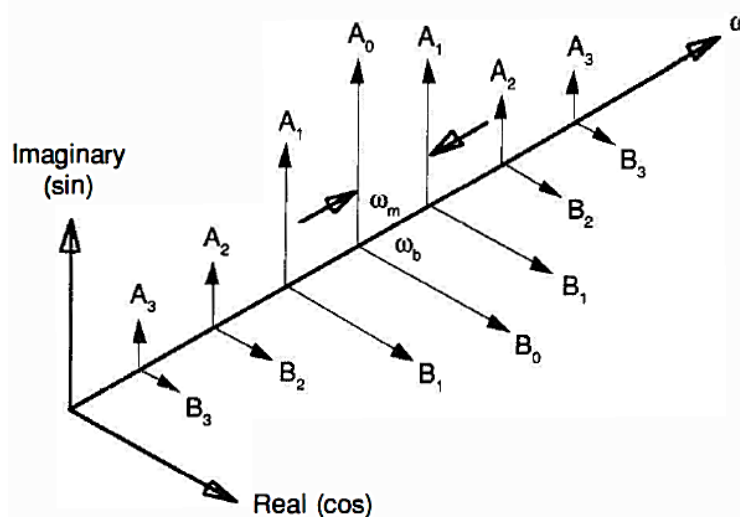
Fig 7-2: Frequency components of signal measured by LDV [133].
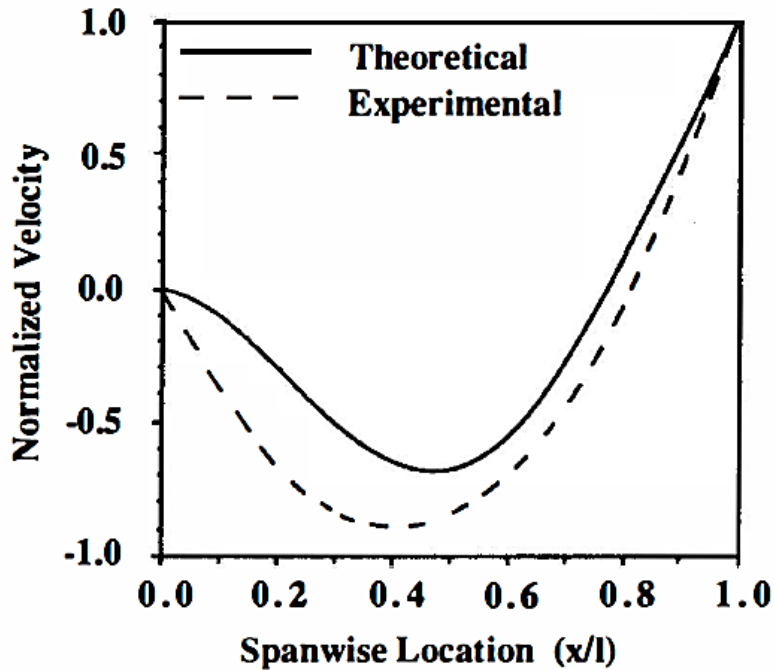
Fig 7-3: Experimental and theoretical second modes for vibrated beam reported in [133].

7.3   Application of wavelet transforms in damage detection

This section explains the use of wavelet analysis as a signal processing analysis technique to detect the damaged regions. Wavelets can be defined as a rapidly decaying wave oscillation with a zero average, originally studied by Alex Grossmann and Jean Morlet Alex Grossmann and Jean Morlet [134]. These wavelets may be in terms of real

or complex functions. Real wavelets are more successful than complex in the detection of sharp signals.

According to the principles of wavelet analysis, a basic wavelet function can be a function of time t or a function of space x. In the current analysis, it is assumed that the independent variable is x. This function can be termed 'mother wavelet' and shown mathematically as $\psi(x)$. This function can be stretched or compressed (dilated) by scaling parameter a $(a \neq 0)$, and position parameter b to create a set of $\psi_{a,b}(x)$ as written by Eq.(7.10) [135].

$$\psi_{a,b}(x) = \frac{1}{\sqrt{a}} \, \psi \left(\frac{x-b}{a} \right) \tag{7.10}$$

The function in the above equation is catered by the value b at expansion proportionate to a. Within wavelet transform, both $f(x)$ and $\psi_{a,b}(x)$ are correlated. Thus, the continuous wavelet transform (CWT) can be determined by the summation of signals' coefficients along the given path. This CWT function $C(a,b)$ can be formulated as per Eq.(7.11).

$$C(a,b) = \frac{1}{\sqrt{a}} \int_{-\infty}^{\infty} f(x) \, \psi \left(\frac{x-b}{a} \right) \, dx = \int_{-\infty}^{\infty} f(x) \, \psi_{a,b}(x) dx \tag{7.11}$$

The output of the wavelet transform can be represented as coefficients that present the correlation of wavelet function with the signal processed. Consequently, the peak transitions which seen in $f(x)$ produce wavelet coefficients at large amplitudes. This feature can be effectively recommended in the damage detection. To do this end, the inverse of CWT can be implemented to regain the signal from the CWT coefficients $(C(a,b))$ as written in Eq.(7.12), where K_ψ is constant depends on the type of wavelet used.

$$f(x) = \frac{1}{K_\psi} \int_{a=-\infty}^{\infty} \int_{b=-\infty}^{\infty} C(a,b) \, \psi_{a,b}(x) \, bd \left(\frac{da}{a^2} \right) \tag{7.12}$$

The biorthogonal wavelet can be used to reduce the limitations of the orthogonal wavelet. In this case, the analysed signal $f(x)$ in the above equation can be written as per (7.13), the output of this signal can be as demonstrated in Fig 7-4 [135].

$$f(x) = \sum_{j,k} \overline{C_{J,k}} \, \psi_{j,k}(x) \qquad (7.13)$$

The calculated coefficients of signal $f(x)$ is written as per Eq.(7.14).

$$\overline{C_{J,k}} = \int f(x) \, \overline{\psi_{J,k}}(x) dx \qquad (7.14)$$

Both equations (7.12) and (7.13), show wavelet transform can be applied to detect the damaged sections via analysis the measured signals. Where calculating the value of coefficients for the analysed signal over all signal domain can show different amplitudes. An example of using the wavelet transforms in crack detection, the analysis of fixed-end beam shown in Fig 7-5, as reported in [135] is discussed. The geometric properties of the cracked beam are; L is the length of beam 3 m, h, w are height and width and both equal to 0.15 m, d crack depth and L_{cr} is crack location. The mechanical properties are, $E = 31 \, GPa$, $\rho = 2.3 \, {kg}/{m^3}$ and $\vartheta = 0.2$. One of the selected results from this work, the intact and cracked deflection for the beam under impact load, as per Fig 7-6. It is clear from this figure the difference between the intact deflection mode and the crack modes, where cracks were created at node 4 and 9. The gap between them suggests the reduction in stiffness, but did not detect the crack location. Calculating the biorthogonal wavelet for crack at node 9 (Fig 7-7) showed a local disturbance associated with crack location. The length of beam in this study was divided to a number of nodes in the analysed signal.

According to above demonstration, Haar wavelet coefficients (Haar index) was calculated using MATLAB R2017$_a$ in the current research, where the command shown in Eq.(7.15), was used to run the calculation of Haar index. In this formula $\left(\emptyset_{ji}''\right)_H$ is the intact curvature index and $\left(\emptyset_{ji}''\right)_D$ is damaged one. In addition, calculating Haar index in this chapter is to upgrade the irregularity index and help in the solution of noise problems that generally associate with experiment.

$$\text{Haar Index} = dwt\left(\left(\left(\emptyset_{ji}''\right)_D - \left(\emptyset_{ji}''\right)_H\right)^2\right), \text{`harr'}; \qquad (7.15)$$

In the current research, the Haar index was calculated and draw versus the number of nodes of each signal. As Haar function was run as a function of space x, then the number of nodes is equivalent to the length of plate (length of plate is divided into equal

30 nodes). Which means, as the damaged area was created in the centre of eight-layer plate samples, the peak of Haar index was found roughly at node number 15 or shifts due to noise as will be discussed in the result sections.
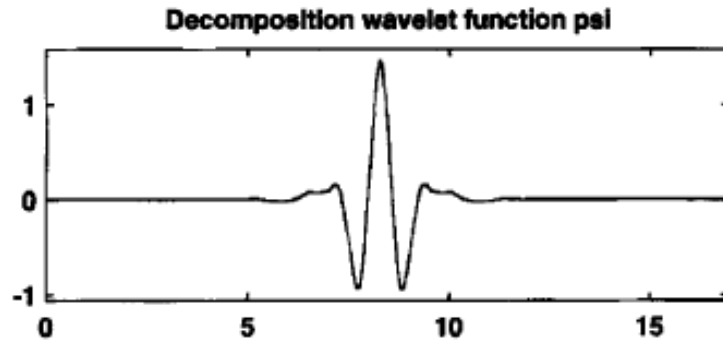
Fig 7-4: Signal of biorthogonal wavelet [135].
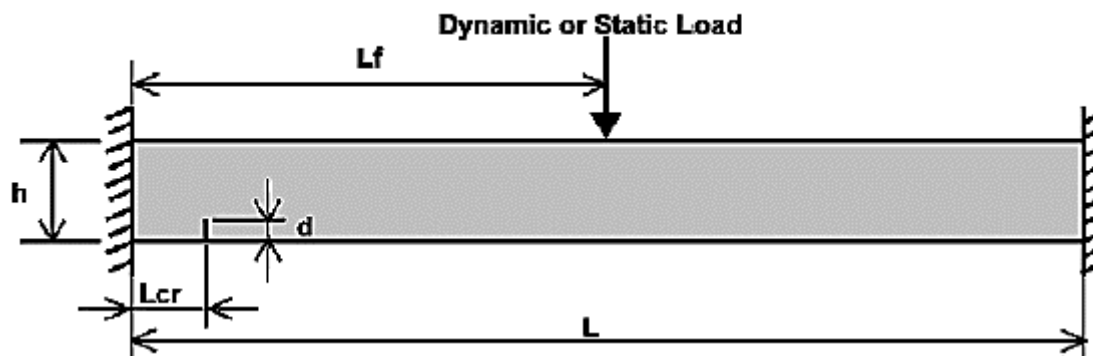
Fig 7-5: Schematic of fixed-end beam under a static or dynamic load [135].
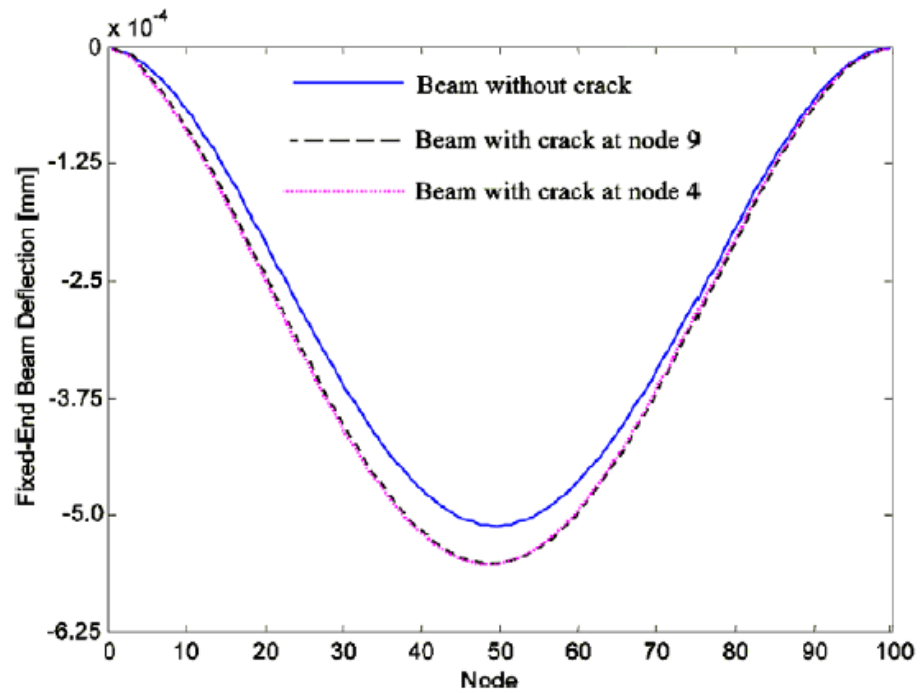
Fig 7-6: Deflection of the fixed-end beam at t = 0.048 s after impact [135].
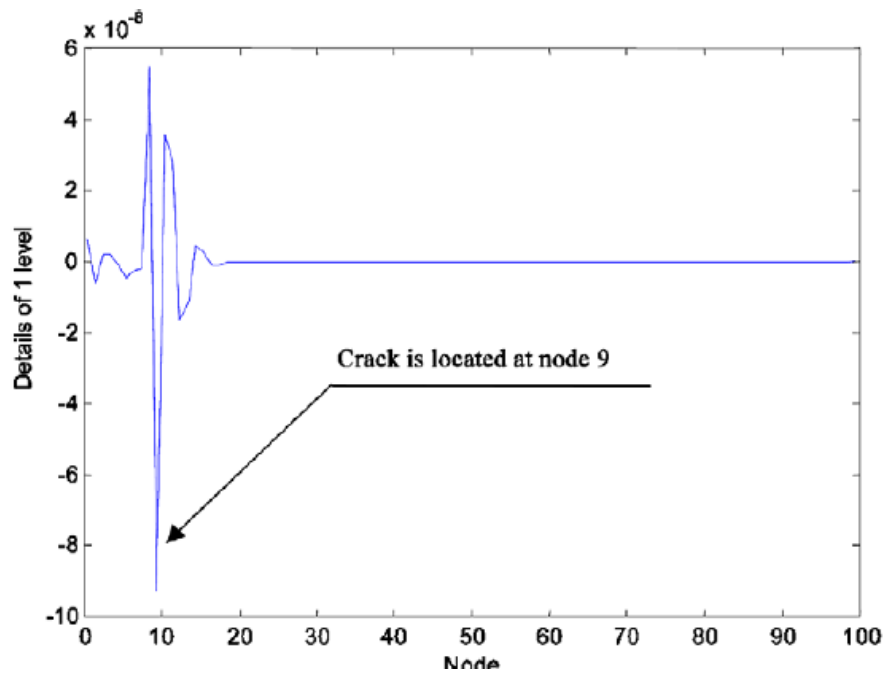
Fig 7-7: Wavelet transform analysis by biorthogonal wavelet (crack model at node 9) [135].

7.4   Statistical analysis of mode shape

To ensure that experimental results were statistically significant, three samples were used to measure each mode shape. Then the average of measurement for each mode was calculated and error bars were added using Excel. The curves shown in Fig 7-8 show the average of second mode for the intact and damaged narrow plates and the error bars indicate the variation of similar measurements. The same curves and error bars were calculated for style B plates and for impact damage style B plates as shown in Fig 7-9 and Fig 7-10 respectively.
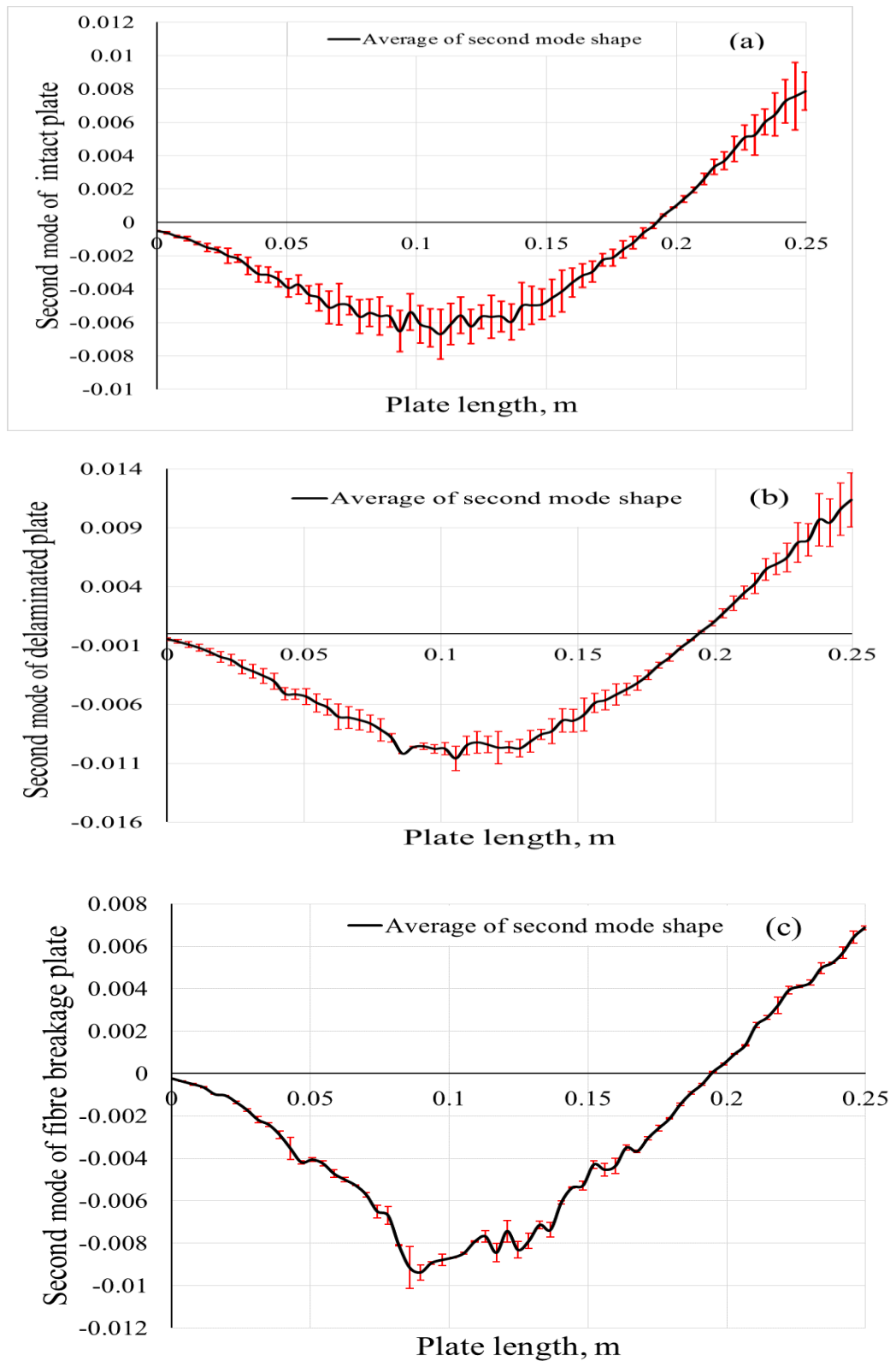
Fig 7-8: Statistical analysis of the experimental second mode of the intact and damaged narrow laminated plates.
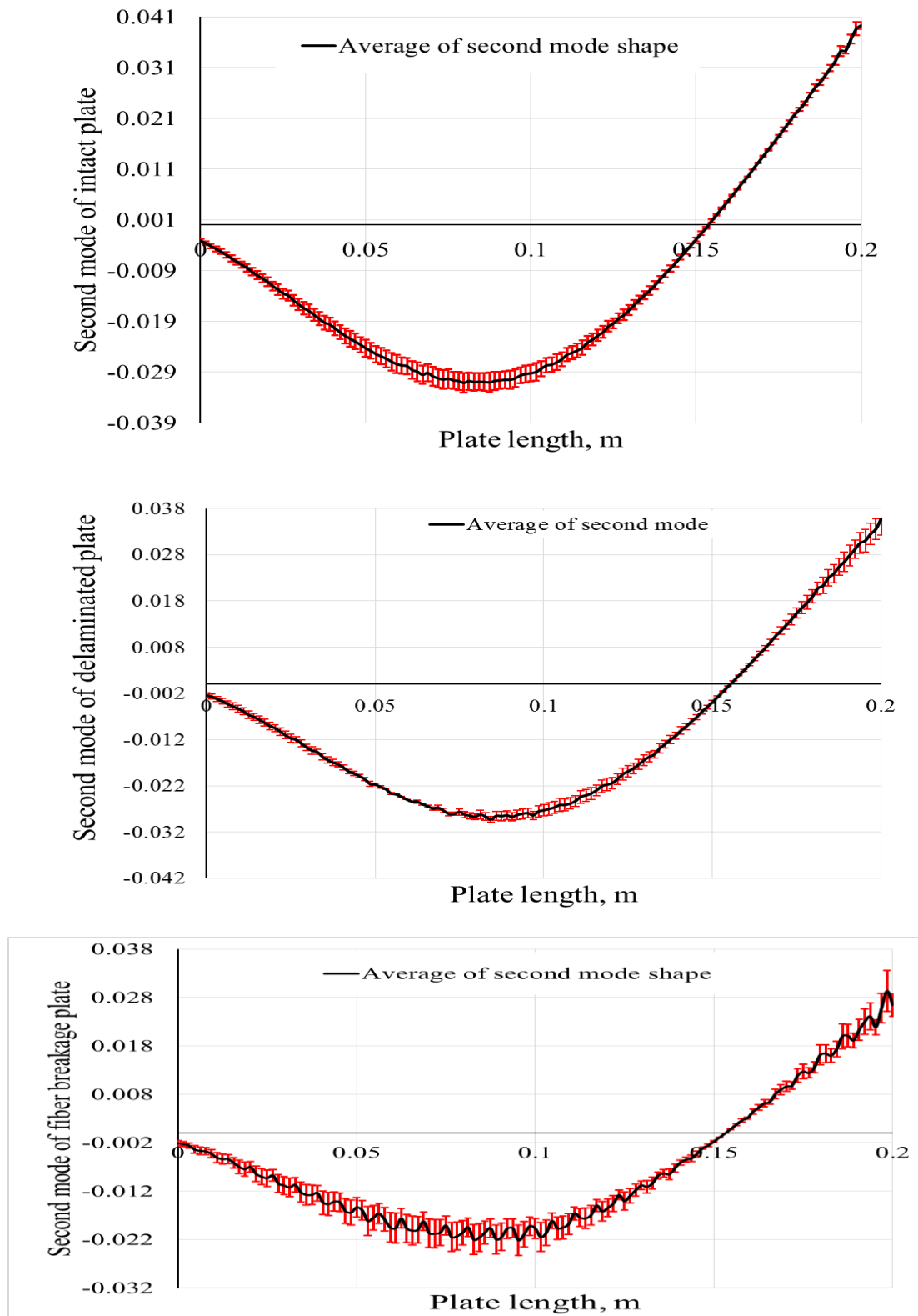
Fig 7-9: Statistical analysis of the experimental second mode of intact and damaged
style B laminated plates.
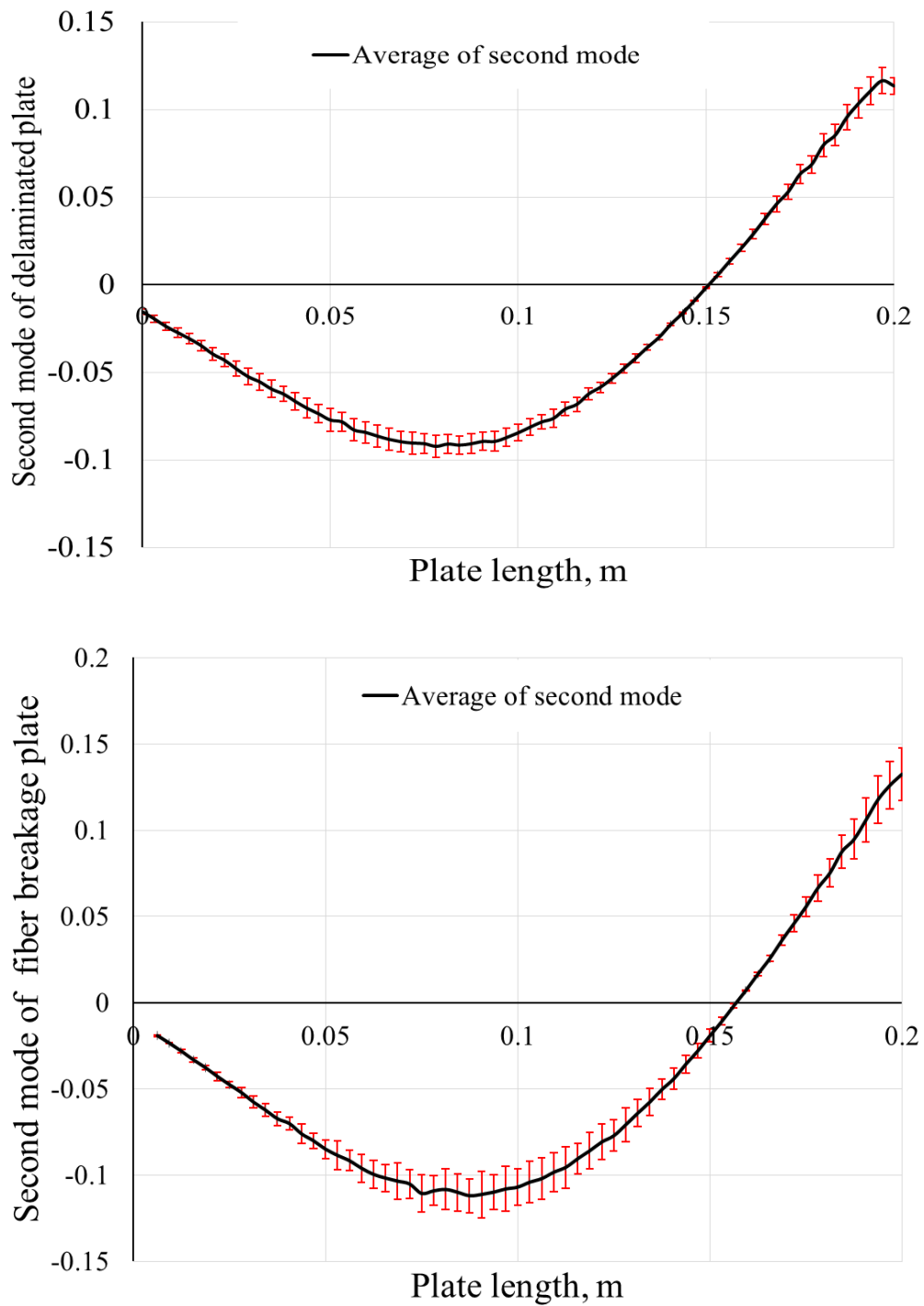
Fig 7-10: Statistical analysis of the experimental second mode for impact damaged eight-layer style B laminated plates.

7.5 Experimental results and discussion of narrow plates

The narrow laminated plate samples shown in Fig 5-8 have been tested experimentally under free vibration conditions. The first three intact and damaged modes of the four-layer narrow laminated plate were measured, as per Fig 7-11. These modes where normalized to the maximum amplitude found for each mode shape. The curve fitting (red line in these figures) was calculated in Excel. As in chapter 6, vibration-based techniques were used to detect the delamination and fibre breakage in all plate structures.

The curvature index formulated in Eq.(4.2) was used, and to improve the damage detection, the irregularity curvature index was calculated, as per Eq.(6.1). The irregularity index represents the square difference between the damaged and intact modes, where $\left(\emptyset''_{ji}\right)_H$ is the intact curvature index and $\left(\emptyset''_{ji}\right)_D$ the damaged. The Haar index (discussed in section 7.3) was calculated to improve the damage detection in laminated structures. As these structures show high strength and stiffness compared with metals, the improved method is significantly needed. Also, Haar index is proposed here to overcome the noise and errors problems, normally associated with experiment. Both of these indexes are used for the first time.

The analysis of the experimental data was compared with the finite element analysis presented in chapter 6 to show the real use of this method. A laser Doppler vibrometer was used to provide the accurate measurement of mode shapes. As demonstrated in Fig 7-11, the first normalized mode is quite noisy, and thus provides a noisy data analysis. In this regard, first mode was efficient for damage detection in any of the laminated plate samples. The normalized second intact and damaged modes for the narrow plates shown in Fig 7-12 show approximately the same (as might expected, experimental modes are more noisy than numerical ones) trend as that calculated in the FEA in chapter 6; however, there is no valuable difference between the intact and delamination modes. In this figure, the amplitude of the intact mode is -0.7, whilst for the delamination mode, the amplitude is -0.8; by contrast, the mode shape for the fibre breakage has a local perturbation close to the damaged area with an amplitude of -1. Also, it was noted that the greater reduction in stiffness due to fibre breakage provides more noisy data, and the effect of the damage can extended to the surrounded area of

damage itself. Further damaged areas cannot be detected by mode shape, although there is a local disturbance in fibre breakage mode near the damaged region. The effect of the noise can be clearly seen in experimental data. As demonstrated in Fig 7-13, the curvature index was not efficient to quantify the damaged sections, even for fibre breakage (fibre breakage is more severe than delamination). The fluctuating curve in this figure does not provide any notable peak, in an identical manner to the FEA analysis. This means neither the mode shape nor its curvature were sufficient to detect the damaged areas.

As in FEA, the irregularity index for both FB and Del showed the damaged area. The curve shown in Fig 7-14 represents the irregularity index of the second mode with FB (fibre breakage) at L_1. The effect of the noise was clear, where small jumps were picked up around the peak at approximately the position of damage (damage at 0.1 m). In this figure, the irregularity index increases sharply close to the damaged area to reach its peak and then decreases to the fluctuating level due to the noise. This can add another evidence that irregularity can overcome the noise effect. The shift in the main peak is entirely dependent on the amount of noise that was measured in experiment. The peak of the irregularity index was 7.7 and was quite close to the damaged area.

In contrast, Fig 7-15 shows the irregularity index of the delaminated area located at L_1. A flat peak was seen at 0.1 m (the delamination position) with an amplitude of 2, confirming the location of the damage. The curve in this figure increases gradually at 0.05 m to its tip at 0.09 m then at 0.12 m declines gradually to the lowest level close the end of plate. This variation is entirely depends on the amount of stiffness reduction which affect the measured mode shape. The difference in both tip form and magnitude for the irregularity index can help to quantify and recognize whether Del or FB is existence in the narrow laminated plate structures. As for finite element analysis, FB still provides a sharper and greater peak than for the delamination. The only difference that the analysis of experimental data analysis provides is a non-smooth index due to effect of noise.

The improved method, which is represented by calculation of the Haar index for both FB and Del, as shown in Fig 7-16 and Fig 7-17. In these figures, the Haar index successfully detect the damaged areas in these structures. The peak of the Haar (coefficients of Haar function vary over the plate length) in FB is 8.1, and in Del is 2.9,

which shows the difference between these two types of damage. According to Haar index premise discussed in section 7.2, the number of nodes are identical to the plate length in all samples (plate length is divided into 30 nodes in this analysis). Which means damage is located at node 12 (0.1 m). The effect of noise causes the shift in the tip of Haar in both FB and Del, also causes the fluctuation found in FB case. Another issue to these figures that the area of delamination (0.02 m^2) which is greater than the area of fibre breakage (0.00002 m^2) and this can explain the extension of tip in Del, as shown in Fig 7-17. Experimental data analysis demonstrated that the decrease in stiffness due to FB is much greater than delamination, which was observed in the difference between the profile and magnitude of the irregularity and Haar indexes. The same conclusion of irregularity index can be drawn for the Haar index, where both of them behave in the same manner.
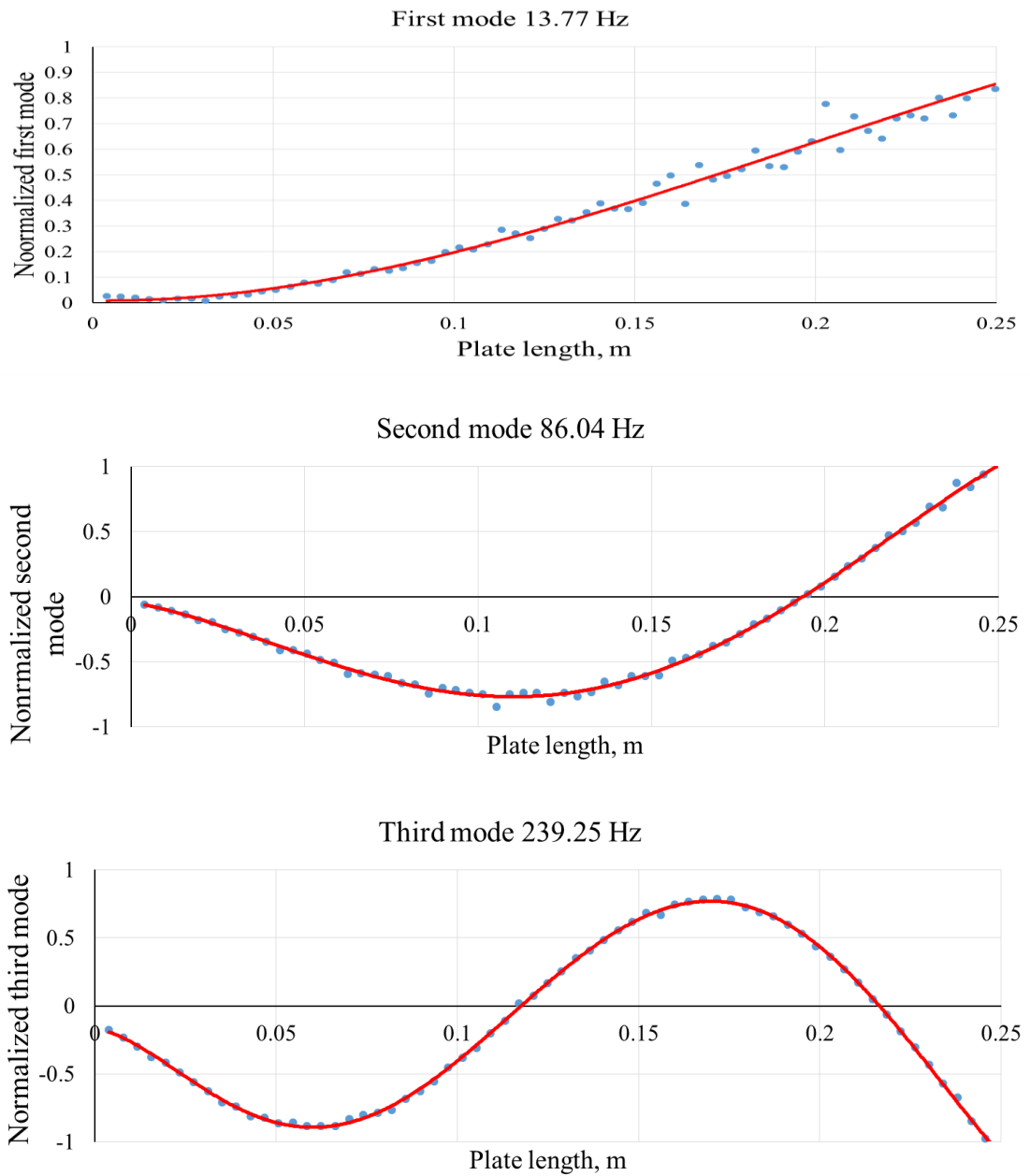
Fig 7-11: First three experimental normalized modes for the narrow delaminated plate, delaminated area is located at 0.1 m. No damage is apparent in this region.
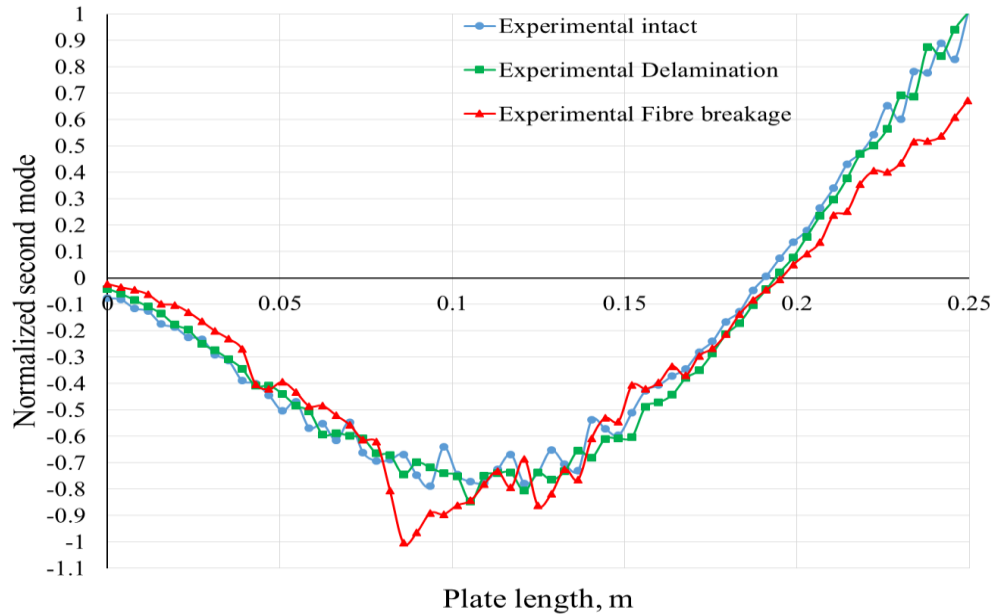
Fig 7-12: Experimental intact and damaged second modes for the four-layer narrow laminated plate, with delamination and fibre breakage located at 0.1 m from the fixed end. The damaged area is not predictable via mode shape, as there is considerable fluctuation in the fibre breakage mode due to the large reduction in stiffness.
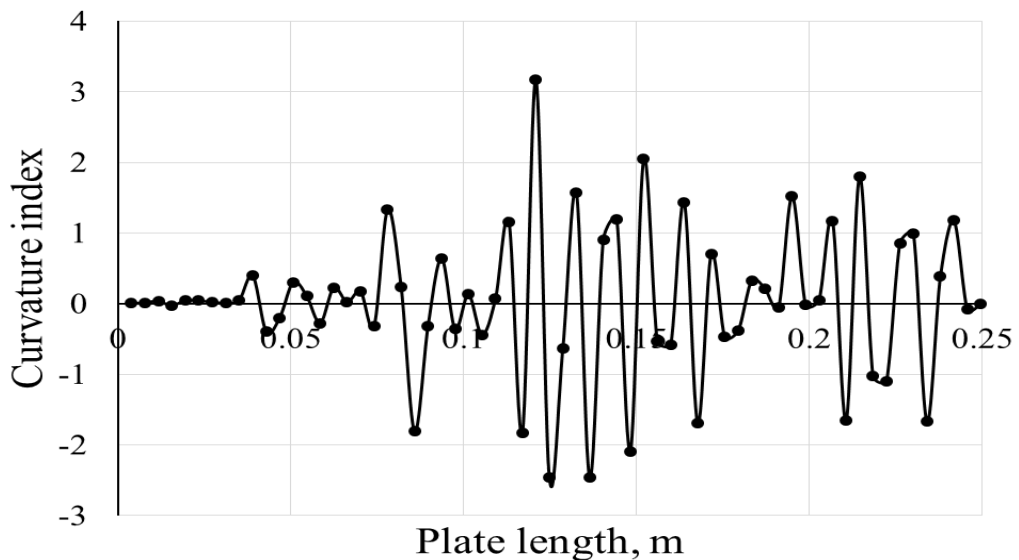
Fig 7-13: Experimental curvature index of fibre breakage at 0.1 m from the fixed end of the laminated narrow plate, curvature does not show the damage location.
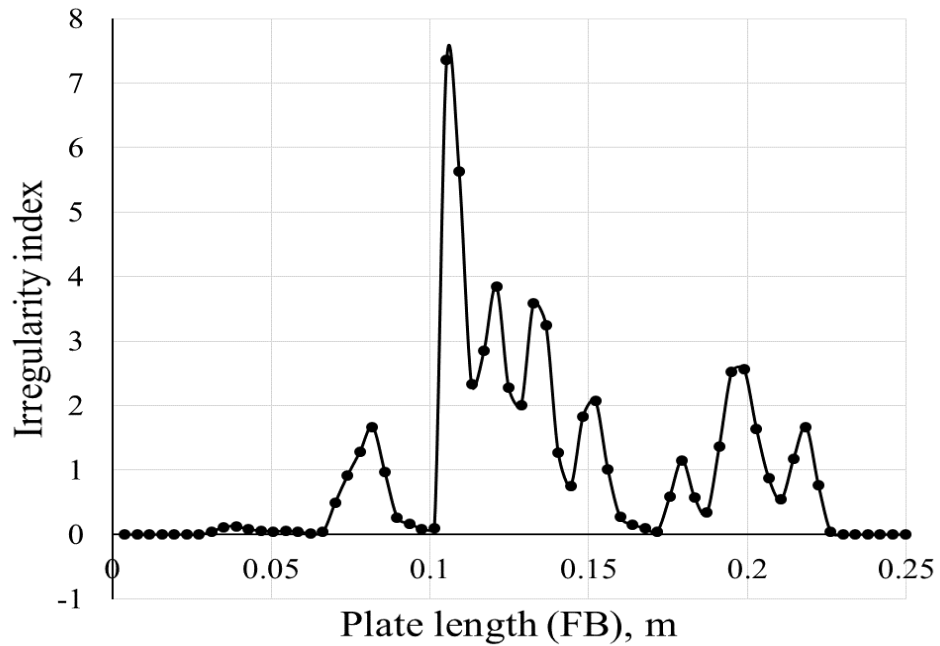
Fig 7-14: Experimental irregularity index of fibre breakage at 0.1 m from the fixed end in the narrow laminated plate. The sharp peak and high magnitude can be considered an acceptable index by which to detect the damaged area.
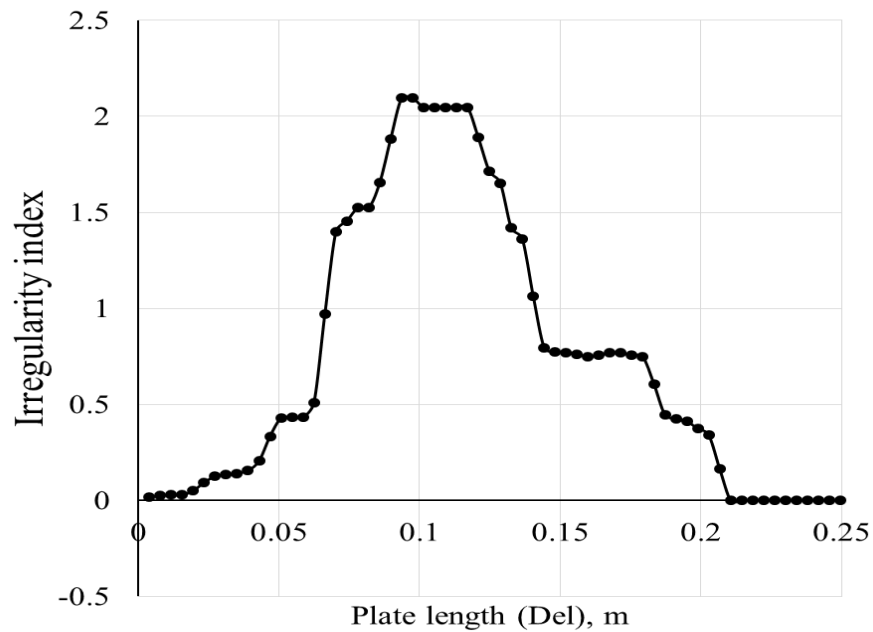
Fig 7-15: Experimental irregularity index of delamination at 0.1 m from the fixed end in the narrow laminated plate. The flat peak can be considered an acceptable index by which to demark the damaged elements.
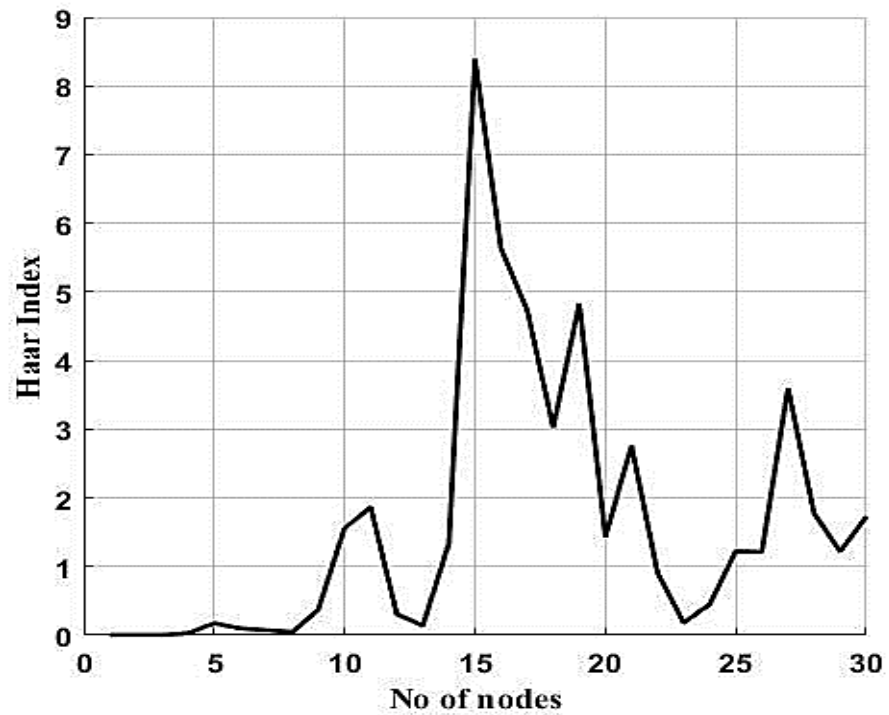
Fig 7-16: Experimental Haar index of fibre breakage in the narrow laminated plate. The sharp peak is related to the presence of a high reduction in local stiffness as a result of fibre breakage.
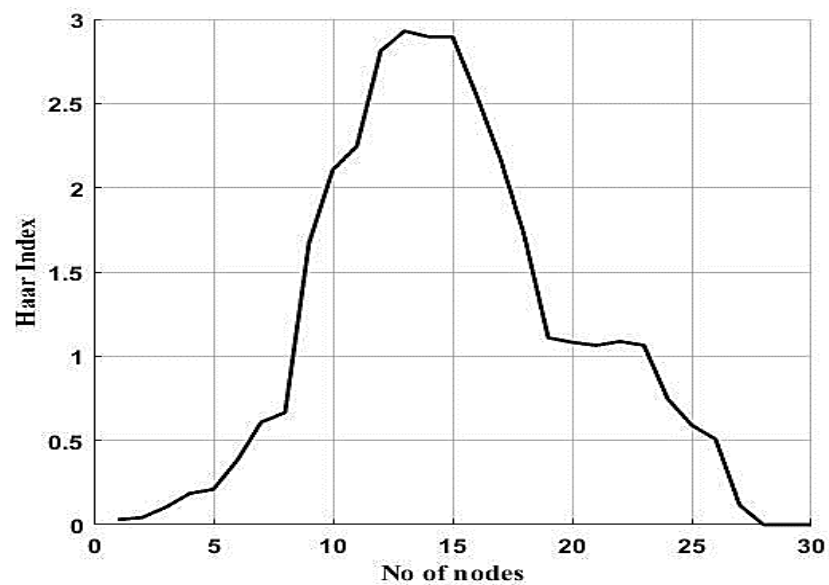
Fig 7-17: Experimental Haar index for delamination in the narrow laminated plate. The flat peak and low magnitude confirm that damage is less severe than fibre breakage.

7.6   Experimental results and discussion of eight-layer plates

The eight-layer plate structures discussed in section 5.2.3.1 were used to investigate the damage detection subject. Two lay-up sequences, A and B, were utilized to determine the difference between the analysis of the intact and damaged dynamic signals. Mode shape, curvature, and irregularity indexes were calculated as a part of damage identification process. Further, the Haar index was calculated as a new index to improve the damage detection.

Experimental work has been achieved using the intact and damaged (samples with artificial damage) composite plates, as seen in Fig 5-15. Delamination and fibre breakage were created to represent damaged areas. As in the previous section, the first three modes were measured, as shown in Fig 7-18, to start the analysis of the dynamic data. A laser Doppler vibrometer was used also to measure these modes.

In this study, it should be noted that the first mode is still noisy, and it is not useful for use with the damage detection subject, as seen in Fig 7-18. For that, the second mode was employed to detect the damaged areas in eight-layer plates. In terms of data analysis, the same concept can be discussed where the reduction in local stiffness caused by the damaged area can be detected via analysis of the intact and damaged dynamic signals. Dynamic signals (here mode shape) can be affected much more by the severe damage. It is clear from Fig 7-19, that there is no difference between the intact and delaminated mode. The amplitudes of normalised intact and delaminated (delamination at 0.1 m) modes are both -0.79, while in the same figure, the mode shape with fibre breakage shows a non-smooth profile. Further, in both damaged modes, FB and Del were not detected.

To quantify and localize the damaged areas, curvature index was calculated, as per Fig 7-20. The fluctuating profile seen in this figure confirms that the curvature index is not efficient to quantify and localize the damaged areas. Thus, the irregularity and Haar indexes were calculated for the purpose of damage detection. Calculating the irregularity index of style A with FB at 0.1 m shows the damaged area quite clearly, as per Fig 7-21, where the peak was located quite close to the FB area with a magnitude of 0.11. In this figure the curve increases gradually to the sharp tip at 0.09 m. A small shift for the tip (FB at 0.1 m) occurred due the noisy data. Then declined to the lower level at

0.13 m. This peak can be considered as indicative of fibre breakage in this structure. Also, the Haar index successfully shows a peak at node 12 (damaged area position), as shown in Fig 7-22. The profile found for the Haar index is roughly similar to that of the irregularity index and its magnitude, 0.15, where the curve rises at node 4 to the sharp tip, and declines to the lower level at node 21.

The same indexes are calculated to detect the delaminated area in style A. The difference in the reduction of local stiffness between FB and Del is clearly apparent through the calculation of these indexes. It was not surprising to find a flat peak at 0.1 m (delamination position) with an amplitude of 0.085, as seen in Fig 7-23, and a similar shape with a magnitude of 0.12 for the Haar peak for the same plate, as per Fig 7-24. In both these figures, curves rise gradually to reach the max magnitude, then stay constant to drop again to the lowest level at last quarter of beam length. Also, it should mention that the size of delamination is greater than FB and that how effects the extension of tip in both irregularity and Haar indexes.

To study the effect of different ply-orientations on damage detection, style B was investigated. Fig 7-25, presents the irregularity index, where curve rises gradually to its sharp tip of 4.3 at 0.09 m then declines progressively to magnitude of 0.5 at 0.13 m. The noise effect causes both shift the peak and the observed fluctuation in this curve. The damaged area can be successfully detected. For the same plate conditions, Haar index is calculated as seen in Fig 7-26. The same gradual increasing and decreasing is found, where curve rises at node 4 to reach its tip of 5.8 at node 12 then declines to 0.5 at node 20. Haar index show smoother profile than the irregularity index, this is considered as a significant issue to overcome the effect of noise.

Delaminated area is detected by calculating the irregularity index, as per Fig 7-27. Within this figure curve had dramatic increase at 0.06 m to reach the flat tip of 0.27 at 0.075 (delamination at 0.1 m), then declined to the fluctuated curve at 0.12 m. This shift caused by the noise effect. The irregularity index did not drop significantly after the damaged area as in style A, this due to the difference in laminate stiffness in between them. According to the laminated structures principles, style B is stiffer than style A. In this analysis Fig 7-28 presents the haar index for style B, curve rises at node 5 to its flat tip of 0.38 and at node 13 drops to 0.25.

According to these figures, the same trend for both FB and Del was found. In brief, for both of those styles, the peak found for fibre breakage was sharper and greater in magnitude than that for delamination, which can be used as a basis by which to differentiate between the fibre breakage and delamination. It is important to note that the Haar index provides a smoother curve than FB, which is of particular importance when dealing with noisy signals.
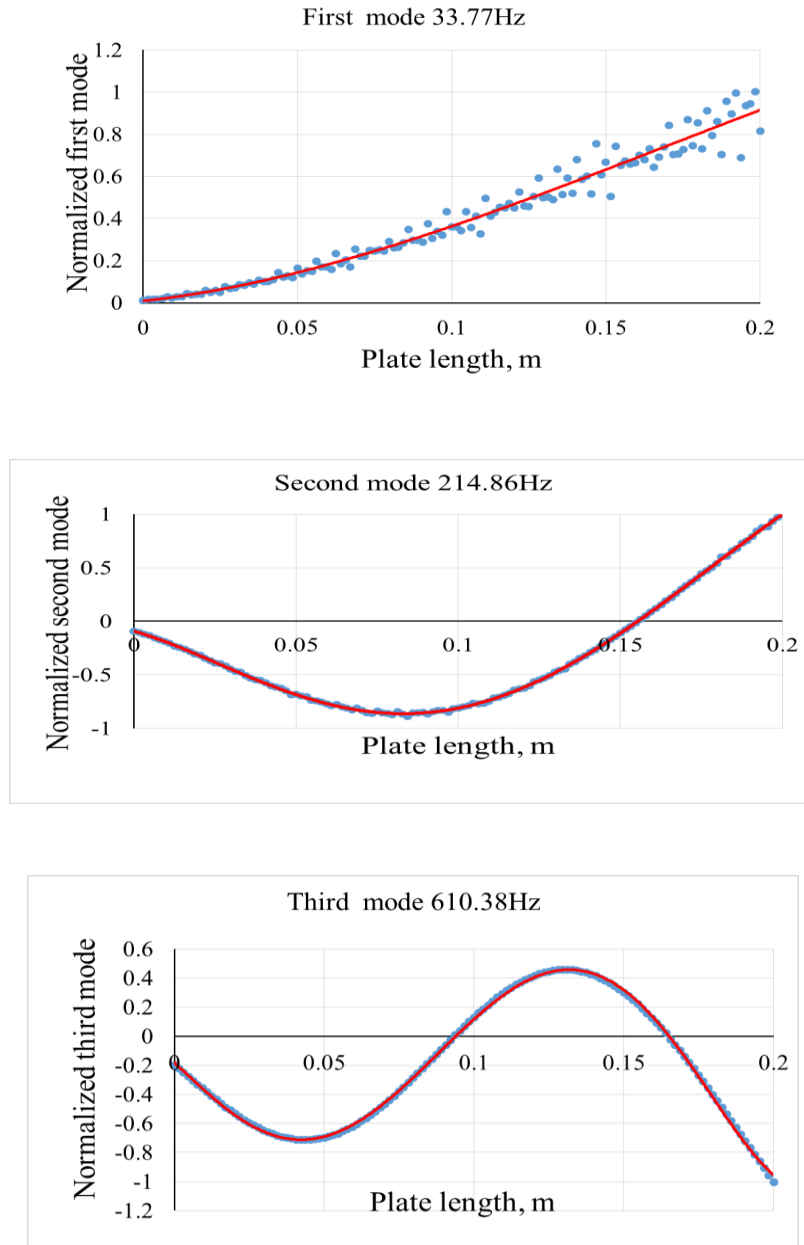
Fig 7-18: First three experimental non-dimensional modes for delaminated plate B, with delaminated area 0.1 m from the fixed end of the plate. The damage cannot be predicted.
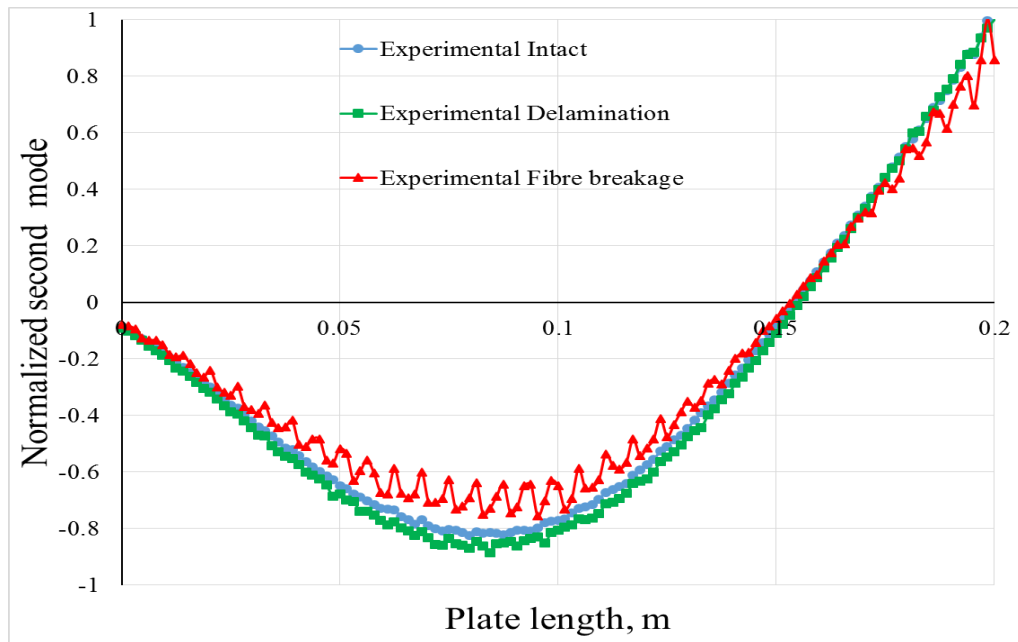
Fig 7-19: Experimental intact and damaged second modes for laminated plate B. Delamination and fibre breakage are located 0.1m from the fixed end. The damaged area is not predicted by the mode shape, though the fibre breakage mode shows considerable fluctuation due to the significant reduction in stiffness.
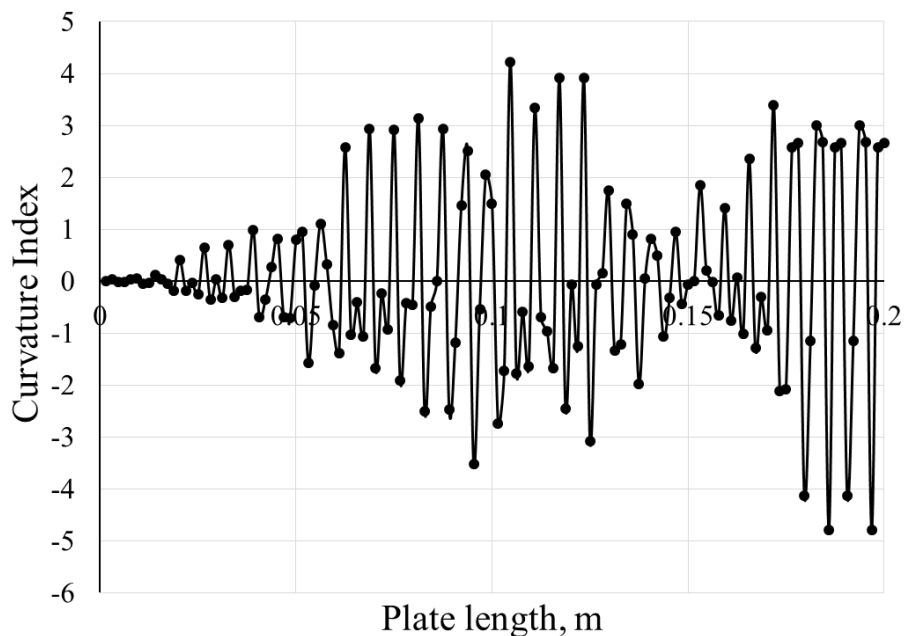
Fig 7-20: Curvature index of experimental second mode with fibre breakage 0.1 m from the fixed end of laminated plate B. The curvature does not show the damage location.
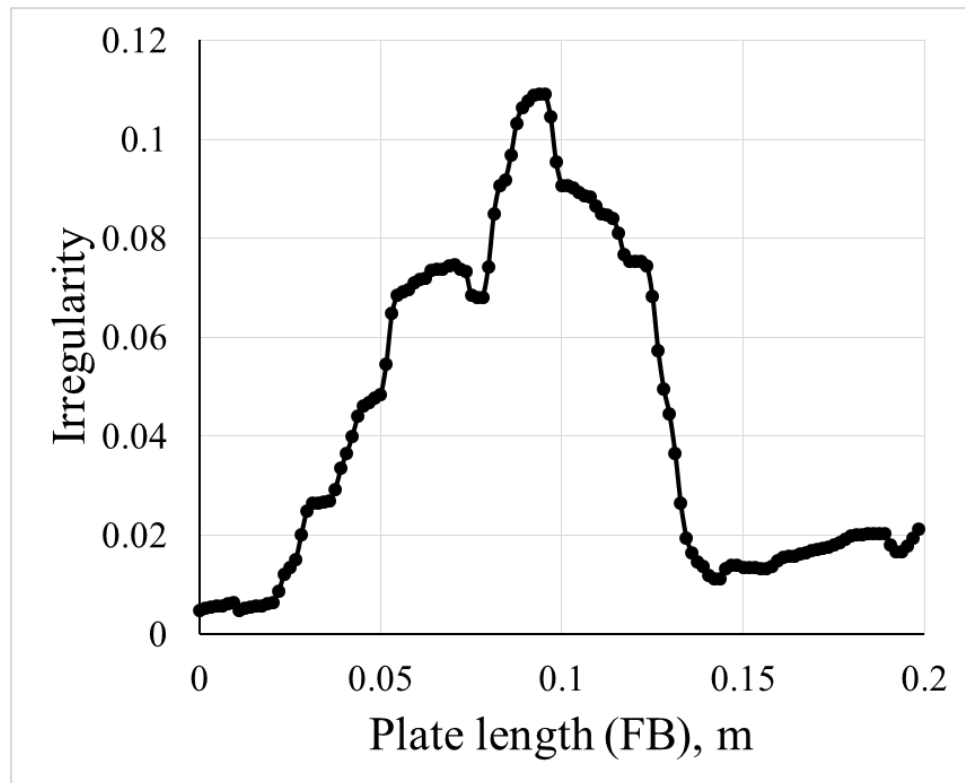
Fig 7-21: Experimental irregularity index for fibre breakage 0.1 m from the fixed end of laminated plate A. The sharp peak gives an indication of the localization of the damaged area.
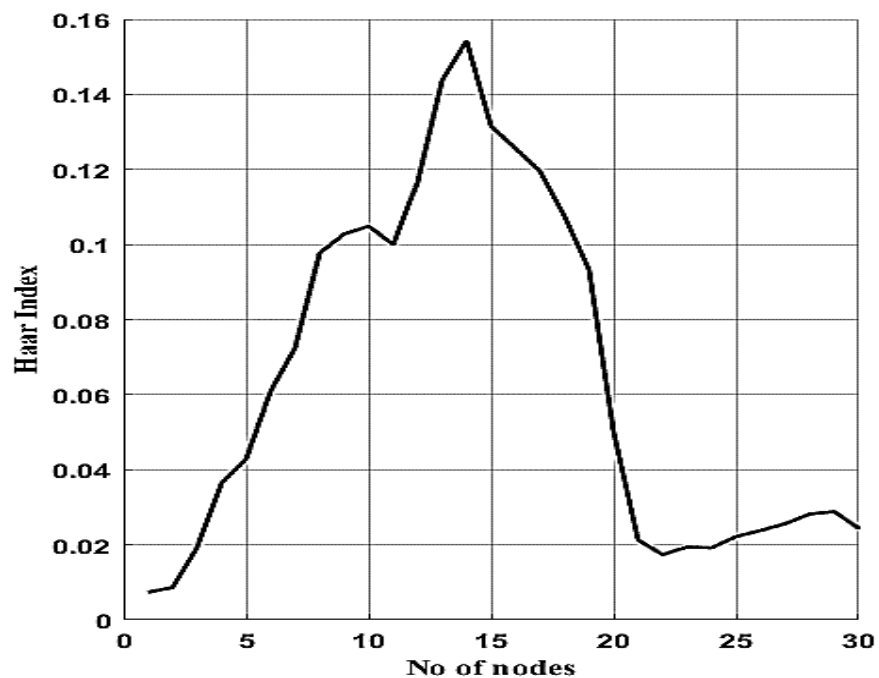
Fig 7-22: Experimental Haar index for fibre breakage 0.1 m from the fixed end of laminated plate A. The sharp peak indicates the presence, and localization of severe damage in the structure.
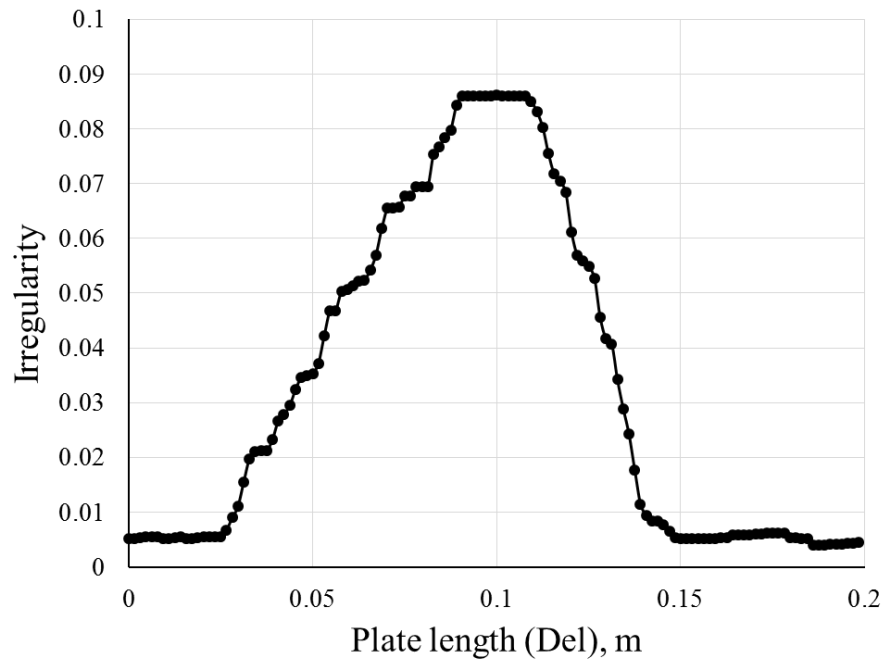
Fig 7-23: Experimental irregularity index of delamination 0.1 m from the fixed end of laminated plate A. The flat top of the curve shown is evidence of the localization of the damaged area.
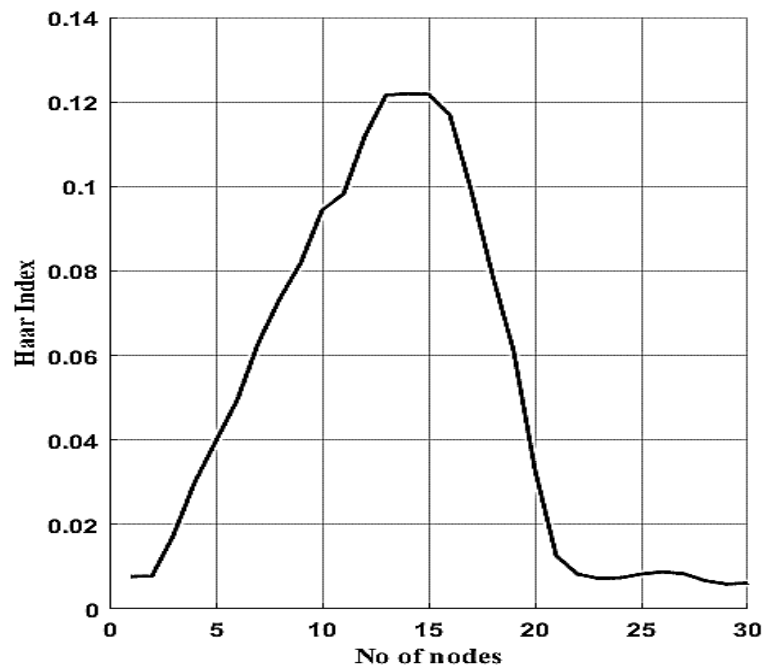
Fig 7-24: Experimental Haar index for delamination 0.1 m from the fixed end of laminated plate A. The flat peak observed indicates that there is little damage to the structure.
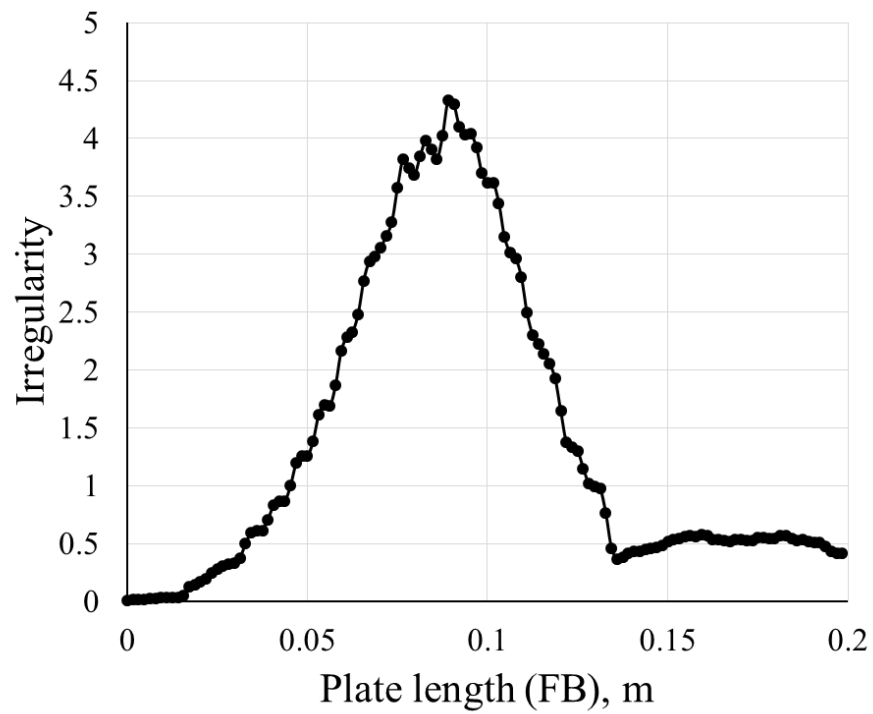
Fig 7-25: Experimental irregularity index of fibre breakage 0.1 m from the fixed end of laminated plate B. The sharp peak indicates the localization of the damaged area.
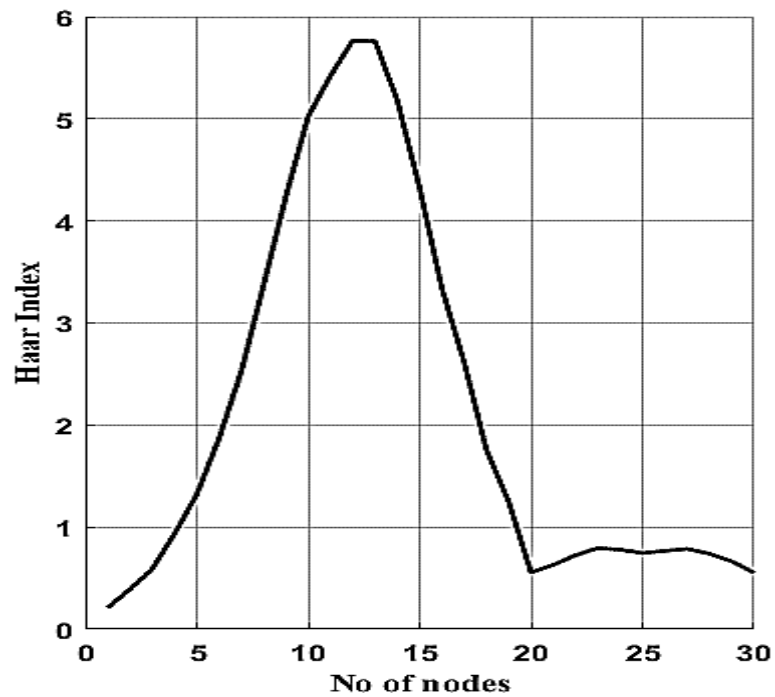
Fig 7-26: Experimental Haar index for fibre breakage 0.1 m from the fixed end of laminated plate B. The sharp peak indicates the presence of severe damage to the structure.
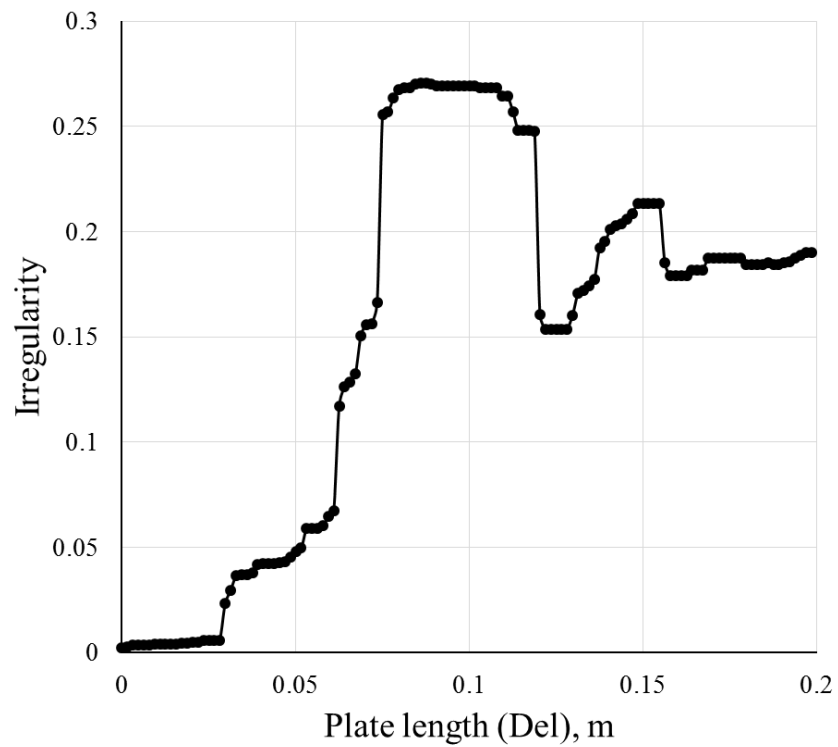
Fig 7-27: Experimental irregularity index for delamination 0.1 m from the fixed end of laminated plate B. The flat top of the curve indicates the localization of the damaged area.
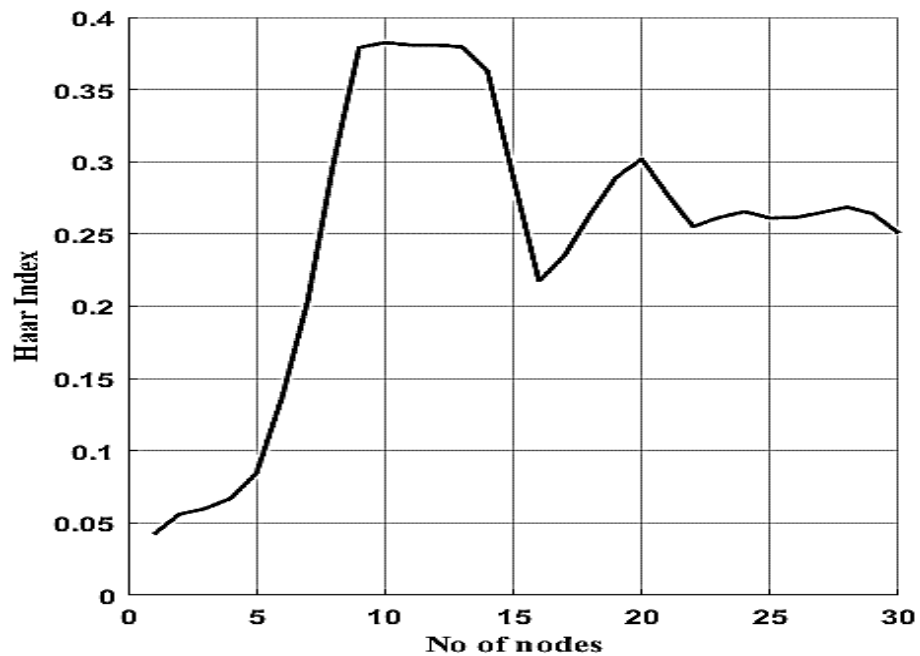
Fig 7-28: Experimental Haar index of delamination 0.1 m from the fixed end of laminated plate B. The flat peak confirms that there is little damage to the structure.

7.7 Experimental results and discussion of eight-layer plates (impact damage)

This section presents the discussion of damage detection in CFRP plates using vibration-based damage techniques. To match the real damage in laminated composite plate structures, fibre breakage and delamination were created using the impact test. Details of creating both of FB and Del are discussed in section 5.2.3.2. Both style A and B were designed as shown in Fig 5-15 for testing using an impact load. The use of two different indenter diameters allows the creation of delamination and fibre breakage (small indenter diameter produces FB, whereas, the delamination will dominate the damage with large diameter).

As for the narrow and eight-layer plate structures, the first three modes were measured using the laser Doppler vibrometer, as per Fig 7-29. In this figure, mode shapes are presented as normalized to the maximum amplitude of each mode shape. The first mode was found to fluctuate (due the measurement of noise and errors), so again was of no use in damage detection. For this, the second mode was selected to detect the damaged areas for both FB and Del.

To start the damage detection procedures, both the intact and damaged modes draw to show if there any difference between them, as per Fig 7-30. From this figure, it can be seen that there is no clear difference between the intact and damaged modes. The amplitude of these modes in the centre of plate ranged between -0.6 and -0.8, which means the reduction in local stiffness due the damage cannot be detected by calculating mode shape, even with FB (severe damage) in these structures. Similarly, the curvature index for style B did not show the fibre breakage at 0.1 m, as per Fig 7-31. The fluctuating shown in this figure with max tip of 0.0015 at 0.15 m did not show the damaged area.

To perform the damage detection, both of the curvature and Haar indexes are calculated. It is notable from Fig 7-32 that a clear peak for the irregularity was found in plate A with fibre breakage at 0.1 m. The peak does not localize at 0.1 m (damage location). This shift occurs due to effect of irregular damaged area (when the indenter hits the sample, the resultant damage extends to the region surrounding the point of impact). Moreover, the effect of noise also contributes to this shift, where the curvature

is quite sensitive to any change in mode shape. The gradually increase of this curve to the sharp tip at 0.09 m and then decreases to the lower level can suggest the damaged area. The same trend was found when the Haar index was calculated, as shown in Fig 7-33. The peak of this index shows the effect of FB on the mode shape, so as it was discussed in the previous section, plate length is dived into 30 equal nodes. So in this figure, damage is created at node 15. The noise and damage itself extensively shift the tip of Haar index from the real position (damage position) to node 11. There is no considerable difference between the irregularity and Haar indexes for FB, where their peak magnitudes are 1.21×10^{-6} and 1.62×10^{-6}.

In contrast, it is clear from Fig 7-34 and Fig 7-35 that there are flat peaks for the irregularity and Harr indexes for style A with delamination at 0.1 m, whose peak magnitudes are 5.9×10^{-8} and 8.2×10^{-8}, respectively. The lower reduction in local stiffness and the large size of delamination are detected via the peak found in these two figures. According to these four figures, it is easy to recognize that the FB peak seen for both the irregularity and Haar indexes are sharper and greater in magnitude than those found for Del. Again, this due the greater reduction of local stiffness caused by FB. The considerable reduction in local stiffness due to fibre breakage makes the peak in these indexes sharper than the analogous peak due to delamination.

The same analysis was applied to style B in terms of the analysis of FB and delamination damage, where Fig 7-36, Fig 7-37, Fig 7-38 and Fig 7-39 show the FB and delamination signal analysis. Within these figures, the trend in mode shape analysis is identical to that found for style A, Where in both of these styles, the FB peak magnitude of the irregularity and Haar indexes is sharper and higher than Del peak. Peak of irregularity index does not localized with the damaged area due to the spread of damage to the surrounding region (out of the contact area of the point of impact of the indenter) and the effect of noisy environment. However, the only difference between these styles was that fibre breakage is more easily detected for style A than style B (the peak value of irregularity index with FB in style A is 1.21×10^{-6} ,while in style B it is 2.9×10^{-7}); otherwise, the trend in the results for both styles is essentially identical.

First mode 34.07 Hz

Second mode 208.64 Hz

Third mode 572.11 Hz
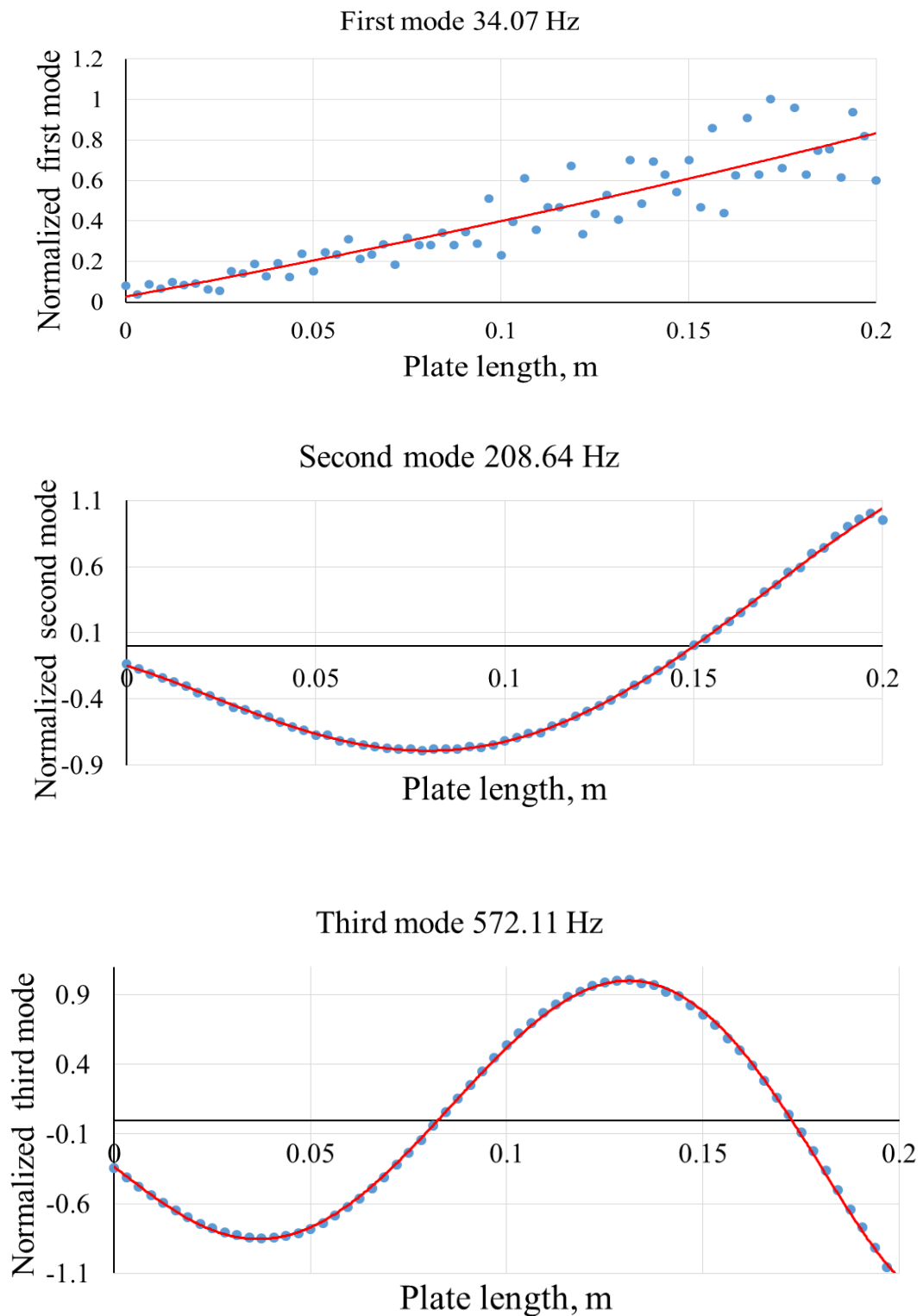
Fig 7-29: First three experimental normalized modes for eight-layer delaminated plate
B. There is no damage shown, although the impact delaminated area is present
0.1 m from the fixed end of the plate.
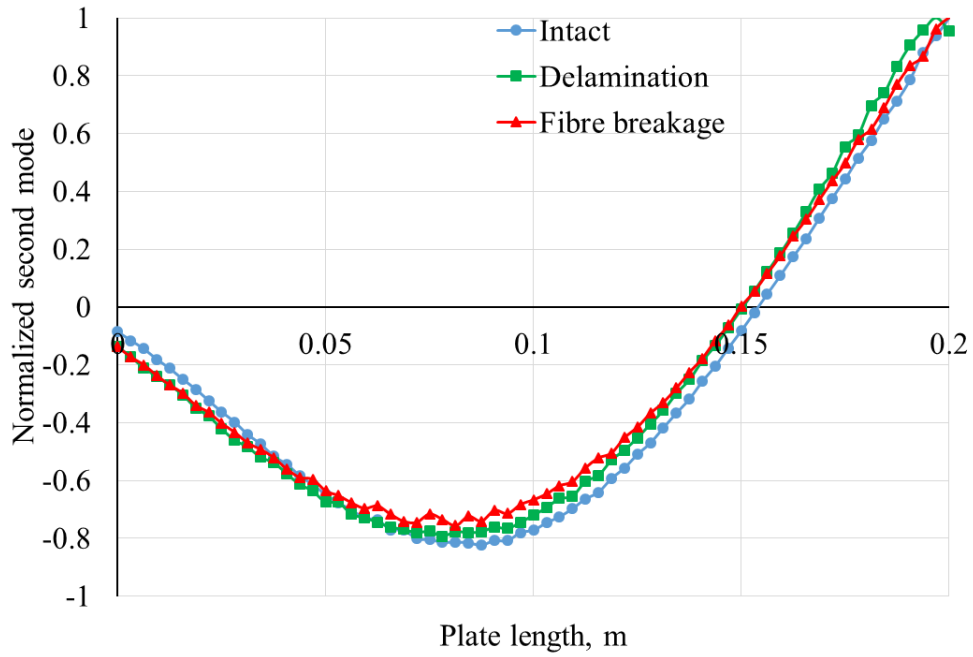
Fig 7-30: Experimental intact and damaged second modes for the eight-layer intact and impact delaminated and fibre breakage laminated plate B. Damage is located at 0.1 m from the fixed end; the damaged area is not apparent from the mode shape.
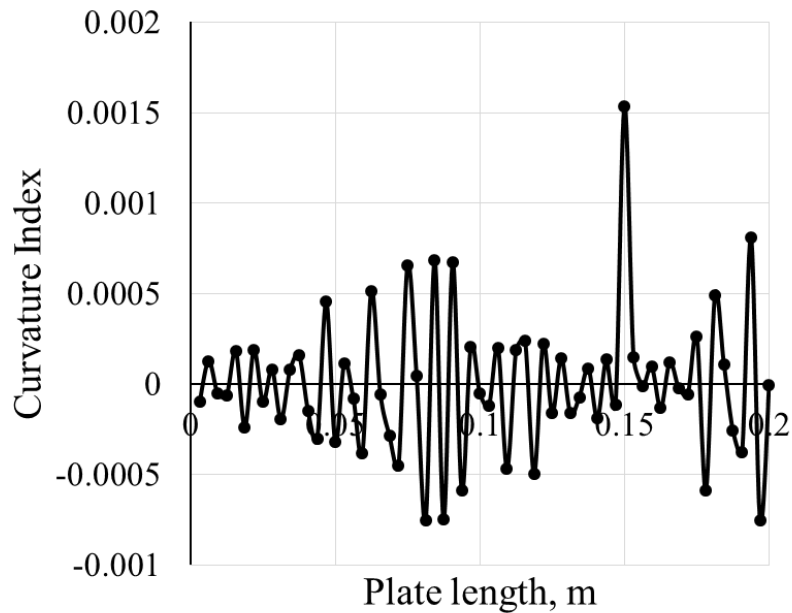
Fig 7-31: Curvature index of experimental second mode with impact fibre breakage at 0.1 m in eight-layer from the fixed end of the eight-layer laminated plate B. The curvature does not show the damage location.
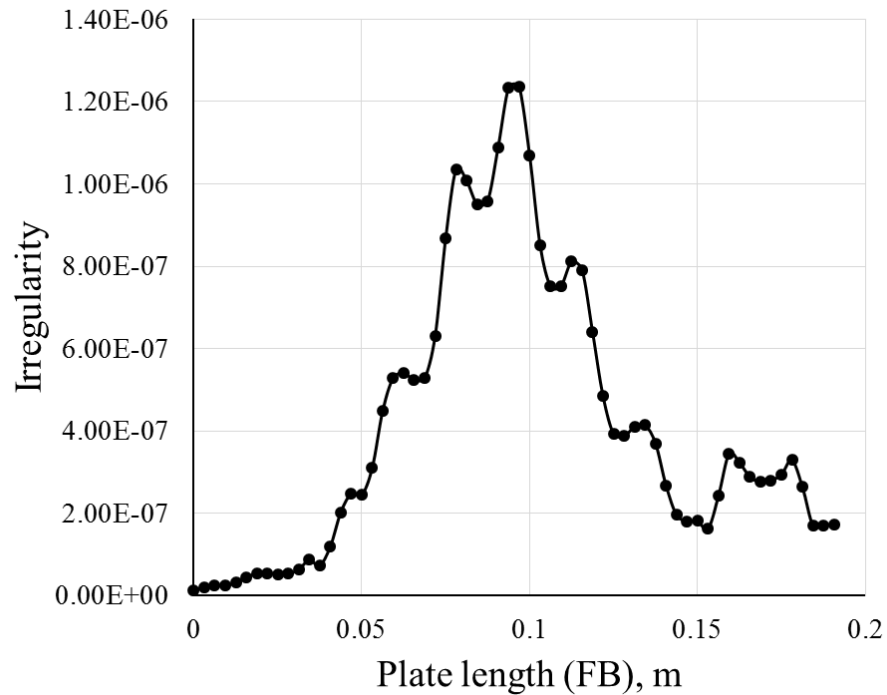
Fig 7-32: Experimental irregularity index for fibre breakage 0.1 m from the fixed end of impact damaged laminated plate A. The sharp peak indicates the detection of the damaged area.
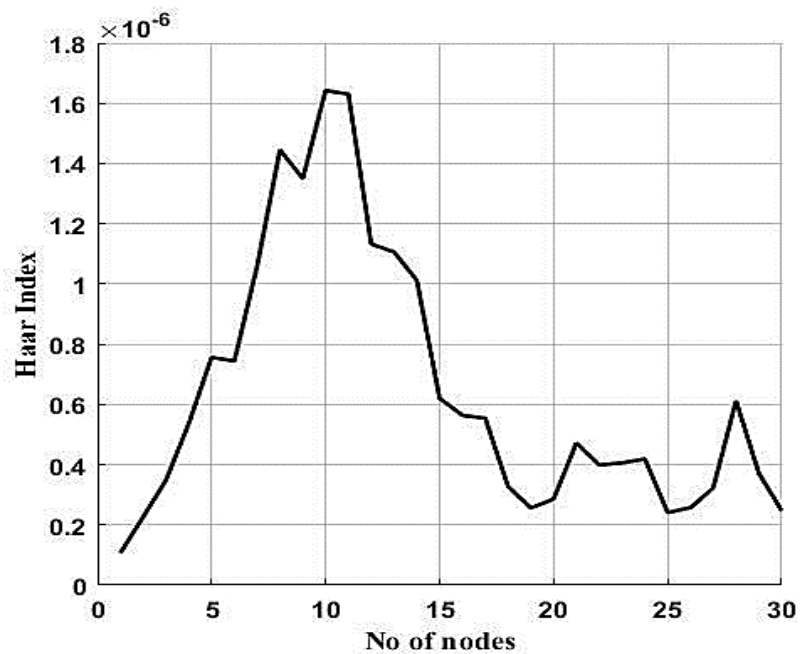
Fig 7-33: Experimental Haar index for fibre breakage 0.1 m from the fixed end of impact damaged laminated plate A. The sharp peak demonstrates the presence of severe damage to the structure.
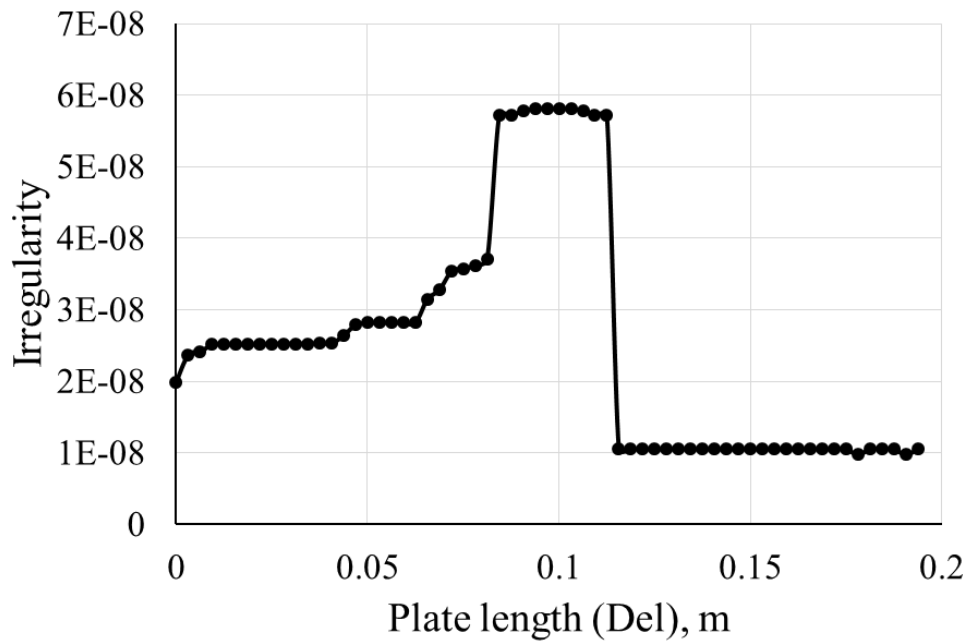
Fig 7-34: Experimental irregularity index for delamination 0.1 m from the fixed end of impact damaged laminated plate A. The flat peak of the curve indicates the localization of the damaged area.
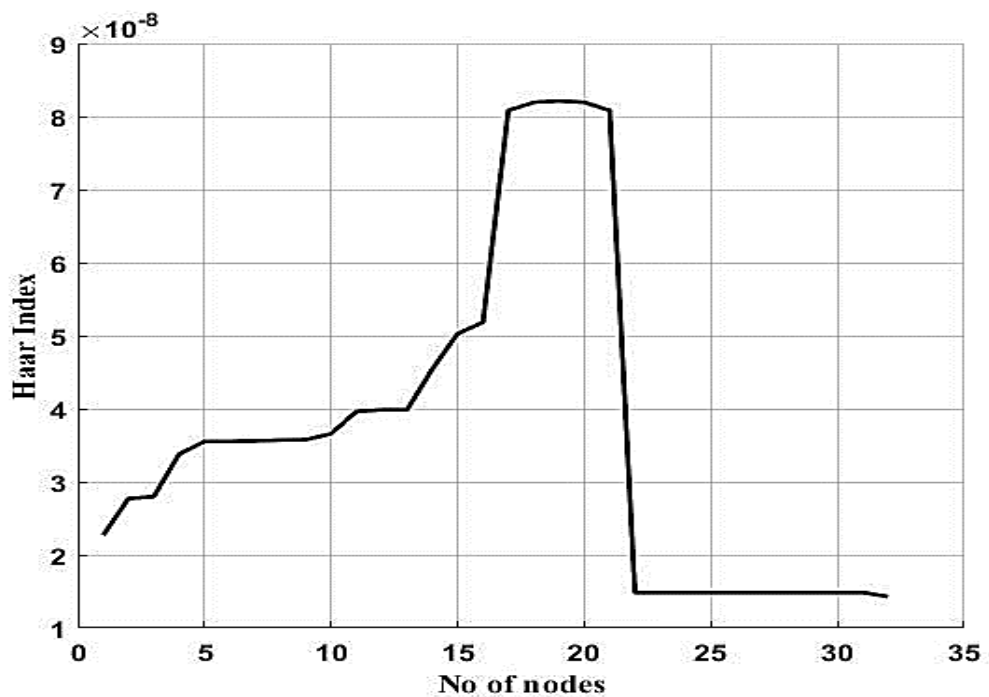
Fig 7-35: Experimental Haar index for delamination 0.1 m from the fixed end of impact damaged laminated plate A. The flat peak confirms that a small amount of damage is present in the structure.
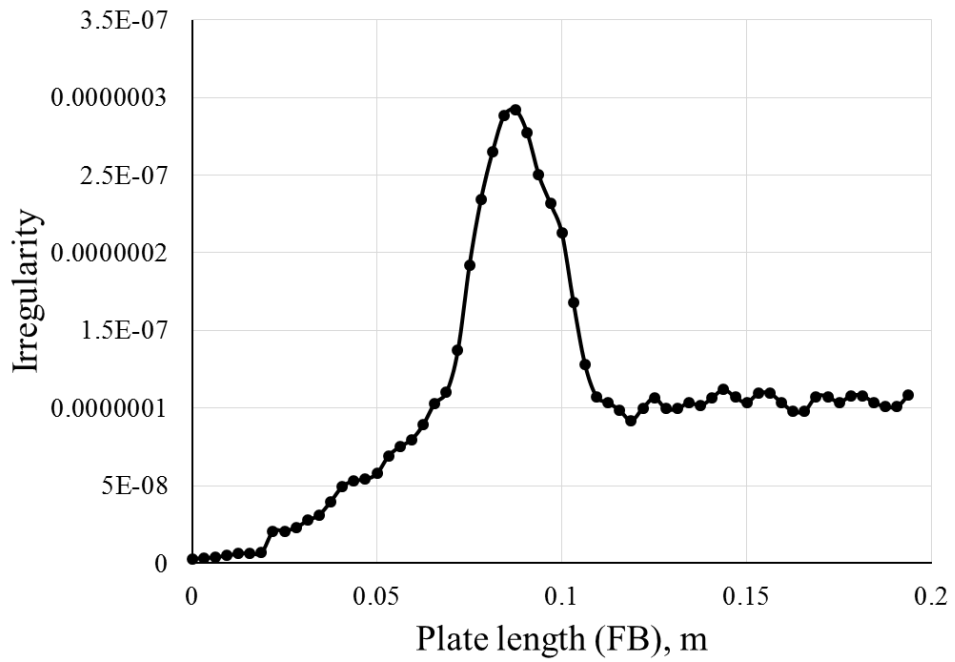
Fig 7-36: Experimental irregularity index for fibre breakage 0.1 m from the fixed end of impact damaged laminated plate B. The sharp peak indicates the detection of the damaged area.
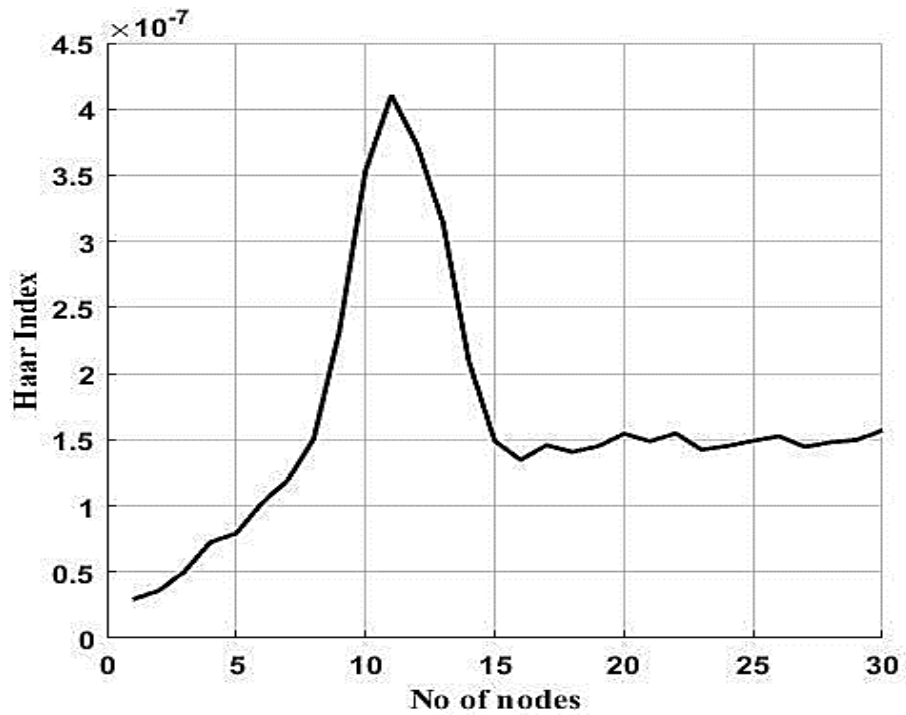

Fig 7-37: Experimental Haar index for fibre breakage 0.1 m from the fixed end of the impact damaged laminated plate B. The sharp peak demonstrates the presence of severe damage to the structure.
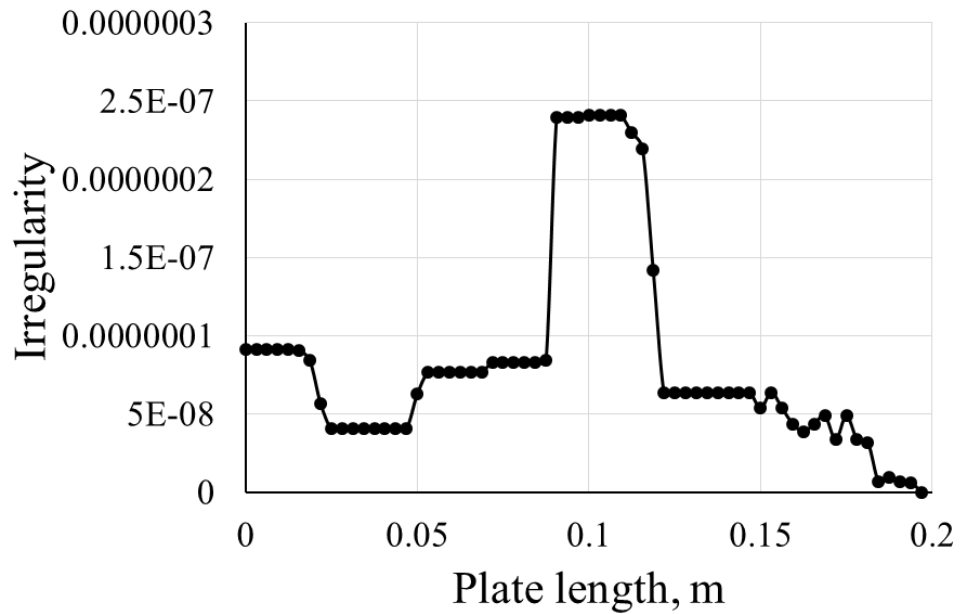
Fig 7-38: Experimental irregularity index for delamination 0.1 m from the fixed end of the impact damaged laminated plate B. The flat peak of the curve indicates the damaged area.
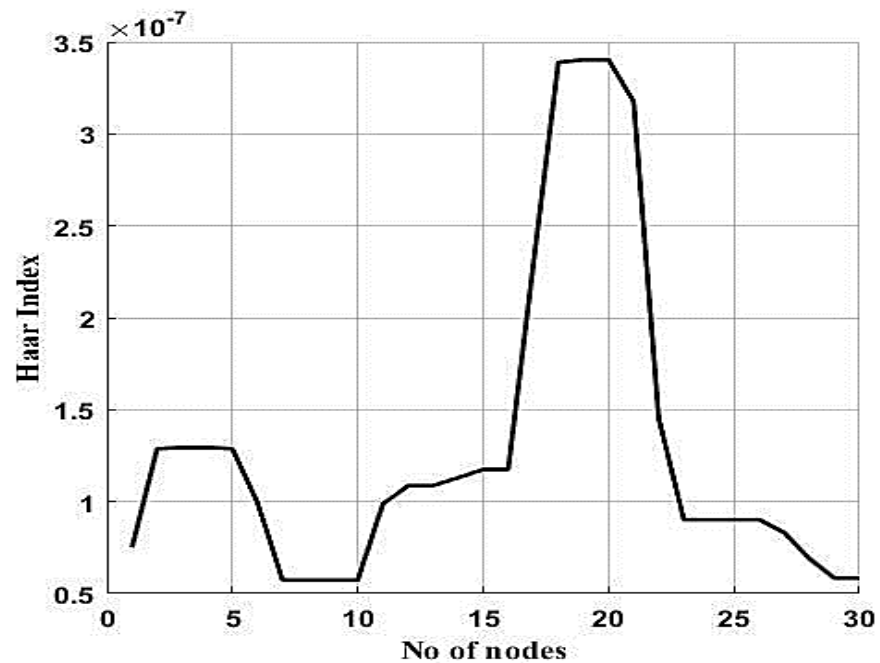

Fig 7-39: Experimental Haar index for delamination 0.1 m from the fixed end of the eight-layer impact damaged laminated plate A. The flat peak observed confirms that a small amount of damage is present in the structure.

7.8 Comparison between FEA and experimental work

This section presents the comparison between the data analysis in both finite element analysis presented in chapter 6 and experiment work reported in this chapter. The key premise in both chapters was the detection of fibre breakage and delamination using vibration-based damage techniques.

Damage detection entirely depends on the effect of these damages on the calculated mode shapes, where any damage causes a reduction in the local stiffness. In general, fibre breakage reduces local stiffness more than delamination, because Young's modulus of fibre is the main parameter in calculating ply-stiffness.

Another issue to be discussed is the effect of noise and errors in the experimental data. These effects influence the damage detection process. Here, the comparison includes relating the theoretical (FEA) and experimental mode shapes, curvature and the irregularity index. The data for narrow laminated plates and style B plates was implemented to perform this comparison.

Within the data of narrow laminated plates, as seen in Fig 7-40, there is no significant difference between theoretical and experimental modes. In this figure, theoretical modes (intact and damaged) shows profile smoother than experimental one. In both theoretical and experimental, mode shape with Del has more fluctuation than the intact mode and less than what observed in fibre breakage (FB) mode. This depends on the small reduction of stiffness in Del compared with FB.

Theoretical mode in FB showed the same experimental amplitude at 0.09 m (FB at 0.1 m), but still provides a smooth curve. It is not surprising to see this fluctuation in experiential data, as this the result of noise effects. In brief, theoretical and experimental modes showed convergence profiles, and in all modes, damaged areas were not detected.

Theoretical and experimental curvature indexes are compared for narrow laminated plate with FB at 0.1 m, as per Fig 7-41a, b, where the theoretical index is shown fluctuating along the plate length with maximum tip 3.6 at 0.1 m (FB location). In the same regard, experimental index shown in Fig 7-41b has a disturbed curve from 0.05 m to the end of plate with a max amplitude of 3.2 at 0.12 m. This means in both there no that difference and they did not detect the FB.

The effect of noise can be clearly seen on the calculating of irregularity index, as per Fig 7-42 a, b. In terms of peak, theoretical index has greater peak than the experimental one, with their values of 13 and 7.5 respectively. The experimental index was quite disturbed compared with the theoretical curve. This fluctuating is clearly observed after the damaged area. The sharp increase in both precisely detects the FB. In the same manner, theoretical and experimental irregularity indexes are compared for delaminated plates, as shown in Fig 7-43a, b. As in FB case, the amplitude of the theoretical irregularity index is greater than experimental value at 4.8 and 2.1. Whilst the flat tip in both is found. For experimental index the centre of the tip was identical to theoretical Del location. The sharp tip in FB case compared with the flat for Del is considered the legend of irregularity index. Also, both theoretical and experimental indexes detect the damaged area.
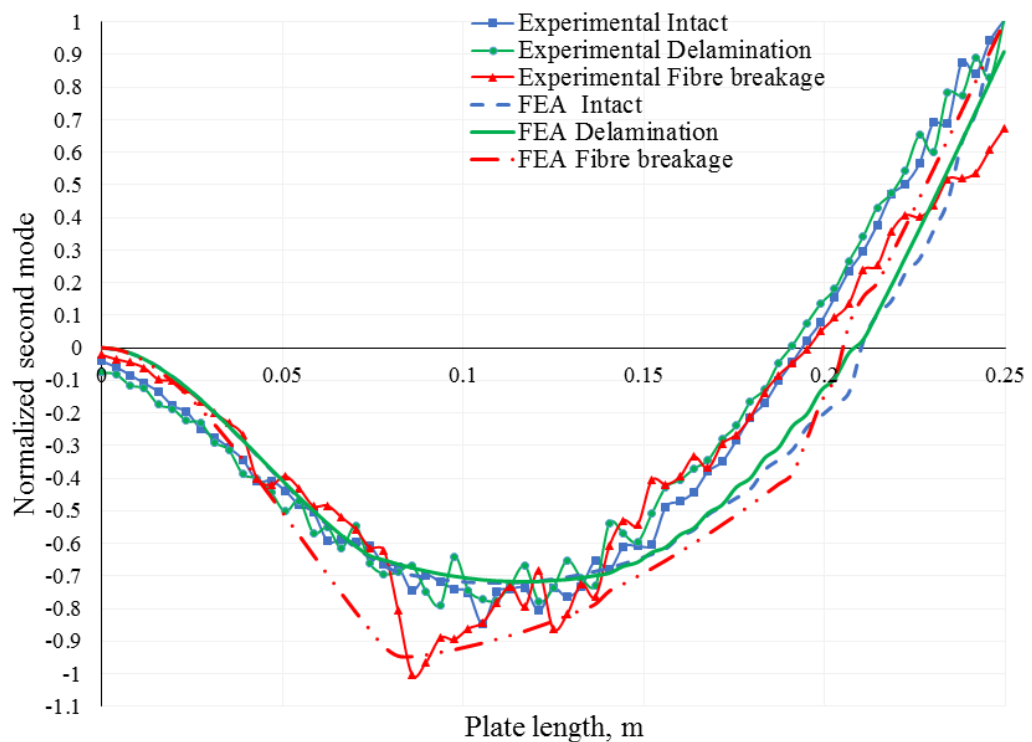
Fig 7-40: Theoretical and experimental intact and damaged normalized second mode shape for narrow laminated plates. FB and Del are located at 0.1m to the fixed edge, there is no a valuable difference between the intact and delamination response, whilst disturbance was found at the middle of plate with FB experimental mode.
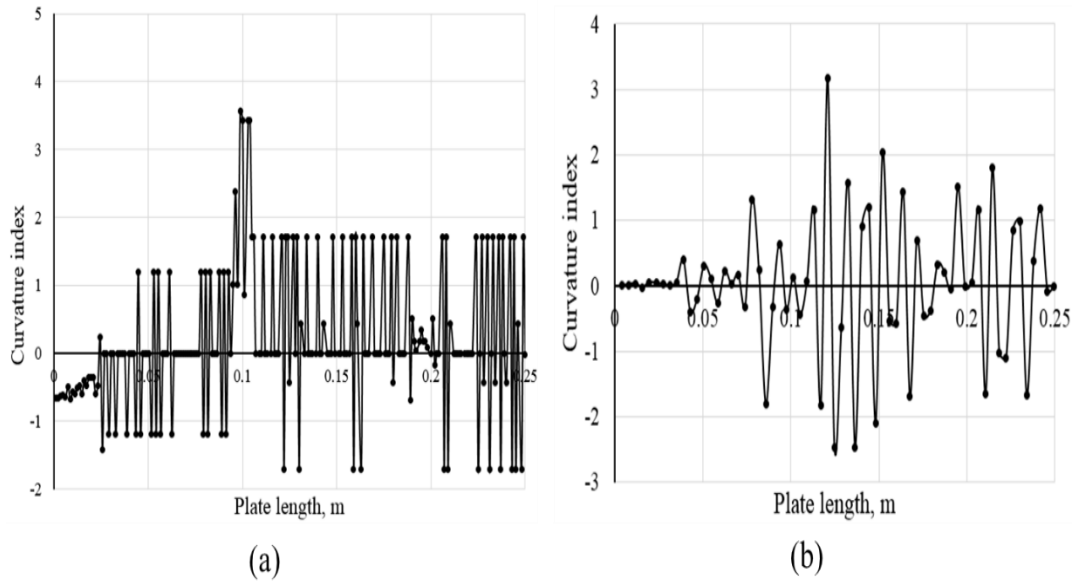
Fig 7-41: Curvature index of second mode shapes for narrow laminated plates with fibre breakage at 0.1m; a) theoretically (the entire curve shows clear disturbance and the damaged location was not detected, and b) experimentally (fluctuating observed along the curve and the damage not detected).
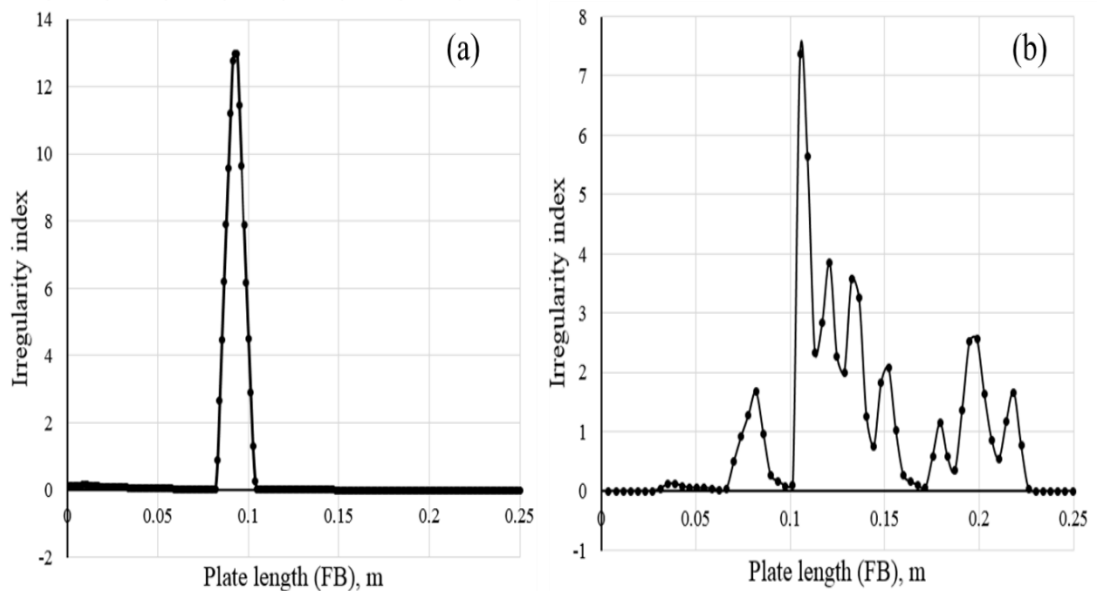
Fig 7-42: Irregularity index of second mode for narrow laminated plates with fibre breakage at 0.1 m; a) theoretical irregularity index, and b) experimental irregularity index, in all cases FB was successfully localized.
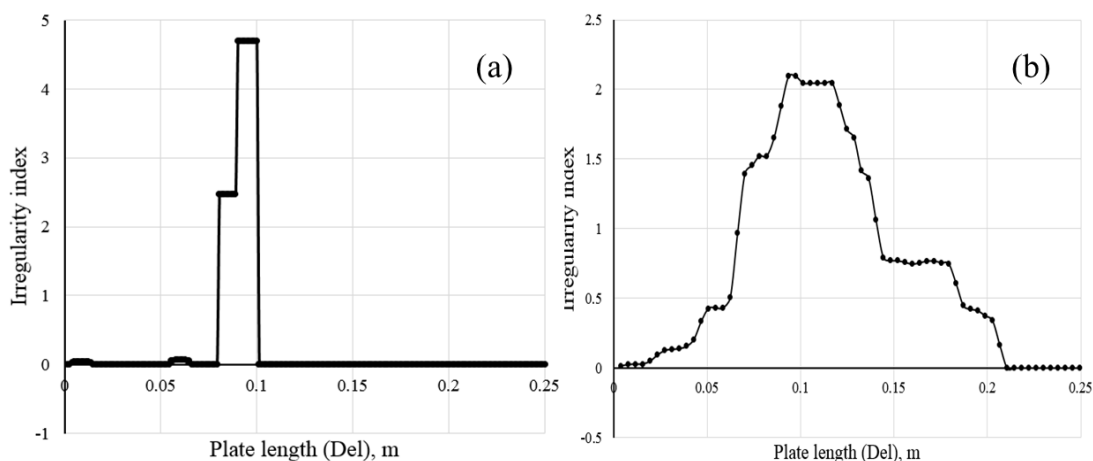
Fig 7-43: Irregularity index of second mode for narrow laminated plates with Del at 0.1 m; a) theoretical irregularity index, and b) experimental irregularity index, in both Del was localized.

The second part in this section is the comparison of theoretical and experimental mode shapes, curvature and irregularity index in style B laminated plates. As can be seen in Fig 7-44, there is no difference between the FEA and experimental modes in both intact and delamination (Del at 0.1 m), where the mode amplitude at 0.1 m is roughly - 0.8. In the same figure, the experimental mode with FB at 0.1 m showed fluctuated profile inverse the smooth curve of FEA mode, although in dynamic analysis this is not considered as a difference. The noise effect is one of the parameter causes for this divergence.

Then, the comparison between the FEA and experimental curvature index for artificial FB in style B plates is presented, as shown in Fig 7-45a, b.

According to the evaluation of curvature as an effective and sensitive index to any small change in the mode shape, a small jump in FEA curvature with value 600 was found at 0.1 m (FB location), as per Fig 7-45a. This jump disappeared in the experimental index as shown in Fig 7-45b. Again, noise reduces the efficiency of the curvature index, where the tip of the curvature is much less than FEA index at maximum 4.1. In brief, there is a difference in the amplitude and profile for FEA and experimental curvature indexes caused by the noisy data and both cannot be considered as an efficient indexes to detect FB and Del.

Finally, the irregularity index for both FEA and experiment is compared, where Fig 7-46a, b shows the comparison between the FE and experimental irregularity

indexes. In Fig 7-46a, the irregularity index showed a sharp peak with value 6.5 at FB location, whilst, experimentally, this value was 4.4 and the curve increased gradually after 0.05 m to its tip and then declined to 0.5 at $\cong 0.13$ m. This results that in both analysis the irregularity curve goes up to the sharp tip but in different manners. Experimentally, the tip of irregularity had a small shift to the damage location due to the noise data. The same issue performed to compare between irregularity indexes for FEA and experimental with Del, as shown in Fig 7-47a, b. For FEA index shown in Fig 7-47a, the peak value is 0.6 and the curve jumps at 0.09 m, then comes to the zero at 0.12 m (Del length is 0.02 m). Experimentally, the tip value was 0.28, as shown Fig 7-47b, the curve rises sharply at 0.075 m to the tip, then declined to 0.15 at plate length 0.12 m. The flat tip and the approximate numerical value for the FEA and experimental indexes emphasises the convergence between them. Also, another comparison in both Fig 7-46 and Fig 7-47 can be drawn, where the irregularity FB index showed sharper and greater magnitude than Del in FEA and experiment.
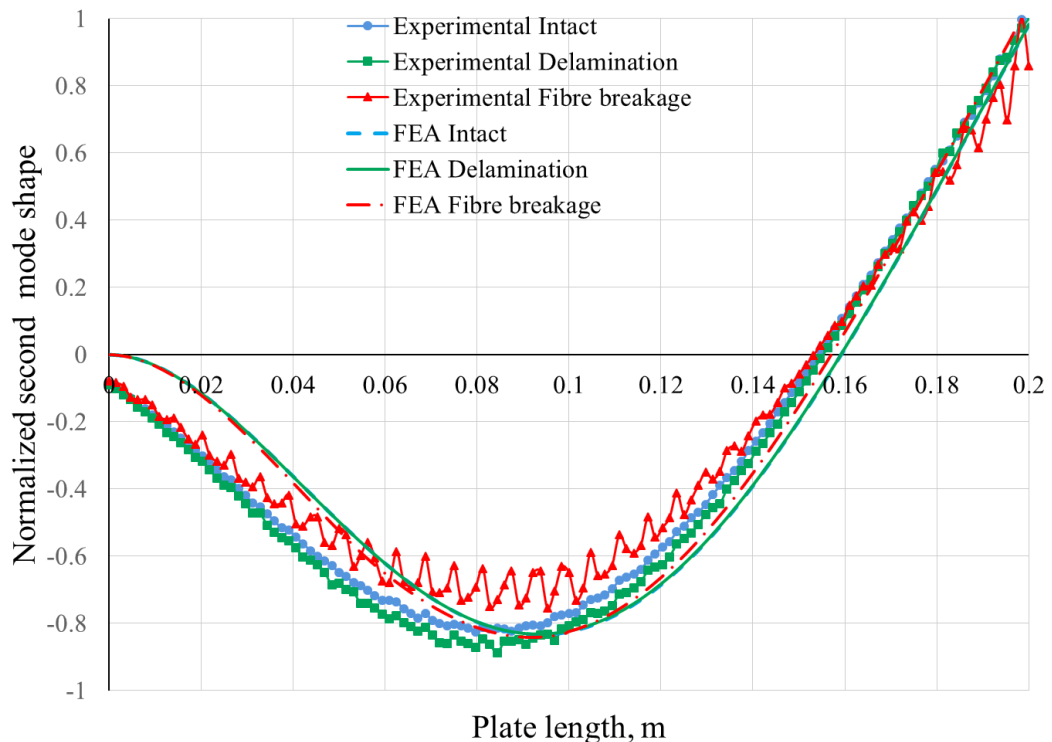
Fig 7-44: Theoretical and experimental intact and damaged normalized second mode shape for style B laminated plate. FB and Del are located at 0.1 m to the fixed edge, there is no a valuable difference between the intact and delamination response, whilst more fluctuation with the experimental FB mode.
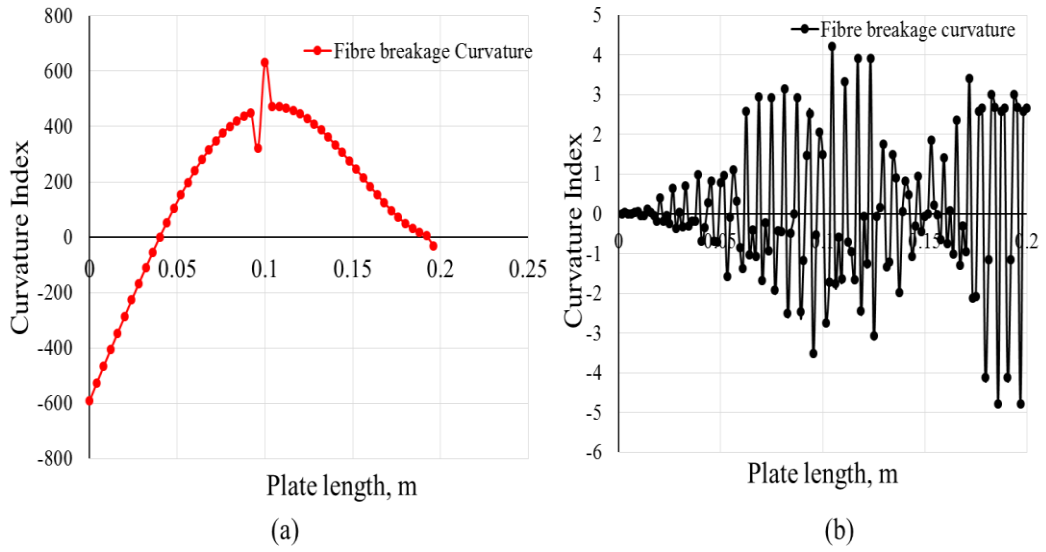
Fig 7-45: Curvature index of second mode shape for style B laminated plates with fibre breakage at 0.1m; a) theoretically (a small disturbance shown at damage location but that not efficient in the real applications, and b) experimentally (the entire cure is disturbed) .
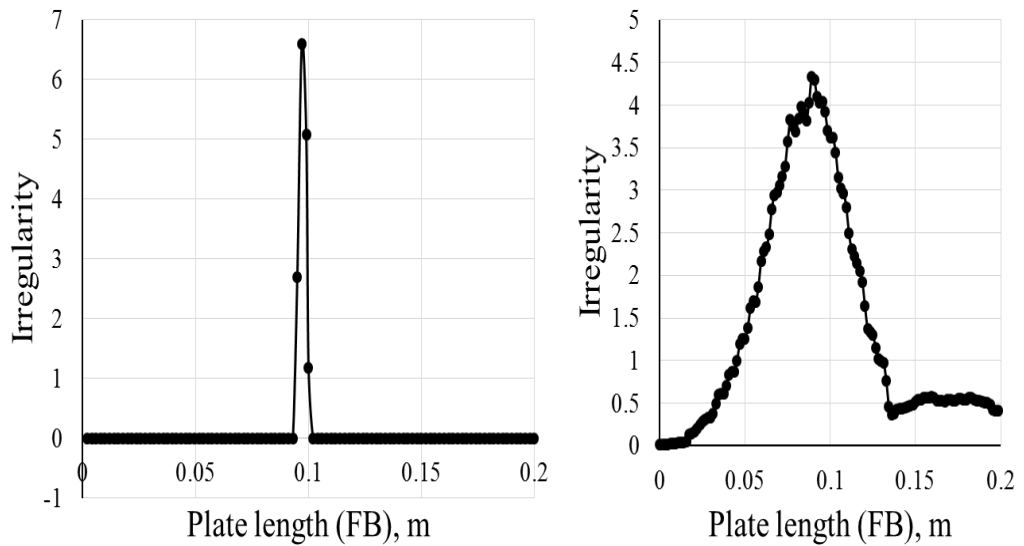
Fig 7-46: Irregularity index of second mode for style B laminated plates with fibre breakage at 0.1 m; a) theoretical irregularity index, and b) experimental irregularity index, in both FB was successfully localized.
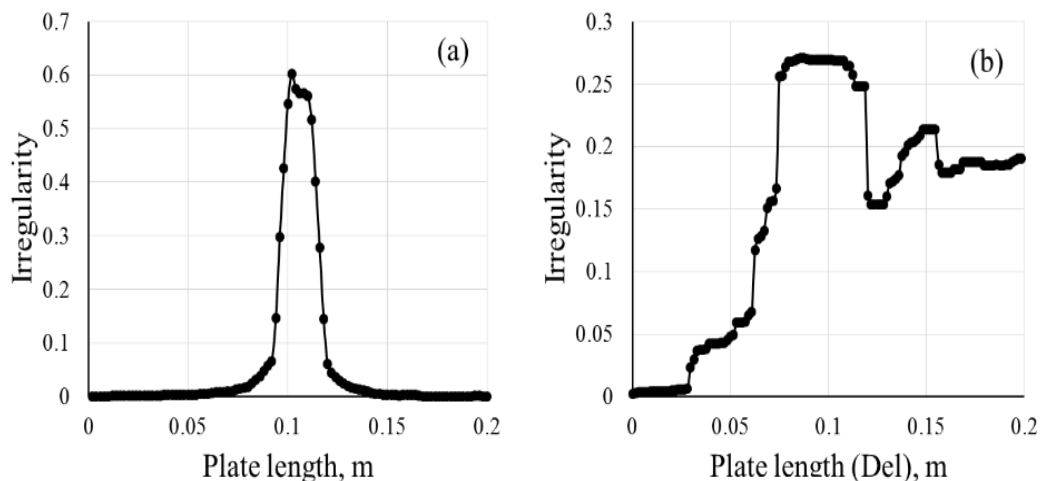
Fig 7-47: Irregularity index of second mode for style B laminated plates with delamination at 0.1 m; a) theoretical irregularity index and b) experimental irregularity index, in both Del was detected.

7.9 Summary

To summarise, this chapter has shown the experimental damage detection analysis of laminated CFRP composite plate structures using vibration-based damage detection techniques. The same laminated plate models discussed in chapter 6 were used to achieve the experimental analysis, whereas narrow and laminated plates with artificial damage, in addition to plates with impact damage, were used in this study. The narrow plates consisted of four symmetric layers, while the other samples consisted of eight symmetric layers. In experiment, the first three mode shapes were measured using a laser Doppler vibrometer. The first mode in each case was found to be extremely noisy, making it inefficient for the detection of damaged sections, whilst the second mode was generally found to be suitable in this regard. The second conclusion in this chapter is that the damaged modes and curvature index did not quantify and localize damaged areas for either artificial or impact damage. In contrast, calculating the irregularity index successfully detect both fibre breakage and delamination. Also, calculating the Haar index (using MATLAB R2017$_a$) as an improved method showed the same efficiency of detection as the irregularity index. Further, the use of both the irregularity and Harr indexes showed that fibre breakage has sharper peaks and grater magnitudes than delamination in laminated structures; the discrimination between delamination and fibre breakage being the main point of this research. This difference occurs due to the

considerably greater reduction in local stiffness due to fibre breakage than the case for delamination. In all cases, the effect of noise was clearly observed during the shift of tip from the real damage position and the fluctuating curves for both the irregularity and Haar indexes.

Chapter 8: Conclusions and future work

8.1   Conclusions

Early detection of damage in laminated structures is one of the most important requirements for structural health monitoring systems to avoid failures. Over the past few decades, vibration-based damage detection techniques have been utilized as a diagnostic method in different types of structures. Fundamentally, these techniques are based on the variation in local flexibility due to the existence of damage. To find the most suitable and yet accurate technique to use for a given problem, a number of parameters such as ease of use, accuracy and economic factors should be taken into consideration.

In this thesis, the vibration techniques to detect the damaged areas in carbon fibre reinforced polymer (CFRP) are developed using two indexes. The first one, which is called the irregularity curvature index, used the intact and damaged modes to assess the normality of these modes. The peak of this index was then utilized to localize and quantify the damaged araes. The second index, which is an improvement on the Haar index, used to perform the data analysis based on the irregularity index profile. The peaks that are picked up in this method added another approach for assessing the existence of damage. Both of these indexes showed the efficiency in damage detection particularly with experimental data.

In order to achieve the objective of this thesis, at first, simple cantilever beams with and without damage were modelled numerically using the finite element software COMSOL Multiphysics 5.1. Numerical simulation was run under free vibration condition to evaluate the efficiency of a number of dynamic response techniques used in damage detection (refer to Chapter 5). All beams were excited at their first two mode shapes. The damaged section was modelled by reducing the local stiffness (EI_d) with different values. In the analysis of the numerical simulation, it was shown that the mode shape and its slope are sensitive and, therefore, suitable for the detection of severe damages. The curvature index (refer to Eq.(4.2)), and fractal dimension (FD) (refer to Eq.(4.3)), also showed high sensitivity in the presence of a damage. The peak in both cases was associated with damaged sections. However, curvature index was much better

than fractal dimension index when noise effect is taken into account. Moreover, the irregularity index of mode shape (refer to Eq.(4.6)), showed a good sensitivity to the discontinuities in mode shape due to damaged sections. These numerical studies provide a significant understanding that, due to its sensitivity, using curvature-based damage detection is one of the most effective indexes that can be used for damage detection.

Secondly, damage detection in laminated composite structures was investigated numerically. Four-layer narrow and eight-layer CFRP laminated plates were used to model the fibre breakage and delamination. This modelling was accomplished using the ABAQUS 6.14-1 software. Cantilever plate condition was used for all plates which were analysed under free vibration condition. In the modelling, the fibre breakage is simulated by adding the mechanical properties of epoxy to the damaged area, and the delamination was modelled by adding a very thin layer (15 μm) of release film properties to the damaged area. The first two modes were calculated in order to detect the damage areas. Mode shape failed to detect both of fibre breakage and delamination in all plates. Applying the curvature index in this case (refer to Eq.(4.2)), did not detect the damaged areas. In contrast, applying the improved formula of irregularity curvature index (refer to Eq.(6.1)), successfully detected and differentiated between fibre breakage and delamination. Importantly, the clear peak with this improved formula of irregularity curvature index was used to show the damaged areas. The irregularity curvature index used in this way has not been reported previously in the literature. In addition, the analysis showed that fibre breakage has a sharper and higher magnitude peak than those found for delamination.

To compare FEA and experimental results, the samples discussed in FE analysis were manufactured to perform the experimental analysis. The artificial and impact damages (fibre breakage and delamination) in CFRP laminated structures were produced for the purpose of being tested. The first three mode shapes were measured using laser Doppler vibrometer located in ASDEC. The same conclusion of FEA can be drawn, where either mode shape or its curvature can detect the damaged area. In contrast, calculating the irregularity and the novel index (the Haar index) detected the damaged areas efficiently. Also they provide the same trend of data analysis, and they both showed peak with fibre breakage being sharper and greater magnitude than delamination. The major difference between FEA and experiment approach was the

noise effect seen in experimental method. This was picked up as random jumps in the irregularity and Haar indexes.

Finally, there are a number of conclusions that can be drawn. For CFRP laminated structures, the first mode was found quite noisy in all plates, rendering it essentially useless for damage detection purpose. The baseline data is extremely important for the detection of damaged areas. The main achievements of this thesis include the following:

- Different vibration-based damage indicators have been evaluated to ensure that most sensitive approach can be used for damage identification. For example, slope, curvature, irregularity and fractal dimension have all been considered in the analysis of intact and damaged data.

- A new method was used to calculate the reduction of the local stiffness of beam structures. This method depends on shifting the neutral axes to another location according to the damaged location.

- The noise effect was investigated to test the efficiency of vibration techniques in analysing a given signal.

- Manufacturing plate structures with and without damage to achieve the experimental part of the current research.

- Curvature index was improved by calculating the irregularity index. Additionally, the novel numerical Haar index is proposed to enhance the analysis of dynamic data. The Haar provides the same peak that can be found using irregularity index.

- Both irregularity and Haar indexes were applied to assess fibre breakage and delamination in the finite element and experimental analyses. Comparison between fibre breakage and delamination was presented.

8.2 Future Work

Vibration-based damage detection techniques are highly recommend to detect damage in different applications, not just laminated composite structures. Accordingly, these methods need to be investigated and developed extensively. Other indexes can be used along with the currently known-indexes to enhance the damage detection techniques. Thus, the future scientific research on this subject focus on the following:

- The application of the Haar and irregularity indexes to localize and quantify damaged area in complicated structures and extend their use to 2D or even 3D dynamic analysis.

- The use of these indexes to detect other types of damage such as those in non-composite structures.

- The current indexes can be used to detect damage in different types of composite materials with multiple damages.

- Other laminated structures such as curved beams, plate, trapezoidal, or triangular structures can be tested with actual impact loads, then current indexes can be used to detect the damaged areas.

- Because the key feature of damage detection depends on the possibility of showing discontinuities in modal characteristics due to the presence of damage, new methods can be developed to enhance the damage detection using this primary feature.

References

1.   Jones, R.M., *Mechanics of composite materials*. 1998: CRC press.

2.   Kaw, A.K., *Mechanics of composite materials*. 2010: CRC press.

3.   Isaac, M.D. and I. Ori, *Engineering mechanics of composite materials.* New York and Oxford, 1994.

4.   Kollár, L.P. and G.S. Springer, *Mechanics of composite structures*. 2003: Cambridge university press.

5.   Campbell, F.C., *Structural composite materials*. 2010: American Society for Metals (ASM)

6.   Vasiliev, V.V. and E. Morozov, *Advanced mechanics of composite materials and structural elements*. 2013: Newnes.

7.   Rana, S. and R. Fangueiro, *Advanced composite materials for aerospace engineering: Processing, properties and applications*. 2016: Woodhead Publishing.

8.   Heslehurst, R.B., *Defects and damage in composite materials and structures*. 2014: CRC Press.

9.   Heslehurst, R., *Repair of Composite and Bonded Structures: Appraisal and Future Needs of the RAAF.* 1991.

10.   Tita, V., J. De Carvalho, and D. Vandepitte, *Failure analysis of low velocity impact on thin composite laminates: Experimental and numerical approaches.* Composite Structures, 2008. **83**(4): p. 413-428.

11.   Zhang, Z., *Assessment of Delaminations in Composite Laminates using Vibration Monitoring*, in *School of Engineering and Information Technology.* August 2013, University of New South Wales Canberra. p. 324.

12.   Zou, Y., L. Tong, and G. Steven, *Vibration-based model-dependent damage (delamination) identification and health monitoring for composite structures—a review.* Journal of Sound and vibration, 2000. **230**(2): p. 357-378.

13.   Doebling, S.W., C.R. Farrar, and M.B. Prime, *A summary review of vibration-based damage identification methods.* Shock and vibration digest, 1998. **30**(2): p. 91-105.

14. Zhang, Z., et al., *Vibration-based delamination detection in composite beams through frequency changes.* Journal of Vibration and Control, 2014: p. 1077546314533584.

15. Hahn, H.T. and S.W. Tsai, *Introduction to composite materials*. Vol. 1. 1980: CRC Press.

16. Daniel, I.M. and O. Ishai, *Engineering mechanics of composite materials*. 2006, Oxford; New York: Oxford University Press.

17. Nettles, A.T., *Basic mechanics of laminated composite plates.* 1994.

18. Menard, K.P., *Dynamic mechanical analysis: a practical introduction*. 2008: CRC press.

19. Thomson, W., *Theory of vibration with applications*. 1996: CRC Press.

20. Inman, D.J., *Engineering vibration*. 1994, Englewood Cliffs, N.J; London: Prentice Hall.

21. Rao, S.S., *Mechanical vibrations.* 1993(Book, Whole).

22. Rao, S.S., *The finite element method in engineering*. 2017: Butterworth-heinemann.

23. Liu, G.-R. and S.S. Quek, *The finite element method: a practical course*. 2013: Butterworth-Heinemann.

24. Yoo, H. and S. Shin, *Vibration analysis of rotating cantilever beams.* Journal of Sound and vibration, 1998. **212**(5): p. 807-828.

25. Doebling, S.W., et al., *Damage identification and health monitoring of structural and mechanical systems from changes in their vibration characteristics: a literature review*. 1996, Los Alamos National Lab., NM (United States).

26. Yam, L., Y. Yan, and J. Jiang, *Vibration-based damage detection for composite structures using wavelet transform and neural network identification.* Composite Structures, 2003. **60**(4): p. 403-412.

27. Yan, Y. and L. Yam, *Detection of delamination damage in composite plates using energy spectrum of structural dynamic responses decomposed by wavelet analysis.* Computers & structures, 2004. **82**(4): p. 347-358.

28. Salawu, O., *Detection of structural damage through changes in frequency: a review.* Engineering structures, 1997. **19**(9): p. 718-723.

29. Messina, A., E. Williams, and T. Contursi, *Structural damage detection by a sensitivity and statistical-based method.* Journal of sound and vibration, 1998. **216**(5): p. 791-808.

30. Chinchalkar, S., *Determination of crack location in beams using natural frequencies.* Journal of Sound and vibration, 2001. **247**(3): p. 417-429.

31. Patil, D. and S. Maiti, *Detection of multiple cracks using frequency measurements.* Engineering Fracture Mechanics, 2003. **70**(12): p. 1553-1572.

32. Kim, J.-T., et al., *Damage identification in beam-type structures: frequency-based method vs mode-shape-based method.* Engineering Structures, 2003. **25**(1): p. 57-67.

33. Lee, J., *Identification of multiple cracks in a beam using natural frequencies.* Journal of sound and vibration, 2009. **320**(3): p. 482-490.

34. Fan, W. and P. Qiao, *Vibration-based damage identification methods: a review and comparative study.* Structural Health Monitoring, 2011. **10**(1): p. 83-111.

35. Farrar, C. and G. James III, *System identification from ambient vibration measurements on a bridge.* Journal of Sound and Vibration, 1997. **205**(1): p. 1-18.

36. Ostachowicz, W. and M. Krawczuk, *Vibration analysis of a cracked beam.* Computers & Structures, 1990. **36**(2): p. 245-250.

37. Abdo, M.-B. and M. Hori, *A numerical study of structural damage detection using changes in the rotation of mode shapes.* Journal of Sound and vibration, 2002. **251**(2): p. 227-239.

38. Ghoshal, A., et al., *Experimental investigation of damage detection in composite material structures using a laser vibrometer and piezoelectric actuators.* Journal of Intelligent Material Systems and Structures, 2003. **14**(8): p. 521-537.

39. Lee, J.J., et al., *Neural networks-based damage detection for bridges considering errors in baseline finite element models.* Journal of Sound and Vibration, 2005. **280**(3): p. 555-578.

40. dos Santos, J.A., et al., *Damage localization in laminated composite plates using mode shapes measured by pulsed TV holography.* Composite structures, 2006. **76**(3): p. 272-281.

41. Yan, Y., et al., *Development in vibration-based structural damage detection technique.* Mechanical Systems and Signal Processing, 2007. **21**(5): p. 2198-2211.

42. Qiao, P., K. Lu, and W. Lestari, *A combined static/dynamic technique for damage detection of laminated composite plates.* Experimental Mechanics, 2008. **48**(1): p. 17-35.

43. Yoon, M.-K., et al., *Local damage detection with the global fitting method using mode shape data in notched beams.* Journal of Nondestructive Evaluation, 2009. **28**(2): p. 63-74.

44. Roy, K. and S. Ray-Chaudhuri, *Fundamental mode shape and its derivatives in structural damage localization.* Journal of Sound and Vibration, 2013. **332**(21): p. 5584-5593.

45. Hemez, F.M., *Uncertainty quantification and the verification and validation of computational models.* Damage Prognosis for Aerospace, Civil and Mechanical Systems, 2004: p. 201-220.

46. Hadjileontiadis, L., E. Douka, and A. Trochidis, *Fractal dimension analysis for crack identification in beam structures.* Mechanical Systems and Signal Processing, 2005. **19**(3): p. 659-674.

47. Hadjileontiadis, L. and E. Douka, *Crack detection in plates using fractal dimension.* Engineering Structures, 2007. **29**(7): p. 1612-1625.

48. Wang, J. and P. Qiao, *Improved damage detection for beam-type structures using a uniform load surface.* Structural Health Monitoring, 2007. **6**(2): p. 99-110.

49. Qiao, P., et al., *Curvature mode shape-based damage detection in composite laminated plates.* Composite Structures, 2007. **80**(3): p. 409-428.

50. Qiao, P. and M. Cao, *Waveform fractal dimension for mode shape-based damage identification of beam-type structures.* International Journal of Solids and Structures, 2008. **45**(22-23): p. 5946-5961.

51. Hadjileontiadis, L.J., E. Douka, and A. Trochidis, *Crack detection in beams using kurtosis.* Computers & structures, 2005. **83**(12): p. 909-919.

52. Li, H., et al., *Fractal Dimension-Based Damage Detection Method for Beams with a Uniform Cross-Section.* Computer-Aided Civil and Infrastructure Engineering, 2011. **26**(3): p. 190-206.

53. Jiang, Y.-Y., et al., *Identification of Crack Location in Beam Structures Using Wavelet Transform and Fractal Dimension.* Shock and Vibration, 2015. **2015**.

54. Liew, K. and Q. Wang, *Application of wavelet theory for crack identification in structures.* Journal of engineering mechanics, 1998. **124**(2): p. 152-157.

55. Wang, Q. and X. Deng, *Damage detection with spatial wavelets.* International journal of solids and structures, 1999. **36**(23): p. 3443-3468.

56. Quek, S.-T., et al., *Sensitivity analysis of crack detection in beams by wavelet technique.* International journal of mechanical sciences, 2001. **43**(12): p. 2899-2910.

57. Douka, E., S. Loutridis, and A. Trochidis, *Crack identification in beams using wavelet analysis.* International Journal of Solids and Structures, 2003. **40**(13-14): p. 3557-3569.

58. Douka, E., S. Loutridis, and A. Trochidis, *Crack identification in plates using wavelet analysis.* Journal of sound and vibration, 2004. **270**(1-2): p. 279-295.

59. Gentile, A. and A. Messina, *On the continuous wavelet transforms applied to discrete vibrational data for detecting open cracks in damaged beams.* International Journal of Solids and Structures, 2003. **40**(2): p. 295-315.

60. Chang, C.-C. and L.-W. Chen, *Damage detection of a rectangular plate by spatial wavelet based approach.* Applied Acoustics, 2004. **65**(8): p. 819-832.

61. Rucka, M. and K. Wilde, *Application of continuous wavelet transform in vibration based damage detection method for beams and plates.* Journal of Sound and Vibration, 2006. **297**(3-5): p. 536-550.

62. Fan, W. and P. Qiao, *A 2-D continuous wavelet transform of mode shape data for damage detection of plate structures.* International Journal of Solids and Structures, 2009. **46**(25-26): p. 4379-4395.

63. Shahsavari, V., L. Chouinard, and J. Bastien, *Wavelet-based analysis of mode shapes for statistical detection and localization of damage in beams using likelihood ratio test.* Engineering Structures, 2017. **132**: p. 494-507.

64. Khan, A., A.B. Stanbridge, and D.J. Ewins, *Detecting damage in vibrating structures with a scanning LDV.* Optics and Lasers in Engineering, 1999. **32**(6): p. 583-592.

65. Pandey, A.K., M. Biswas, and M.M. Samman, *Damage detection from changes in curvature mode shapes.* Journal of Sound and Vibration, 1991. **145**(2): p. 321-332.

66. Salawu, O. and C. Williams. *Damage location using vibration mode shapes.* in *Proceedings of the 12th International Modal Analysis.* 1994.

67. Swamidas, A. and Y. Chen, *Monitoring crack growth through change of modal parameters.* Journal of Sound and Vibration, 1995. **186**(2): p. 325-343.

68. Ratcliffe, C.P., *Damage detection using a modified Laplacian operator on mode shape data.* Journal of Sound and Vibration, 1997. **204**(3): p. 505-517.

69. Ratcliffe, C.P. and W.J. Bagaria, *Vibration technique for locating delamination in a composite beam.* AIAA journal, 1998. **36**(6): p. 1074-1077.

70. Sampaio, R., N. Maia, and J. Silva, *Damage detection using the frequency-response-function curvature method.* Journal of Sound and Vibration, 1999. **226**(5): p. 1029-1042.

71. Wahab, M.A. and G. De Roeck, *Damage detection in bridges using modal curvatures: application to a real damage scenario.* Journal of Sound and Vibration, 1999. **226**(2): p. 217-235.

72. Ratcliffe, C.P., *A frequency and curvature based experimental method for locating damage in structures.* Journal of vibration and acoustics, 2000. **122**(3): p. 324-329.

73. Hamey, C.S., et al., *Experimental damage identification of carbon/epoxy composite beams using curvature mode shapes.* Structural Health Monitoring, 2004. **3**(4): p. 333-353.

74. Lestari, W. and P. Qiao, *Damage detection of fiber-reinforced polymer honeycomb sandwich beams.* Composite Structures, 2005. **67**(3): p. 365-373.

75. Kim, B.H., T. Park, and G.Z. Voyiadjis, *Damage estimation on beam-like structures using the multi-resolution analysis.* International Journal of Solids and Structures, 2006. **43**(14): p. 4238-4257.

76. Hu, C. and M.T. Afzal, *A statistical algorithm for comparing mode shapes of vibration testing before and after damage in timbers.* Journal of Wood Science, 2006. **52**(4): p. 348-352.

77. Mosti, F., G. Quaranta, and W. Lacarbonara. *Numerical and experimental assessment of the modal curvature method for damage detection in plate structures.* in *MATEC Web of Conferences.* 2014. EDP Sciences.

78. Dessi, D. and G. Camerlengo, *Damage identification techniques via modal curvature analysis: overview and comparison.* Mechanical Systems and Signal Processing, 2015. **52**: p. 181-205.

79. Chandrashekhar, M. and R. Ganguli, *Damage assessment of composite plate structures with material and measurement uncertainty.* Mechanical Systems and Signal Processing, 2016. **75**: p. 75-93.

80. Pandey, A. and M. Biswas, *Damage detection in structures using changes in flexibility.* Journal of sound and vibration, 1994. **169**(1): p. 3-17.

81. Zhang, Z. and A. Aktan, *Application of modal flexibility and its derivatives in structural identification.* Research in Nondestructive Evaluation, 1998. **10**(1): p. 43-61.

82. Wu, D. and S. Law, *Damage localization in plate structures from uniform load surface curvature.* Journal of Sound and Vibration, 2004. **276**(1-2): p. 227-244.

83. Wu, D. and S. Law, *Sensitivity of uniform load surface curvature for damage identification in plate structures.* Journal of vibration and acoustics, 2005. **127**(1): p. 84-92.

84. Bernagozzi, G., et al., *Application of modal flexibility-based deflections for damage diagnosis of a steel frame structure.* Procedia Engineering, 2017. **199**: p. 2026-2033.

85. Hellier, C., *Handbook of nondestructive evaluation.* Vol. 10. 2001: Mcgraw-hill New York.

86. Dutton, A., *Flaw detection in composite materials using infra-red thermography by the method of external heating.* Proceedings of the Institution of Mechanical Engineers, Part C: Journal of Mechanical Engineering Science, 1996. **210**(5): p. 399-407.

87. Genest, M., et al., *Pulsed thermography for non-destructive evaluation and damage growth monitoring of bonded repairs.* Composite Structures, 2009. **88**(1): p. 112-120.

88. Avdelidis, N.P., et al., *Aircraft composites assessment by means of transient thermal NDT.* Progress in Aerospace Sciences, 2004. **40**(3): p. 143-162.

89. Meola, C., et al., *Detection of delamination in carbon-fibre-reinforced polymers with lock-in thermography.* Proceedings of the Institution of Mechanical Engineers, Part G: Journal of Aerospace Engineering, 2010. **224**(11): p. 1219-1227.

90. Shull, P.J., *Nondestructive evaluation: theory, techniques, and applications.* 2016: CRC press.

91.   Fiori, F., et al., *Crack detection in Al alloy using phase-contrast neutron radiography and tomography.* Measurement Science and Technology, 2006. **17**(9): p. 2479.

92.   Xu, J., et al., *Automatic X-ray crack inspection for aircraft wing fastener holes.* NDT in Aerospace, 2010.

93.   De Albuquerque, V.H.C., J.M.R. Tavares, and L.M. Durão, *Evaluation of delamination damage on composite plates using an artificial neural network for the radiographic image analysis.* Journal of Composite Materials, 2010. **44**(9): p. 1139-1159.

94.   Holford, K.M., et al., *Damage location in steel bridges by acoustic emission.* Journal of intelligent material systems and structures, 2001. **12**(8): p. 567-576.

95.   Hatta, H., et al., *Damage detection of C/C composites using ESPI and SQUID techniques.* Composites Science and Technology, 2005. **65**(7-8): p. 1098-1106.

96.   Elforjani, M. and D. Mba, *Accelerated natural fault diagnosis in slow speed bearings with acoustic emission.* Engineering Fracture Mechanics, 2010. **77**(1): p. 112-127.

97.   Gupta, S., D.S. Singh, and A. Ray, *Statistical pattern analysis of ultrasonic signals for fatigue damage detection in mechanical structures.* NDT & E International, 2008. **41**(7): p. 491-500.

98.   Harri, K., P. Guillaume, and S. Vanlanduit, *On-line damage detection on a wing panel using transmission of multisine ultrasonic waves.* NDT & E International, 2008. **41**(4): p. 312-317.

99.   Valdes, S.D. and C. Soutis, *Delamination detection in composite laminates from variations of their modal characteristics.* Journal of sound and vibration, 1999. **228**(1): p. 1-9.

100.   Kim, H.-Y. and W. Hwang, *Effect of debonding on natural frequencies and frequency response functions of honeycomb sandwich beams.* Composite Structures, 2002. **55**(1): p. 51-62.

101. Lestari, W., P. Qiao, and S. Hanagud, *Curvature mode shape-based damage assessment of carbon/epoxy composite beams.* Journal of intelligent material systems and structures, 2007. **18**(3): p. 189-208.

102. Wang, J. and P. Qiao, *On irregularity-based damage detection method for cracked beams.* International Journal of Solids and Structures, 2008. **45**(2): p. 688-704.

103. Cao, M., et al., *Sensitivity of fundamental mode shape and static deflection for damage identification in cantilever beams.* Mechanical Systems and Signal Processing, 2011. **25**(2): p. 630-643.

104. Bazardehi, S.R.K. and M.A. Kouchakzadeh, *Detection of delamination in composite laminated plates using filtered mode shapes.* Proceedings of the Institution of Mechanical Engineers, Part C: Journal of Mechanical Engineering Science, 2012. **226**(12): p. 2902-2911.

105. Ullah, I. and J.K. Sinha, *A Novel Method for Delamination Detection in Composites.* International Journal of Innovation and Applied Studies, 2013. **2**(1): p. 34-42.

106. Eraky, A., et al., *Damage detection of flexural structural systems using damage index method – Experimental approach.* Alexandria Engineering Journal, 2015(0).

107. Ghosh, G. and S. Ray-Chaudhuri, *Location sensitivity of fundamental and higher mode shapes in localization of damage within a building.* Journal of Sound and Vibration, 2016. **365**: p. 244-259.

108. Jaureguiz, C.R.F.a.D.A., *Comparative study of damage identification algorithms applied to abridge: I. Experiment.* Smart Materials & Structures, 1998. **7**: p. 704–719.

109. Farrar, C.R. and D.A. Jauregui, *Comparative study of damage identification algorithms applied to a bridge: II. Numerical study.* Smart materials and structures, 1998. **7**(5): p. 720.

110. Ndambi, J.-M., J. Vantomme, and K. Harri, *Damage assessment in reinforced concrete beams using eigenfrequencies and mode shape derivatives.* Engineering Structures, 2002. **24**(4): p. 501-515.

111. Chati, M., R. Rand, and S. Mukherjee, *Modal analysis of a cracked beam.* Journal of Sound and Vibration, 1997. **207**(2): p. 249-270.

112. Barad, K.H., D. Sharma, and V. Vyas, *Crack detection in cantilever beam by frequency based method.* Procedia Engineering, 2013. **51**: p. 770-775.

113. Chandrashekhar, M. and R. Ganguli, *Damage assessment of structures with uncertainty by using mode-shape curvatures and fuzzy logic.* Journal of Sound and Vibration, 2009. **326**(3): p. 939-957.

114. Katz, M.J., *Fractals and the analysis of waveforms.* Computers in biology and medicine, 1988. **18**(3): p. 145-156.

115. Allen, M.S. and M.W. Sracic, *A new method for processing impact excited continuous-scan laser Doppler vibrometer measurements.* Mechanical Systems and Signal Processing, 2010. **24**(3): p. 721-735.

116. Stanbridge, A. and D. Ewins, *Modal testing using a scanning laser Doppler vibrometer.* Mechanical Systems and Signal Processing, 1999. **13**(2): p. 255-270.

117. Rothberg, S., Baker,J., and Halliwell,N.A.,, *Laser Vibrometry: Pseudo-Vibrations.* Engineering structures, 1989. **28**: p. 1803-1815.

118. Sriram, P., et al., *Scanning laser Doppler technique for velocity profile sensing on a moving surface.* Applied optics, 1990. **29**(16): p. 2409-2417.

119. Sriram, P., J. Craig, and S. Hanagud, *Scanning laser Doppler techniques for vibration testing.* Experimental Techniques, 1992. **16**(6): p. 21-26.

120. Stanbridge, A. and D. Ewins. *Using a continuously-scanning laser doppler vibrometer for modal testing.* in *Proceedings-Spie The International Society For Optical Engineering.* 1996. Spie International Society for Optical.

121. Stanbridge, A., D. Ewins, and A. Khan, *Modal testing using impact excitation and a scanning LDV.* Shock and Vibration, 2000. **7**(2): p. 91-100.

122. Di Maio, D. and D. Ewins, *Continuous Scan, a method for performing modal testing using meaningful measurement parameters; Part I.* Mechanical Systems and Signal Processing, 2011. **25**(8): p. 3027-3042.

123. Bougard, A.J. and B. Ellis, *Laser measurement of building vibration and displacement.* Shock and vibration, 2000. **7**(5): p. 287-298.

124. Kaito, K., M. Abe, and Y. Fujino. *An experimental modal analysis for RC bridge decks based on non-contact vibration measurement.* in *Proceedings of the International Modal Analysis Conference-IMAC.* 2001. Society for Experimental Mechanics.

125. Yang, S. and M.S. Allen, *Lifting approach to simplify output-only continuous-scan laser vibrometry.* Mechanical Systems and Signal Processing, 2014. **45**(2): p. 267-282.

126. Yang, S. and M.S. Allen, *Harmonic transfer function to measure translational and rotational velocities with continuous-scan laser Doppler vibrometry.* Journal of Vibration and Acoustics, 2014. **136**(2): p. 021025.

127. Banwell, G.H., et al., *Understanding the dynamic behaviour of a tennis racket under play conditions.* Experimental Mechanics, 2014. **54**(4): p. 527-537.

128. Rothberg, S., et al., *An international review of laser Doppler vibrometry: Making light work of vibration measurement.* Optics and Lasers in Engineering, 2016.

129. Aktaş, M., et al., *An experimental investigation of the impact response of composite laminates.* Composite Structures, 2009. **87**(4): p. 307-313.

130. Albrecht, H.-E., et al., *Laser Doppler and phase Doppler measurement techniques.* 2013: Springer Science & Business Media.

131. Bathe, K.J. and E.N. Dvorkin, *A formulation of general shell elements—the use of mixed interpolation of tensorial components.* International Journal for Numerical Methods in Engineering, 1986. **22**(3): p. 697-722.

132. Castellini, P., M. Martarelli, and E. Tomasini, *Laser Doppler Vibrometry: Development of advanced solutions answering to technology's needs.* Mechanical Systems and Signal Processing, 2006. **20**(6): p. 1265-1285.

133. Sriram, P., Hanagud,S.,Craig,J.I.,, *Mode shape measurement using a scanning laser Doppler vibrometer.* The International journal of analytical and experimental modal analysis July 1992. **7(3)**: p. 169-178.

134. Mallat, S.G., *A theory for multiresolution signal decomposition: the wavelet representation.* IEEE transactions on pattern analysis and machine intelligence, 1989. **11**(7): p. 674-693.

135. Ovanesova, A. and L. Suarez, *Applications of wavelet transforms to damage detection in frame structures.* Engineering structures, 2004. **26**(1): p. 39-49.